

JANUARY 2024

AJNR

VOLUME 45 • PP 1-126

AJNR

AMERICAN JOURNAL OF NEURORADIOLOGY

Official Journal ASNR • ASFNR • ASHNR • ASPNR • ASSR

JANUARY 2024 | VOLUME 45 | NUMBER 1 | WWW.AJNR.ORG

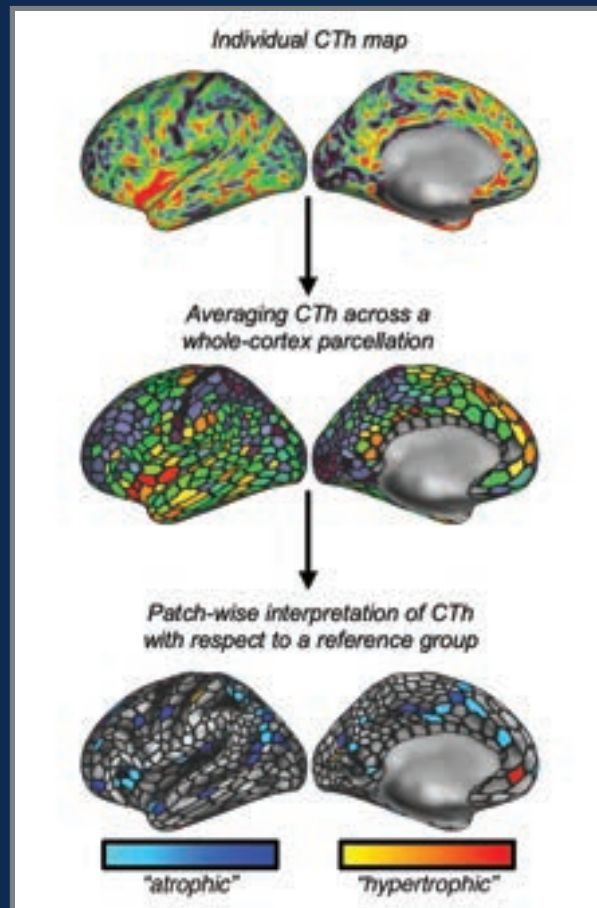
THE JOURNAL OF DIAGNOSTIC AND INTERVENTIONAL NEURORADIOLOGY

Real-time monitoring by MR thermometry in MRgFUS

Clinical relevance of contrast extravasation on DECT after endovascular thrombectomy

Central vein sign in MS on 7T

Temporal characteristics of CSF venous fistulas on dynamic decubitus CT myelography



FRED™ X™

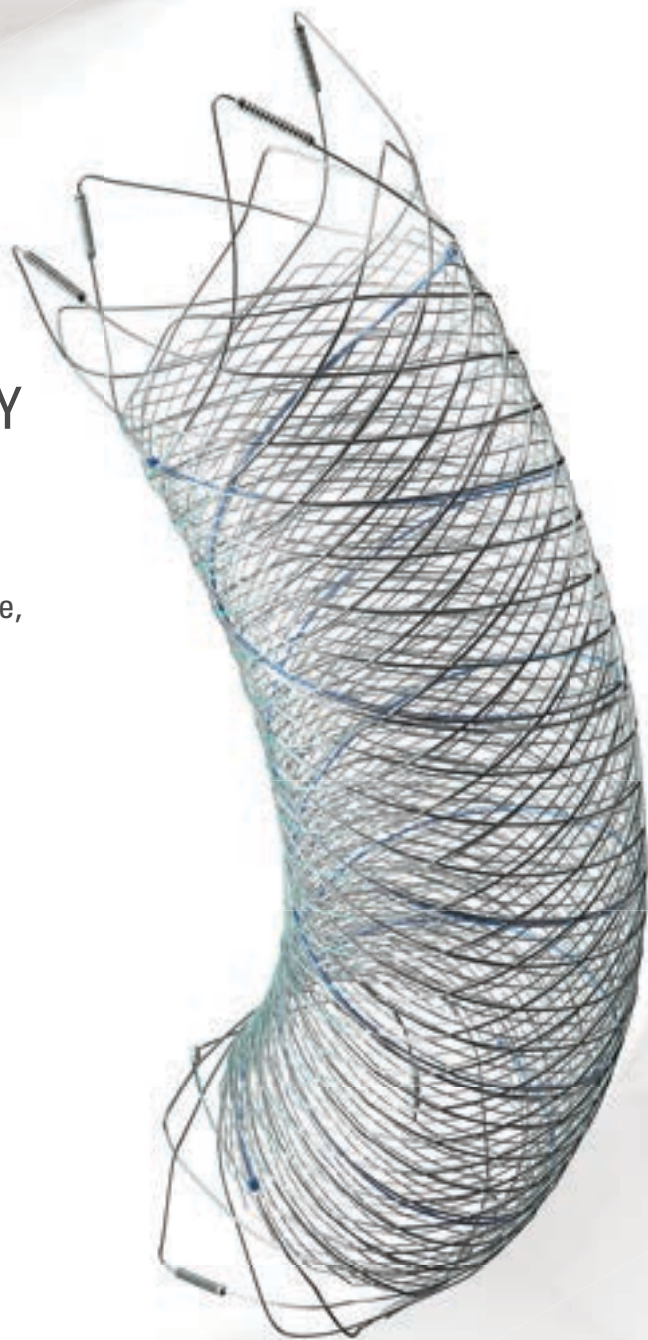
Flow Diverter Stent

THE NEXT ADVANCEMENT IN FLOW DIVERSION TECHNOLOGY

The FRED™ X Flow Diverter features the same precise placement and immediate opening of the FRED™ Device, now with X Technology. X Technology is a covalently bonded, nanoscale surface treatment, designed to:

- **REDUCE MATERIAL THROMBOGENICITY¹**
- **MAINTAIN NATURAL VESSEL HEALING RESPONSE^{2,3,4}**
- **IMPROVE DEVICE DELIVERABILITY AND RESHEATHING¹**

The only FDA PMA approved portfolio with a 0.021" delivery system for smaller device sizes, and no distal lead wire.



For more information, contact your local MicroVention sales representative or visit our website. www.microvention.com

 **MicroVention™**
TERUMO

^{*} Data is derived from in vivo and ex vitro testing and may not be representative of clinical performance.

¹ Data on file

² Tanaka M et al. Design of biocompatible and biodegradable polymers based on intermediate water concept. *Polymer Journal*. 2015;47:114-121.

³ Tanaka M et al. Blood compatible aspects of poly(2-methoxyethylacrylate) (PMEA) – relationship between protein adsorption and platelet adhesion on PMEAs surface. *Biomaterials*. 2000;21:1471-1481.

⁴ Schiel L et al. X Coating™: A new biopassive polymer coating. *Canadian Perfusion Canadienne*. June 2001;11(2):9.

Indications for Use: The FRED X System is indicated for use in the internal carotid artery from the petrous segment to the terminus for the endovascular treatment of adult patients (22 years of age or older) with wide-necked (neck width 4 mm or dome-to-neck ratio < 2) saccular or fusiform intracranial aneurysms arising from a parent vessel with a diameter 2.0 mm and 5.0 mm.

Rx Only: Federal (United States) law restricts this device to sale by or on the order of a physician. For Healthcare professionals intended use only.

MICROVENTION, FRED and HEADWAY are registered trademarks of MicroVention, Inc. in the United States and other jurisdictions. Stylized X is a trademark of MicroVention, Inc. © 2022 MicroVention, Inc. MM1222 US 03/22

WEB™ 17

Aneurysm Embolization System

LOWER PROFILE



NEW SIZES



MORE ACCESS OPTIONS



INDICATIONS FOR USE:

The WEB Aneurysm Embolization System is intended for the endovascular embolization of ruptured and unruptured intracranial aneurysms and other neurovascular abnormalities such as arteriovenous fistulae (AVF). The WEB Aneurysm Embolization System is also intended for vascular occlusion of blood vessels within the neurovascular system to permanently obstruct blood flow to an aneurysm or other vascular malformation.

POTENTIAL COMPLICATIONS:

Potential complications include but are not limited to the following: hematoma at the site of entry, aneurysm rupture, emboli, vessel perforation, parent artery occlusion, hemorrhage, ischemia, vasospasm, clot formation, device migration or misplacement, premature or difficult device detachment, non-detachment, incomplete aneurysm filling, revascularization, post-embolization syndrome, and neurological deficits including stroke and death. For complete indications, potential complications, warnings, precautions, and instructions, see instructions for use (IFU provided with the device).

VIA 21, 27, 33 - The VIA Microcatheter is intended for the introduction of interventional devices (such as the WEB device/stents/flow diverters) and infusion of diagnostic agents (such as contrast media) into the neuro, peripheral, and coronary vasculature.

VIA 17,17 Preshaped - The VIA Microcatheter is intended for the introduction of interventional devices (such as the WEB device/stents/flow diverters) and infusion of diagnostic agents (such as contrast media) into the neuro, peripheral, and coronary vasculature.

The VIA Microcatheter is contraindicated for use with liquid embolic materials, such as n-butyl 2-cyanoacrylate or ethylene vinyl alcohol & DMSO (dimethyl sulfoxide).

The device should only be used by physicians who have undergone training in all aspects of the WEB Aneurysm Embolization System procedure as prescribed by the manufacturer.

RX Only: Federal law restricts this device to sale by or on the order of a physician.

For healthcare professional intended use only.



MicroVention Worldwide
Innovation Center PH +1.714.247.8000

35 Enterprise
Aliso Viejo, CA 92656 USA
MicroVention UK Limited PH +44 (0) 191 258 6777
MicroVention Europe, S.A.R.L. PH +33 (1) 39 21 77 46
MicroVention Deutschland GmbH PH +49 211 210 798-0
Website microvention.com



WEB™ and VIA™ are registered trademarks
of Sequent Medical, Inc. in the United States.

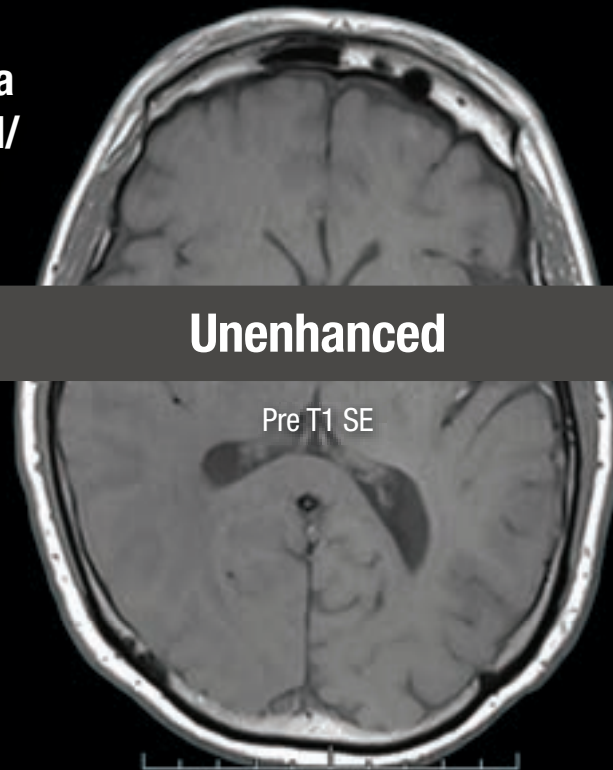
©2021 MicroVention, Inc. MM1184 WW 11/2021

THIS IS HALF Gd*

***Effective contrast enhancement at half the gadolinium dose (0.05 mmol/kg) vs a macrocyclic GBCA at a dose of 0.1 mmol/kg in approved indications in the U.S.^{1-6†}**


Vueway[®]
[gadopichlenol] injection
485.1 mg/mL

**NO COMPROMISE IN MRI FROM BRACCO,
YOUR TRUSTED PARTNER**



[†]Phase III CNS Study Design (Study GDX-44-010): Intra-individual, crossover comparison of 0.05 mmol/kg VUEWAY (gadopichlenol) injection vs. 0.1 mmol/kg Gadavist[®] in MRI of the CNS. Patients with known or suspected CNS lesions. Three primary visualization endpoints (lesion border delineation, lesion internal morphology, degree of contrast enhancement). The CNS study included 256 patients with known or highly suspected CNS lesion(s) with a mean age of 57 years (range: 18-84 years), and 53% female patients.

Please see Brief Summary of Prescribing Information including Boxed Warning on adjacent page.

VUEWAY[®] (gadopichlenol) solution for injection

Indications

VUEWAY injection is indicated in adults and children aged 2 years and older for use with magnetic resonance imaging (MRI) to detect and visualize lesions with abnormal vascularity in:

- the central nervous system (brain, spine and surrounding tissues),
- the body (head and neck, thorax, abdomen, pelvis, and musculoskeletal system).

IMPORTANT SAFETY INFORMATION

WARNING: NEPHROGENIC SYSTEMIC FIBROSIS (NSF)

Gadolinium-based contrast agents (GBCAs) increase the risk for NSF among patients with impaired elimination of the drugs. Avoid use of GBCAs in these patients unless the diagnostic information is essential and not available with non-contrasted MRI or other modalities. NSF may result in fatal or debilitating fibrosis affecting the skin, muscle and internal organs.

- **The risk for NSF appears highest among patients with:**
 - **Chronic, severe kidney disease (GFR < 30 mL/min/1.73 m²), or**
 - **Acute kidney injury.**

- **Screen patients for acute kidney injury and other conditions that may reduce renal function. For patients at risk for chronically reduced renal function (e.g. age > 60 years, hypertension, diabetes), estimate the glomerular filtration rate (GFR) through laboratory testing.**
- **For patients at highest risk for NSF, do not exceed the recommended VUEWAY dose and allow a sufficient period of time for elimination of the drug from the body prior to any re-administration.**

Contraindications

VUEWAY injection is contraindicated in patients with history of hypersensitivity reactions to VUEWAY.

Warnings

Risk of **nephrogenic systemic fibrosis** is increased in patients using GBCA agents that have impaired elimination of the drugs, with the highest risk in patients with chronic, severe kidney disease as well as patients with acute kidney injury. Avoid use of GBCAs among these patients unless the diagnostic information is essential and not available with non-contrast MRI or other modalities.

Hypersensitivity reactions, including serious hypersensitivity reactions, could occur during use or shortly following VUEWAY administration. Assess all patients for any history of a reaction to contrast media, bronchial asthma and/or allergic disorders, administer VUEWAY only in

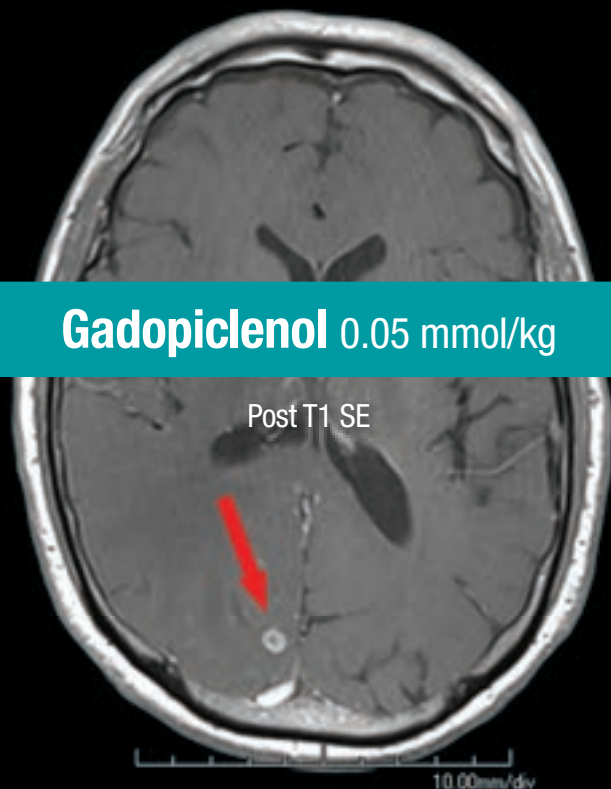


LIFE FROM INSIDE

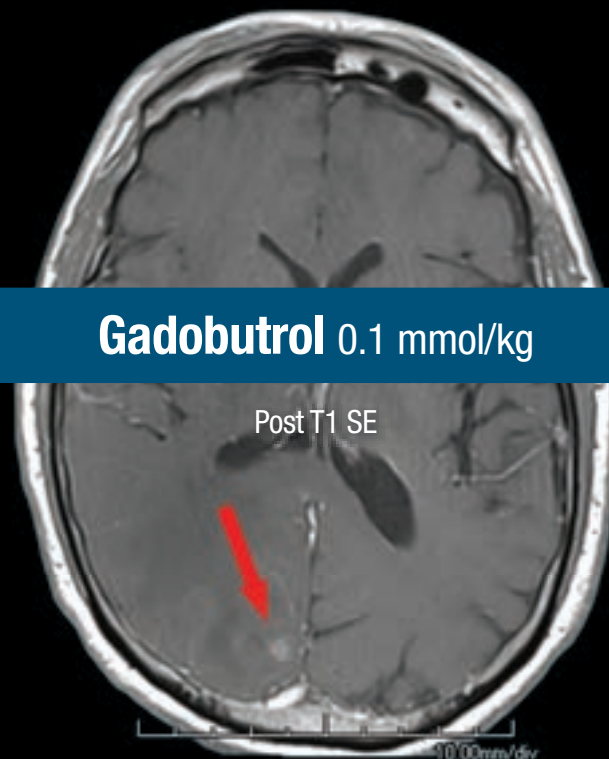
65-year-old man – 3.0 T Siemens
Brain metastasis from lung adenocarcinoma⁷

SE = Spin Echo. These are representative images from reference studies; individual results may vary.

Gadopictenol 0.05 mmol/kg



Gadobutrol 0.1 mmol/kg



situations where trained personnel and therapies are promptly available for the treatment of hypersensitivity reactions, and observe patients for signs and symptoms of hypersensitivity reactions after administration.

Gadolinium retention can be for months or years in several organs after administration. The highest concentrations (nanomoles per gram of tissue) have been identified in the bone, followed by other organs (brain, skin, kidney, liver and spleen). Minimize repetitive GBCA imaging studies, particularly closely spaced studies, when possible.

Acute kidney injury requiring dialysis has occurred with the use of GBCAs in patients with chronically reduced renal function. The risk of acute kidney injury may increase with increasing dose of the contrast agent.

Ensure catheter and venous patency before injecting as **extravasation** may occur, and cause tissue irritation.

VUEWAY may **impair the visualization of lesions** seen on non-contrast MRI. Therefore, caution should be exercised when VUEWAY MRI scans are interpreted without a companion non-contrast MRI scan.

The most common adverse reactions (incidence \geq 0.5%) are injection site pain (0.7%), and headache (0.7%).

You are encouraged to report negative side effects of prescription drugs to the FDA. Visit www.fda.gov/medwatch or call 1-800-FDA-1088.

Please see BRIEF SUMMARY of Prescribing Information for VUEWAY, including BOXED WARNING on Nephrogenic Systemic Fibrosis.

Manufactured for Bracco Diagnostics Inc. by Liebel-Flarsheim Company LLC - Raleigh, NC, USA 27616.

VUEWAY is a trademark of Bracco Imaging S.p.A.

All other trademarks and registered trademarks are the property of their respective owners.

References: **1.** VUEWAY[®] (gadopiclenol) solution for injection, 485.1 mg/mL Full Prescribing Information and Patient Medication Guide. Monroe Twp., NJ: Bracco Diagnostics Inc.; September 2022. **2.** Robic C, Port M, Rousseaux O, et al. Physicochemical and pharmacokinetic profiles of gadopiclenol: a new macrocyclic gadolinium chelate with high T1 relaxivity. *Invest Radiol.* 2019 Aug;54:475-484. **3.** GADAVIST[®] (gadobutrol) Injection. Full Prescribing Information. Bayer HealthCare Pharmaceuticals Inc. Whippany, NJ; April 2022. **4.** DOTAREM[®] (gadoterate meglumine) Injection. Full Prescribing Information. Guerbet LLC. Princeton, NJ; April 2022. **5.** CLARISCAN[™] (gadoterate meglumine) injection for intravenous use. Full Prescribing Information. GE Healthcare. Chicago, IL; February 2020. **6.** ProHance[®] (Gadoteridol) Injection, 279.3 mg/mL Full Prescribing Information and Patient Medication Guide. Monroe Twp., NJ: Bracco Diagnostics Inc.; June 2022. **7.** Loevner LA, Kolumban B, Hutóczki G, et al. Efficacy and safety of gadopiclenol for contrast-enhanced MRI of the central nervous system: the PICTURE randomized clinical trial. *Invest Radiol.* 2023 May;58(5):307-313.

Bracco Diagnostics Inc.
259 Prospect Plains Road, Building H
Monroe Township, NJ 08831 USA
Phone: 609-514-2200
Toll-Free: 1-877-272-2269 (U.S. only)
Fax: 609-514-2446

© 2023 Bracco Diagnostics Inc.
All Rights Reserved. US-VW-2300022 08/23



VISIT
VUEWAY.COM
FOR MORE
INFORMATION

Vueway™
(gadopiclenol) injection, for intravenous use

BRIEF SUMMARY: Please see package insert of full prescribing information.

WARNING: NEPHROGENIC SYSTEMIC FIBROSIS (NSF)
Gadolinium-based contrast agents (GBCAs) increase the risk for NSF among patients with impaired elimination of the drugs. Avoid use of GBCAs in these patients unless the diagnostic information is essential and not available with non-contrast MRI or other modalities. NSF may result in fatal or debilitating fibrosis affecting the skin, muscle and internal organs.

- The risk for NSF appears highest among patients with:
 - Chronic, severe kidney disease (GFR <30 mL/min/1.73 m²), or
 - Acute kidney injury.
- Screen patients for acute kidney injury and other conditions that may reduce renal function. For patients at risk for chronically reduced renal function (e.g. age >60 years, hypertension, diabetes), estimate the glomerular filtration rate (GFR) through laboratory testing.
- For patients at highest risk for NSF, do not exceed the recommended Vueway dose and allow a sufficient period of time for elimination of the drug from the body prior to any re-administration [see Warnings and Precautions (5.1) in the full Prescribing Information].

INDICATIONS AND USAGE

Vueway™ (gadopiclenol) is a gadolinium-based contrast agent indicated in adult and pediatric patients aged 2 years and older for use with magnetic resonance imaging (MRI) to detect and visualize lesions with abnormal vascularity in:

- the central nervous system (brain, spine, and associated tissues),
- the body (head and neck, thorax, abdomen, pelvis, and musculoskeletal system).

CONTRAINDICATIONS

Vueway is contraindicated in patients with history of hypersensitivity reactions to gadopiclenol.

WARNINGS AND PRECAUTIONS

Nephrogenic Systemic Fibrosis Gadolinium-based contrast agents (GBCAs) increase the risk for nephrogenic systemic fibrosis (NSF) among patients with impaired elimination of the drugs. Avoid use of GBCAs among these patients unless the diagnostic information is essential and not available with non-contrast MRI or other modalities. The GBCA-associated NSF risk appears highest for patients with chronic, severe kidney disease (GFR <30 mL/min/1.73 m²) as well as patients with acute kidney injury. The risk appears lower for patients with chronic, moderate kidney disease (GFR 30-59 mL/min/1.73 m²) and little, if any, for patients with chronic, mild kidney disease (GFR 60-89 mL/min/1.73 m²). NSF may result in fatal or debilitating fibrosis affecting the skin, muscle, and internal organs. Report any diagnosis of NSF following Vueway administration to Bracco Diagnostics Inc. (1-800-257-5181) or FDA (1-800-FDA-1088 or www.fda.gov/medwatch).

Screen patients for acute kidney injury and other conditions that may reduce renal function. Features of acute kidney injury consist of rapid (over hours to days) and usually reversible decrease in kidney function, commonly in the setting of surgery, severe infection, injury or drug-induced kidney toxicity. Serum creatinine levels and estimated GFR may not reliably assess renal function in the setting of acute kidney injury. For patients at risk for chronically reduced renal function (e.g., age >60 years, diabetes mellitus or chronic hypertension), estimate the GFR through laboratory testing.

Among the factors that may increase the risk for NSF are repeated or higher than recommended doses of a GBCA and the degree of renal impairment at the time of exposure. Record the specific GBCA and the dose administered to a patient. For patients at highest risk for NSF, do not exceed the recommended Vueway dose and allow a sufficient period of time for elimination of the drug prior to re-administration. For patients receiving hemodialysis, physicians may consider the prompt initiation of hemodialysis following the administration of a GBCA in order to enhance the contrast agent's elimination [see Use in Specific Populations (8.6) and Clinical Pharmacology (12.3) in the full Prescribing Information]. The usefulness of hemodialysis in the prevention of NSF is unknown.

Hypersensitivity Reactions With GBCAs, serious hypersensitivity reactions have occurred. In most cases, initial symptoms occurred within minutes of GBCA administration and resolved with prompt emergency treatment.

- Before Vueway administration, assess all patients for any history of a reaction to contrast media, bronchial asthma and/or allergic disorders. These patients may have an increased risk for a hypersensitivity reaction to Vueway.
- Vueway is contraindicated in patients with history of hypersensitivity reactions to Vueway [see Contraindications (4) in the full Prescribing Information].
- Administer Vueway only in situations where trained personnel and therapies are promptly available for the treatment of hypersensitivity reactions, including personnel trained in resuscitation.
- During and following Vueway administration, observe patients for signs and symptoms of hypersensitivity reactions.

Gadolinium Retention Gadolinium is retained for months or years in several organs. The highest concentrations (nanomoles per gram of tissue) have been identified in the bone, followed by other organs (e.g. brain, skin, kidney, liver, and spleen). The duration of retention also varies by tissue and is longest in bone. Linear GBCAs cause more retention than macrocyclic GBCAs. At equivalent doses, gadolinium retention varies among the linear agents with gadodiamide causing greater retention than other linear agents such as gadoxetate disodium, and gadobenate dimeglumine. Retention is lowest and similar

among the macrocyclic GBCAs such as gadoterate meglumine, gadobutrol, gadoteridol, and gadopiclenol.

Consequences of gadolinium retention in the brain have not been established. Pathologic and clinical consequences of GBCA administration and retention in skin and other organs have been established in patients with impaired renal function [see Warnings and Precautions (5.1) in the full Prescribing Information]. There are rare reports of pathologic skin changes in patients with normal renal function. Adverse events involving multiple organ systems have been reported in patients with normal renal function without an established causal link to gadolinium.

While clinical consequences of gadolinium retention have not been established in patients with normal renal function, certain patients might be at higher risk. These include patients requiring multiple lifetime doses, pregnant and pediatric patients, and patients with inflammatory conditions. Consider the retention characteristics of the agent when choosing a GBCA for these patients. Minimize repetitive GBCA imaging studies, particularly closely spaced studies, when possible.

Acute Kidney Injury in patients with chronically reduced renal function, acute kidney injury requiring dialysis has occurred with the use of GBCAs. The risk of acute kidney injury may increase with increasing dose of the contrast agent. Do not exceed the recommended dose.

Extravasation and Injection Site Reactions Injection site reactions such as injection site pain have been reported in the clinical studies with Vueway [see Adverse Reactions (6.1) in the full Prescribing Information]. Extravasation during Vueway administration may result in tissue irritation [see Nonclinical Toxicology (13.2) in the full Prescribing Information]. Ensure catheter and venous patency before the injection of Vueway.

Interference with Visualization of Lesions Visible with Non-Contrast MRI As with any GBCA, Vueway may impair the visualization of lesions seen on non-contrast MRI. Therefore, caution should be exercised when Vueway MRI scans are interpreted without a companion non-contrast MRI scan.

ADVERSE REACTIONS

The following serious adverse reactions are discussed elsewhere in labeling:

- Nephrogenic Systemic Fibrosis [see Warnings and Precautions (5.1) in the full Prescribing Information]
- Hypersensitivity Reactions [see Contraindications (4) and Warnings and Precautions (5.2) in the full Prescribing Information]

Clinical Trials Experience Because clinical trials are conducted under widely varying conditions, adverse reaction rates observed in the clinical trials of a drug cannot be directly compared to rates in the clinical trials of another drug and may not reflect the rates observed in clinical practice.

The safety of Vueway was evaluated in 1,047 patients who received Vueway at doses ranging from 0.025 mmol/kg (one half the recommended dose) to 0.3 mmol/kg (six times the recommended dose). A total of 708 patients received the recommended dose of 0.05 mmol/kg. Among patients who received the recommended dose, the average age was 51 years (range 2 years to 88 years) and 56% were female. The ethnic distribution was 79% White, 10% Asian, 7% American Indian or Alaska native, 2% Black, and 2% patients of other or unspecified ethnic groups.

Overall, approximately 4.7% of subjects receiving the labeled dose reported one or more adverse reactions.

Table 1 lists adverse reactions that occurred in >0.2% of patients who received 0.05 mmol/kg Vueway.

TABLE 1. ADVERSE REACTIONS REPORTED IN >0.2% OF PATIENTS RECEIVING VUEWAY IN CLINICAL TRIALS	
Adverse Reaction	Vueway 0.05 mmol/kg (n=708) (%)
Injection site pain	0.7
Headache	0.7
Nausea	0.4
Injection site warmth	0.4
Injection site coldness	0.3
Dizziness	0.3
Local swelling	0.3

Adverse reactions that occurred with a frequency < 0.2% in patients who received 0.05 mmol/kg Vueway included: maculopapular rash, vomiting, worsened renal impairment, feeling hot, pyrexia, oral paresthesia, dysgeusia, diarrhea, pruritus, allergic dermatitis, erythema, injection site paresthesia, Cystatin C increase, and blood creatinine increase.

Adverse Reactions in Pediatric Patients

One study with a single dose of Vueway (0.05 mmol/kg) was conducted in 80 pediatric patients aged 2 years to 17 years, including 60 patients who underwent a central nervous system (CNS) MRI and 20 patients who underwent a body MRI. One adverse reaction (maculopapular rash of moderate severity) in one patient (1.3%) was reported in the CNS cohort.

USE IN SPECIFIC POPULATIONS

Pregnancy Risk Summary There are no available data on Vueway use in pregnant women to evaluate for a drug-associated risk of major birth defects, miscarriage or other adverse maternal or fetal outcomes. GBCAs cross the human placenta and result in fetal exposure and gadolinium retention. The available human data on GBCA exposure during pregnancy and adverse fetal outcomes are limited and inconclusive (see Data). In animal reproduction studies, there were no adverse developmental effects observed in rats or rabbits with intravenous administration of Vueway during organogenesis (see Data). Because of the potential risks of gadolinium to the fetus, use Vueway only if imaging is essential during pregnancy and cannot be delayed. The estimated background risk of major birth defects and miscarriage for the indicated population(s) are unknown. All pregnancies have a background risk of birth defect, loss, or other adverse outcomes. In the U.S. general population, the estimated background risk of major birth defects and miscarriage in clinically recognized pregnancies is 2% to 4% and 15% to 20% respectively. Data Human Data Contrast enhancement is visualized in the placenta and fetal tissues after maternal GBCA administration. Cohort studies and case reports on exposure to GBCAs during pregnancy have not reported a clear association between GBCAs and adverse effects in the exposed neonates. However, a retrospective cohort study comparing pregnant women who had a GBCA MRI to pregnant women who did not have an MRI reported a higher occurrence of stillbirths and neonatal deaths in the group receiving GBCA MRI. Limitations of this study include a lack of comparison with non-contrast MRI and lack of information about the maternal indication for MRI. Overall, these data preclude

a reliable evaluation of the potential risk of adverse fetal outcomes with the use of GBCAs in pregnancy.

Animal Data Gadolinium Retention: GBCAs administered to pregnant non-human primates (0.1 mmol/kg on gestational days 85 and 135) result in measurable gadolinium concentration in the offspring in bone, brain, skin, liver, kidney, and spleen for at least 7 months. GBCAs administered to pregnant mice (2 mmol/kg daily on gestational days 16 through 19) result in measurable gadolinium concentrations in the pups in bone, brain, kidney, liver, blood, muscle, and spleen at one-month postnatal age.

Reproductive Toxicology: Animal reproduction studies conducted with gadopiclenol showed some signs of maternal toxicity in rats at 10 mmol/kg and rabbits at 5 mmol/kg (corresponding to 52 times and 57 times the recommended human dose, respectively). This maternal toxicity was characterized in both species by swelling, decreased activity, and lower gestation weight gain and food consumption.

No effect on embryo-fetal development was observed in rats at 10 mmol/kg (corresponding to 52 times the recommended human dose). In rabbits, a lower mean fetal body weight was observed at 5 mmol/kg (corresponding to 57 times the recommended human dose) and this was attributed as a consequence of the lower gestation weight gain.

Lactation Risk Summary There are no data on the presence of gadopiclenol in human milk, the effects on the breastfed infant, or the effects on milk production. However, published lactation data on other GBCAs indicate that 0.01% to 0.04% of the maternal gadolinium dose is excreted in breast milk. Additionally, there is limited GBCA gastrointestinal absorption in the breast-fed infant. Gadopiclenol is present in rat milk. When a drug is present in animal milk, it is likely that the drug will be present in human milk (see Data). The developmental and health benefits of breastfeeding should be considered along with the mother's clinical need for Vueway and any potential adverse effects on the breastfed infant from Vueway or from the underlying maternal condition. Data In lactating rats receiving single intravenous injection of [¹⁵²Gd]-gadopiclenol, 0.3% and 0.2% of the total administered radioactivity was transferred to the pups via maternal milk at 6 hours and 24 hours after administration, respectively. Furthermore, in nursing rat pups, oral absorption of gadopiclenol was 3.6%.

Pediatric Use The safety and effectiveness of Vueway for use with MRI to detect and visualize lesions with abnormal vascularity in the CNS (brain, spine, and associated tissues), and the body (head and neck, thorax, abdomen, pelvis, and musculoskeletal system) have been established in pediatric patients aged 2 years and older.

Use of Vueway in this age group is supported by evidence from adequate and well-controlled studies in adults with additional pharmacokinetic and safety data from an open-label, uncontrolled, multicenter, single dose study of Vueway (0.05 mmol/kg) in 80 pediatric patients aged 2 to 17 years. The 80 patients consisted of 60 patients who underwent a CNS MRI and 20 patients who underwent a body MRI [see Adverse Reactions (6.1) and Clinical Pharmacology (12.3) in the full Prescribing Information].

The safety and effectiveness of Vueway have not been established in pediatric patients younger than 2 years of age.

Geriatric Use Of the total number of Vueway-treated patients in clinical studies, 270 (26%) patients were 65 years of age and over, while 62 (6%) patients were 75 years of age and over. No overall differences in safety or efficacy were observed between these subjects and younger subjects.

This drug is known to be substantially excreted by the kidney, and the risk of adverse reactions to this drug may be greater in patients with impaired renal function. Because elderly patients are more likely to have decreased renal function, it may be useful to monitor renal function.

Renal Impairment in patients with renal impairment, the exposure of gadopiclenol is increased compared to patients with normal renal function. This may increase the risk of adverse reactions such as nephrogenic systemic fibrosis (NSF). Avoid use of GBCAs among these patients unless the diagnostic information is essential and not available with non-contrast MRI or other modalities. No dose adjustment of Vueway is recommended for patients with renal impairment. Vueway can be removed from the body by hemodialysis [see Warnings and Precautions (5.1, 5.3, 5.4) and Clinical Pharmacology (12.3) in the full Prescribing Information].

OVERDOSAGE

Among subjects who received a single 0.3 mmol/kg intravenous dose of gadopiclenol (6 times the recommended dose of Vueway), headache and nausea were the most frequently reported adverse reactions. Gadopiclenol can be removed from the body by hemodialysis [see Clinical Pharmacology (12.3) in the full Prescribing Information].

PATIENT COUNSELING INFORMATION Advise the patient to read the FDA-approved patient labeling (Medication Guide).

Nephrogenic Systemic Fibrosis Inform the patient that Vueway may increase the risk for NSF among patients with impaired elimination of the drugs and that NSF may result in fatal or debilitating fibrosis affecting the skin, muscle and internal organs.

Instruct the patients to contact their physician if they develop signs or symptoms of NSF following Vueway administration, such as burning, itching, swelling, scaling, hardening and tightening of the skin; red or dark patches on the skin; stiffness in joints with trouble moving, bending or straightening the arms, hands, legs or feet; pain in the hip bones or ribs; or muscle weakness [see Warnings and Precautions (5.1) in the full Prescribing Information].

Gadolinium Retention Advise patients that gadolinium is retained for months or years in brain, bone, skin, and other organs following Vueway administration even in patients with normal renal function. The clinical consequences of retention are unknown. Retention depends on multiple factors and is greater following administration of linear GBCAs than following administration of macrocyclic GBCAs [see Warnings and Precautions (5.3) in the full Prescribing Information].

Injection Site Reactions Inform the patient that Vueway may cause reactions along the venous injection site, such as mild and transient burning or pain or feeling of warmth or coldness at the injection site [see Warnings and Precautions (5.5) in the full Prescribing Information].

Pregnancy Advise pregnant women of the potential risk of fetal exposure to Vueway [see Use in Specific Populations (8.1) in the full Prescribing Information].

Rx only

US Patent No. 10,973,934
Manufactured for Bracco Diagnostics Inc. by Liebel-Flarsheim Company LLC - Raleigh, NC, USA 27616.
Toll Free: 1-877-272-2269 (U.S. only)
Revised November 2022

**I am a global citizen.
I am patient-centered care.
I am an academic neuroradiologist.
I am a researcher.
I am a life-long learner.
I am determined.
I am curious.
I am a collaborative team player.
I am a volunteer.
I am ASNR.**

Don't miss out on the tools, resources and relationships you've come to rely on. Log in and renew your ASNR membership today! www.asnr.org



The ASNR Career Center

The Go-To Job Site for Neuroradiology Employers and Job Seekers

For Job Seekers

- Access to an expanded network of jobs via the National Healthcare Career Network
- Confidential resume posting
- Professional online profile

For Employers

- Employer resources to help you recruit top talent
- Multiple pricing options, including free Fellowship listings
- Resume search

Start here: careers.asnr.org

JOIN US!

ASNR24

LAS VEGAS
MAY 18-22, 2024

CELEBRATING NEURORADIOLOGISTS



Join us at ASNR24 where we plan on **Celebrating Neuroradiologists** and showcasing and celebrating our field's many accomplishments. Both in-person and on-demand registration options are available, allowing you to attend the Annual Meeting the way that works best for you!

Register today at www.asnr.org/annualmeeting!

ASNR24 will feature:

- Symposium on *Neuroradiology: The New Frontier*, including sessions on VR/AI, photon counting, psychiatric disease, brain tumor imaging, health policy issues and genetic therapies for neurologic diseases.
- Sessions feature emerging topics, neuroradiology essentials, policy and practice updates, and discussions with international and industry colleagues. Many sessions this year will also feature case presentations, panel discussions, and audience response polling.
- Approximately 200 podium presentations and 500 ePosters and Educational Exhibits on the latest advancements in research, technology, policy and practice innovations for neuroradiology.
- Social and fun community connection experiences, including the Presidential Gala, Happy Hour with Partners and a Pool Party.
- Special sessions and social events for community and specialty groups, including Spine, Head and Neck, Healthcare, Pediatrics, Functional, AI, Interventional, Young Professionals, New Retirees, Fellowship Directors, International Affiliates, and many more.

ASNR24 Host Hotel and Conference Location

Caesars Palace
3570 S Las Vegas Blvd.
Las Vegas, NV 89109

Play, dine and unwind like royalty at Caesars Palace Las Vegas, the remarkable, palatial center-Strip resort. After a day of learning and networking, enjoy being just steps away from a variety of activities, ranging from world-class shopping and dining to outdoor adventures and shows. For ease and convenience, book in the ASNR hotel room block.



Accreditation Statement

The American Society of Neuroradiology is accredited by the Accreditation Council for Continuing Medical Education (ACCME) to provide continuing medical education for physicians and takes responsibility for the content, quality and scientific integrity of this CME activity.

The American Society of Neuroradiology designates this live activity for a maximum of 27.25 AMA PRA Category 1 Credits™. Physicians should claim only the credit commensurate with the extent of their participation in the activity. The American Society of Neuroradiology designates this enduring material for a maximum of 62.25 AMA PRA Category 1 Credits™. Physicians should claim only the credit commensurate with the extent of their participation in the activity.

Visit www.asnr.org/annualmeeting for complete details and to register.

AJNR

AMERICAN JOURNAL OF NEURORADIOLOGY

JANUARY 2024
VOLUME 45
NUMBER 1
WWW.AJNR.ORG

Publication Preview at www.ajnr.org features articles released in advance of print.
Visit www.ajnrblog.org to comment on AJNR content and chat with colleagues.

- REVIEW ARTICLE**
-  1 **MR Thermometry during Transcranial MR Imaging–Guided Focused Ultrasound Procedures: A Review** *Raghav R. Mattay, et al.* **NEUROINTERVENTION**
- STATE OF PRACTICE**
-  9 **The Pediatric Neuroradiologist’s Practical Guide to Capture and Evaluate Pre- and Postoperative Velopharyngeal Insufficiency** *Michael S. Kuwabara, et al.* **PEDIATRIC NEUROIMAGING**
- GENERAL CONTENTS**
-  16 **Correlation of Flow Diverter Malapposition at the Aneurysm Neck with Incomplete Aneurysm Occlusion in Patients with Small Intracranial Aneurysms: A Single-Center Experience** *Shuhai Long, et al.* **NEUROINTERVENTION**
-  22 **Ischemic Stroke Thrombus Perviousness Is Associated with Distinguishable Proteomic Features and Susceptibility to ADAMTS13-Augmented Thrombolysis** *Derrek Schartz, et al.* **NEUROINTERVENTION**
-  30 **Determinants and Clinical Relevance of Iodine Contrast Extravasation after Endovascular Thrombectomy: A Dual-Energy CT Study** *Clémence Hoche, et al.* **NEUROVASCULAR/STROKE IMAGING**
-  37 **Assessing Perfusion in Steno-Occlusive Cerebrovascular Disease Using Transient Hypoxia-Induced Deoxyhemoglobin as a Dynamic Susceptibility Contrast Agent** *Ece Su Sayin, et al.* **NEUROVASCULAR/STROKE IMAGING**
-   44 **The Choroid Plexus as an Alternative Locus for the Identification of the Arterial Input Function for Calculating Cerebral Perfusion Metrics Using MRI** *Olivia Sobczyk, et al.* **NEUROVASCULAR/STROKE IMAGING**
-  51 **CTA and CTP for Detecting Distal Medium Vessel Occlusions: A Systematic Review and Meta-analysis** *João André Sousa, et al.* **NEUROVASCULAR/STROKE IMAGING**
-  57 **Disconnection-Based Prediction of Poststroke Dysphagia** *Kyung Jae Yoon, et al.* **NEUROIMAGING PHYSICS/FUNCTIONAL NEUROIMAGING/CT AND MRI TECHNOLOGY**
-  66 **Glymphatic System Dysfunction in Myelin Oligodendrocyte Glycoprotein Immunoglobulin G Antibody–Associated Disorders: Association with Clinical Disability** *Akifumi Hagiwara, et al.* **ULTRA-HIGH-FIELD MRI/IMAGING OF EPILEPSY/DEMYELINATING DISEASES/INFLAMMATION/INFECTION**

AJNR (Am J Neuroradiol) ISSN 0195–6108 is a journal published monthly, owned and published by the American Society of Neuroradiology (ASNR), 820 Jorie Boulevard, Oak Brook, IL 60523. Annual dues for the ASNR include approximately 19% for a journal subscription. The journal is printed by Intellicor Communications, 330 Eden Road, Lancaster, PA 17601; Periodicals postage paid at Oak Brook, IL and additional mailing offices. Printed in the U.S.A. POSTMASTER: Please send address changes to American Journal of Neuroradiology, P.O. Box 3000, Denville, NJ 07834, U.S.A. Subscription rates: nonmember \$452 (\$530 foreign) print and online, \$320 online only; institutions \$520 (\$594 foreign) print and basic online, \$1029 (\$1103 foreign) print and extended online, \$380 online only (basic), \$825 online only (extended); single copies are \$35 each (\$40 foreign). Indexed by PubMed/MEDLINE, BIOSIS Previews, Current Contents (Clinical Medicine and Life Sciences), EMBASE, Google Scholar, HighWire Press, Q-Sensei, RefSeek, Science Citation Index, SCI Expanded, ReadCube, and Semantic Scholar. Copyright © American Society of Neuroradiology.

- 72 **Prevalence of Developmental Venous Anomalies in Association with Sporadic Cavernous Malformations on 7T MRI**
Petrice M. Cogswell, et al.
- ★ 76 **Central Vein Sign in Multiple Sclerosis: A Comparison Study of the Diagnostic Performance of 3T versus 7T MRI**
Lela Okromelidze, et al.
- ☰ 82 **Cortical Thin Patch Fraction Reflects Disease Burden in MS: The Mosaic Approach** *Marlene Tahedl, et al.*
- ☰ 90 **Delayed Gadolinium Leakage in Ocular Structures on Brain MR Imaging: Prevalence and Associated Factors** *Richard Olatunji, et al.*
- 96 **Application of a Denoising High-Resolution Deep Convolutional Neural Network to Improve Conspicuity of CSF-Venous Fistulas on Photon-Counting CT Myelography** *Ajay A. Madhavan, et al.*
- ★ 100 **Temporal Characteristics of CSF-Venous Fistulas on Dynamic Decubitus CT Myelography: A Retrospective Multi-Institution Cohort Study** *Andrew L. Callen, et al.*
- ☰ 105 **Lateral Decubitus Dynamic CT Myelography with Real-Time Bolus Tracking (dCTM-BT) for Evaluation of CSF-Venous Fistulas: Diagnostic Yield Stratified by Brain Imaging Findings** *Thien J. Huynh, et al.*
- ☰ 113 **Prevalence of Incidental Extraspinal Findings on MR Imaging of the Lumbar Spine in Adults: A Systematic Review and Meta-analysis**
Philip J. Broadhurst, et al.
- ✍ 119 **Frequency of Coexistent Spinal Segment Variants: Retrospective Analysis in Asymptomatic Young Adults** *Edward S. Yoon, et al.*

ULTRA-HIGH-FIELD MRI/
IMAGING OF EPILEPSY/
DEMYELINATING DISEASES/
INFLAMMATION/INFECTION

ULTRA-HIGH-FIELD MRI/
IMAGING OF EPILEPSY/
DEMYELINATING DISEASES/
INFLAMMATION/INFECTION

ULTRA-HIGH-FIELD MRI/
IMAGING OF EPILEPSY/
DEMYELINATING DISEASES/
INFLAMMATION/INFECTION

HEAD AND NECK
IMAGING

SPINE IMAGING AND
SPINE IMAGE-GUIDED
INTERVENTIONS

SPINE IMAGING AND
SPINE IMAGE-GUIDED
INTERVENTIONS

SPINE IMAGING AND
SPINE IMAGE-GUIDED
INTERVENTIONS

SPINE IMAGING AND
SPINE IMAGE-GUIDED
INTERVENTIONS

SPINE IMAGING AND
SPINE IMAGE-GUIDED
INTERVENTIONS

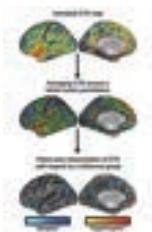
ONLINE FEATURES

LETTER

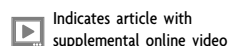
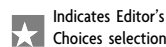
- E1 **Response to Letter Regarding the Article “Automated Segmentation of Intracranial Thrombus on NCCT and CTA in Patients with Acute Ischemic Stroke Using a Coarse-to-Fine Deep Learning Model”**
Kairan Zhu, et al.

BOOK REVIEWS *R.M. Quencer, Section Editor*

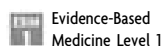
Please visit www.ajnrblog.org to read and comment on Book Reviews.



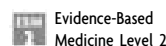
Tahedl, et al assessed the validity of the “mosaic approach,” the patch-wise, individual interpretation of cortical thickness data, to identify gray matter pathology in patients with MS. The thin patch fraction was shown to be a valid neuroimaging biomarker not only able to discriminate between patients with MS and healthy controls, as well as to discriminate among MS phenotypes, but also was associated with disease burden, including the Expanded Disability Status Scale, cognitive and fatigue scores, and lesion volume.



Indicates Fellows' Journal Club selection



Indicates open access to non-subscribers at www.ajnr.org



Indicates article with supplemental online data

Official Journal:

American Society of Neuroradiology
American Society of Functional Neuroradiology
American Society of Head and Neck Radiology
American Society of Pediatric Neuroradiology
American Society of Spine Radiology

JANUARY 2024 • VOLUME 45 • NUMBER 1 • WWW.AJNR.ORG

EDITOR-IN-CHIEF

Max Wintermark, MD, MAS, FASFN, FICIS

*Frank T. McGraw Memorial Chair in the Study of Cancer
Professor and Chair of Neuroradiology
The University of Texas MD Anderson Center*

DEPUTY EDITOR

Lubdha M. Shah, MD, MS

Professor of Radiology and Director of Spine Imaging
Department of Radiology and Imaging Sciences
University of Utah

SPECIAL ADVISORS TO THE EDITOR-IN-CHIEF

Mauricio Castillo, MD, FACR

MA Mauro Distinguished Professor of Radiology
University of North Carolina-Chapel Hill

Robert Quencer, MD

Professor Emeritus
Department of Radiology
University of Miami

ARTIFICIAL INTELLIGENCE

Senior Editor

Reza Forghani, MD, PhD

Professor of Radiology & Artificial Intelligence
Vice Chair of AI
Director, Radiomics & Augmented Intelligence Laboratory (RAIL)
Department of Radiology
University of Florida College of Medicine

Associate Editors

Andreas Rauschecker, MD, PhD

Assistant Professor-in-Residence
Co-Executive Director and Clinical Director,
Center for Intelligent Imaging (ci²)
Department of Radiology & Biomedical Imaging
University of California, San Francisco

Sam (Seyedmehdi) Payabvash, MD

Assistant Professor of Radiology
Yale School of Medicine
Connecticut

BRAIN TUMOR IMAGING

Senior Editor

Ben Ellingson, MD

Professor and Director of MRI Research
Director, UCLA Brain Tumor Imaging Laboratory
Department of Radiological Sciences
David Geffen School of Medicine
University of California, Los Angeles

Associate Editors

Ali Nabavizadeh, MD

Assistant Professor of Radiology
Division of Neuroradiology
University of Pennsylvania

Mark S. Shiroishi, MD, MS, FASFN

Assistant Professor, Division of Neuroradiology,
Department of Radiology
Director of Neuro-Oncology Imaging - USC Brain Tumor Center
Chief of Pediatric Neuroradiology – Los Angeles General Medical Center
Affiliated Faculty - USC Imaging Genetics Center
Mark and Mary Stevens Neuroimaging and Informatics Institute
Keck School of Medicine of USC
University of Southern California

EMERGENCY NEURORADIOLOGY

Senior Editor

Karen Buch, MD

Assistant Professor of Radiology
Massachusetts General Hospital

Associate Editors

Melissa A. Davis, MD, MBA

Vice Chair of Medical Informatics
Associate Professor
Department of Radiology and Biomedical Imaging
Yale School of Medicine
Connecticut

Jason Talbott, MD, PhD

Associate Professor, Neuroradiology Section
Department of Radiology and Biomedical Imaging
University of California, San Francisco and
Zuckerberg San Francisco General Hospital

HEAD AND NECK IMAGING

Senior Editor

Amy Juliano, MD

Associate Professor of Radiology
Massachusetts Eye and Ear
Harvard Medical School

Associate Editors

Burce Ozgen, MD

Clinical Professor of Radiology
University of Illinois at Chicago

David Zander, MD

Assistant Professor, Radiology
University of Colorado School of Medicine

HEALTH POLICIES/QUALITY IMPROVEMENT/ EVIDENCE-BASED NEUROIMAGING

Senior Editor

Nadja Kadom, MD, FACR, FAAP

Professor, Department of Radiology and Imaging Sciences
Emory University School of Medicine
Pediatric Neuroradiologist, Department of Radiology
Children's Healthcare of Atlanta

Associate Editors

Melissa M. Chen, MD

Associate Professor,
Department of Neuroradiology, Division of Diagnostic Imaging
The University of Texas MD Anderson Center

Ajay Malhotra, MBBS, MD, MMM

Professor of Radiology and Biomedical Imaging and Neurosurgery
Yale School of Medicine
Connecticut

MOLECULAR NEUROIMAGING/NUCLEAR MEDICINE

Senior Editor

Ana M. Franceschi, MD, PhD

Associate Professor of Radiology
Donald and Barbara Zucker School of Medicine at Hofstra/Northwell
The Feinstein Institutes for Medical Research
Neuro-PET Imaging
Lenox Hill Hospital
New York

Associate Editors

Nadya Pyatigorskaya, MD, PhD

Neuroradiology Department, Pitié-Salpêtrière Hospital
Researcher, Brain Institute (ICM)
France

Marc Daniel Benayoun, PhD, MD

Assistant Professor of Radiology
Co-Section Head of Nuclear Medicine
Medical Director of Nuclear Medicine and PET
Vice Chair of Radiation Drug Research Committee
Atrium Wake Forest Health
North Carolina

NEURODEGENERATIVE DISORDER IMAGING

Senior Editor

Gloria Chiang, MD

Associate Professor, Co-Director of the Brain Health Imaging Institute
Department of Radiology
Weill Cornell Medicine/NewYork-Presbyterian Hospital

Associate Editors

Fang Frank Yu, MD

Assistant Professor of Radiology
Division of Neuroradiology, Department of Radiology
Advanced Imaging Research Center
University of Texas Southwestern Medical Center

Priya Rajagopalan, MBBS, MPH

Assistant Professor of Radiology, Division of Neuroradiology
Associate Program Director, Neuroradiology Fellowship
Medical Director, Center for Image Acquisition Mark and Mary Stevens Neuroimaging and Informatics Institute
Keck School of Medicine, University of Southern California

NEUROIMAGING PHYSICS/FUNCTIONAL NEUROIMAGING/CT AND MRI TECHNOLOGY**Senior Editor****Hongyu An, DSc**

Professor, Mallinckrodt Institute of Radiology Neurology, Biomedical Engineering, Electrical and Systems Engineering, Division of Biology and Biomedical Sciences
Director, Biomedical Magnetic Resonance Center
Associate Director, Center for Clinical Imaging Research
Washington University in St. Louis

Associate Editors**Timothy J. Carroll, PhD**

Professor, Department of Radiology
University of Chicago

Hugo de Jong, PhD

Professor of Medical Physics Radiology and Nuclear Medicine
UMC Utrecht
the Netherlands

NEUROINTERVENTION**Senior Editor****Steven Hetts, MD, FACR**

Co-Chief, NeuroEndovascular Surgery Service Line
Chief of Interventional Neuroradiology, Mission Bay Hospitals
Professor of Radiology, Biomedical Imaging, and Neurological Surgery
University of California, San Francisco

Associate Editors**Kristine Blackham, MD**

Associate Professor
Diagnostic and Interventional Neuroradiology
Clinic for Radiology and Nuclear Medicine
University Hospital of Basel

Maksim Shapiro, MD

Clinical Associate Professor
Departments of Radiology, Neurosurgery, and Neurology
Division of Neurointerventional Radiology
NYU Langone Health and Bellevue NYCH + Hospitals
New York

NEUROPSYCHIATRIC IMAGING**Senior Editor****Jody Tanabe, MD**

Professor
Chief of Neuroradiology
University of Colorado-Anschutz Medical Campus

Associate Editors**John-Paul J. Yu, MD, PhD**

Assistant Professor of Radiology, Psychiatry, and Biomedical Engineering
University of Wisconsin School of Medicine and Public Health

J. Eric Schmitt, MD, PhD

Assistant Professor of Radiology and Psychiatry
Division of Neuroradiology
Perelman School of Medicine, University of Pennsylvania

NEUROVASCULAR/STROKE IMAGING**Senior Editor****Ajay Gupta, MD, MS**

Alexander R. Margulis, MD, Distinguished Professor in Radiology
Weill Cornell Medical College
New York

Associate Editors**Shalini Amukotuwa, MB BS, PhD, FRANZCR**

Head of Neuroradiology and Director of MRI, Monash Health
Associate Professor of Radiology, Monash University
Australia

Mahmud Mossa-Basha, MD

Professor of Radiology, Neurology and Electrical Engineering
Vice Chair of Clinical Research and Clinical Transformation
Co-Director of the Research Vascular Imaging Lab
University of Washington School of Medicine

PEDIATRIC NEUROIMAGING**Senior Editor****Caroline D. Robson, MBChB**

Division Chief & Endowed Chair, Neuroradiology
Director, Head & Neck Imaging
Department of Radiology
Department of Otolaryngology
Boston Children's Hospital
Harvard Medical School

Associate Editors**Anna Trofimova, MD, PhD**

Assistant Professor, Radiology and Imaging Sciences, Emory University
Pediatric Neuroradiologist, Children's Healthcare of Atlanta

Matthew Whitehead, MD

Department of Radiology, Division of Neuroradiology
Children's Hospital of Philadelphia
Associate Professor of Radiology
Perelman School of Medicine, University of Pennsylvania

SPINE IMAGING AND SPINE IMAGE-GUIDED INTERVENTIONS**Senior Editor****J. Levi Chazen, MD**

Associate Professor, Neuroradiology
Director, Spine Imaging
Hospital for Special Surgery
Weill Cornell Medicine
New York

Associate Editors**Jennifer McCarty, MD**

UTHealth Houston

Vinil Shah, MD

Associate Professor of Radiology Neuroradiology
Division Chief
University of California, San Francisco

ULTRA-HIGH-FIELD MRI/IMAGING OF EPILEPSY/DEMYELINATING DISEASES/INFLAMMATION/INFECTION**Senior Editor****Erik Middlebrooks, MD**

Professor of Radiology
Mayo Clinic Florida

Associate Editors**Susie Y. Huang, MD, PhD**

Associate Professor of Radiology, Harvard Medical School
Associate Chair, Faculty Affairs, Department of Radiology
Director of Translational Neuro MR Imaging & Connectomics, Athinoula A. Martinos Center for Biomedical Imaging
Massachusetts General Hospital

Girish Bathla, MD, FRCR

Associate Professor, Neuroradiology
Mayo Clinic
Minnesota

OUTREACH AND EDUCATION**Senior Editor****Lea Alhilali, MD**

Radiology Partners, HonorHealth Research Institute
Arizona

DIGITAL MEDIA AND ENGAGEMENT**Senior Editor****Kevin Hsu, MD**

Clinical Assistant Professor
Department of Radiology
NYU Grossman School of Medicine
New York

Case Collection Editors**Matylda Machnowska, BMedSc, MD, FRCSC, ABR**

Assistant Professor of Radiology, University of Toronto
Neuroradiologist, Sunnybrook Health Sciences Centre

Anvita Pauranik, MD

Clinical Assistant Professor of Radiology
BC Children's Hospital
University of British Columbia

Sandy Cheng-Yu Chen, MD

Chair, Translational Imaging Research Center
Taipei Medical University Hospital
Vice President of Taipei Medical University

Social Media Editor**Kimberly Seifert, MD, MS**

Stanford University
California

Assistant Social Media Editors**Ani Hoxha, MD**

Mother Theresa UHC
Albania

Maxwell Opoku, MD

Novosibirsk State Research University
Russia

Podcast Editor

Kevin Hiatt, MD

Assistant Professor, Radiology
Wake Forest University School of Medicine
North Carolina

Deputy Podcast Editor

George K. Vilanilam, MD

PGY5 Resident Physician, Department of Radiology
University of Arkansas for Medical Sciences

STATISTICS

Senior Editor

Bryan A. Comstock, MS

Senior Biostatistician, Department of Biostatistics
University of Washington

EDITORIAL FELLOWS

Alexandre Boutet, MD, PhD

Neuroradiologist
Joint Department of Medical Imaging
University of Toronto

Nicholas S. Cho, MD/PhD Candidate

University of California, Los Angeles

Burak Berksu Ozkara, MD

Research Fellow
Department of Neuroradiology
The University of Texas MD Anderson Center

BOOK REVIEW EDITOR

Robert Quencer, MD

Professor Emeritus
Department of Radiology
University of Miami

Founding Editor

Juan M. Taveras

Editors Emeriti

Mauricio Castillo, Robert I. Grossman,
Michael S. Huckman, Robert M. Quencer,
Jeffrey S. Ross

Managing Editor

Karen Halm

Assistant Managing Editor

Laura Wilhelm

Executive Director, ASNR

Mary Beth Hepp

MR Thermometry during Transcranial MR Imaging–Guided Focused Ultrasound Procedures: A Review

Raghav R. Mattay,¹ Kisoo Kim,² Lubdha Shah,³ Bhavya Shah,⁴ Leo Sugrue,⁵ Fatima Safoora,⁶ Eugene Ozhinsky,⁷ and Kazim H. Narsinh⁸



ABSTRACT

SUMMARY: Interest in transcranial MR imaging–guided focused ultrasound procedures has recently grown. These incisionless procedures enable precise focal ablation of brain tissue using real-time monitoring by MR thermometry. This article will provide an updated review on clinically applicable technical underpinnings and considerations of proton resonance frequency MR thermometry, the most common clinically used MR thermometry sequence.

ABBREVIATIONS: CEM43 = cumulative equivalent minutes at 43°C; 2DFT = 2D Cartesian Fourier transform; GRE = gradient recalled-echo; HIFU = high-intensity focused ultrasound; LIFU = low-intensity focused ultrasound; MRgFUS = MR imaging–guided focused ultrasound; MRT = MR thermometry; NPV = non-perfused volume; PRF = proton resonance frequency

Transcranial MR imaging–guided focused ultrasound (MRgFUS) is an incisionless technique to precisely deliver energy through an intact skull for the treatment of a wide range of neurologic disorders, because the technique is minimally invasive and has a rapid recovery time.^{1–4} MRgFUS is most commonly used to ablate brain tissue in a targeted fashion.⁵ The FDA cleared MRgFUS for ablation of the ventralis intermediate nucleus of the thalamus to treat essential tremor in 2016⁶ and, more recently, for the globus pallidus interna for treatment of advanced Parkinson disease.⁷ Currently, the FDA-cleared system for transcranial MRgFUS is the ExAblate Neuro system (Insightec). The Insightec ExAblate Neuro system can be used with 2 different frequency transducers, referred to colloquially as high-intensity focused ultrasound (HIFU) and low-intensity focused ultrasound (LIFU). Operating at 650 kHz, the HIFU transducer enables precise ablation of brain tissue, while the LIFU transducer, operating low-intensity pulsed ultrasound at a frequency of 220 kHz, enables neuromodulation, BBB disruption, and acoustic activation of drug agents. Transcranial MRgFUS

systems have shown potential in clinical trials for treating trigeminal neuralgia (HIFU),⁸ disrupting the BBB (LIFU),^{9,10} activating sonodynamic therapy (LIFU),¹¹ or treating obsessive-compulsive disorders (LIFU).¹² Because HIFU causes thermal ablation, MR thermometry (MRT) is of the utmost importance. Depending on the clinical indication and location of the target, LIFU can be used with or without MRT. Laser interstitial therapy, a minimally invasive neurologic surgery using a laser on a probe, can also thermally ablate tissue, also requiring MRT for intraprocedural guidance.

Most of the current HIFU target structures are in the subcortical brain surrounded by critical fiber tracts.¹³ In the treatment of essential tremor, the ventralis intermediate nucleus abuts the corticospinal tract laterally. Submillimetric errors in localization can result in complications such as gait imbalance or hemiplegia. The ventralis caudalis and medial lemniscus, located in proximity posteriorly, pose a potential risk of unintended heating that could lead to sensory abnormalities such as paresthesia, including the dreaded complication of anesthesia dolorosa (we will use the Hassler classification of thalamic nuclei for this article). HIFU ablation in the brain typically requires “align” (or “test”) sonications to raise focal zone temperatures above 40°C and “verify” (or “stun”) sonications to raise focal zone temperatures to approximately 50–52°C. The align sonications allow submillimetric triangulation and correction of the focal zone, while verify sonications produce a reversible physiologic effect allowing assessment of treatment response and adverse effects before the final ablative sonications that raise focal zone temperatures above 55°C. In general, with increasing temperatures, the exposure time needed to reach the ablation threshold drops exponentially. LIFU induces

Received May 16, 2023; accepted after revision August 4.

From the Departments of Radiology and Biomedical Imaging (R.R.M., K.K., L. Sugrue, F.S., E.O., K.H.N.), Psychiatry (L. Sugrue), and Neurological Surgery (K.H.N.), University of California San Francisco, California; Department of Radiology and Neurosurgery (L. Shah), University of Utah, Salt Lake City, Utah; and Department of Radiology (B.S.), University of Texas Southwestern, Dallas, Texas.

Drs Raghav R. Mattay, and Kisoo Kim are co-first authors.

Drs Eugene Ozhinsky, and Kazim H. Narsinh are co-corresponding authors.

Please address correspondence to Kazim H. Narsinh, MD, University of California San Francisco, 505 Parnassus Ave, San Francisco, CA 94143; e-mail: kazim.narsinh@ucsf.edu; @DrKazNIR; @UCSFimaging; @UCSF_NIR

Indicates open access to non-subscribers at www.ajnr.org

<http://dx.doi.org/10.3174/ajnr.A8038>

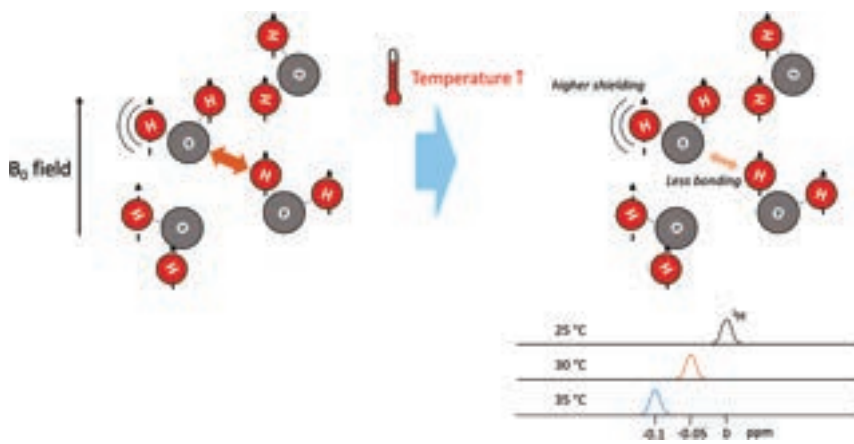


FIG 1. PRF is dependent on temperature. The B_0 field denotes the direction of the magnetic field and thus the spins of the hydrogen protons (H). An increase in temperature leads to less hydrogen bonding and higher electron shielding of protons, making them less susceptible to the B_0 field and decreasing their resonant frequency.

physiologic and biologic effects without an appreciable increase in temperature (eg, $<0.1^\circ\text{C}$) within the target region, while avoiding tissue damage and microbleeding.¹⁴ Real-time and noninvasive MRT is critical to achieve precise and controlled transcranial focused ultrasound treatments.

MRT comprises a set of thermal-sensitive MR imaging parameters, such as proton resonance frequency (PRF) shift, T1 and T2 relaxation times, diffusion, proton density, and magnetization transfer.¹⁵ Some of these methodologies could be useful in nonaqueous tissues such as breast or bone but are less than optimal for clinical intracranial applications because they often require longer acquisition times to obtain an adequate SNR. A recent review discusses MRT in cerebrovascular disease as a versatile tool for diagnosis, prognostication, and monitoring treatment response.¹⁶ For MRgFUS, PRF thermometry is the mainstay for current clinical applications due to fast acquisition times and high temperature sensitivity within aqueous tissues. Several factors can influence the optimal measurement of temperature change in the target tissue using PRF, including heterogeneous heat deposition at the focal zone, tissue properties, tissue inhomogeneity, the presence of increased susceptibility, timing of the acquisition, and motion artifacts. The consideration of these factors is imperative to ensure the successful implementation of transcranial MRgFUS applications.

This review aims to provide a basic introduction to PRF thermometry and to discuss factors that influence temperature measurements in transcranial MRgFUS applications for both physicians and scientists wishing to further develop the safety and efficacy of this exciting emerging technology.

PRF Thermometry

Within the B_0 magnetic field, hydrogen protons in water and fat precess around their axis at their resonant frequencies according to their gyromagnetic ratio. Temperature variations in tissue cause changes in the angular frequency of the proton precession. For hydrogen nuclei, which comprise a single proton, temperature effects result in frequency shifts less than a few 100 Hz at 1.5T, but

they remain detectable (for comparison, the resonance frequency of a proton at 1.5T is 63.87 MHz).

The electron cloud of a hydrogen atom intrinsically shields the proton within the nucleus from the surrounding magnetic field. While hydrogen atoms in individual water molecules are strongly linked through covalent bonds to their associated oxygen atoms, they also experience weaker attraction to the oxygen atoms of neighboring water molecules through hydrogen bonding. Hydrogen bonding causes some of the electron clouds of hydrogen to be pulled away by the electrophilic oxygen atom, resulting in deshielding the hydrogen protons.

With this deshielding, protons within water molecules experience a stronger local magnetic field. The local magnetic field can be addressed as follows:

$$\text{Equation 1} \quad B_{loc}(T) = (1 - s(T) + \chi(T))B_0,$$

$$\text{Equation 2} \quad s(T) = \alpha T,$$

where T is a temperature, $s(T)$ is the shielding constant of water molecules, $\chi(T)$ is the magnetic susceptibility of tissue, B_0 is the strength of the main MR imaging magnetic field, and α is the temperature coefficient of the water proton, approximately 0.01 ppm/ $^\circ\text{C}$ (the coefficient ranges from -0.00739 to -0.0135 ppm/ $^\circ\text{C}$).^{17,18}

Increasing the temperature of tissue disrupts hydrogen bonding within water molecules, improving the shielding of hydrogen protons. In contrast, in aqueous tissues, the temperature-dependent magnetic susceptibility of tissue $\chi(T)$ can be negligible because it is much smaller than effects due to changes in the shielding of hydrogen protons.

$$\text{Equation 3} \quad \omega(T) = \gamma B_{loc}(T),$$

where ω is the Larmor angular frequency and γ is the gyromagnetic ratio of the hydrogen nuclei (267.522×10^6 rad/s/T). Hydrogen nuclei in water at higher temperatures have lower corresponding resonant frequencies due to decreased hydrogen bonding (Fig 1). PRF thermometry relies on these changes in resonance frequency in hydrogen nuclei within water¹⁷ in response to local changes in tissue temperature. For example, in a 1.5T magnetic field, an increase of 1°C would result in a decrease in the PRF of 0.6387 Hz.¹⁹ Hence, temperature changes result in local resonant frequency variations. The measured temperature change is relative and is based on the assumption that the reference body temperature is 37°C .

There are several methods to estimate the temperature using the relationship between water proton frequency and temperature. MRS imaging provides the nuclear magnetic resonance signal spectrum, allowing monitoring the frequency peak of the water proton.

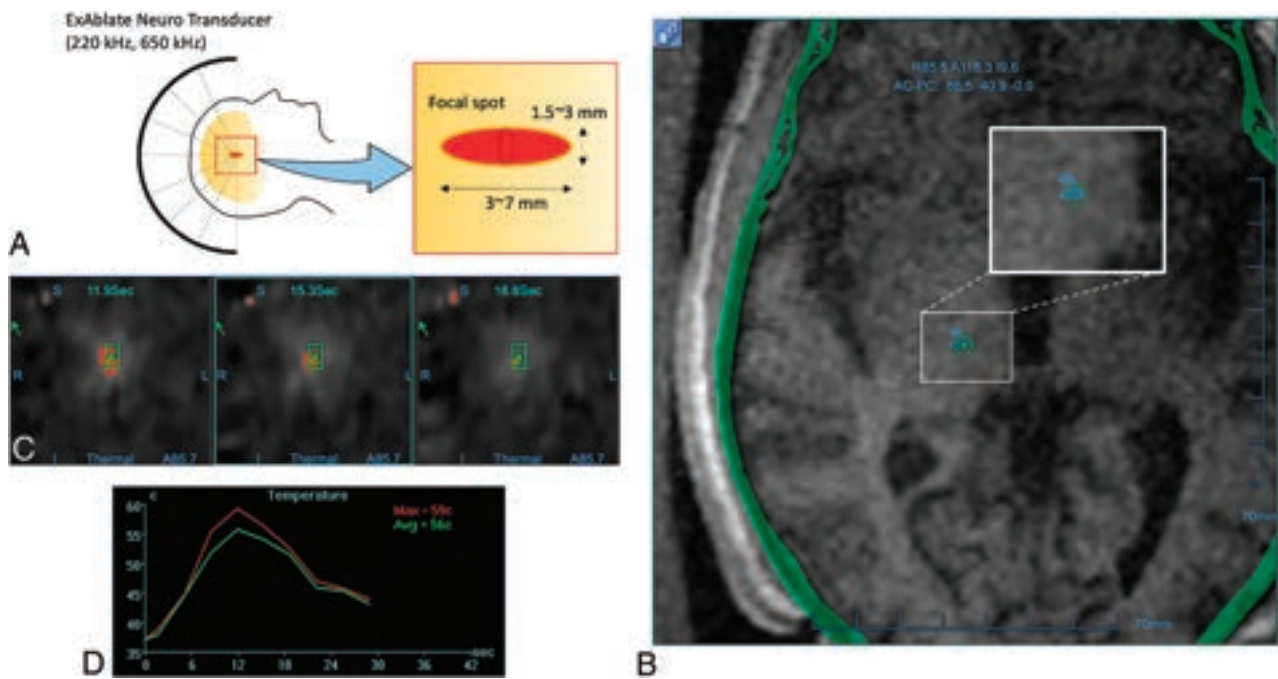


FIG 2. MR imaging thermometry during transcranial focused ultrasound. *A*, The focal spot of the ExAblate Neuro transducer takes a prolate ellipsoid shape, measuring approximately 1.5 mm in diameter and 3 mm in length at 650 kHz and approximately 3 mm in diameter and 7 mm in length at 220 kHz. *B*, The PRF thermal dose map shows an accumulated thermal dose in light blue, which is based on the CEM43 model. The thermal dose map visualizes the amount of heat deposited into the target tissue, allowing clinicians to optimize treatment parameters and positioning while minimizing the risk of normal tissue damage. *C*, Multiple MRT images are obtained during sonication. In this example, images are acquired at 11.9 seconds (*left panel*), 15.3 seconds (*middle panel*), and 18.8 seconds (*right panel*) after the sonication has begun, generating images of tissue temperature at the focal spot according to a user-determined color scale. The time intervals between images will vary depending on the user-determined settings, such as the addition of presonation baseline phases or changing from multiple- to single-echo thermometry. The duration of the sonication is often set so that peak temperatures are achieved in sync with the MRT acquisition. The alignment of the focal spot to the target is best assessed in the phase-encoding direction. *D*, After sonication, a temperature graph is generated to show average and maximal temperatures across time within the ROI. Avg indicates average; Max, maximum.

On the basis of spectroscopic imaging, the temperature can be estimated by observing the frequency difference between the water proton and the reference, such as the tissue lipid²⁰ or contrast agents.²¹ PRF-based MRS imaging is the sole method capable of measuring absolute temperature with high accuracy (eg, 0.3°C for 1-mL voxels²²). Nevertheless, most MRS techniques are limited in terms of spatial resolution and real-time MR imaging acquisition, which are necessary for rapid temperature monitoring in transcranial MRgFUS applications. The other approach is to use MR phase mapping because changes in the temperature can alter the MR resonance frequency. In phase mapping-based PRF thermometry, temperature-induced local frequency variations can be detected using spoiled gradient recalled-echo (GRE) sequences to acquire phase maps before and during tissue heating. By subtracting the baseline phase images from the subsequent phase images acquired during heating, chemical shift effects that are not temperature-dependent are theoretically removed. Phase differences caused by field deviations within biologic tissues can be used for estimating relative changes in temperature as follows:

Equation 4
$$\Delta T = \frac{\phi(T) - \phi(T_0)}{\gamma \alpha B_0 TE},$$

where ΔT is the temperature difference relative to the reference image, $\phi(T)$ is the current phase image, $\phi(T_0)$ is the reference

phase image, γ is the gyromagnetic ratio, α is the temperature-sensitive coefficient, B_0 is the main magnetic field, and TE is the echo time. The reference phase image (before heating) is subtracted from the current phase image (during heating). Finally, relative changes in temperature can be calculated.

PRF thermometry allows temperature maps to be acquired in seconds,¹⁵ noting that it has suboptimal performance in adipose tissue, making it less ideal for body applications of HIFU but appropriate for transcranial HIFU. Because HIFU generally creates a focal spot in a prolate ellipsoid shape that is 3–4 mm in diameter and 4–5 mm in height²³ (Fig 2), the PRF sequence resolution must have an in-plane resolution of at least 1–2 mm and a section thickness maximum of 3 mm.²⁴ In general, clinical imaging systems have a temperature precision of approximately 1°–2°C²⁵ and are typically acquired during ablation,²⁶ with the most important image acquired after the sonication peak. Specifically, for the transcranial HIFU Insightec ExAblate Neuro system using a body coil for receive and transmit and a gradient-echo sequence (FOV = 280 mm; frequency = 256; phase = 128; section thickness = 3 mm; matrix = 256 × 256), the spatial resolution is 1.09 × 1.09 × 3 mm and the temporal resolution is ~3.5 seconds per dynamic image with a total acquisition of <1 minute for each sonication. Currently a standard diagnostic head imaging coil cannot be used with the Insightec ExAblate Neuro device. Also, current MRT used for

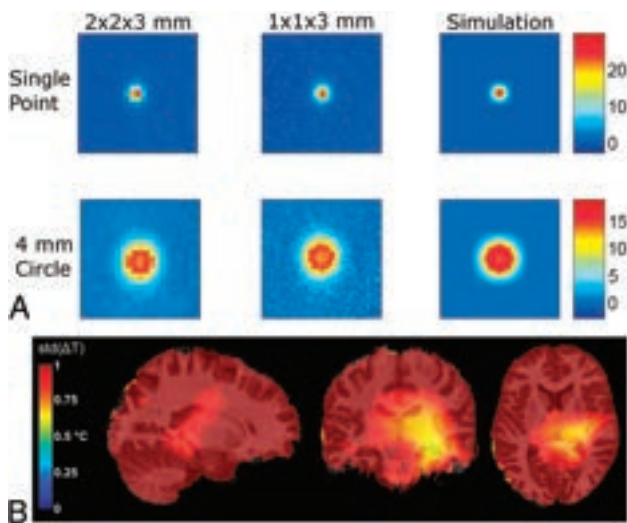


FIG 3. Sources of error in MR imaging thermometry. *A*, Temperature maps during HIFU heating using different spatial resolutions (left to right: $2 \times 2 \times 3 \text{ mm}^3$, $1 \times 1 \times 3 \text{ mm}^3$, $0.1 \times 0.1 \times 0.1 \text{ mm}^3$ simulation). This experiment showed that imaging with a spatial resolution of $1.0 \times 1.0 \times 3.0 \text{ mm}^3$ or higher with slices oriented perpendicular to the beam path resulted in the best accuracy of temperature measurement (figure reproduced from Todd et al²⁴ with permission). *B*, Temporal SD (std) of PRF temperature maps overlaid on sagittal, coronal, and axial MR images demonstrate errors in temperature measurement due to motion (eg, B_0 field drift, cardiac pulsation, respiratory motion; figure reproduced from Le Ster⁷⁵).

transcranial HIFU with Insightec equipment can only be acquired in 2 dimensions and must be acquired in 1 of 3 orthogonal planes during sonication.

Thermal Dosimetry

Dosimetry models are used to estimate thermal tissue damage during HIFU procedures. When the PRF temperature map is obtained, the cumulative equivalent minutes at 43°C (CEM43) model can be used to estimate a thermal isoeffect dose through the exposure time.^{27,28}

$$\text{Equation 5} \quad \text{CEM43} = \int_0^t R^{(43-T)} dt,$$

where R is the factor depending on temperature range: 0.25 ($T \leq 43^\circ\text{C}$) and 0.5 ($T > 43^\circ\text{C}$). van Rhooen et al²⁸ reported the challenges in establishing precise thermal thresholds for brain tissue due to the substantial differences in species, data availability, and a lack of such data in humans. However, previous investigations reported that thermal tissue damage can occur in the range of 10 CEM43, and a thermal dose as low as 0.1 CEM43 can result in changes in the BBB permeability, metabolism, CBF, and neural activity.²⁹ Hence, close monitoring and careful control of the thermal dose are especially helpful to ensure the safety and efficacy of transcranial HIFU (Fig 2B). Of note, when performing LIFU for neuromodulation in neuropsychiatric diseases, it is recommended to keep the thermal dose below 0.1 CEM43 to minimize uncontrolled physiologic changes. Thus, depending on the clinical indication and target, thermometry is often not used for LIFU.

Optimization of PRF Thermometry

Trade-Offs. As in other MR imaging, in PRF thermometry there are trade-offs among spatial resolution, temporal resolution, and SNR. Todd et al²⁴ showed that the spatial resolution needed to capture nonuniform temperature distributions created by HIFU (Fig 3A) is highly dependent on the shape of temperature distribution. Low-resolution imaging was sufficient in accurate measurement of a temperature distribution that changes linearly in space. However, higher spatial resolution is needed when the temperature distribution is nonlinear, which is often the case in HIFU, in which the distribution is based on the shape and size of the focal zone, the heating trajectory, and the ultrasound power and deposition. Their experiments showed that imaging with a spatial resolution of $1.0 \times 1.0 \times 3.0 \text{ mm}^3$ or higher with slices oriented perpendicular to beam path resulted in the best accuracy of temperature measurement. Because the HIFU thermal ablation lesion at the focal zone is elongated in the craniocaudal direction (as a prolate ellipsoid), there is inherently less curvature of the temperature distribution in the direction of the beam, allowing thicker acquisition slices to be used. Thus, PRF thermometry is often acquired in the axial plane because small errors in section prescription on coronal or sagittal imaging may result in missing the hot spot.

Image SNR

The phase-dependent SNR from these images is proportional to the PRF change as well as the sequence TE.¹⁵ As shown in Equation 2, when the $T2^*$ relaxation time of brain tissues is equal to the TE, the optimal SNR can be achieved.

$$\text{Equation 6} \quad \text{SNR} \propto TEe^{-\frac{TE}{T_2^*}}.$$

To perform MRT that has sensitivity on the order of 0.01 ppm, a high degree of magnetic field homogeneity is required. In standard 2D Cartesian Fourier transform (2DFT) thermometry, when all available time in a TR is used for sampling to maximize the SNR, the result is a long imaging time, which makes the images more sensitive to off-resonance/local frequency change.

Magnetic Field Inhomogeneity

Magnetic field inhomogeneity can be conceptualized in terms of external magnetic flux and local magnetic susceptibility. These sources of error include magnetic field drift and susceptibility changes.^{31,32} Magnetic field drift refers to the change in the magnetic field flux due to extrinsic factors such as the flux in the earth's own magnetic field and gradient system heating that occurs when applying large gradients.³² Magnetic field phase drifts in clinical scanners while scanning have been reported to be from 0.01 to 0.06 ppm/min (or $0.6 \times 3.6 \text{ ppm/h}$), which could result in up to approximately $6^\circ\text{C}/\text{min}$ of scan time (assuming a PRF coefficient of $-0.008 \text{ ppm}/^\circ\text{C}$).³³ Depending on the polarity, these field drifts can result in both over- and underestimation.³⁴ Because the drift is small during acquisition, it can be corrected with postprocessing using internal or external references such as aqueous tissue outside the heating zone (as in referenceless thermometry described below) or fat-based tissues (with minimal phase shift due to heat).³⁵

Susceptibility changes due to inhomogeneity in a patient's tissues can also greatly affect temperature measurement. Briefly, susceptibility is caused by paramagnetic, ferromagnetic, or diamagnetic substances (ie, Ca^{2+}) and is particularly noticed at the interface of 2 different substances (eg, between gas and bone).³⁶ Blood flow parameters also greatly affect magnetic inhomogeneity, such as deoxyhemoglobin concentration, blood flow, hematocrit, red blood cell integrity, and vessel orientation. Additionally, other relevant factors that affect homogeneity include molecular diffusion, pH, and prior contrast use.³⁷

Off-Resonance Sensitivity

The multiecho approach is an effective method for mitigating off-resonance sensitivity while maintaining SNR. In early multiecho 2DFT sequences, temperature was estimated by determining the slope of the linear fit of the phase versus TEs.³⁸ While multiecho sequences were of similar scan length to those of single-echo gradient images with long TEs, they allowed less aliasing/phase wrapping (ie, the ability to detect temperature increases of $\geq 100^\circ\text{C}$). The multiecho approach compared with the single-echo gradient approach showed less aliasing at sites of bone and fat as well.³⁸ Furthermore, the multiecho images showed less degradation from motion and greater ability to identify areas with multiple spectral components. Newer approaches combining multiple independent temperature estimates can be performed to optimize temperature SNR.^{39,40}

Electrical Properties

Temperature change in ablated tissue can also lead to change in the electrical properties of the tissue, causing a constant incremental phase shift per unit change in temperature completely independent of the TE.⁴¹ Increasing temperature leads to an increase in electrical conductivity, causing more attenuation in the amplitude of the MR radiofrequency pulses used for imaging acquisition, affecting the phase and ultimately temperature measurement. This typically affects procedures that heat larger tissue volumes like deep regional hyperthermia and is less consequential in ablative procedures like MRgFUS, in which the ablation zone is smaller and much more focused.

Spatial Sampling: Frequency versus Phase-Encoding Direction

Chemical shift artifacts are noted on spin-echo anatomic imaging at the interface between fat and water due to slightly different resonant frequencies of hydrogen nuclei within lipid and water (because there is no deshielding of the hydrogen nuclei in lipid). These cause a spatial misregistration of the fat and water molecules in the frequency-encoding direction. For standard gradient-echo sequences and PRF thermometry, the sensitivity of these distortions is larger in the frequency-encoding than in the phase-encoding direction.⁴² This phenomenon should be considered when performing geometric adjustments in the ExAblate Neuro system. If a focal spot is generated with an offset between the current and planned spot location, the system allows electronic adjustments to the focal spot. In this process, the frequency direction can be ignored because MR images may display shifted geometric information, making it unnecessary to consider the

frequency-encoding direction during the adjustment procedure. Thus, intraoperative thermal measurements only in the phase-encoding direction are recommended (Fig 2C).

Motion Sensitivity

Current clinical MRT sequences typically use a single baseline to reconstruct temperature maps so that a single preheating acquisition is subtracted from a postheating acquisition. This feature has been shown to work well in phantoms and stationary tissues but is susceptible to substantial artifacts when motion occurs. Currently, the Insightec ExAblate Neuro system performs a motion-detection scan in which areas of high contrast (eg, interface between pia mater/ependyma and CSF) are monitored during treatment. If motion is detected, sonication is aborted.

Motion leads to phase errors in the PRF calculation in various ways (Fig 3B). First, voxel-by-voxel phase subtraction results in a significant temperature error if there is image misregistration. Second, susceptibility changes of the magnetic field result in an additional phase value in the PRF calculation. Third, organ movement during MR image acquisition generates blurring and ghost artifacts, which may cause temperature bias or uncertainty, even if those artifacts may not directly affect PRF temperature maps. While more important in body clinical applications of HIFU due to the presence of respiratory motion, cardiac motion, and gut peristalsis, motion also degrades intracranial MRT, especially when considering that thermal ablative lesions in the thalamus require submillimetric precision to avoid complications. Head motion, brain pulsation (due to the effect of the cardiac cycle on cerebral perfusion⁴³ and CSF flow⁴⁴), and facial motion (of the eyelids, tongue, pharynx, or jaw)^{25,45} can all lead to aliasing artifacts and reduced SNR in single baseline imaging.

There are multiple additional methods to acquire thermometry, avoiding single baseline artifacts due to periodic and non-periodic motion, including multibaseline subtraction⁴⁶⁻⁴⁸ and referenceless⁴⁹⁻⁵¹ and hybrid multibaseline/referenceless thermometry.⁵² In multibaseline subtraction, a whole set of baseline images before heating is acquired over the entire respiratory and/or cardiac cycle to create a library. After heating, either the best baseline image of the library or an averaged composite image is used for baseline subtraction^{46,53} In referenceless reconstruction, the baseline image is not used, but instead the temperature increase in every image is used. This is performed by estimating the background phase outside the heated region by fitting an equation/polynomial to the phase (ie, phase-regression analysis). This polynomial is then extrapolated to the location of heating, and a phase is estimated, which replaces the traditional baseline phase when calculated for phase shift and temperature. With this technique, there is a complete elimination of misregistration of images with the baseline data due to frame-to-frame motion.⁵⁰ However, the background phase at tissue interfaces requires larger polynomial orders to fit in referenceless reconstruction, potentially increasing the risk of underestimating the thermal dose.

In intracranial applications of MRgFUS, it is important to have whole-brain coverage, because it is important for monitoring potential heating of tissue in the near and far field of the ultrasound beam. However, it is difficult to apply a low-order

polynomial to the whole brain, especially in the frontal region and structures at the base of the brain that are adjacent to air-filled sinuses and nasal cavities.²⁵ A hybrid reconstruction combining both multibaseline and referenceless acquisitions was described in detail by Grissom et al⁵² and is reported to be more robust to both motion-related artifacts and varying anatomic configurations in moving organs (liver and heart).

Rieke et al²⁵ compared absolute temperature error and temporal temperature uncertainty of different reconstruction techniques: single baseline subtraction, multibaseline subtraction (with 30 library images), hybrid single baseline/referenceless reconstruction, and hybrid multibaseline/referenceless reconstruction. In patients undergoing transcranial MRgFUS, hybrid reconstruction yielded only approximately 5% of pixels with $>1^{\circ}\text{C}$ of error. Hybrid multibaseline/referenceless reconstruction showed little improvement compared with multibaseline subtraction in the cases in which volunteers were instructed to be as still as possible; however, it substantially outperformed traditional multibaseline reconstruction when nonrepetitive motion was present (tongue or jaw motion). While hybrid multibaseline/referenceless reconstruction achieves the best results, it requires a longer time to acquire. A hybrid single-baseline/referenceless reconstruction can substantially reduce temperature errors and is adequate for measuring temperature within the central brain for the currently FDA-approved indications for transcranial MRgFUS (essential tremor and Parkinson disease), targeting nuclei within the thalamus and globus pallidus.

Recent technical developments for motion-robust MRT have been proposed, such as principal component analysis,⁵⁴ background field removal methods,⁵⁵ motion correction using machine learning,⁵⁶ and *k*-space-based methods.⁵⁷ However, most techniques have inherent trade-offs among spatial coverage, computational costs, and the accuracy of temperature measurement.

Coil Use

During transcranial MRgFUS, ultrasound hardware surrounds the head, occupying the space typically occupied by an MR imaging head coil during diagnostic imaging. Therefore, large-diameter coils such as a body coil are used for MRT acquisition currently, but these yield markedly lower SNR. Body coils are single-channel; therefore, techniques that use multiple receiver channels such as parallel imaging cannot be currently used.⁵⁸ Recently, a 2-channel receive-only head coil was designed specifically for use in conjunction with the ExAblate Neuro system and is being offered by Insightec to be used with 3T scanners.⁵⁹ Unlike a standard head coil, this coil is made integral with the membranes used in the Insightec machine and is disposable. As reported, the head coil improved the SNR on T2-weighted images compared with the volume body coil by 3–4 times. A higher SNR may have the potential to provide better treatment-planning, more precise temperature measurements, and ultimately better clinical results. Development of MRgFUS-compatible coil arrays that allow parallel imaging is a burgeoning area of research, because the currently developed MRgFUS coil arrays still have fewer coils than those used in conventional anatomic or functional parallel imaging (11 versus 32).⁶⁰

Large-Brain-Volume MRT

Typically, PRF MRT is acquired using a spoiled GRE sequence in which temperature-induced local frequency variations lead to phase changes in the MR signal. As previously mentioned, the temperature sensitivity is maximized when the TE is the same as or closest to the T2* relaxation time within tissues. This required TE naturally leads to a longer TR in the GRE sequence, leading to extended total acquisition times and increased susceptibility to motion. Hence, acceleration strategies should be considered to improve the temporal resolution when measuring temperature over a large brain volume.

The Insightec ExAblate Neuro system offers 2 options for image acquisition: a single-section acquisition using a 2DFT GRE sequence or multisection acquisition (typically 3–5 slices) using EPI. While EPI can cover multiple slices, it is often associated with a lower SNR and susceptibility artifacts, which can cause spatial shifts in the resulting images. Other acceleration approaches include spiral and radial readout trajectories, as well as compressed sensing.^{61–63} Recently, there has been growing interest in using accelerated imaging techniques to measure temperature over a large brain volume.⁶⁴

Future Considerations

Beam Localization without MRT. The MR acoustic radiation force imaging technique is an emerging method that allows one to image the location of the focal spot without a small temperature rise.^{65,66} A long sonographic impulse (1–20 ms) produces an acoustic radiation force that can create tissue displacements locally led by shear wave propagation. This displacement can be encoded in the phase direction of the MR image using bipolar motion-sensitizing gradients.⁶⁶ This step enables accurate spot localization, evaluation, calibration, and refocusing of the ultrasound focal zone without the test sonication that causes a small temperature rise.

MR Imaging Assessment of Treatment Outcomes

After MRgFUS treatment, the criterion standard assessment of the ablation zone is to measure nonperfused volume (NPV) using gadolinium-based contrast-enhanced MR imaging. After gadolinium injection, the region without enhancement characterizes the NPV, which is associated with the coagulated tissue.^{67,68} However, intraprocedural postcontrast NPV assessment is generally not performed due to safety concerns regarding heating of the contrast as well as potential errors of MRT.^{69–71} In clinical practice, DWI is obtained postprocedurally to estimate the ablation zone.

Alternatively, the cumulative thermal dose can offer important information for tissue response in HIFU treatment. In MRgFUS treatments for essential tremor, Huang et al⁷² demonstrated that an accumulated thermal dose in the range of 17–240 CEM43 is highly correlated with lesion size measured by T1- and T2-weighted MR images. This finding may suggest that the cumulative thermal dose can help clinicians determine treatment end points in the procedure.

Multiple additional MR imaging methods are being developed and evaluated to detect treatment effects after MRgFUS, including T1/T2 mapping, magnetization transfer ratio, amide proton transfer, and MR elastography.^{70,73,74} A combination of emerging

multiparametric MR imaging techniques may be needed to obtain a more comprehensive evaluation of tissue-level changes during and after MRgFUS.

CONCLUSIONS

As enthusiasm for incisionless transcranial MRgFUS continues to grow for a continually expanding set of indications; work to optimize reconstruction methods, mitigate common artifacts, and create dedicated coils will further improve PRF MRT for clinical use. An in-depth understanding of the MRT sequences, including pitfalls and limitations, will enable avoidance of complications during MRgFUS procedures by using real-time image guidance.

Disclosure forms provided by the authors are available with the full text and PDF of this article at www.ajnr.org.

REFERENCES

- Meng Y, Hynynen K, Lipsman N. **Applications of focused ultrasound in the brain: from thermoablation to drug delivery.** *Nat Rev Neurol* 2021;17:7–22 CrossRef Medline
- Abraham A, Meng Y, Llinas M, et al. **First-in-human trial of blood-brain barrier opening in amyotrophic lateral sclerosis using MR-guided focused ultrasound.** *Nat Commun* 2019;10:4373 CrossRef Medline
- Nicodemus NE, Becerra S, Kuhn TP, et al. **Focused transcranial ultrasound for treatment of neurodegenerative dementia.** *Alzheimers Dement (N Y)* 2019;5:374–81 CrossRef Medline
- Chen SG, Tsai CH, Lin CJ, et al. **Transcranial focused ultrasound pulsation suppresses pentylenetetrazol induced epilepsy in vivo.** *Brain Stimul* 2020;13:35–46 CrossRef Medline
- Dai H, Chen F, Yan S, et al. **In vitro and in vivo investigation of high-intensity focused ultrasound (HIFU) hat-type ablation mode.** *Med Sci Monit* 2017;23:3373–82 CrossRef Medline
- Premarket Approval (PMA).** <https://www.accessdata.fda.gov/scripts/cdrh/cfdocs/cfPMA/pma.cfm>. Accessed December 20, 2022
- FDA. Exablate Model 4000 Type 1.0 and 1.1 System (“Exablate Neuro”)-P150038/S014.** January 3, 2022. <https://www.fda.gov/medical-devices/recently-approved-devices/exablate-model-4000-type-10-and-11-system-exablate-neuro-p150038s014>. Accessed December 20, 2022
- Gandhi D. **MR Guided Focused Ultrasound (FUS) for the Treatment of Trigeminal Neuralgia.** 2022. <https://clinicaltrials.gov/ct2/show/NCT04579692>. Accessed December 19, 2022
- Gandhi K, Barzegar-Fallah A, Banstola A, et al. **Ultrasound-mediated blood-brain barrier disruption for drug delivery: a systematic review of protocols, efficacy, and safety outcomes from preclinical and clinical studies.** *Pharmaceutics* 2022;14:833 CrossRef Medline
- InSightec. **Blood-brain Barrier (BBB) Disruption Using Exablate Focused Ultrasound With Standard of Care Treatment of NSCLC Brain Mets.** 2022. <https://clinicaltrials.gov/ct2/show/NCT05317858>. Accessed December 19, 2022
- Bunevicius A, Pikis S, Padilla F, et al. **Sonodynamic therapy for gliomas.** *J Neurooncol* 2022;156:1–10 CrossRef Medline
- Goodman W. **Imaging-Guided Low Intensity Focused Ultrasound (LIFU) (LIFU).** 2022. <https://classic.clinicaltrials.gov/ct2/show/NCT05467085>. Accessed October 20, 2022
- Feltrin FS, Chopra R, Pouratian N, et al. **Focused ultrasound using a novel targeting method four-tract tractography for magnetic resonance-guided high-intensity focused ultrasound targeting.** *Brain Commun* 2022;4:fcac273 CrossRef Medline
- Baek H, Pahk KJ, Kim H. **A review of low-intensity focused ultrasound for neuromodulation.** *Biomed Eng Lett* 2017;7:135–42 CrossRef Medline
- Rieke V, Butts Pauly K. **MR thermometry.** *J Magn Reson Imaging* 2008;27:376–90 CrossRef Medline
- Dehkharghani S, Qiu D. **MR thermometry in cerebrovascular disease: physiologic basis, hemodynamic dependence, and a new frontier in stroke imaging.** *AJNR Am J Neuroradiol* 2020;41:555–65 CrossRef Medline
- Ishihara Y, Calderon A, Watanabe H, et al. **A precise and fast temperature mapping using water proton chemical shift.** *Magn Reson Med* 1995;34:814–23 CrossRef Medline
- Kuroda K. **Non-invasive MR thermography using the water proton chemical shift.** *Int J Hyperthermia* 2005;21:547–60 CrossRef Medline
- Lewa CJ, de Certaines JD. **Body temperature mapping by magnetic resonance imaging.** *Spectrosc Lett* 1994;27:1369–419 CrossRef
- Kuroda K, Mulkern RV, Oshio K, et al. **Temperature mapping using the water proton chemical shift: self-referenced method with echo-planar spectroscopic imaging.** *Magn Reson Med* 2000;43:220–25 CrossRef Medline
- Lindner LH, Reinl HM, Schlemmer M, et al. **Paramagnetic thermosensitive liposomes for MR-thermometry.** *Int J Hyperthermia* 2005;21:575–88 CrossRef Medline
- Marshall I, Karaszewski B, Wardlaw JM, et al. **Measurement of regional brain temperature using proton spectroscopic imaging: validation and application to acute ischemic stroke.** *Magn Reson Imaging* 2006;24:699–706 CrossRef Medline
- Jeanmonod D, Werner B, Morel A, et al. **Transcranial magnetic resonance imaging-guided focused ultrasound: noninvasive central lateral thalamotomy for chronic neuropathic pain.** *Neurosurg Focus* 2012;32:E1 CrossRef Medline
- Todd N, Vyas U, de Bever J, et al. **The effects of spatial sampling choices on MR temperature measurements.** *Magn Reson Med* 2011;65:515–21 CrossRef Medline
- Rieke V, Instrella R, Rosenberg J, et al. **Comparison of temperature processing methods for monitoring focused ultrasound ablation in the brain.** *J Magn Reson Imaging* 2013;38:1462–71 CrossRef Medline
- Kim YS, Trillaud H, Rhim H, et al. **MR thermometry analysis of sonication accuracy and safety margin of volumetric MR imaging-guided high-intensity focused ultrasound ablation of symptomatic uterine fibroids.** *Radiology* 2012;265:627–37 CrossRef Medline
- Sapareto SA, Dewey WC. **Thermal dose determination in cancer therapy.** *Int J Radiat Oncol Biol Phys* 1984;10:787–800 CrossRef Medline
- van Rhooen GC, Samaras T, Yarmolenko PS, et al. **CEM43°C thermal dose thresholds: a potential guide for magnetic resonance radiofrequency exposure levels?** *Eur Radiol* 2013;23:2215–27 CrossRef Medline
- Yarmolenko PS, Moon EJ, Landon C, et al. **Thresholds for thermal damage to normal tissues: an update.** *Int J Hyperthermia* 2011;27:320–43 CrossRef Medline
- Schmidt R, Frydman L. **Alleviating artifacts in 1H MRI thermometry by single scan spatiotemporal encoding.** *MAGMA* 2013;26:477–90 CrossRef Medline
- Marx M, Pauly KB. **Improved MRI thermometry with multiple-echo spirals.** *Magn Reson Med* 2016;76:747–56 CrossRef Medline
- El-Sharkawy AM, Schär M, Bottomley PA, et al. **Monitoring and correcting spatio-temporal variations of the MR scanner’s static magnetic field.** *MAGMA* 2006;19:223–36 CrossRef Medline
- Odeón H, Parker DL. **Magnetic resonance thermometry and its biological applications: physical principles and practical considerations.** *Prog Nucl Magn Reson Spectrosc* 2019;110:34–61 CrossRef Medline
- De Poorter J, De Wagter C, De Deene Y, et al. **Noninvasive MRI thermometry with the proton resonance frequency (PRF) method: in vivo results in human muscle.** *Magn Reson Med* 1995;33:74–81 CrossRef Medline
- Hofstetter LW, Yeo DT, Dixon WT, et al. **Fat-referenced MR thermometry in the breast and prostate using IDEAL.** *J Magn Reson Imaging* 2012;36:722–32 CrossRef Medline
- Haacke EM, Xu Y, Cheng YCN, et al. **Susceptibility weighted imaging (SWI).** *Magn Reson Med* 2004;52:612–18 CrossRef Medline
- Hermier M, Nighoghossian N. **Contribution of susceptibility-weighted imaging to acute stroke assessment.** *Stroke* 2004;35:1989–94 CrossRef Medline

38. Mulkern RV, Panych LP, McDannold NJ, et al. **Tissue temperature monitoring with multiple gradient-echo imaging sequences.** *J Magn Reson Imaging* 1998;8:493–502 CrossRef Medline
39. Madore B, Panych LP, Mei CS, et al. **Multipathway sequences for MR thermometry.** *Magn Reson Med* 2011;66:658–68 CrossRef Medline
40. Todd N, Diakite M, Payne A, et al. **In vivo evaluation of multi-echo hybrid PRF/T1 approach for temperature monitoring during breast MR-guided focused ultrasound surgery treatments.** *Magn Reson Med* 2014;72:793–99 CrossRef Medline
41. Peters RD, Henkelman RM. **Proton-resonance frequency shift MR thermometry is affected by changes in the electrical conductivity of tissue.** *Magn Reson Med* 2000;43:62–71 CrossRef Medline
42. Maier SE, Scheidegger MB, Liu K, et al. **Accurate velocity mapping with FAcE.** *Magn Reson Imaging* 1996;14:163–71 CrossRef Medline
43. Greitz D, Wirestam R, Franck A, et al. **Pulsatile brain movement and associated hydrodynamics studied by magnetic resonance phase imaging: the Monro-Kellie doctrine revisited.** *Neuroradiology* 1992;34:370–80 CrossRef Medline
44. Enzmann DR, Pelc NJ. **Brain motion: measurement with phase-contrast MR imaging.** *Radiology* 1992;185:653–60 CrossRef Medline
45. Peters NH, Bartels LW, Sprinkhuizen SM, et al. **Do respiration and cardiac motion induce magnetic field fluctuations in the breast and are there implications for MR thermometry?** *J Magn Reson Imaging* 2009;29:731–35 CrossRef Medline
46. Kim K, Diederich C, Narsinh K, et al. **Motion-robust, multi-slice, real-time MR thermometry for MR-guided thermal therapy in abdominal organs.** *Int J Hyperthermia* 2023;40:2151649 CrossRef Medline
47. Vigen KK, Daniel BL, Pauly JM, et al. **Triggered, navigated, multi-baseline method for proton resonance frequency temperature mapping with respiratory motion.** *Magn Reson Med* 2003;50:1003–10 CrossRef Medline
48. de Senneville BD, Mougnot C, Moonen CTW. **Real-time adaptive methods for treatment of mobile organs by MRI-controlled high-intensity focused ultrasound.** *Magn Reson Med* 2007;57:319–30 CrossRef Medline
49. Grissom WA, Lustig M, Holbrook AB, et al. **Reweighted ℓ_1 referenceless PRF shift thermometry.** *Magn Reson Med* 2010;64:1068–77 CrossRef Medline
50. Rieke V, Vigen KK, Sommer G, et al. **Referenceless PRF shift thermometry.** *Magn Reson Med* 2004;51:1223–31 CrossRef Medline
51. Kuroda K, Kokuryo D, Kumamoto E, et al. **Optimization of self-reference thermometry using complex field estimation.** *Magn Reson Med* 2006;56:835–43 CrossRef Medline
52. Grissom WA, Rieke V, Holbrook AB, et al. **Hybrid referenceless and multibaseline subtraction MR thermometry for monitoring thermal therapies in moving organs.** *Med Phys* 2010;37:5014–26 CrossRef Medline
53. Shmatukha AV, Bakker CJG. **Correction of proton resonance frequency shift temperature maps for magnetic field disturbances caused by breathing.** *Phys Med Biol* 2006;51:4689–705 CrossRef Medline
54. Toupin S, Senneville B. D, Ozanne V, et al. **Combination of principal component analysis and optical-flow motion compensation for improved cardiac MR thermometry.** *Phys Med Biol* 2017;62:1208–24 CrossRef Medline
55. Wu M, Mulder HT, Baron P, et al. **Correction of motion-induced susceptibility artifacts and B_0 drift during proton resonance frequency shift-based MR thermometry in the pelvis with background field removal methods.** *Magn Reson Med* 2020;84:2495–511 CrossRef Medline
56. de Senneville BD, Coupé P, Ries M, et al. **Deep correction of breathing-related artifacts in real-time MR-thermometry.** *Comput Med Imaging Graph* 2021;87:101834 CrossRef Medline
57. Parker DL, Payne A, Odéen H. **A k-space-based method to measure and correct for temporal B_0 field variations in MR temperature imaging.** *Magn Reson Med* 2022;88:1098–111 CrossRef Medline
58. Pruessmann KP, Weiger M, Scheidegger MB, et al. **SENSE: sensitivity encoding for fast MRI.** *Magn Reson Med* 1999;42:952–62
59. Bitton RR, Sheingauz E, Assif B, et al. **Evaluation of an MRI receive head coil for use in transcranial MR guided focused ultrasound for functional neurosurgery.** *Int J Hyperthermia* 2021;38:22–29 CrossRef Medline
60. Minalga E, Payne A, Merrill R, et al. **An 11-channel radio frequency phased array coil for magnetic resonance guided high-intensity focused ultrasound of the breast.** *Magn Reson Med* 2013;69:295–302 CrossRef Medline
61. Gaur P, Grissom WA. **Accelerated MRI thermometry by direct estimation of temperature from undersampled k-space data.** *Magn Reson Med* 2015;73:1914–25 CrossRef Medline
62. Fielden SW, Feng X, Zhao L, et al. **A spiral-based volumetric acquisition for MR temperature imaging.** *Magn Reson Med* 2018;79:3122–27 CrossRef Medline
63. Zhang L, Armstrong T, Li X, et al. **A variable flip angle golden-angle-ordered 3D stack-of-radial MRI technique for simultaneous proton resonant frequency shift and T1-based thermometry.** *Magn Reson Med* 2019;82:2062–76 CrossRef Medline
64. Jonathan SV, Grissom WA. **Volumetric MRI thermometry using a three-dimensional stack-of-stars echo-planar imaging pulse sequence.** *Magn Reson Med* 2018;79:2003–13 CrossRef Medline
65. Pauly BK. **Magnetic resonance acoustic radiation force (impulse) imaging (MR-ARFI).** *J Ther Ultrasound* 2015;3:O34 CrossRef
66. Kaye EA, Chen J, Pauly KB. **Rapid MR-ARFI method for focal spot localization during focused ultrasound therapy.** *Magn Reson Med* 2011;65(3):738–743 CrossRef Medline
67. Hectors SJ, Jacobs I, Moonen CTW, et al. **MRI methods for the evaluation of high intensity focused ultrasound tumor treatment: current status and future needs.** *Magn Reson Med* 2016;75:302–17 CrossRef Medline
68. Wijlemans JW, Deckers R, van den Bosch MA, et al. **Evolution of the ablation region after magnetic resonance-guided high-intensity focused ultrasound ablation in a Vx2 tumor model.** *Invest Radiol* 2013;48:381–86 CrossRef Medline
69. Dinger SC, Fridjhon P, Rubin DM. **Thermal excitation of gadolinium-based contrast agents using spin resonance.** *PLoS One* 2016;11:e0158194 CrossRef Medline
70. Morochnik S, Ozhinsky E, Rieke V, et al. **T2 mapping as a predictor of nonperfused volume in MRgFUS treatment of desmoid tumors.** *Int J Hyperthermia* 2019;36:1272–77 CrossRef Medline
71. Hölscher T, Raman R, Fisher DJ, et al. **Effects of varying duty cycle and pulse width on high-intensity focused ultrasound (HIFU)-induced transcranial thrombolysis.** *J Ther Ultrasound* 2013;1:18 CrossRef Medline
72. Huang Y, Lipsman N, Schwartz ML, et al. **Predicting lesion size by accumulated thermal dose in MR-guided focused ultrasound for essential tremor.** *Med Phys* 2018;45:4704–10 CrossRef Medline
73. Hundt W, Yuh EL, Steinbach S, et al. **Effect of continuous high intensity focused ultrasound in a squamous cell carcinoma tumor model compared to muscle tissue evaluated by MRI, histology, and gene expression.** *Technol Cancer Res Treat* 2009;8:85–98 CrossRef Medline
74. Hectors SJ, Jacobs I, Strijkers GJ, et al. **Multiparametric MRI analysis for the identification of high intensity focused ultrasound-treated tumor tissue.** *PLoS One* 2014;9:e99936 CrossRef Medline
75. Le Ster C, Mauconduit F, Mirkes C, et al. **Measuring radiofrequency field-induced temperature variations in brain MRI exams with motion compensated MR thermometry and field monitoring.** *Magn Reson Med* 2022;87:1390–1400 CrossRef Medline

The Pediatric Neuroradiologist's Practical Guide to Capture and Evaluate Pre- and Postoperative Velopharyngeal Insufficiency

Michael S. Kuwabara, Thomas J. Sitzman, Kathryn A. Szymanski, Jamie L. Perry, Jeffrey H. Miller, and Patricia Cornejo



ABSTRACT

SUMMARY: Up to 30% of children with cleft palate will develop a severe speech disorder known as velopharyngeal insufficiency. Management of velopharyngeal insufficiency typically involves structural and functional assessment of the velum and pharynx by endoscopy and/or videofluoroscopy. These methods cannot provide direct evaluation of underlying velopharyngeal musculature. MR imaging offers an ideal imaging method, providing noninvasive, high-contrast, high-resolution imaging of soft-tissue anatomy. Furthermore, focused-speech MR imaging techniques can evaluate the function of the velum and pharynx during sustained speech production, providing critical physiologic information that supplements anatomic findings. The use of MR imaging for velopharyngeal evaluation is relatively novel, with limited literature describing its use in clinical radiology. Here we provide a practical approach to perform and interpret velopharyngeal MR imaging examinations. This article discusses the velopharyngeal MR imaging protocol, methods for interpreting velopharyngeal anatomy, and examples illustrating its clinical applications. This knowledge will provide radiologists with a new, noninvasive tool to offer to referring specialists.

ABBREVIATIONS: LVP = levator veli palatini; VPI = velopharyngeal insufficiency

The most common craniofacial anomaly is cleft palate and/or lip, occurring in 0.33 of every 1000 live births worldwide.¹ Although the timing of primary palatoplasty to repair the cleft of the palate varies across the globe, in the United States and Europe a one-stage repair is typically performed before 12 months of age.² One of the primary goals of cleft palate repair is to establish anatomy that will result in normal speech function. However, up to 30% of children^{3,4} will continue to present with hypernasal speech and/or nasal air emission due to velopharyngeal insufficiency (VPI), which is a form of velopharyngeal dysfunction. In VPI, the velopharyngeal valve does not close completely and/or consistently during the production of oralized sounds.⁵ The presence of hypernasal speech can limit a child's ability to effectively

communicate with others and has been shown to negatively impact peer relationships and academic performance.⁶ Management of VPI involves surgical intervention either seeking to restore the normal anatomy and physiology of the velopharyngeal mechanism or to narrow the velopharyngeal portal through use of a pharyngeal flap or sphincter pharyngoplasty, for example.⁶ Surgical planning for patients with VPI includes a perceptual speech evaluation performed by a speech-language pathologist and direct and/or indirect instrumentation. Selection of the appropriate surgical procedure requires reliable imaging to depict each patient's specific velopharyngeal anatomy and physiology.

Nasopharyngoscopy and videofluoroscopy are common direct imaging tools used to examine VPI.^{7,8} MR imaging is a relatively newer clinical imaging diagnostic tool in cleft care that is being introduced into cleft craniofacial care units, particularly in the United States.⁹⁻¹¹ The interest in velopharyngeal MR imaging is primarily due to the advantage of MR imaging in visualizing the velopharyngeal musculature, which is not possible using nasopharyngoscopy and videofluoroscopy.⁹⁻¹¹ Similar to videofluoroscopy, MR imaging can be used to accurately quantify key velopharyngeal structures with the added benefits of section specificity (eg, the ability to select a precise midsagittal section without head rotation) and lack of ionizing radiation, which is present, though minimal, in videofluoroscopy. The use of MR imaging in the clinical assessment process may be particularly important when muscle reconstruction is

Received June 16, 2023; accepted after revision October 3.

From the Radiology Department (M.S.K., J.H.M., P.C.), and Plastic Surgery Division (T.J.S.), Phoenix Children's Hospital, Phoenix, Arizona; Creighton University School of Medicine (K.A.S.), Phoenix Regional Campus, Phoenix, Arizona; and Department of Communication Sciences and Disorders (J.L.P.), East Carolina University, Greenville, North Carolina.

T.J.S. and J.L.P. received support from the National Institute of Dental and Craniofacial Research of the National Institutes of Health under award U01DE029750.

Please address correspondence to Michael S. Kuwabara, MD, Phoenix Children's Hospital, 1919 E Thomas Rd, Phoenix, AZ 85016; e-mail: mkuwabara@phoenixchildrens.com

Indicates open access to non-subscribers at www.ajnr.org

Indicates article with online supplemental data.

<http://dx.doi.org/10.3174/ajnr.A8055>

being considered to treat VPI¹² or following a failed VPI surgery.¹³ In such cases, details related to the position of the primary velar muscle (levator veli palatini [LVP] muscle) relative to the posterior hard palate and/or cohesiveness of the LVP muscle can be provided using MR imaging and add value to the clinical process.¹² A recent survey sampling 80 cleft palate craniofacial centers across the United States demonstrated that 93.5% of respondents think that MR imaging brings value to clinical assessment; however, only 11% reported using velopharyngeal MR imaging in their clinical workflows.¹¹ A key challenge to the widespread clinical use of velopharyngeal MR imaging is the limited technical and interpretive training of key personnel.¹⁴

Previously published guidance in the use of MR imaging for VPI has not addressed a clinical radiology audience, instead focusing heavily on the feasibility and clinical interpretations of velopharyngeal MR imaging findings for the surgical team.^{8,15-18} This article provides radiologists with a focused practical review of the MR imaging technique and interpretation for evaluating the velopharynx in patients with VPI. We will outline the velopharyngeal MR imaging protocol, explain the methods for anatomic interpretation, and provide examples of clinical applications from velopharyngeal MR imaging interpretations. Such increased training and support for radiologists in velopharyngeal MR imaging has the potential to optimize surgical planning and improve clinical care for patients with VPI.

Velopharyngeal MR Imaging Protocol

Ninety-three percent of patients with surgical planning for VPI are between 4 and 8 years of age.¹⁹ As a result, most patients scheduled for velopharyngeal MR imaging will typically be between these ages; however, velopharyngeal MR imaging has been demonstrated in VPI surgical planning for patients ranging in age from 3 to 39 years ($n = 113$ patients) at a single cleft craniofacial center in the United States.¹⁰ Patients are required to be imaged both at rest and while producing and sustaining specific sounds. While typical MR imaging in young children is often performed with sedation or general anesthesia with use of a laryngeal mask airway to support the airway for breathing, successful velopharyngeal MR imaging requires that the patient be fully awake using a nonsedated protocol with no contrast or laryngeal mask airway. Because patients are fully awake for the entire MR imaging protocol and are imaged without contrast, patient and family preparation before MR imaging is critical to its overall success. The involvement of support staff such as a speech-language pathologist in such preparation is invaluable, as acknowledged in current protocols for speech videofluoroscopy and other fully awake, nonsedated, noncontrast MR imaging protocols.^{20,21} Patients should receive anticipatory guidance about scanner noise, expectations (what to wear/bring, length of study, who will be with them in the scanner, and so forth), hearing protection, and use of a head coil. Multiple supplementary resources such as checklists, links to websites to be used with families and patients to prepare for the MR imaging, and protocol sheets have been published^{12,22} and shown to facilitate patient preparation and improve results in >95% of cases.²² Additionally hospital resources are published online and provide support for radiology staff in understanding the velopharyngeal

anatomy and making measurements of key velopharyngeal variables (details available at <https://cahs.ecu.edu/speechimaging/mri-resources-for-hospitals/>).

Example MR imaging protocol and sequence parameters are outlined in the Online Supplemental Data. Unlike brain imaging, which localizes to the nasion, velopharyngeal MR imaging should be localized to the nose tip to place the ROI at the level of the speech mechanism. The imaging protocol starts in a neutral head position. For resting sequences, patients should keep their lips together and breathe through their nose; initially, a high-resolution anatomic imaging, 3D T2-weighted sequence, is performed of the whole head. Subsequent imaging consists of rapid thicker-section sagittal and oblique coronal images, with focused FOVs including the muscular structures associated with the velopharyngeal speech mechanism. Baseline resting sagittal TSE T2-weighted images consist of 4–8 slices, scanned from 1 lateral pharyngeal wall to the contralateral side. This procedure is followed by a TSE T2 oblique coronal image, obtained at rest, acquired at a 50°–60° angle to the plane of the cribriform plate and aligned with the sphenoparietal junction (Fig 1). The oblique coronal plane is selected to visualize the entire muscle body of the LVP, the key muscle involved in velar elevation during speech production. Setting the correct plane requires training, practice, and careful image review; online training and resources are also available.²³ The oblique coronal sequence should consist of 4–8 slices, scanning from the posterior aspect of the hard palate to the tip of the uvula.^{15,24} Maximal viewing of the LVP in the oblique coronal plane is crucial. If the LVP cannot be visualized completely within this plane, the scan angle should be adjusted, and the sequence repeated before proceeding to scanning during phonation. Most frequently, the imaging plane needs to be rotated further clockwise into a more horizontal position.

After collection of sagittal and oblique coronal images at rest, additional sequences mirroring these image parameters are obtained while the child sustains phonation of selected speech sounds. The angle of the oblique coronal image plane at rest should be copied over onto the subsequent speech sequences. The speech-language pathologist should predetermine the speech sounds required for the MR imaging study and indicate these to the radiology team. The speech pathologist should select sounds that the child is able to successfully produce and sustain for the duration of the 6- to 9-second MR imaging sequence. Ideally, the patient should practice these sounds with the speech language pathologist before the MR imaging procedure, to be familiar with the tasks that will be performed during the velopharyngeal MR imaging study.

While dynamic MR imaging using speech samples has been described,²⁵⁻²⁸ these methods are not fully translated to all clinical MR imaging scanners. Clinical sites that have begun to use velopharyngeal MR imaging have, therefore, adopted the use of sustained phonation tasks, typically by using sustained phonation of /i/ (“ee” sound, as in “seek”) and /s/ (“sss” sound, as in “hiss”). These sounds are commonly used for several reasons. First, most children at the typical age for VPI surgical evaluation (4–8 years of age)¹⁹ are able to produce a sustained /i/ sound without error because this is a basic vowel sound that is acquired early in phonological development. This sound also represents a high back

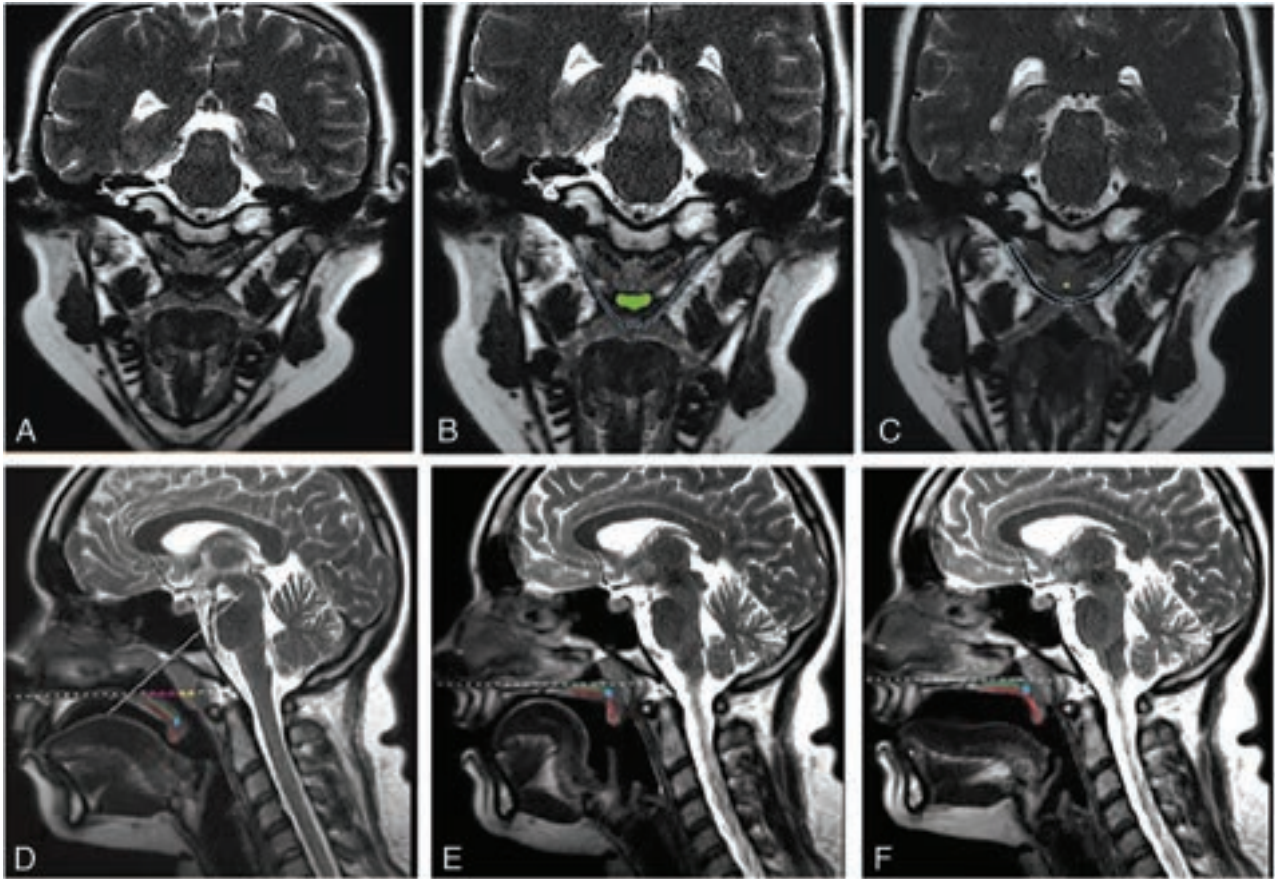


FIGURE. A, Coronal oblique T2 image along the plane of the LVP (*blue outline*, B and C) at the level of the velopharyngeal port during rest. The normal appearance of the LVP is T2-hypointense and intact along its length. B, Coronal oblique T2 with the velopharyngeal port appropriately open (*green outline*). C, Coronal oblique T2 during phonation with the velopharyngeal port appropriately closed. D, Sagittal midline T2 image through the head at rest showing the 50–60° coronal oblique plane (*solid white line*), effective length (*green line*), the total velar length (*red line*), and the palatal plane (*dotted line*). E and F, Sagittal midline T2 image during both i and s phonation, respectively. Note the appropriate elevation of the velum with closure of the velopharyngeal port as well as the tongue position.

vowel and has been shown to be a sound produced in individuals with normal velopharyngeal anatomy and physiology with the greatest degree of velar closure force.²⁹ The use of /s/ is often to assess the patient's ability to produce a consonant that can be easily sustained. The /s/ sound should be produced by the patient with an oral airflow. In many children with VPI, production of this sound may be in error with the sound being produced through the velopharynx, nasopharynx, and/or nasal passage.⁵ This is referred to as a compensatory misarticulation. If the patient uses this type of error, the speech language pathologist should advise against the use of this sound. Other consonants that the child can produce with accuracy may be used, such as /f, v, z/, which can be typically sustained for the duration of the sequence.

It is critically important to run the sequence exactly when the cue is given to the child to start sound production to ensure that the child is phonating during the entire sequence. Additionally, progressing from 1 sequence to the next as fast as possible prevents movement and improves the likelihood of obtaining the velopharyngeal muscles in each of the oblique coronal sequences. Because it can be challenging during image review to distinguish between voluntary failure to phonate and

paralysis of the palate muscles, the MR imaging technician should also listen carefully to confirm phonation during the entire image sequence. Only images collected with sustained phonation throughout the entire sequence should be accepted and saved for radiologist interpretation.

If a patient is unable to sustain phonation for 8 full seconds, sagittal sequences can be reduced to cover only the midsagittal region, and oblique coronal images can be reduced to the region representing the long axis of the LVP muscle into the velum. While these changes may limit the scope of information collected, these scans can still often provide sufficient information to inform surgical decision-making while reducing the time of the scanning substantially.

Interpreting Velopharyngeal Anatomy

LVP. Normal resonance during speech involves the coordination of several velopharyngeal muscles. The LVP is primarily responsible for elevation and posterior movement of the velum (Online Supplemental Data).^{30,31} Qualitative evaluation of LVP muscle integrity (eg, relative size, position, and cohesiveness) can be determined via oblique coronal T2-weighted sequences during rest and phonation scans (Fig 1A–C). Comparisons between rest (Fig 1A)

Table 1: The definitions for pertinent measurements for quantitatively examining VPI^{a,44}

Variable	Description
Pharyngeal depth	Linear distance (mm) from PNS to PPW or adenoid pad as seen on the midsagittal image
Velar length	Curvilinear distance (mm) from the posterior nasal spine to the tip of the uvula as seen on the midsagittal image
VP ratio	Calculation obtained from the dividing velar length by pharyngeal depth
Effective velar length	Linear distance (mm) from the posterior border of the hard palate to the point of levator muscle insertion into the velum as seen on the midsagittal image
EVP ratio	Calculation obtained from dividing effective velar length by the pharyngeal depth
Adenoid depth	Linear distance (mm) along the palatal plane from the adenoid pad to the posterior end of the adenoid

Note:—PNS indicates posterior nasal spine; PPW, posterior pharyngeal wall; VP, velopharyngeal; EVP, effective VP.

^a Adapted with permission from Perry JL, Kotlarek KJ, Sutton BP, et al. Variations in velopharyngeal structure in adults with repaired cleft palate. *Cleft Palate Craniofac J* 2018;55:1409-18.

Table 2: The mean (SD) of pertinent variables for quantitatively examining VPI and results of analysis of variance^{a,b,31}

Variable	Infants (4–23 mo.)	Children (4–9 yr)	Adolescents (10–19 yr)	Adults (20+ yr)
Pharyngeal depth	11.43 (4.46)	17.80 (4.79)	21.45 (4.62)	20.92 (4.14)
Velar length	20.27 (3.32)	27.63 (4.17)	30.98 (5.10)	34.85 (4.79)
VP ratio	2.08 (0.94)	1.70 (0.69)	1.51 (0.42)	1.73 (0.42)
Effective velar length	8.58 (1.46)	12.07 (2.43)	13.12 (3.32)	13.72 (3.46)
EVP ratio	0.89 (0.43)	0.74 (0.30)	0.63 (0.19)	0.67 (0.19)
Adenoid depth	11.36 (4.38)	9.66 (5.49)	9.96 (5.49)	5.18 (3.88)

Note:—EVP indicates effective velopharyngeal; VP, velopharyngeal.

^a Measurements are listed in millimeters with the exception of VP ratio measures.

^b Adapted from Haenssler et al.³¹ Table 3 which is copyrighted material and included here with the permission of the American Speech-Language-Hearing Association (ASHA).

and phonation (Fig 1B–C) oblique coronal images can also provide insight into the function of the LVP muscle (ie, amount of muscle shortening/contraction).

Pharyngeal Adenoidal Tissue. The pharyngeal adenoidal tissue (“fat pad”) contributes to creating a functional seal for appropriate sound production, particularly in patients with typical velar-to-adenoid contact. This tissue can vary in size; a small fat pad has a concave outer border, whereas a medium-sized fat pad has a relatively straight oblique line, and a large fat pad has a convex border extending into the nasopharynx (Online Supplemental Data).¹⁴ Adenoid tissue depth can be measured by drawing a line from the oropharynx side of the velum posteriorly and superiorly to the point where the palatal plane intersects the adenoids. In many cases, the adenoids are not measured because they rest above the level of the palatal plane and thereby play no role in velopharyngeal closure.

The Palate. The palatal plane is approximated by the anterior and posterior nasal spines, important anatomic landmarks of the hard palate. The velum is measured in the midsagittal plane at rest by adding the distance from the posterior nasal spine or posterior palate to the LVP and the distance from the LVP to the posterior tip of the velum (Fig 1D).³¹ The intersection of the palatal plane with the posterior wall of the pharynx defines the typical point of closure for children and separates the nasopharynx from the oropharynx. Pharyngeal port depth is measured in the midsagittal plane at rest from the posterior region of the hard palate to the posterior pharyngeal wall along the palatal plane reference line.³¹ Although it is rarely a point of velar contact,³² some patients may attempt velopharyngeal contact along a Passavant ridge. This is a muscular projection that extends as a muscle band anteriorly off the posterior pharyngeal wall during speech. If this is present and appears to be the point of attempted contact, the pharyngeal port depth should be drawn to the anterior region of this ridge. The

portion of the velum that provides the closure of the velopharyngeal port is called the effective velar length. Effective velar length is measured from the posterior hard palate along the velum to the middle of the horizontal portion of the LVP, which lies within the body of the velum (Fig 1D).³¹ The length of the velum at rest should be in excess of the pharyngeal port depth to achieve closure of the velum against the posterior pharyngeal wall.^{31,33} Relevant definitions, as well as normal anatomic measurements/ratios of the velum, velopharyngeal port, and LVP, are summarized in Tables 1 and 2.

Preoperative Applications of Velopharyngeal MR Imaging

Anatomic and physiologic MR imaging findings are key in surgical decision-making. VPI surgery aims to facilitate closure of the velopharyngeal port during speech production via palatal or pharyngeal approaches.⁶ Palate operations include LVP reconstruction and/or soft-palate lengthening; the integrity of the LVP and the length of the velum with respect to the size of the velopharyngeal port are, therefore, of central importance. In contrast, pharyngeal operations seek to narrow or partially obstruct the velopharyngeal port. When planning these operations, measurements of adenoid pad size, the contribution of lateral pharyngeal wall movement, the posterior pharyngeal wall movement, the amount of velar excursion, and the velopharyngeal closure pattern are important. For example, the use of a pharyngeal flap assumes that the patient has adequate lateral pharyngeal wall movement to close off the lateral ports that are otherwise open for breathing and nasal sound productions. Thus, describing the degree of lateral pharyngeal wall movement during the velopharyngeal MR imaging is valuable information for the cleft craniofacial team. Surgeons may also use velopharyngeal MR imaging data related to the size and length of the velum, LVP integrity (cohesiveness), the size of the adenoid pad, and the velopharyngeal closure pattern to determine VPI surgical strategy.

Velum Assessment. A short velum may be unable to reach the posterior pharyngeal wall to achieve velopharyngeal closure necessary for speech production, leading the surgeon to pursue a palatal lengthening operation (Online Supplemental Data).³⁴ Poor elevation of the velum on i or s phonation or failure of the LVP to shorten during phonation can suggest a hypodynamic LVP. This is often difficult to correct, potentially resulting in narrowing the overall size of the velopharyngeal cavity (Online Supplemental Data) via a pharyngeal flap or sphincter pharyngoplasty.³⁵

LVP Integrity. Discontinuity of the LVP within the velum is identified as an interruption in the T2-hypointense band of tissue running along the velar portion of the muscular sling, visualized in coronal oblique scans (Online Supplemental Data). When discontinuity is identified on MR imaging, LVP muscle reconstruction will be required.

Closure Pattern. Specific velopharyngeal closure patterns seen on oblique coronal imaging can also play an important role in surgical decision-making. There are 3 primary variants of velopharyngeal closure morphology: circular, coronal, and sagittal (Online Supplemental Data).³⁶⁻³⁸ Velopharyngeal closure can include any degree of velar excursion, lateral pharyngeal wall movement, and posterior pharyngeal wall movement. The degree of involvement of these structures in velopharyngeal closure determines the type of closure pattern observed. While closure pattern alone cannot be used to determine the surgical type, it can provide valuable insight when considering whether to perform a pharyngeal flap (generally more ideal in sagittal closure pattern types when there is ample lateral pharyngeal wall movement) or sphincter pharyngoplasty (generally ideal when there is a coronal closure pattern type evident by good velar movement but limited lateral pharyngeal wall involvement). While it is conceptually distinct, assigning a specific closure pattern can be difficult, particularly when there is incomplete velopharyngeal closure or when there is limited motion of both the velum and pharynx.³⁹

Postoperative Applications of Velopharyngeal MR Imaging

Velopharyngeal MR imaging is also used to examine anatomic and functional changes following VPI surgery. While the protocol of postoperative imaging is identical to that of preoperative imaging, there are several key differences in interpretation. An adequate surgical and clinical history is paramount to allow appropriate interpretation by the radiologist.

Without a consensus guide for the surgical approach to VPI treatment, selection is traditionally based on a multimodality evaluation of patient mechanics and speech production.³⁵ Four common procedures for repair of VPI are revisional palatoplasty, palate lengthening with buccal myomucosal flaps, a pharyngeal flap, and sphincter pharyngoplasty.^{34,35,40,41} The common goal of these procedures is to improve the closure of the velopharyngeal port by creating a tight seal between the velum and pharyngeal walls during speech production. While surgical preferences should not be discounted, the descriptions contained within the Online Supplemental Data provide a general guide for radiologists on the 4 most common surgical approaches for VPI repair.

Potential Imaging Pitfalls

Determining the optimal angular position of the oblique coronal section for visualization of the LVP is a common challenge when performing velopharyngeal MR imaging. The imaging plane should sit at 50°–60° with respect to a line drawn through the cribriform plate. If not performed correctly, the LVP will not be visualized well on a single section; this issue can lead to misdiagnosis of LVP discontinuity in midline.

Another common issue in velopharyngeal MR imaging arises in cuing the patient to produce the desired sounds during the phonation sequences. If the timing of phonation and scanning is not synchronized, a false appearance of an incomplete closure of the velopharyngeal port can be observed. Observation of tongue position is crucial to confirm appropriate phonation. During /i/ sound production, the tongue should have a convex upper margin along the superficial surface at the midportion. The tip of the tongue should also be posterior to the mandibular central incisors. During /s/ sound production, the tongue should be flattened, while the tip of the tongue protrudes just beyond the mandibular central incisors. Anecdotally, the best way to remember these positions is to make the /i/ and /s/ sounds yourself, noting the position of your own tongue (Fig 1E, -F). An incorrect tongue position can also result in a falsely closed velopharyngeal port. Careful assessment of the posterior aspect of the tongue may reveal compensatory elevation of the velum by the tongue itself.

Another limitation of the protocol outlined within this study is that the stimuli used are limited to sustained phonation tasks. There are, however, key clinical biomarkers that are best derived from static MR imaging, including levator muscle cohesiveness, length, relative position to hard palate, pharyngeal depth, velar length, adenoid involvement and size, and pharyngeal flap position.¹² These variables would be difficult to obtain using current dynamic MR imaging methods. Because speech is a dynamic event, it is important that MR imaging technologies expand to also include dynamic speech at word-, phrase-, and sentence-level productions as described by Perry and colleagues.⁴² These developments are already underway to support the translation of dynamic protocols into clinical scanners,⁴³ which will require an update to these outlined protocols. However, it is likely that sustained phonation tasks will still be of value, given the aforementioned reasons. Until such developments are available to cleft craniofacial clinics, the use of MR imaging may supplement dynamic methods of nasoendoscopy and videofluoroscopy, particularly when dynamic speech data and muscle imaging are a priority to the surgical planning.

Last, a limitation of this study surrounds issues related to access of MR imaging resources to cleft craniofacial teams throughout the world. While reports have published costs of MR imaging similar to those of other imaging methods (nasopharyngoscopy and videofluoroscopy) in the United States,¹² these costs are not universal. Many regions of the world do not have access to MR imaging for clinical use and/or costs are not realistic for patient care currently. Additionally, hospitals may not have access to training resources on site to develop and implement velopharyngeal MR imaging, and costs associated with personnel and such resources may not be feasible. Therefore, while

velopharyngeal MR imaging may be actualized in some regions of the world, it may not be globally accessible, which is true for other direct and indirect imaging tools used in cleft care.

CONCLUSIONS

The combination of higher contrast anatomic detail and rapid dynamic techniques of MR imaging allow new, innovative techniques in the assessment of VPI. Particularly attractive is the elimination of ionizing radiation, which was previously standard of care with fluoroscopic examinations. MR imaging is also noninvasive and hence much better tolerated than nasopharyngoscopy. Additionally, MR imaging provides the clinician with information on LVP muscle continuity, position, and contraction, which is not available with the currently used imaging methods of nasopharyngoscopy or multiview videofluoroscopy. Discussion and feedback among radiologists and clinicians can ensure optimal study results. Although the use of MR imaging is currently supplemental to direct visualization, continued technologic advancement and further experience may soon negate the need for other invasive techniques.

Disclosure forms provided by the authors are available with the full text and PDF of this article at www.ajnr.org.

REFERENCES

1. Salari N, Darvishi N, Heydari M, et al. **Global prevalence of cleft palate, cleft lip and cleft palate and lip: a comprehensive systematic review and meta-analysis.** *J Stomatol Oral Maxillofac Surg* 2022;123:110–20 CrossRef Medline
2. Shaw W, Semb G, Lohmander A, et al. **Timing of Primary Surgery for cleft palate (TOPS): protocol for a randomised trial of palate surgery at 6 months versus 12 months of age.** *BMJ Open* 2019;9:e029780 CrossRef Medline
3. Crockett DJ, Goudy SL. **Cleft lip and palate.** *Facial Plast Surg Clin North Am* 2014;22:573–86 CrossRef Medline
4. Woo AS. **Velopharyngeal dysfunction.** *Semin Plast Surg* 2012;26:170–7 CrossRef Medline
5. Kummer A. **Types and causes of velopharyngeal dysfunction.** *Semin Speech Lang* 2011;32:150–58 CrossRef Medline
6. de Blacam C, Smith S, Orr D. **Surgery for velopharyngeal dysfunction: a systematic review of interventions and outcomes.** *Cleft Palate Craniofac J* 2018;55:405–22 CrossRef Medline
7. Fisher DM, Sommerlad BC. **Cleft lip, cleft palate, and velopharyngeal insufficiency.** *Plast Reconstr Surg* 2011;128:342e–60e CrossRef Medline
8. Perry JL, Sutton BP, Kuehn DP, et al. **Using MRI for assessing velopharyngeal structures and function.** *Cleft Palate Craniofac J* 2014;51:476–85 CrossRef Medline
9. Sitzman TJ, Baylis AL, Perry JL, et al; VPI-OPS Study Consortium. **Protocol for a prospective observational study of revision palatoplasty versus pharyngoplasty for treatment of velopharyngeal insufficiency following cleft palate repair.** *Cleft Palate Craniofac J* 2022 Dec 23 [Epub ahead of print] CrossRef Medline
10. Sitzman TJ, Williams JL, Singh DJ, et al. **MRI of the velopharynx: clinical findings in patients with velopharyngeal insufficiency.** *Plast Reconstr Surg* 2023 Jun 23 [Epub Ahead of Print] CrossRef
11. Mason KN. **Magnetic resonance imaging for assessing velopharyngeal function: current applications, barriers, and potential for future clinical translation in the United States.** *Cleft Palate Craniofac J* 2022 Aug 29 [Epub Ahead of Print] CrossRef Medline
12. Perry JL, Snodgrass TD, Gilbert IR, et al. **Establishing a clinical protocol for velopharyngeal MRI and interpreting imaging findings.** *Cleft Palate Craniofac J* 2022 Nov 3 [Epub Ahead of Print] CrossRef Medline
13. Mason KN, Black J. **Incorporating velopharyngeal MRI into the clinical decision-making process for a patient presenting with velopharyngeal dysfunction following a failed palatoplasty.** *Cleft Palate Craniofac J* 2023 May 4 [Epub Ahead of Print] CrossRef Medline
14. Jaws TS, Sheu RS, Liu GC, et al. **Development of adenoids: a study by measurement with MR images.** *Kaohsiung J Med Sci* 1999;15:12–18 Medline
15. Ettema SL, Kuehn DP, Perlman AL, et al. **Magnetic resonance imaging of the levator veli palatini muscle during speech.** *Cleft Palate Craniofac J* 2002;39:130–44 CrossRef Medline
16. Atik B, Bekerecioglu M, Tan O, et al. **Evaluation of dynamic magnetic resonance imaging in assessing velopharyngeal insufficiency during phonation.** *J Craniofac Surg* 2008;19:566–72 CrossRef Medline
17. Akgüner M, Karacá C, Barutçú A, et al. **Evaluation of velopharyngeal pathophysiology and velopharyngeal insufficiency with magnetic resonance imaging.** *Eur J Plastic Surg* 1998;21:118–23
18. Drissi C, Mitrofanoff M, Talandier C, et al. **Feasibility of dynamic MRI for evaluating velopharyngeal insufficiency in children.** *Eur Radiol* 2011;21:1462–69 CrossRef Medline
19. Pitkänen VV, Alaluusua SA, Geneid A, et al. **How early can we predict the need for VPI surgery?** *Plast Reconstr Surg Glob Open* 2022;10:e4678 CrossRef Medline
20. Harrington SG, Jaimes C, Weagle KM, et al. **Strategies to perform magnetic resonance imaging in infants and young children without sedation.** *Pediatr Radiol* 2022;52:374–81 CrossRef Medline
21. Tyson ME, Bohl DD, Blickman JG. **A randomized controlled trial: child life services in pediatric imaging.** *Pediatr Radiol* 2014;44:1426–32 CrossRef Medline
22. Kotlarek KJ, Sitzman TJ, Williams JL, et al. **Nonsedated magnetic resonance imaging for visualization of the velopharynx in the pediatric population.** *Cleft Palate Craniofac J* 2023;60:249–52 CrossRef Medline
23. Cleft Palate Speech Imaging & Visualization Laboratory. **Setting Up an MRI Protocol.** East Carolina University. 2023. <https://cahs.ecu.edu/speechimaging/setting-up-an-mri-protocol/>. Accessed November 21, 2023
24. Kuehn DP, Ettema SL, Goldwasser MS, et al. **Magnetic resonance imaging of the levator veli palatini muscle before and after primary palatoplasty.** *Cleft Palate Craniofac J* 2004;41:584–92 CrossRef Medline
25. Jin R, Shosted RK, Xing F, et al. **Enhancing linguistic research through 2-mm isotropic 3D dynamic speech MRI optimized by sparse temporal sampling and low-rank reconstruction.** *Magn Reson Med* 2023;89:652–64 CrossRef Medline
26. Jin R, Liang ZP, Sutton BP. **Increasing three-dimensional coverage of dynamic speech magnetic resonance imaging.** In: *Proceedings of the Annual Meeting of the International Society for Magnetic Resonance in Medicine and the International Society for MR Radiographers & Technologists.* May 15–20, 2021; Virtual
27. Fu M, Barlaz MS, Holtrop JL, et al. **High-frame-rate full-vocal-tract 3D dynamic speech imaging.** *Magn Reson Med* 2017;77:1619–29 CrossRef Medline
28. Fu M, Barlaz MS, Shosted RK, et al. **High-resolution dynamic speech imaging with deformation estimation.** *Annu Int Conf IEEE Eng Med Biol Soc* 2015;2015:1568–71 CrossRef Medline
29. Moon JB, Kuehn DP, Huisman JJ. **Measurement of velopharyngeal closure force during vowel production.** *Cleft Palate Craniofac J* 1994;31:356–63 CrossRef Medline
30. Moon J, Smith AE, Folkens JW, et al. **Coordination of velopharyngeal muscle activity during positioning of the soft palate.** *Cleft Palate Craniofac J* 1994;31:45–55 CrossRef Medline
31. Haenssler AE, Fang X, Perry JL. **Effective velopharyngeal ratio: a more clinically relevant measure of velopharyngeal function.** *J Speech Lang Hear Res* 2020;63:3586–93 CrossRef Medline
32. Perry JL. **Anatomy and physiology of the velopharyngeal mechanism.** *Semin Speech Lang* 2011;32:83–92 CrossRef Medline
33. Kollara L, Baylis AL, Kirschner RE, et al. **Velopharyngeal structural and muscle variations in children with 22q11.2 deletion syndrome:**

- an unsedated MRI study.** *Cleft Palate Craniofac J* 2019;56:1139–48 CrossRef Medline
34. Mann RJ, Neaman KC, Armstrong SD, et al. **The double-opposing buccal flap procedure for palatal lengthening.** *Plast Reconstr Surg* 2011;127:2413–18 CrossRef Medline
 35. Nam SM. **Surgical treatment of velopharyngeal insufficiency.** *Arch Craniofac Surg* 2018;19:163–67 CrossRef Medline
 36. Smith BE, Kuehn DP. **Speech evaluation of velopharyngeal dysfunction.** *J Craniofac Surg* 2007;18:251–61 CrossRef Medline
 37. Siegel-Sadewitz VL, Shprintzen RJ. **Nasopharyngoscopy of the normal velopharyngeal sphincter: an experiment of biofeedback.** *Cleft Palate J* 1982;19:194–200 Medline
 38. El-Anwar MW, El-Sheikh E, El-Nakeb N. **Patterns and grade of velopharyngeal closure in candidates for adenotonsillectomy.** *Iran J Otorhinolaryngol* 2018;30:27–31 Medline
 39. Perry JL, Mason K, Sutton BP, et al. **Can dynamic MRI be used to accurately identify velopharyngeal closure patterns?** *Cleft Palate Craniofac J* 2018;55:499–507 CrossRef Medline
 40. Yoshida H, Stella JP, Ghali GE, et al. **The modified superiorly placed pharyngeal flap, Part IV: position of the base of the flap.** *Oral Surg Oral Med Oral Pathol* 1992;73:13–18 CrossRef Medline
 41. Yamaguchi K, Lonic D, Lee CH, et al. **A treatment protocol for velopharyngeal insufficiency and the outcome.** *Plast Reconstr Surg* 2016;138:290e–99e CrossRef Medline
 42. Perry JL, Kuehn DP, Sutton BP, et al. **Velopharyngeal structural and functional assessment of speech in young children using dynamic magnetic resonance imaging.** *Cleft Palate Craniofac J* 2017;54:408–22 CrossRef Medline
 43. Perry JL, Gilbert IR, Xing F, et al. **Preliminary development of an MRI atlas for application to cleft care: findings and future recommendations.** *Cleft Palate Craniofac J* 2023 Jun 19 [Epub ahead of Print] CrossRef Medline
 44. Perry JL, Kotlarek KJ, Sutton BP, et al. **Variations in velopharyngeal structure in adults with repaired cleft palate.** *Cleft Palate Craniofac J* 2018;55:1409–18 CrossRef Medline

Correlation of Flow Diverter Malapposition at the Aneurysm Neck with Incomplete Aneurysm Occlusion in Patients with Small Intracranial Aneurysms: A Single-Center Experience

Shuhai Long, Shuailong Shi, Qi Tian, Zhuangzhuang Wei, Ji Ma, Ye Wang, Jie Yang, Xinwei Han, and Tengfei Li



ABSTRACT

BACKGROUND AND PURPOSE: Flow diversion treatment repairs aneurysms by altering the hemodynamics of the aneurysmal sac and providing a scaffold for endothelial cell adhesion. The purpose of this study was to investigate the correlation of flow diverter (FD) malapposition at the aneurysm neck with incomplete occlusion of small intracranial aneurysms (IAs) and investigate other factors that are possibly related to incomplete occlusion.

MATERIALS AND METHODS: From January 2019 to June 2022, the clinical and imaging data for 153 patients (175 aneurysms) with unruptured small IAs treated with flow diversion were retrospectively analyzed. FD apposition at the aneurysm neck was evaluated by high-resolution conebeam CT (HR-CBCT), and the complete occlusion rate for aneurysms was judged according to the latest follow-up conventional angiography findings (≥ 6 months). Multivariate logistic regression analysis was used to determine factors associated with incomplete aneurysm occlusion.

RESULTS: In total, 159 FDs were implanted in 153 patients. HR-CBCT performed after the deployment revealed FD malapposition at the aneurysm neck in 18 cases. According to the latest follow-up angiograms (average: 9.47 ± 3.35 months), the complete aneurysm occlusion rate was 66.9%. The complete occlusion rates for incomplete and complete stent apposition at the neck were 38.9% (7/18) and 70.1% (110/157), respectively. The results of regression analysis showed that an aneurysm sac with branch vessels (OR, 2.937; $P = .018$), incomplete stent apposition at the aneurysm neck (OR, 3.561; $P = .023$), and a large aneurysm diameter (OR, 1.533; $P = .028$) were positive predictors of incomplete aneurysm occlusion.

CONCLUSIONS: An aneurysm sac with branch vessels, a large aneurysm diameter, and malapposition at the aneurysm neck significantly affect aneurysm repair after FD stent-only treatment for small IAs.

ABBREVIATIONS: FD = flow diverter; HR-CBCT = high-resolution cone-beam CT; IAs = intracranial aneurysms; ISA = incomplete stent apposition; OKM = O'Kelly-Marotta

Flow diverter (FD) implantation is one of the most commonly used methods for endovascular treatment of unruptured intracranial aneurysms (IAs), with adequate safety and definite efficacy.¹⁻⁴ However, 5% of aneurysms may show incomplete occlusion even after 5 years of follow-up.¹ Therefore, it is necessary to investigate

the factors affecting incomplete aneurysm occlusion.⁵ Incomplete stent apposition (ISA) is associated with delayed stent endothelialization, the occurrence of ischemic events, and in-stent stenosis.⁶⁻⁸ In addition, animal experiments have confirmed that ISA at the aneurysm neck, also known as communicating malapposition, is closely related to incomplete aneurysm occlusion.^{9,10} However, there are a few reports of clinical or animal experiments, this correlation needs to be confirmed by further systematic clinical research and exploration.^{5,8,10} The use of high-resolution conebeam CT (HR-CBCT) and postprocessing software can facilitate accurate observation of stent alignment with the vessel wall after placement.^{11,12} Accordingly, the aim of the present study was to investigate the correlation of FD malapposition at the aneurysm neck with incomplete occlusion of small IAs by using HR-CBCT. In addition, multivariate logistic regression analysis was used to explore other factors that are possibly related to incomplete occlusion.

Received August 6, 2023; accepted after revision October 29.

From the Department of Interventional Radiology, the First Affiliated Hospital of Zhengzhou University, Zhengzhou, China.

This work was supported by National Natural Science Foundation of China Grant 81801806; Henan Provincial and Ministerial Co-construction Youth Project of Medical Science and Technology Research Plan Grant YXKC2022029; and Medical Science and Technology Project for Health Commission of Henan Province Grant KYDZ2020120441.

Please address correspondence to Prof Tengfei Li, Department of Interventional Radiology, the First Affiliated Hospital of Zhengzhou University, Jianshe Rd No. 1, Erqi district, Zhengzhou, Henan, China; e-mail: 50632953@qq.com



Indicates article with online supplemental data.

<http://dx.doi.org/10.3174/ajnr.A8079>

MATERIALS AND METHODS

Population

Patients with small IAs treated with flow diversion at our center from January 2019 to June 2022 were identified from the hospital's picture archiving and communication system. The exclusion criteria were as follows: aneurysms with a maximum diameter of >10 mm; aneurysms without angiographic follow-up or aneurysms with angiographic follow-up data obtained at <6 months; aneurysms that could not be observed because of parent artery occlusion; aneurysms treated with coiling or aneurysms classified as traumatic aneurysms, fusiform aneurysms, or dissecting aneurysms; aneurysms without intraoperative HR-CBCT or reconstructed images that were not clear enough to determine stent apposition; and aneurysms with previous or new subarachnoid hemorrhage. Each patient provided written informed consent for the publication of this article and any related photos. The First Affiliated Hospital of Zhengzhou University Ethics Committee approved this study, which complied with the requirements of the 2013 revision of the Declaration of Helsinki (www.wma.net/what-we-do/medical-ethics/declaration-of-helsinki/).

Clinical and Imaging Data

The specific method of FD implantation was similar to that described in related literature.^{3,13} All patients were subjected to pharmacogenetic testing for aspirin and clopidogrel, and those who were sensitive to both drugs took aspirin (100 mg/day) and clopidogrel (75 mg/day) at least 5 days before surgery. Patients who were insensitive to one or both drugs were required to increase their doses or switch to ticagrelor (60 mg/day). Tirofiban (0.15 $\mu\text{g}/\text{kg}/\text{min}$) was administered for 12–24 h if no contrast agent leakage was observed on postoperative brain CBCT. The patients received continuous oral administration of dual antiplatelet drugs according to the preoperative regimen after stent placement. After continuous angiographic follow-up, dual antiplatelet therapy was continued if the aneurysm was not completely occluded; single antiplatelet therapy was adjusted if the aneurysm was completely occluded but <1 year had passed since stent placement, whereas platelet therapy was discontinued if the aneurysm had completely occluded and >1 year had passed after stent placement.

Baseline data, such as age, sex, and underlying diseases, were recorded. The shape, location (anterior or posterior circulation), and diameter of the aneurysm; neck width; diameter of the parent artery; flow incidence angle for the aneurysm sac (defined as the angle between the extension line between the midpoint of the aneurysm neck and the aneurysm apex and the midline of the proximal segment of parent artery after stent placement); and the presence of sac with branch vessels were also recorded. The degree of filling in the aneurysm sac and the residual time of the contrast medium in the lumen after the immediate implantation of FD were assessed by using the O'Kelly-Marotta (OKM) grading scale.^{2,14}

Observation of FD Apposition

The detailed procedure for observation of FD apposition was as follows. If the patient underwent HR-CBCT with diluted contrast media during the surgery, the scanning information was directly

used to reconstruct and observe stent apposition at the postprocessing workstation. The scanning methods and parameters used for HR-CBCT with diluted contrast media are described in the literature.¹⁵ For patients who did not undergo HR-CBCT with diluted contrast media, HR-CBCT and 3D scan data for the parent artery were loaded into the workstation, and images of the stent and parent artery were fused and reconstructed by the dual-volume fusion reconstruction method for the observation of stent apposition. The scanning methods and parameters for the stent and vascular dual-volume fusion reconstruction technology are described in the literature.¹¹ The FD diameter and FD apposition at the aneurysm neck were recorded. Malapposition at the neck was defined as ISA in the parent artery proximal to the aneurysm that extended into the neck of the aneurysm, effectively creating a much larger neck area.⁹ When ISA at the neck was observed intraoperatively, massage with a "J"-shaped microwire was attempted multiple times for correction of the malapposition; this was followed by another HR-CBCT scan to confirm stent apposition at the neck. If the malapposition persisted, no further treatment was attempted, and the case was considered ISA at the aneurysm neck.

Angiographic Follow-up and Analysis

The time of the latest angiography was recorded to determine the occlusion status of the aneurysm and the degree of in-stent stenosis. Complete occlusion was considered when the primary aneurysm showed an OKM filling grade of D.¹⁶

Aneurysms were divided into the occlusion and incomplete occlusion groups, and general clinical data for the 2 groups were analyzed and compared. Patient characteristics (eg, age, sex, smoking history, etc), aneurysm characteristics (eg, diameter, neck width, presence of sac with branch vessels, etc), characteristics of the parent artery (eg, diameter of the proximal and distal ends of the artery), stent characteristics (eg, diameter, stent apposition, etc), the OKM grade immediately after FD deployment, and other general factors that could affect aneurysm occlusion were analyzed.^{5,13,17–25} Following univariate analysis of the above factors, those with a *P* value of <.10 were included in the multivariate logistic regression model, and independent influencing factors for incomplete aneurysm occlusion after FD deployment were identified.

Data Analysis

All data were independently judged or measured by 2 experienced neurointerventionalists. Quantitative variables were averaged, and the results were determined after consultation regarding any differences in categorical variables. All statistical analyses were performed by using SPSS 26.0 (IBM) software. Quantitative variables are expressed as mean \pm SD and were compared between groups by using 1-way ANOVA. Categorical variables are presented as number with percentage and were compared between groups by using the χ^2 test or Fisher exact test. The predictors of incomplete aneurysm occlusion were determined by 1-way ANOVA, and factors with *P* <.10 were included in the logistic multivariate regression model for further analysis. A *P* value of <.05 was considered statistically significant.

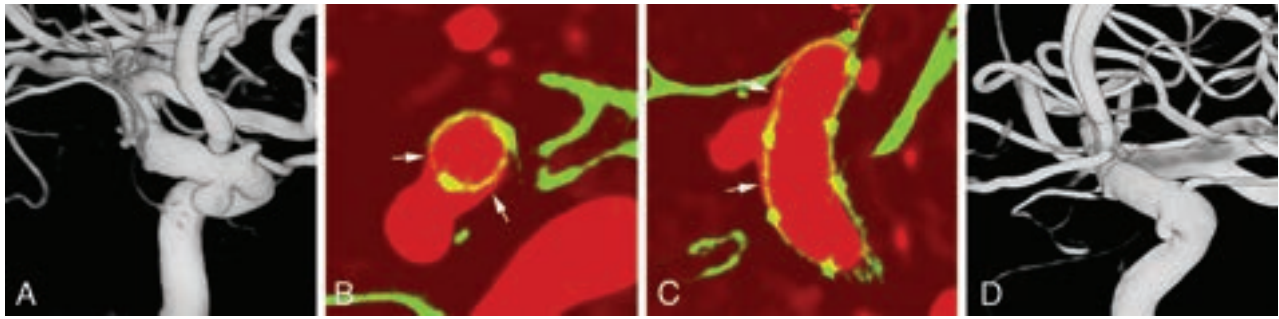


FIG 1. Representative case of FD malapposition resulting in incomplete occlusion. *A*, Image represents a hypophyseal aneurysm in the left internal carotid artery. *B* and *C*, These images were obtained by the dual-volume fusion reconstruction method. ISA on both sides of the aneurysm neck can be observed in the transverse (*B*) and sagittal planes (*C*) (white arrows). *D*, At 9 months after stent placement, the aneurysm has reduced in size, though the angiographic filling grade is B per the OKM grading scale.

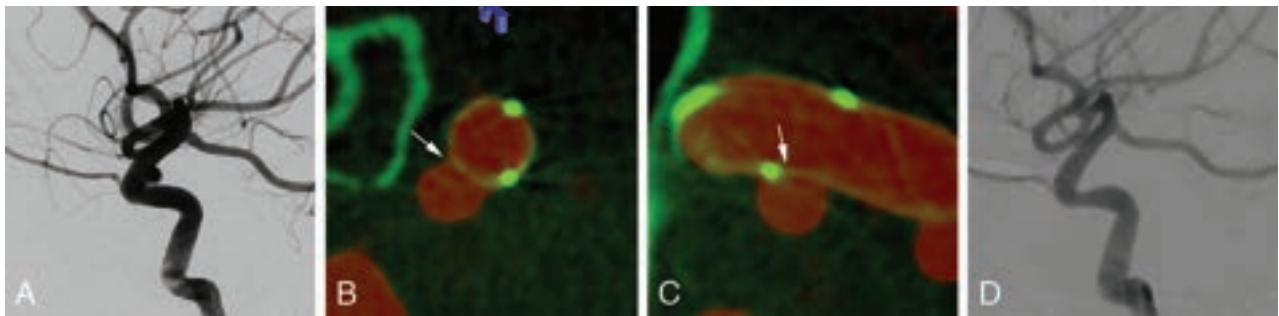


FIG 2. Representative case of complete stent apposition resulting in complete occlusion. *A*, Image represents a hypophyseal aneurysm in the left internal carotid artery. *B* and *C*, These images were obtained by the dual-volume fusion reconstruction method. Complete stent apposition at the aneurysm neck can be observed in the transverse (*B*) and sagittal planes (*C*) (white arrows). *D*, At 12 months after stent placement, the aneurysm is completely occluded with grade D angiographic filling per the OKM grading scale.

RESULTS

Study Cohort Characteristics

From January 2019 to June 2022, a total of 272 patients with 317 small IAs were treated with flow diversion at our center. From these, 47 IAs without angiographic follow-up or with angiographic follow-up data obtained at <6 months and 2 IAs that could not be observed because of parent artery occlusion were excluded. Moreover, 61 IAs that were treated with coiling or classified as traumatic aneurysms, fusiform aneurysms, or dissection aneurysms were excluded, along with 22 IAs without intraoperative HR-CBCT or with reconstruction images that were not clear enough for observation of stent apposition. Finally, 10 IAs with previous or new subarachnoid hemorrhage were excluded. Therefore, a total of 175 aneurysms in 153 patients were included in the study cohort. FDs were implanted for the treatment of a single aneurysm in 132 patients and the treatment of 2 or more aneurysms in 21 patients. A total of 137 Tubridge (MicroPort) and 22 Pipeline embolization devices (Covidien) were implanted. One FD was implanted in 147 patients, and 2 FDs were implanted in 6 patients because of the presence of aneurysms in the bilateral internal carotid artery. All stents were successfully placed.

Observation of FD Apposition

Immediately after stent placement, 23 cases of ISA at the aneurysm neck, termed immediate ISA at the neck (Fig 1), were observed, and the remaining aneurysms showed satisfactory stent

apposition (Fig 2). For 13 of these cases, a microguidewire was used to form a “J” shape for correction of ISA. From these 13 cases, 5 showed improvement after this intervention and were considered to have complete stent apposition (Fig 2). The remaining 8 cases and another 10 cases of malapposition identified by retrospective analysis of imaging data were analyzed as cases of ISA at the neck (Online Supplemental Data), with the segments of the internal carotid artery classified per the nomenclature proposed by Bouthillier et al.²⁶ For different types of FD, the incidence of ISA at the neck immediately after release of the Tubridge and Pipeline devices was 12.5% (19/152) and 17.4% (4/23), respectively, with no significant difference ($P = .512$).

Imaging Follow-up and Analysis

The mean follow-up time for all aneurysms was 9.47 ± 3.35 months, and 58 (33.1%) aneurysms showed incomplete occlusion. The cohort was divided into the occlusion and incomplete occlusion groups and statistically analyzed. In univariate analysis, a younger age, a large aneurysm diameter, a large neck width, an aneurysm sac with branch vessels, and ISA at the neck were significantly associated with incomplete occlusion, as shown in the Online Supplemental Data ($P < .10$ for all). These factors were included in multivariate logistic regression analysis to identify predictors of incomplete aneurysm occlusion, and the predictors were identified as a sac with branch vessels, a large aneurysm diameter, and ISA at the neck, as shown in Table 1. It is worth

Table 1: Multivariable analysis of factors associated with incomplete occlusion of small IAs treated with flow diversion

	P Value	OR (95% CI)
Age	.100	1.026 (0.995–1.058)
Aneurysm diameter	.028	1.533 (1.048–2.244)
Neck width	.701	0.884 (0.471–1.659)
Sac with branch vessels	.018	2.937 (1.199–7.190)
ISA at the neck	.023	3.561 (1.187–10.679)

Table 2: Outcomes of immediate ISA at the aneurysm neck after flow diversion treatment for small IAs

	Complete Occlusion	Incomplete Occlusion	P Value
Complete stent apposition after intervention for ISA	2	3	1.000 ^a
ISA even after intervention	3	5	

^aFisher exact test.

mentioning that the incomplete occlusion rates were 46.2% (12/26) and 70.5% (105/149) for sacs with branch vessels and those without branch vessels, respectively, and 38.9% (7/18) and 70.1% (110/157) for ISA at the neck and complete stent apposition at the neck, respectively. Moreover, the mean sizes of the unoccluded and occluded aneurysms were 5.8 and 4.9 mm, respectively. For cases of immediate ISA at the neck, there was no significant difference in the occlusion rate between the complete stent apposition and incomplete stent apposition after intervention with the “J”-shaped microguidewire, as shown in Table 2. With regard to the FD types, the overall occlusion rates for the Tubridge and Pipeline devices were similar ($P = .767$) at 66.4% (101/152) and 69.6% (16/23), respectively. In cases involving postoperative ISA at the neck, the occlusion rates for the Tubridge and Pipeline devices were 37.5% (6/16) and 50% (1/2), respectively, with no significant difference ($P = .512$).

DISCUSSION

FD malapposition after treatment of IAs is associated with adverse events, such as delayed endothelialization, ischemic events, and in-stent stenosis.^{6–8} In animal studies, ISA at the neck was associated with a higher incidence of incomplete aneurysm occlusion.^{8–10} However, previous clinical studies by using FDs for the treatment of IAs have not adequately judged and classified ISA; and, to our knowledge, none has systematically investigated the effect of ISA at the neck on aneurysm occlusion in clinical practice.^{2,13} The use of HR-CBCT and postprocessing software can facilitate accurate observation of stent alignment with the vessel wall after placement.^{11,27} In the present study, HR-CBCT was used to scan the stent area and reconstruct the image so that stent apposition at the neck immediately after FD deployment could be observed. The incidence of immediate ISA at the neck was 13.1% (23/175), which reduced to 10.3% (18/175) after intraoperative intervention for partial patients.

The occlusion rates for IAs treated with flow diversion varies from 56% to 95% among different centers and follow-up times, with the rate even reaching 95% at 5 years.^{1–3,16,20} In the present study, at the last follow-up (9.47 ± 3.35 months), the aneurysm occlusion rate was 66.9%, with complete occlusion rates of 38.9% (7/18) and 70.1% (110/157) for ISA at the neck and complete

stent apposition at the neck ($P = .008$). Further multivariate analysis showed that ISA at the neck was an independent predictor of incomplete aneurysm occlusion (OR, 3.561; $P = .023$). There may be various reasons for this finding. First, ISA at the neck may have caused persistent endoleakage at the aneurysm neck and affected the hemodynamic effect of FD. Thus, the aneurysm neck and dome would continue to show a high blood flow vector and high wall shear stress. Second, Kadirvel et al²⁸ showed that the endothelialization process of the stent at the neck gradually developed from the periphery to the center of the neck. Therefore, FD malapposition to the vascular wall at the neck may have resulted in delayed endothelialization of the stent, with the continuous impact of blood flow on the dome resulting in incomplete occlusion. Third, the large neck width could be a factor affecting occlusion of the aneurysm;²⁰ furthermore, ISA at the neck may have enlarged the area of the neck.

Although HR-CBCT can detect ISA in a timely manner during the surgery, whether or how to deal with ISA remains controversial.^{9,29} Zhang et al²⁹ reduced the postoperative incidence of ISA from 18.7% to 2.5% by active intervention. However, this led to problems, such as stent migration, vessel puncture caused by stent microfilaments, and thrombosis. In an animal study by King et al,⁹ ISA at the aneurysm neck that was successfully corrected by balloon angioplasty showed a higher occlusion rate, which was statistically significant. In the present study, aneurysms with complete stent apposition after intervention by a “J”-shaped microguidewire showed a higher occlusion rate than did those with ISA despite the intervention (40% versus 37.5%), but the difference was not statistically significant, possibly because of the small sample size. In addition, considering the risk of balloon dilation at the neck, ISA at the neck was only managed by multiple attempts at massage with the “J”-shaped microwire, followed by another HR-CBCT scan to evaluate stent apposition at the neck. If the malapposition persisted, no further treatment was attempted for various reasons, including the limited effect of the treatment, possibility of stent displacement and intimal damage, increased patient exposure to radiation because of the multiple HR-CBCT scans, and, most importantly, the lack of clinical evidence showing the benefits of active treatment for malapposition at the aneurysm neck. Therefore, the conditions for active treatment of FD malapposition at the neck may need to be explored in further studies.

We observed complete occlusion rates of 46.2% (12/26) and 70.5% (105/149) for sacs with branch vessels and those without branch vessels, respectively ($P = .015$). Further multivariate analysis showed that a sac with branch vessels was an independent predictor of incomplete occlusion of aneurysms (OR, 2.937; $P = .018$), consistent with the findings of previous studies.^{2,5,16,19,25} Branch vessels, such as the ophthalmic artery and anterior choroidal artery, are mostly patent at the long-term follow-up after FD implantation; this is related to the high blood flow through the branch vessels without distal collateral branches and the high-pressure gradient at the opening of the parent vessels.¹⁹ Similarly, we speculate that the vessels branching from the sac have a pressure difference that allows continuous blood flow into the aneurysm dome and influences intraluminal thrombus formation. In a study by Zetchi et al,²⁵ further analysis of the

subgroup with sacs with branch vessels showed that a larger angle between the parent artery and branch vessel could result in greater intra-aneurysmal vorticity and a lower occlusion rate; this confirmed our suspicion. Furthermore, the mean sizes of unoccluded and occluded aneurysms in this study were 5.8 and 4.9 mm, respectively, and multivariate analysis in the present study found that the aneurysm diameter was one of the independent factors affecting aneurysm occlusion (OR, 1.533; $P = .028$), similar to the findings of previous studies.^{17,30} Therefore, use of multiple devices or combination with coiling in cases involving branching aneurysms or larger aneurysms may be effective in increasing the rate of obliteration.^{31,32}

This study had several limitations. First, some patients failed to undergo angiographic follow-up within the prescribed time for various reasons, so there were some time differences in the observation of aneurysm occlusion, which may have affected the accuracy of our results. Second, endovascular imaging techniques, such as intravascular sonography and optical coherence tomography, have not been used to determine stent apposition. Third, the follow-up period was short, so the relationship between aneurysm occlusion and time could not be further analyzed. Fourth, this study primarily focused on results for the Tubridge device; therefore, the findings should be applied with caution to other devices. Finally, this was a single-center, retrospective analysis with a small sample size, and its conclusions need to be verified in further multicenter, prospective, randomized controlled studies.

CONCLUSIONS

An aneurysm sac with branch vessels, a large aneurysm diameter, and ISA at the aneurysm neck significantly affect aneurysm repair after FD stent-only treatment for small IAs. A younger age and a larger neck width may also be related to aneurysm persistence. Detection of FD malapposition at the aneurysm neck by using HR-CBCT followed by appropriate intervention can facilitate appropriate occlusion and repair of the aneurysm.

Disclosure forms provided by the authors are available with the full text and PDF of this article at www.ajnr.org.

REFERENCES

1. Becske T, Brinjikji W, Potts MB, et al. **Long-term clinical and angiographic outcomes following Pipeline embolization device treatment of complex internal carotid artery aneurysms: five-year results of the Pipeline for Uncoilable or Failed Aneurysms trial.** *Neurosurgery* 2017;80:40–48 CrossRef Medline
2. Bender MT, Colby GP, Lin LM, et al. **Predictors of cerebral aneurysm persistence and occlusion after flow diversion: a single-institution series of 445 cases with angiographic follow-up.** *J Neurosurg* 2018;130:259–67 CrossRef Medline
3. Kang H, Zhou Y, Luo B, et al. **Pipeline embolization device for intracranial aneurysms in a large Chinese cohort: complication risk factor analysis.** *Neurotherapeutics* 2021;18:1198–206 CrossRef Medline
4. Lee KS, Zhang JJ, Nguyen V, et al. **The evolution of intracranial aneurysm treatment techniques and future directions.** *Neurosurg Rev* 2022;45:1–25 CrossRef Medline
5. Shapiro M, Becske T, Nelson PK. **Learning from failure: persistence of aneurysms following Pipeline embolization.** *J Neurosurg* 2017;126:578–85 CrossRef Medline
6. Kwon MY, Ko YS, Kwon SM, et al. **Evaluation of stent apposition in the LVIS blue stent-assisted coiling of distal internal carotid artery**

aneurysms: correlation with clinical and angiographic outcomes. *J Korean Neurosurg Soc* 2022;65:801–15 CrossRef Medline

7. Räber L, Mintz GS, Koskinas KC, ESC Scientific Document Group, et al. **Clinical use of intracoronary imaging: 1. Guidance and optimization of coronary interventions: an expert consensus document of the European Association of Percutaneous Cardiovascular Interventions.** *Eur Heart J* 2018;39:3281–300 CrossRef Medline
8. Aquarius R, de Korte A, Smits D, et al. **The importance of wall apposition in flow diverters.** *Neurosurgery* 2019;84:804–10 CrossRef Medline
9. King RM, Brooks OW, Langan ET, et al. **Communicating malapposition of flow diverters assessed with optical coherence tomography correlates with delayed aneurysm occlusion.** *J Neurointerv Surg* 2018;10:693–97 CrossRef Medline
10. King RM, Peker A, Anagnostakou V, et al. **High-frequency optical coherence tomography predictors of aneurysm occlusion following flow diverter treatment in a preclinical model.** *J Neurointerv Surg* 2023;15:919–23 CrossRef Medline
11. Li TF, Ma J, Han XW, et al. **Application of high-resolution C-arm CT combined with streak metal artifact removal technology for the stent-assisted embolization of intracranial aneurysms.** *AJNR Am J Neuroradiol* 2019;40:1752–58
12. Raz E, Sharashidze V, Nossek E, et al. **SuperDyna: unlocking the potential of post-treatment device evaluation.** *J Neurointerv Surg* 2023. Advance online publication. Retrieved Jun 14, 2023. doi: 10.1136/jnis-2023-020357
13. Miller TR, Kole MJ, Le EJ, et al. **Pipeline diameter significantly impacts the long-term fate of jailed side branches during treatment of intracranial aneurysms.** *AJNR Am J Neuroradiol* 2018;39:2270–77 CrossRef Medline
14. O’Kelly CJ, Krings T, Fiorella D, et al. **A novel grading scale for the angiographic assessment of intracranial aneurysms treated using flow diverting stents.** *Interv Neuroradiol* 2010;16:133–37 CrossRef Medline
15. Kato N, Yuki I, Ishibashi T, et al. **Visualization of stent apposition after stent-assisted coiling of intracranial aneurysms using high resolution 3D fusion images acquired by C-arm CT.** *J Neurointerv Surg* 2020;12:192–96 CrossRef Medline
16. Brasieliense LB, Aguilar-Salinas P, Miller DA, et al. **Analysis of predictors and probability of aneurysm occlusion in the internal carotid artery after treatment with Pipeline embolization device.** *World Neurosurg* 2017;107:641–48 CrossRef Medline
17. Guédon A, Thépenier C, Shotar E, et al. **Predictive score for complete occlusion of intracranial aneurysms treated by flow-diverter stents using machine learning.** *J Neurointerv Surg* 2021;13:341–46 CrossRef Medline
18. Meng H, Wang Z, Kim M, et al. **Saccular aneurysms on straight and curved vessels are subject to different hemodynamics: implications of intravascular stenting.** *AJNR Am J Neuroradiol* 2006;27:1861–65.
19. Bonney PA, Connor M, Fujii T, et al. **Failure of flow diverter therapy: predictors and management strategies.** *Neurosurgery* 2020;86:S64–S73 CrossRef Medline
20. Paliwal N, Tutino VM, Shallwani H, et al. **Ostium ratio and neck ratio could predict the outcome of sidewall intracranial aneurysms treated with flow diverters.** *AJNR Am J Neuroradiol* 2019;40:288–94 CrossRef Medline
21. Cebral JR, Mut F, Raschi M, et al. **Analysis of hemodynamics and aneurysm occlusion after flow-diverting treatment in rabbit models.** *AJNR Am J Neuroradiol* 2014;35:1567–73 CrossRef Medline
22. Abdelkhalik H, Abdelhameed EA, Zakarea A, et al. **Predictors of flow diverter stent in large and giant unruptured intracranial aneurysms, single-center experience.** *Neurol Sci* 2022;43:6399–405 CrossRef Medline
23. Hussein AE, Shownkeen M, Thomas A, et al. **2D parametric contrast time-density analysis for the prediction of complete aneurysm occlusion at six months’ post-flow diversion stent.** *Interv Neuroradiol* 2020;26:468–75 CrossRef Medline

24. Janot K, Fahed R, Rouchaud A, et al. **Parent artery straightening after flow-diverter stenting improves the odds of aneurysm occlusion.** *AJNR Am J Neuroradiol* 2022;43:87–92 CrossRef Medline
25. Zetchi MA, Dmytriw AA, Chiu AH, et al. **Entry remnants in flow-diverted aneurysms: does branch geometry influence aneurysm closure?** *Interv Neuroradiol* 2018;24:624–30 CrossRef Medline
26. Bouthillier A, van Loveren HR, Keller JT. **Segments of the internal carotid artery: a new classification.** *Neurosurgery* 1996;38:425–33; discussion 32–33 CrossRef
27. Li T, Wang Y, Ma J, et al. **Application of high-resolution flat detector computed tomography in stent implantation for intracranial atherosclerotic stenosis.** *Front Neurosci* 2021;15:655594 CrossRef Medline
28. Kadirvel R, Ding YH, Dai D, et al. **Cellular mechanisms of aneurysm occlusion after treatment with a flow diverter.** *Radiology* 2014;270:394–99 CrossRef Medline
29. Zhang H, Gao X, Liang H, et al. **Incomplete stent apposition of low-profile visualized intraluminal support stents in the treatment of cerebral aneurysms.** *J Neurointerv Surg* 2020;12:591–97 CrossRef Medline
30. Benaissa A, Barbe C, Pierot L. **Analysis of recanalization after endovascular treatment of intracranial aneurysm (ARETA trial): presentation of a prospective multicenter study.** *J Neuroradiol* 2015;42:80–85 CrossRef Medline
31. Shapiro M, Raz E, Becske T, et al. **Variable porosity of the Pipeline embolization device in straight and curved vessels: a guide for optimal deployment strategy.** *AJNR Am J Neuroradiol* 2014;35:727–33 CrossRef Medline
32. Chen Z, Gong W, You W, et al. **Efficacy and safety of flow diverter combined with coil embolization and evidence-based antithrombotic regimen in the treatment of ruptured aneurysms.** *Neurosurg Focus* 2023;54:E3 CrossRef Medline

Ischemic Stroke Thrombus Perviousness Is Associated with Distinguishable Proteomic Features and Susceptibility to ADAMTS13-Augmented Thrombolysis

Derrek Schartz, Sajal Medha K. Akkipeddi, Redi Rahmani, Nathaniel Ellens, Clifton Houk, Gurkirat Singh Kohli, Logan Worley, Kevin Welle, Tarun Bhalla, Thomas Mattingly, Craig Morrell, and Matthew T. Bender



ABSTRACT

BACKGROUND AND PURPOSE: Perviousness is the differential attenuation on CT of an intracranial arterial occlusive thrombus before and after IV contrast administration. While perviousness/permeability has been shown to be related to various clinical outcomes and reflects histopathologic composition, it remains unclear whether perviousness is also associated with differences in proteomic composition.

MATERIALS AND METHODS: Retrieved clots from 59 patients were evaluated with quantitative mass spectrometry. Proteomic differences between high-perviousness (≥ 11 HU) and low-perviousness (< 11 HU) clots were investigated. Perviousness as a continuous variable was also correlated with protein abundance. Last, an ex vivo lysis assay was performed to investigate the differential susceptibility to tPA, deoxyribonuclease, and ADAMTS13 thrombolysis as a function of perviousness.

RESULTS: In total, 2790 distinct proteins were identified. Thrombus perviousness was associated with distinct proteomic features, including depletion of the macrophage marker CD14 ($P = .039$, $z = 1.176$) and hemoglobin subunit ζ ($P = .046$, $z = 1.68$) in pervious clots. Additionally, proteins involved in platelet cytoskeleton remodeling (tropomyosin α -3-chain) and granule secretion/aggregation (synaptotagmin-like protein 4/FC region receptor II-a) were associated with increasing perviousness ($P < .006$), among numerous other proteins. Monocyte/macrophage-associated proteins (apoptosis-associated specklike protein containing a CARD/SAMHD1) were also depleted in pervious emboli ($P < .002$). Ex vivo lysis indicated that pervious clots were more susceptible to ADAMTS13-augmented tPA thrombolysis compared with impervious clots ($P < .05$), though without differences in deoxyribonuclease digestion.

CONCLUSIONS: Thrombus perviousness is associated with complex proteomic features, including differential abundance of platelet-related proteins in highly permeable clots with monocyte/macrophage depletion. This association may help to explain why highly pervious thrombi were also found more susceptible to ADAMTS13-augmented thrombolysis.

ABBREVIATIONS: CARD = Caspase Recruitment Domain; DNase = deoxyribonuclease; dNTPase = deoxynucleoside triphosphohydrolase; Fc γ RIIA = FC region receptor II-a; FC = fold change; log₂FC = log₂ fold change; PYCARD/ASC = apoptosis-associated specklike protein containing a CARD; RBC = red blood cell; SYTL4 = synaptotagmin-like protein 4; TPM3 = tropomyosin α -3 chain; vWF = von Willebrand factor; WBC = white blood cell

NCCT and contrast-enhanced CTA are typically performed in suspected cases of acute ischemic stroke. Previous studies have demonstrated that characterization of ischemic stroke thrombus with CT can be used to delineate histopathologic composition and even stroke etiology.¹⁻⁴ One such imaging feature is

thrombus perviousness, or permeability, which is defined as the degree of clot enhancement and the difference in attenuation between the NCCT and CTA phases, and it is thought to reflect the relative porosity of the thrombus.^{2,5} Clot permeability has also been shown to be strongly associated with various clinical outcomes, including endovascular thrombectomy efficacy and susceptibility to IV thrombolysis.⁶⁻⁸ While prior research has investigated how thrombus perviousness relates to histopathologic composition, it remains unclear whether this imaging feature is also linked to more distinguishable protein biology.^{2-4,9} Likewise, susceptibility to different treatments or enzymatic lysis might be a function of granular protein content, not able to be delineated on rudimentary histopathology. In this study, we leveraged quantitative mass spectrometry to investigate whether the perviousness of ischemic stroke thrombus is associated with a distinct proteomic composition.

Received July 13, 2023; accepted after revision October 20.

From the Departments of Imaging Sciences (D.S., L.W.) and Neurosurgery (D.S., S.M.K.A., R.R., N.E., C.H., G.S.K., K.W., T.B., T.M., M.T.B.), and Aab Cardiovascular Research Institute (C.M.), University of Rochester Medical Center, Rochester, New York.

Funding was provided by the Department of Neurosurgery of the University of Rochester Medical Center.

Please address correspondence to Derrek Schartz, MD, Department of Imaging Sciences, University of Rochester Medical Center, 601 Elmwood Ave, Rochester, NY 14642; e-mail: derrek_schartz@urmc.rochester.edu; @D_SchartzMD

Indicates article with online supplemental data.

<http://dx.doi.org/10.3174/ajnr.A8069>

MATERIALS AND METHODS

The authors certify that this article conforms to the International Committee of Medical Journal Editors recommendations for conduct, reporting, editing, and publication of scholarly work in medical journals and is hereby ethically sound. This study was approved by our institutional review board; documentation is available on request.

Sample Collection and Patient Characteristics

This study was approved by our institutional review board. Patients were consecutively enrolled during the study period and were included only after obtaining consent from either the patient when able or from next of kin/designated health care proxy. Whole ischemic stroke thromboembolic material was collected from 59 patients via mechanical thrombectomy at our single-center tertiary care institution. All thromboemboli were kept moist after being retrieved and were then moved into a Cryo Tube (Thermo Fisher Scientific) and immediately stored at -80°C until thawing for quantitative mass spectrometry analysis. Clinical data from all included patients were also collected and included sex, age, relevant medication, pertinent medical history, and clot location, among other clinical variables. A Fisher exact test was then used to evaluate any differences in patient clinical characteristics between patients with high- and low-thrombus permeability. Evaluation of clot permeability is further described below.

Imaging Analysis of Thrombus Perviousness

All NCCT and CTA studies were obtained on either a 128-section (Ingenuity Core; Phillips Healthcare) or a 256-section (Brilliance iCT; Phillips Healthcare) helical CT scanner. Standard scan parameters for NCCT were the following: 120 kV(peak) tube voltage; 350-mA tube current with occasional fluctuation, no dose modulation; 2.5-mm section thickness. For CTA studies, parameters were the following: 120-kV(p) tube voltage and 415-mA tube current, without dose modulation. On the CTA study, the lowest section thickness (most often 0.8 mm) was used for analysis and data collection. All imaging data collection was completed blinded to clinical outcomes and proteomic composition. NCCT and CTA images were not coregistered but were, instead, read simultaneously on diagnostic monitors within the PACS system to best localize intraluminal thrombus. ROIs were placed to measure thrombus attenuation in Hounsfield units. Up to 3 ROIs were positioned for each clot on the basis of the size, location, and visualization on NCCT and CTA imaging. If >1 ROI was measured, the mean thrombus attenuation in Hounsfield units was calculated and used. Whenever possible, 3 ROIs were used because they have been shown to most accurately assess thrombus attenuation and limit observer variability.¹⁰ This technique has been previously used to measure thrombus permeability/perviousness and has been well-described in prior studies.^{2-4,9,10}

Absolute perviousness was calculated as the differences between Hounsfield units on NCCT (HU_{NCCT}) and CTA (HU_{CTA}) (or, perviousness = $\text{HU}_{\text{CTA}} - \text{HU}_{\text{NCCT}}$). The perviousness ratio was also calculated and was defined as $\text{HU}_{\text{CTA}}/\text{HU}_{\text{NCCT}}$ to better account for the initial thrombus attenuation. For example, while 2 separate clots measuring 50 HU and 25 HU on initial

NCCT could both enhance by 20 HU ($\text{HU}_{\text{CTA}} = 70$ and 45, respectively) and thus have the same perviousness, their perviousness ratios would differ ($\text{HU}_{\text{CTA}}/\text{HU}_{\text{NCCT}} = 1.4$ and 1.8, respectively). Thrombi were categorized as either “high perviousness” or “low perviousness” by the median value across all samples, which was calculated as ≥ 11 HU and is in line with prior investigations.^{2,4} Similarly, the median value across all samples was also taken to categorize a high- or low-perviousness ratio, which was ≥ 1.2 . An example of a thrombus permeability measurement and calculation can be seen in Fig 1.

Mass Spectrometry Proteomic and Bioinformatic Analyses

All retrieved thromboembolic specimens were gently washed with $1\times$ phosphate buffered saline before being subsequently sonicated, solubilized, and centrifuged. Bicinchoninic acid (Thermo Scientific) was then used to determine the protein concentration within the supernatant with all samples and then was diluted to a final concentration of 1 mg/mL before being digested with trypsin and resuspended. Samples were then processed by our institutional core Mass Spectrometry Resource lab using an Orbitrap Fusion Lumos Tribrid quantitative mass spectrometer (Thermo Fischer Scientific). Resulting raw proteomic data were processed and analyzed using the library-free analysis mode in DIA-NN, Version 1.8.1 (<https://github.com/vdemichev/DiaNN>). Several bioanalytic methods were used to investigate how clot permeability relates to protein composition: 1) abundance analysis, to assess broad differences in the abundance of proteins between permeable and impermeable clots, and 2) linear analysis, to investigate associations between protein content and permeability as a spectrum/continuous variable.

Functional analysis was also completed to explain possible mechanistic differences based on thrombus perviousness using The Gene Ontology (GO; <https://geneontology.org/>) Resource enrichment analyses with g:Profiler (Version e109_eg56_p17_1d3191d; <https://biit.cs.ut.ee/gprofiler/gost>) to identify differentially over-represented GO terms in relation to clot permeability.¹¹ Wilcoxon rank-sum tests were used to compare the median abundance of individual proteins between clots with high perviousness compared with those with low perviousness. Throughout the investigation, significant differences (defined as a $P < .05$) are described by the fold change (FC) in abundance and are reported with the corresponding absolute z score. Furthermore, correlation between the continuous variable of the perviousness ratio as a function of specific protein abundance was investigated with Spearman rank correlation coefficients and described using the Spearman ρ test statistic.

Evaluation of Susceptibility to Ex Vivo Thrombolysis

To relate perviousness to clot lysis and susceptibility to various lytic enzymes, we completed an ex vivo lysis assay. There were sufficient samples for ex vivo thrombolysis in 26 of the total 59 samples. These samples were thawed from -80°C and portioned into 4 qualitatively representative segments. A small piece of each segment was collected and pooled for mass spectrometry to generate a proteome for the corresponding thrombus. The remainder of the 4 segments was subjected to 1 hour of in vitro lysis at 37°C in

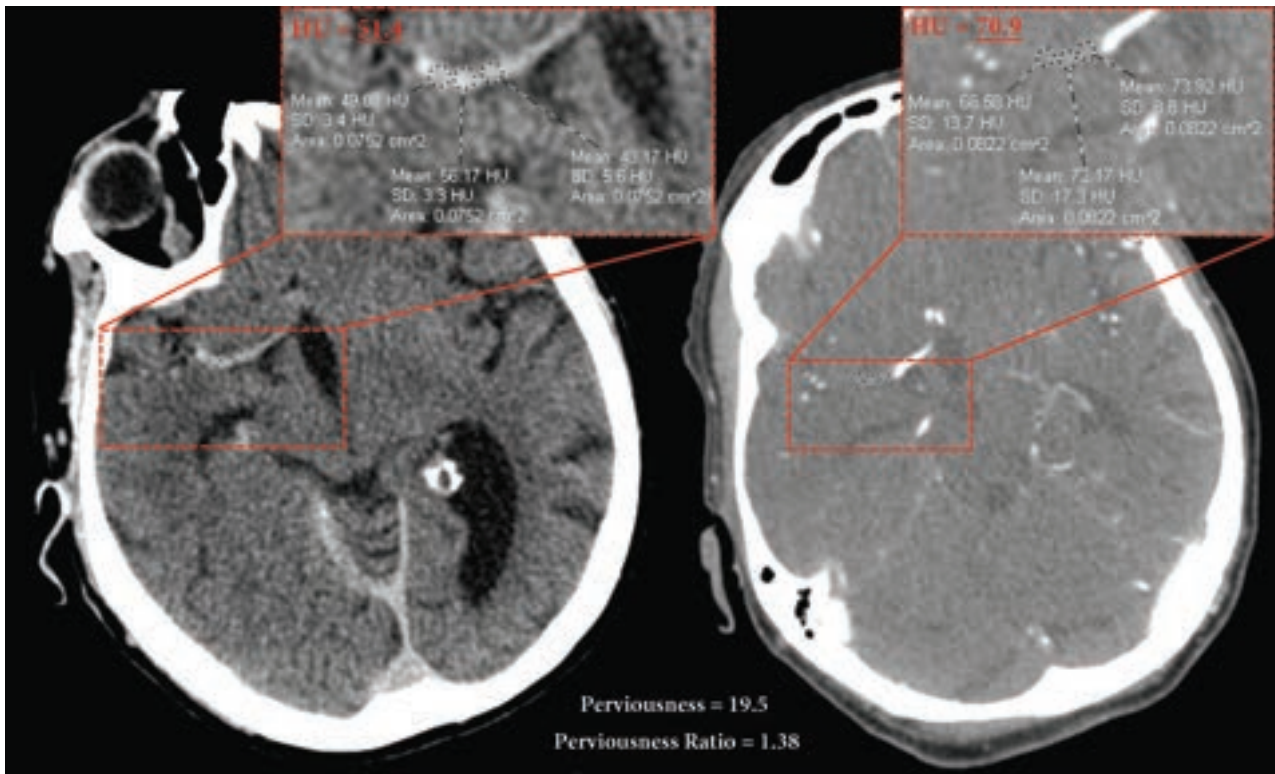


FIG 1. Sample calculation of thrombus perviousness/permeability on admission NCCT (*left*) and CTA (*right*). The image on the left demonstrates NCCT with 3 ROIs placed on the thrombus, with the thrombus attenuation in Hounsfield units calculated as the mean among the ROI values. The image on the right demonstrates a similar thrombus attenuation calculation on CTA. Perviousness was then calculated as the difference in Hounsfield units between CTA and NCCT. Likewise, the perviousness ratio was calculated as the ratio of Hounsfield units of the CTA over NCCT.

1 of 4 lytic solutions with the standard-of-care tPA at 5 $\mu\text{g}/\text{mL}$ (T; MyBioSource, MBS142404), tPA + von Willebrand factor (vWF)-cleaving ADAMTS13 at 2.5 $\mu\text{g}/\text{mL}$ (TA; MyBioSource, MBS636953), tPA along with DNA-cleaving DNase I at 100 U/mL (Td; MyBioSource, MBS142460), and all 3 enzymes (TDA) at the previously mentioned concentrations. Postlysis residual, characterized by the postlysis thrombus weight as a percentage of the prelysis weight, was compared across the 4 solutions. Spearman coefficients were used to describe the association between lysis and the abundance of all proteins identified by mass spectrometry.

RESULTS

Patient Characteristics

In total, 59 patients were included in the study with 30 (50.8%) retrieved clots being categorized as high perviousness (≥ 11 HU), and 29 (49.2%), as low perviousness (< 11 HU). Overall, patients were an average age of 68.6 years, and 50.8% were men. There were no significant differences in medical history or overall clinical characteristics between the 2 groups (Online Supplemental Data). In total, a history of previously diagnosed atrial fibrillation was present in 30.5% of patients; prior stroke, in 11.9%; active cancer of any form, in 11.9%; hypertension, in 76.3%; and a history of hypercoagulability/clotting disorder, in 5.1% of patients. There was no significant difference in time from last known well to recanalization between clots with high perviousness (mean, 487 [SD, 384] minutes) and low perviousness (mean, 353 [SD,

286] minutes) ($P = .14$). Furthermore, 28.8% of patients were previously on aspirin, 10.2% were on warfarin, and 40.8% were on a statin, without differences between the 2 groups.

On CTA, the thrombi were located within the ICA in 3.4% of cases and the ICA with extension into the M1 division of the MCA in 13.6% of cases. In 47.5% of the occlusions, the thrombus was located only in the M1 division of the MCA, 20.3% of occlusions were in the M1 with extension into the M2 division, and 10.2% of cases were isolated M2 occlusions. Last, 5.1% of clots were in the basilar artery. Additionally, in 86% (25/29) of low-pervious clots and in 93% (28/30) of high-pervious clots, the location was congruent on CTA and neuroangiography, without significant difference between the groups ($P = .38$). We also observed no differences in first-pass effect, 90-day functional outcomes (mRS 0–2), or 90-day mortality between the 2 groups. Full details regarding baseline patient characteristics within the study can be seen in the Online Supplemental Data.

Thrombus Perviousness is Associated with Distinguishable Proteomic Features

From the 59 mechanical thrombectomy–retrieved thromboembolic samples, a total of 2790 distinct proteins were identified by mass spectrometry, of which 147 were significantly enriched or depleted on the basis of thrombus permeability (Fig 2). Two proteins were found to be significantly more abundant with a > 0.05 log₂FC: immunoglobulin heavy variable 1 ($P = .04$, $z = 1.7$) and BCL2 interacting protein ($P = .16$, $z = 2.15$) (Fig 2). Several other

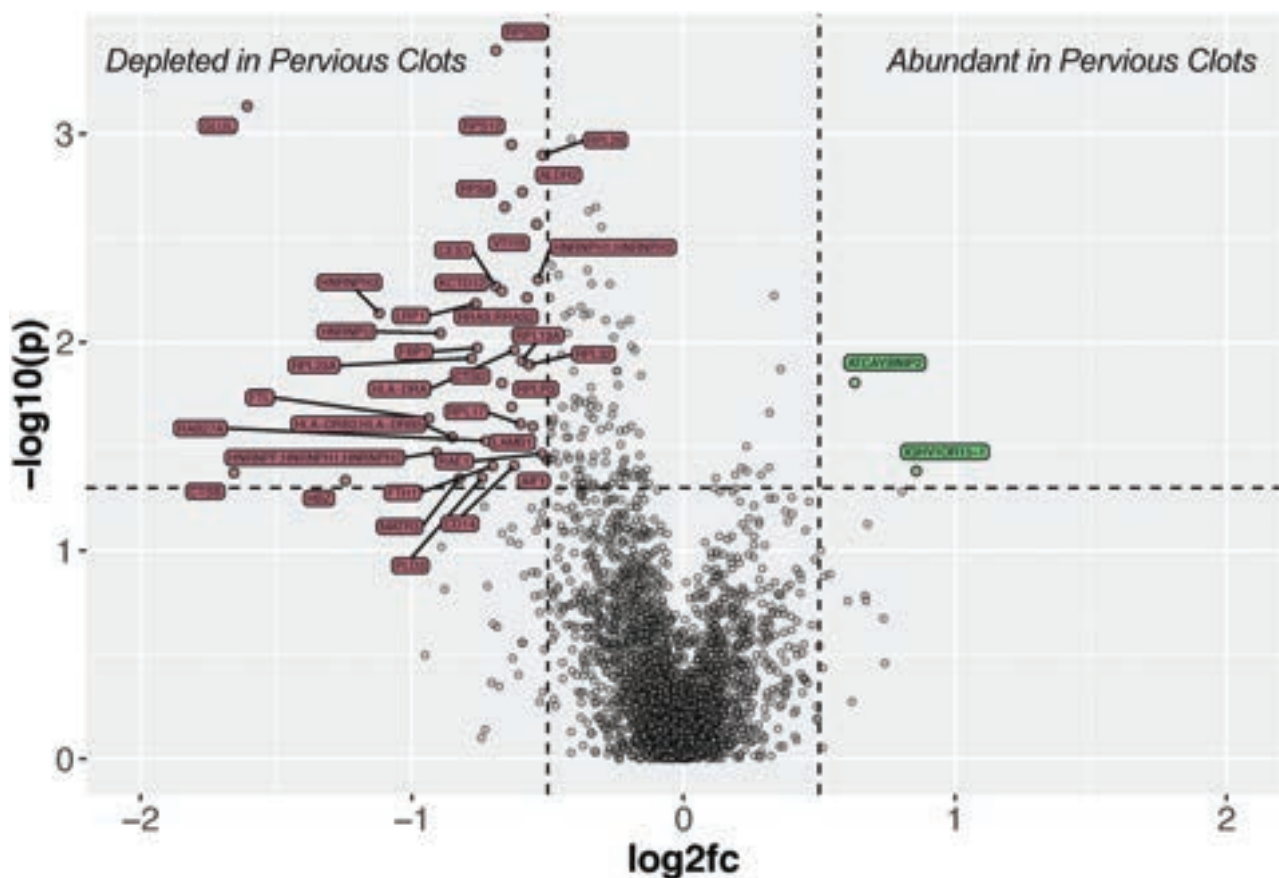


FIG 2. Volcano plot depicting the proteomic landscape of pervious acute ischemic stroke clots. The *left side* of the graph depicts proteins that are significantly depleted (red), while the *right side* depicts those that are differentially abundant (green).

proteins ($n = 12$) were significantly more abundant in highly pervious clots though with a \log_2FC of <0.05 , notable among which were tropomyosin α -3 chain ($P = .0059$, $z = 2.51$), farnesyl pyrophosphate synthase ($P = .013$, $z = 2.21$), and GTPase NRAS ($P = .022$, $z = 2.02$).

Many more proteins were found to be significantly depleted in pervious clots relative to impervious clots: most substantially glutamine synthetase ($P = .0007$, $z = 3.2$), several ribosomal 40S/60S proteins (S2/S12/L28/L27, all $P < .003$, $z < -2.8$), and aldehyde dehydrogenase 2 ($P = .002$, $z = -2.90$). Other notable proteins included the following: monocyte/macrophage differentiation antigen CD14 ($P = .039$, $z = -1.176$), NF- κ B-kinase subunit β ($P = .007$, $z = -2.44$), and receptor of activated protein C kinase 1 ($P = .009$, $z = -2.36$). A summary of those proteins with the most significant FCs is seen in the Table. For a complete list of all statistically significant differentially abundant proteins as a function of thrombus permeability refer to the Online Supplemental Data.

GO analysis using g:Profiler (Version e109_eg56_p17_1d3191d) of 35 depleted proteins with both $P < .05$ and a \log_2FC of -0.05 in pervious clots revealed that the most significantly represented molecular functions involved ribosomal constituents or RNA binding proteins ($P < .0001$). Similarly, the most significantly depleted biologic processes included those involved in translation ($P < .0001$), with cytosolic ribosomes being the most significantly represented cellular compartment among the proteins. Furthermore, pervious

clots were depleted in intracellular ferritin complex binding and iron sequestration (all $P < .05$).

Differential protein abundance was also evaluated as a function of the thrombus perviousness ratio as a surrogate for clot permeability. Among 2790 proteins, 254 were significantly enriched or depleted at a threshold of $P < .05$, and 69, at a threshold of $P < .01$. Notable among the latter group, low-affinity immunoglobulin γ FC region receptor II-a (*FCGR2A/Fc γ RIIA*) was significantly associated with increasing perviousness ($P = .0091$, $R = 0.34$) (Fig 3A). An increasing thrombus perviousness/perviousness ratio was also associated with increased abundance of synaptotagmin-like protein 4 (*SYTL4*) ($P = .0057$, $R = 0.36$) (Fig 3B) and tropomyosin α -3 chain (*TPM3*) ($P = .00089$, $R = 0.42$) (Fig 3C). Conversely, there was a significant negative association between perviousness and hemoglobin subunit ζ ($P = .0046$, $R = -0.37$) (Fig 3D), apoptosis-associated specklike protein containing a CARD (*PYCARD/ASC*) ($P = .0019$, $R = -0.4$) (Fig 3E), and deoxynucleoside triphosphohydrolase (*dNTPase*) *SAMHD1* ($P = .0019$, $R = -0.4$) (Fig 3F). Additional numerous proteins were either positively or negatively associated with clot perviousness and are listed in the Online Supplemental Data.

Thrombus Perviousness is Associated with Differential Susceptibility to ADAMTS13 Ex Vivo Thrombolysis

To investigate whether clot permeability is related to susceptibility to thrombolysis by different enzymatic degradations, we conducted

Proteins with the most significant abundance and depletion in highly pervious clots

Protein Name	log2fc	P Value
40S Ribosomal protein S23	-0.690129341	.00039
Glutamine synthetase	-1.606714657	.00073
40S Ribosomal protein S2	-0.413995286	.001
40S Ribosomal protein S12	-0.633724478	.001
60S Ribosomal protein L28	-0.519178688	.001
Aldehyde dehydrogenase, mitochondrial	-0.593729139	.0019
60S Ribosomal protein L27	-0.321892776	.0022
40S Ribosomal protein S8	-0.658129234	.0022
Electron transfer flavoprotein-ubiquinone oxidoreductase, mitochondrial	-0.348210926	.0023
Vesicle transport through interaction with t-SNAREs homolog 1B	-0.540383664	.0027
Immunoglobulin heavy variable 1/ORI5-1 (nonfunctional) (fragment)	0.85769177	.04
BCL2/adenovirus E1B 19 kDa protein-interacting protein 2.0.311	0.630567877	.015
Farnesyl pyrophosphate synthase	0.357444057	.013
Tropomyosin α -3 chain.0.2616	0.333697844	.005
GTPase NRAS.0.1703	0.316709736	.02
Cullin-4A..0.636	0.314913909	.04
V-type proton ATPase subunit G 1	0.285104241	.04
Protein phosphatase 1 regulatory subunit 7	0.232882868	.04
Dedicator of cytokinesis protein 10	0.231574532	.03

an ex vivo thrombolysis assay on 26 of the same mechanical thrombectomy-retrieved thromboemboli. We found no difference in thrombolysis between high- and low-pervious clots when defined as being greater or less than 11 HU (Fig 4A). Given this null result, we subsequently evenly distributed the 26 clots on the basis of perviousness, which stratified them by ≥ 18 HU, and found that clots with high perviousness ($n = 13$) were more susceptible to thrombolysis with tPA-combined ADAMTS13 than clots with low perviousness ($n = 13$) (mean, 66.1% [SD, 22.3%] versus 91.1% [SD, 28.6%], respectively; $P = .034$) (Fig 4B). However, there was no difference in ex vivo thrombolysis with tPA alone, combining tPA with DNase, or when combining tPA with ADAMTS13 and DNase (Fig 4B). Likewise, clots with a high perviousness ratio defined as ≥ 1.2 ($n = 15$) were more susceptible to thrombolysis with tPA combined with ADAMTS13 than thrombi with low perviousness ($n = 11$) (mean, 68.1% [SD, 21.8%] versus 92.9% [SD, 30.5%], respectively; $P = .047$) (Fig 4C). However, there was no difference in thrombolysis with the other enzymatic combinations. Most important, there was no significant difference in prethrombectomy IV tPA use between the clots with high (≥ 18 HU) and low perviousness ($P = .19$), or based on a high- and low-perviousness ratio ($P = .07$).

DISCUSSION

We present the first study to investigate whether ischemic stroke thrombus perviousness is associated with a distinguishable proteomic signature. Leveraging quantitative mass spectrometry, we found that retrieved thromboemboli have distinct proteomic features when categorized as high (≥ 11 HU) or low (< 11 HU) perviousness. We also found direct associations between numerous proteins and increasing perviousness, providing insights into cerebral thrombus biology not previously gleaned from prior histopathologic studies. Last, we related clot permeability to an ex vivo lysis assay, revealing that highly pervious clots may be particularly vulnerable to ADAMTS13-augmented tPA thrombolysis. Moreover, this study further demonstrates the feasibility of

relating clot imaging characteristics to proteomic composition and ex vivo lysis, a novel technique for thrombus characterization of ischemic stroke.

Thrombus permeability/perviousness has been shown to be associated with clinical outcomes in acute ischemic stroke. For example, post hoc analysis of 165 patients from the COMPASS Trial: A Direct Aspiration First Pass Technique⁷ found that clot perviousness was related to first-pass success with frontline aspiration thrombectomy, whereas stent retriever success was not dependent on thrombus permeability. Likewise, data from the The Multicenter Randomized Clinical Trial of Endovascular Treatment for Acute Ischemic Stroke in the Netherlands (MR CLEAN) trial⁶ also found that thrombus perviousness was strongly associated with higher recanalization rates, smaller final infarct volume, and improved functional outcomes. Permeable thrombi have also been shown to be more likely to result in recanalization and favorable functional outcomes following IV tPA administration.^{6,12} However, likely due to suspected underpowering, we did not detect a difference in clinical outcomes based on clot perviousness within our small cohort of 59 specimens.

A handful of studies have investigated how clot permeability is associated with histopathologic composition; however, data are conflicted, and no studies have examined how it relates to proteomic composition. Benson et al² studied retrieved thrombi from 57 patients and found that pervious clots were more red blood cell (RBC)-rich, whereas impervious clots had a higher proportion of fibrin and white blood cells (WBCs). By contrast, both Patel et al³ and Berndt et al⁹ reported that pervious clots had a lower proportion of RBCs and a higher fibrin/platelet content. Additionally, a previous study investigated 24 retrieved ischemic stroke clots and explored how the hyperdense cerebral artery sign was related to proteomic composition; however, thrombus permeability was not evaluated as an imaging variable.¹³

Our proteomic data suggest depletion of RBCs and iron processing with an abundance of platelet proteins in pervious thrombi. We found that RBC hemoglobin ζ was significantly depleted in pervious clots (Online Supplemental Data) and that decreasing

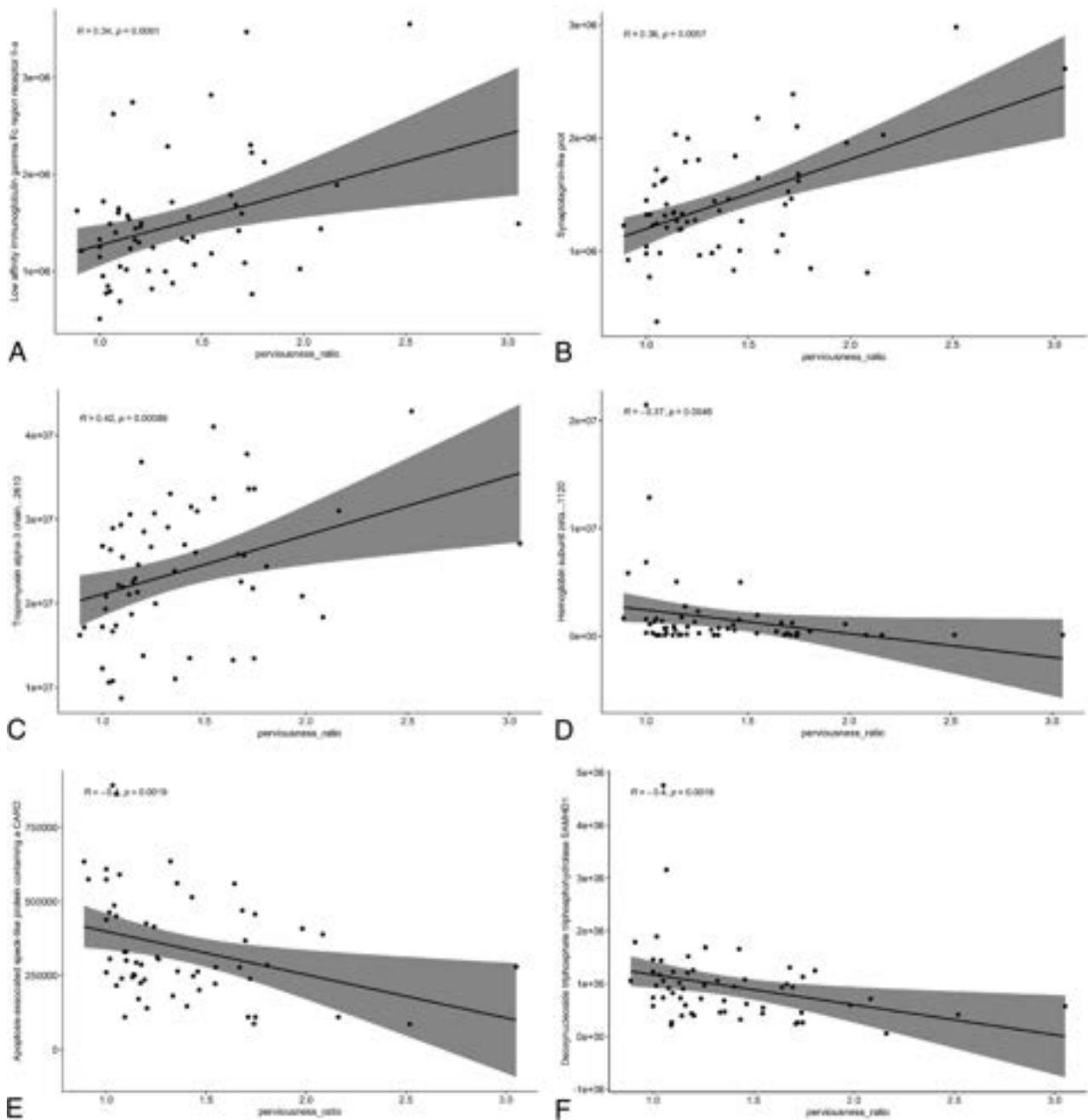


FIG 3. Association between specific protein content and the thrombus perviousness ratio. The relation between increasing perviousness ratio and low-affinity *FCGR2A/FcγRIIA* (A), *SYTL4* (B), *TPM3* (C), hemoglobin subunit ζ (D), *PYCARD/ASC* (E), and dNTPase *SAMHD1* (F).

perviousness was significantly correlated with decreasing hemoglobin ζ content ($P = .0046$, Fig 3D), though the remaining hemoglobin subunits were not significantly different on the basis of clot permeability. GO data found that pervious clots were significantly depleted in ferritin-processing and iron-binding, suggesting depletion of iron-rich RBCs. On the other hand, several platelet activation-related proteins were directly related to thrombus permeability on CT. *TPM3* was associated with increasing perviousness and has been suggested to play a role in platelet cytoskeleton remodeling ($P = .00089$, Fig 3C).¹⁴ Likewise, *SYTL4* was also significantly associated with increased thrombus perviousness ($P = .0057$, Fig 3B). *SYTL4* is expressed in human platelets and

has been shown to regulate attenuated granule secretion.^{15,16} Moreover, human platelets express *FcγRIIA*, an immune complex receptor that fully activates platelets for aggregation/secretion and plays a complex role in immunothrombosis and was found to be significantly correlated with clot perviousness ($P = .0091$, Fig 3A).^{17,18}

Our observed differences in several monocyte-associated proteins may suggest specific roles of immune-mediated thrombosis in relation to clot permeability. The macrophage-specific marker *CD14* was significantly less abundant in pervious clots ($P = .039$, $z = 1.176$). Similarly, *PYCARD/ASC*, which is a component of the macrophage/monocyte inflammasome, was negatively associated

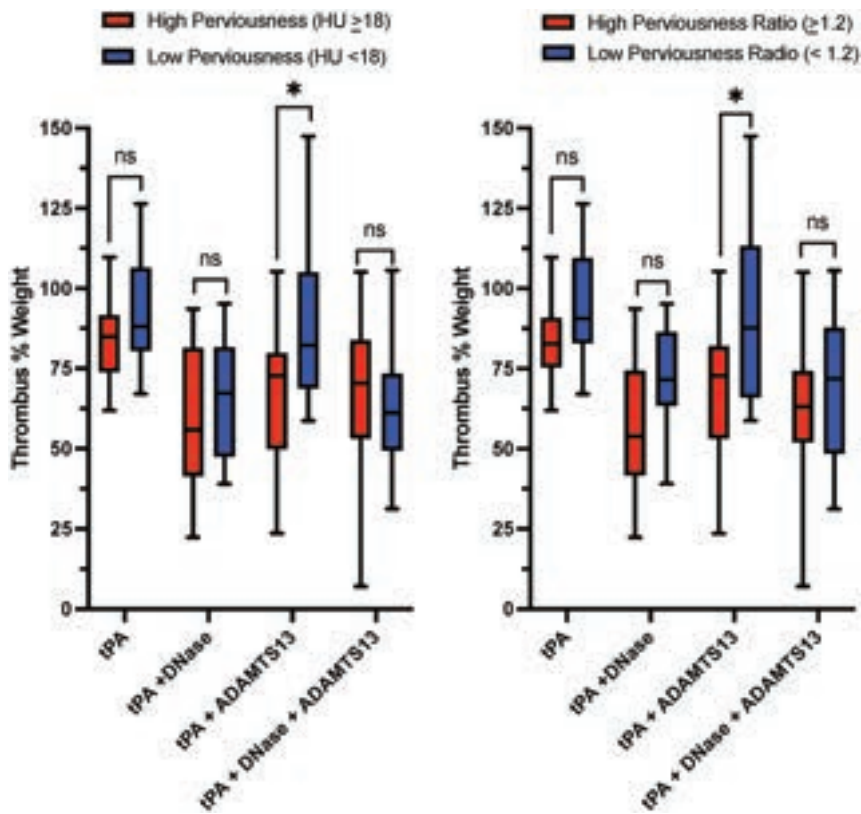


FIG 4. Thrombus perviousness is associated with differential susceptibility to ADAMTS13-augmented thrombolysis. Ns indicates not significant. * $P < .05$.

with increasing thrombus permeability ($P = .0019$, Fig 3E).¹⁹ Likewise, dNTPase of SAMHD1, which is expressed in monocytes/macrophages, was negatively associated with increasing permeability ($P = .0019$, Fig 3F).²⁰ These findings are in line with prior observations by Benson et al,² who reported that impervious clots were more likely to be WBC-rich relative to permeable thrombi ($P = .01$). Because we did not observe differences in other granulocyte abundances, this prior finding may be reflective of monocyte content. However, Patel et al³ found no significant difference in WBC content based on clot permeability in 40 received embolectomy samples. Evolving research is indicating a complex role of immune cells in acute ischemic stroke thrombogenesis, with significant heterogeneity within the thrombus immune landscape.²¹

Enhanced susceptibility to ADAMTS13 of pervious clots was the only difference on ex vivo lysis, validating the importance of a preponderance of platelet-associated proteins in pervious emboli on proteomic analysis. ADAMTS13 is an enzyme that cleaves vWF and thus inhibits vWF-mediated platelet aggregation and fibrinogenesis. A prior study found a positive association between fibrin content and vWF concentration in ischemic stroke clots ($P = .0085$) and that vWF-rich/tPA-resistant clots were dose-dependently dissolved by ADAMTS13 administration.²² Together, our findings provide further evidence that pervious clots are fibrin/platelet rich, which might be leveraged to enhance stroke thrombolysis with ADAMTS13. However, we detected a difference in ADAMTS13 lysis only when clots were stratified by 18 HU (the median perviousness value of those

clots that were lysed), suggesting that only very highly permeable clots might be vulnerable to this lysis strategy.

This study has several limitations that need to be considered. First, as with all studies of retrieved stroke thromboemboli, this investigation reflects only clots that were retrievable, with nonretrievable/failed thrombectomy samples being inherently excluded, and may have separate proteomic features. Furthermore, the ex vivo lysis assay was completed on only 44% (26/59) of the thrombus samples, making this analysis relatively less robust compared with the other proteomic analyses reported here. Another consideration is that prethrombectomy IV tPA may have unknowingly influenced some of the results. Although it has been previously shown that IV tPA does not alter histopathologic composition²³ and we found no significant difference in tPA use between groups in both the proteomic and lysis analyses, this influence should still be considered. Additionally, given that stroke imaging proteomics is essentially uncharted territory, we used a less stringent methodology for protein identification without

a strict false discovery rate criteria. Consequently, it is necessary to bolster and expand our work with larger sample sizes that allow more stringent statistical analysis.

CONCLUSIONS

CT perviousness of acute ischemic stroke thrombus is associated with proteomic differences related to platelet and immune protein content, among other differences. Given that pervious thrombi exhibit enhanced lysis with ADAMTS13, this feature may open the door for better chemical lysis pathways in which tPA may be less effective.

Disclosure forms provided by the authors are available with the full text and PDF of this article at www.ajnr.org.

REFERENCES

- Wei L, Zhu Y, Deng J, et al. **Visualization of thrombus enhancement on thin-slab maximum intensity projection of CT angiography: an imaging sign for predicting stroke source and thrombus compositions.** *Radiology* 2021;298:374–81 CrossRef Medline
- Benson JC, Fitzgerald ST, Kadirvel R, et al. **Clot permeability and histopathology: is a clot's perviousness on CT imaging correlated with its histologic composition?** *J Neurointerv Surg* 2020;12:38–42 CrossRef Medline
- Patel TR, Fricano S, Waqas M, et al. **Increased perviousness on CT for acute ischemic stroke is associated with fibrin/platelet-rich clots.** *AJNR Am J Neuroradiol* 2021;42:57–64 CrossRef Medline
- Ye G, Cao R, Lu J, et al. **Histological composition behind CT-based thrombus density and perviousness in acute ischemic stroke.** *Clin Neurol Neurosurg* 2021;207:106804 CrossRef Medline

5. Staessens S, François O, Brinjikji W, et al. **Studying stroke thrombus composition after thrombectomy: what can we learn?** *Stroke* 2021;52:3718–27 CrossRef Medline
6. Santos EM, Marquering HA, den Blanken MD, et al; MR CLEAN Investigators. **Thrombus permeability is associated with improved functional outcome and recanalization in patients with ischemic stroke.** *Stroke* 2016;47:732–41 CrossRef Medline
7. Mokin M, Waqas M, Fifi J, et al. **Clot perviousness is associated with first pass success of aspiration thrombectomy in the COMPASS trial.** *J Neurointerv Surg* 2021;13:509–14 CrossRef Medline
8. Chen Z, Shi F, Gong X, et al. **Thrombus permeability on dynamic CTA predicts good outcome after reperfusion therapy.** *AJNR Am J Neuroradiol* 2018;39:1854–59 CrossRef Medline
9. Berndt M, Friedrich B, Maegerlein C, et al. **Thrombus permeability in admission computed tomographic imaging indicates stroke pathogenesis based on thrombus histology.** *Stroke* 2018;49:2674–82 CrossRef Medline
10. Santos EM, Yoo AJ, Beenen LF, et al; MR CLEAN Investigators. **Observer variability of absolute and relative thrombus density measurements in patients with acute ischemic stroke.** *Neuroradiology* 2016;58:133–39 CrossRef Medline
11. Eden E, Navon R, Steinfeld I, et al. **GOrilla: a tool for discovery and visualization of enriched GO terms in ranked gene lists.** *BMC Bioinformatics* 2009;10:48 CrossRef Medline
12. Bilgic AB, Gocmen R, Arsava EM, et al. **The effect of clot volume and permeability on response to intravenous tissue plasminogen activator in acute ischemic stroke.** *J Stroke Cerebrovasc Dis* 2020;29:104541 CrossRef Medline
13. Schartz D, Akkipeddi SM, Chittaranjan S, et al. **CT hyperdense cerebral artery sign reflects distinct proteomic composition in acute ischemic stroke thrombus.** *J Neurointerv Surg* 2023;15:1264–68 CrossRef Medline
14. Marin-Quílez A, Vuelta E, Díaz-Ajenjo L, et al. **A novel nonsense variant in TPM4 caused dominant macrothrombocytopenia, mild bleeding tendency and disrupted cytoskeleton remodeling.** *J Thromb Haemost* 2022;20:1248–55 CrossRef Medline
15. Hampson A, O'Connor A, Smolenski A. **Synaptotagmin-like protein 4 and Rab8 interact and increase dense granule release in platelets.** *J Thromb Haemost* 2013;11:161–68 CrossRef Medline
16. Neumüller O, Hoffmeister M, Babica J, et al. **Synaptotagmin-like protein 1 interacts with the GTPase-activating protein Rap1GAP2 and regulates dense granule secretion in platelets.** *Blood* 2009;114:1396–404 CrossRef Medline
17. McKenzie SE, Taylor SM, Malladi P, et al. **The role of the human Fc receptor Fc gamma RIIA in the immune clearance of platelets: a transgenic mouse model.** *J Immunol* 1999;162:4311–18
18. Arman M, Krauel K. **Human platelet IgG Fc receptor FcγRIIA in immunity and thrombosis.** *J Thromb Haemost* 2015;13:893–908 CrossRef Medline
19. Martinon F, Burns K, Tschopp J. **The inflammasome: a molecular platform triggering activation of inflammatory caspases and processing of proIL-beta.** *Mol Cell* 2002;10:417–26 CrossRef Medline
20. Laguette N, Sobhian B, Casartelli N, et al. **SAMHD1 is the dendritic- and myeloid-cell-specific HIV-1 restriction factor counteracted by Vpx.** *Nature* 2011;474:654–57 CrossRef Medline
21. Renedo D, Sujjantararat N, Antonios J, et al. **Single-cell immune landscape of human clot retrieved at mechanical thrombectomy: association with stroke origin.** *Stroke* 2023;54:A15 CrossRef
22. Denorme F, Langhauser F, Desender L, et al. **ADAMTS13-mediated thrombolysis of t-PA-resistant occlusions in ischemic stroke in mice.** *Blood* 2016;127:2337–45 CrossRef Medline
23. Brinjikji W, Abbasi M, Mereuta OM, et al. **Histological composition of retrieved emboli in acute ischemic stroke is independent of prethrombectomy alteplase use.** *J Stroke Cerebrovasc Dis* 2022;31:106376 CrossRef Medline

Determinants and Clinical Relevance of Iodine Contrast Extravasation after Endovascular Thrombectomy: A Dual-Energy CT Study

Clémence Hoche, Alba Henderson, Héloïse Ifergan, Marie Gaudron, Christophe Magni, Igor Maldonado, Jean-Philippe Cottier, Marco Pasi, Grégoire Boulouis, and Clara Cohen



ABSTRACT

BACKGROUND AND PURPOSE: Iodine contrast extravasation (ICE) is common in patients with acute ischemic stroke (AIS) after endovascular-thrombectomy (EVT). The aim of our study was to evaluate the incidence of ICE assessed by dual-energy CT (DECT), its determinants, and associations with clinical outcome.

MATERIALS AND METHODS: We retrospectively examined imaging parameters and clinical factors from consecutive patients with AIS treated with EVT who had a DECT 24 hours thereafter, identified at a single academic center. Associations between ICE, clinical, imaging, and procedural parameters, as well as clinical outcome were explored by using univariable and multivariable models.

RESULTS: A total of 197 consecutive patients were included (period 2019–2020), of which 53 (27%) demonstrated ICE that was pure ICE in 30/53 (57%) and mixed with intracranial hemorrhage (ICH) in 23/53 (43%). Low initial-ASPECTS, high per-procedural-contrast volume injected, and high admission-glycemia were independently associated with ICE (respectively, OR = 0.43, 95% CI, 0.16–1.13, $P = .047$; OR = 1.02, 95% CI, 1.00–1.04, $P = .003$; OR = 8.92, 95% CI, 0.63–125.77, $P = .043$). ICE was independently associated with ICH ($P = .047$), but not with poorer clinical outcome (6-month mRS > 2, $P = .223$). Univariate analysis demonstrated that low ADC, higher ischemic volume, ICA occlusion, mass effect, longer procedure duration, combined thrombectomy technique, higher number of device passes, and lower recanalization rate were associated with ICE (respectively, $P = .002$; <.001; .002; <.001; .002; 0.011; <0.001; 0.015).

CONCLUSIONS: ICE evaluated with DECT is a relatively frequent finding after EVT, present in almost one-third of patients. Lower admission ASPECTS, higher glycemia, and high contrast volume injected per procedure were associated with ICE. We also found an association between ICE and ICH, confirming blood–brain barrier alteration as a major determinant of ICH.

ABBREVIATIONS: AIS = acute ischemic stroke; BBB = blood-brain barrier; DECT = dual-energy computed tomography; EVT = endovascular thrombectomy; HU = Hounsfield units; ICC = intraclass correlation coefficient; ICE = iodine contrast extravasation; ICH = intracranial hemorrhage; IOM = iodine overlay map; VNC = virtual noncontrast

Intracranial hemorrhage (ICH), especially when symptomatic, represents a significant complication in individuals experiencing acute ischemic stroke, being associated with increased mortality and worse functional outcome.^{1,2} The determinants of symptomatic ICH following endovascular treatment (EVT) have been extensively studied in recent works, but there remain areas of uncertainty.³ Among pathophysiological mechanisms of ICH, a severe disruption of the blood–brain barrier (BBB) has been

shown to play a pivotal role, and can be readily identified when intraparenchymal iodine contrast extravasation (ICE) is seen on control imaging. Prior studies have shown that ICE is common following EVT,^{4–6} and is associated with ICH as well as poor clinical outcome.^{7–9} These works suggest an interplay between ICE and ICH that may be of direct relevance for our pathophysiological understanding of the determinants of ICH, for patients' post-acute antithrombotic regimen adaptation and possibly to better inform clinical prognosis following EVT. On follow-up imaging though, increased intraparenchymal attenuation may indicate ICE and/or ICH, making them typically indistinguishable by using single-energy CT. Conversely, dual-energy CT (DECT) has high discriminative capacities for blood and iodine contrast,^{10–16} allowing it to differentiate ICE from ICH and evaluate their distinct incidence, determinants, and independent contributions to clinical prognosis.

In a single-institution retrospective, observational study, where DECT is routinely used for 24 h follow-up imaging after EVT, we aimed to evaluate the incidence of ICE, its association

Received December 19, 2022; accepted after revision October 29, 2023.

From the Departments of Diagnostic and Interventional Neuroradiology (H.I., J.-P.C., G.B.) and Neurology (C.H., M.G., M.P.), University Hospital of Tours, Tours, France; University of Tours (I.M.), Tours, France; and Department of Diagnostic Neuroradiology (A.H., C.M., C.C.), University Regional Hospital of Orleans, Orléans, France.

Please address correspondence to Clara Cohen, MD, Department of Neuroradiology, University Regional Hospital of Orleans, 14 Ave de l'Hôpital, 45100 Orléans, France; e-mail: clara.cohen@chu-orleans.fr

Indicates open access to non-subscribers at www.ajnr.org

Indicates article with online supplemental data.

<http://dx.doi.org/10.3174/ajnr.A8081>

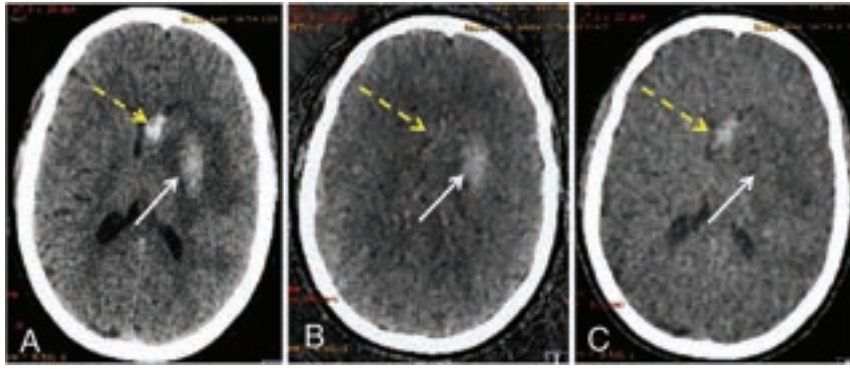


FIG 1. Association of ICE and ICH diagnosed on DECT performed 24 hours after endovascular thrombectomy. A, Native DECT demonstrating 2 spontaneous hyperattenuations: one in the left capsulo-lenticular region (white arrow, 43 HU), and another in the left caudate nucleus head (yellow dotted arrow, 58 HU). B, IOM, confirming ICE in the capsulo-lenticular region (white arrow) and hemorrhagic washout in the caudate nucleus (yellow dotted arrow). C, VNC image, at a 70 KeV level, demonstrating ICH in the caudate nucleus head (yellow dotted arrow), without contrast extravasation (white arrow). This case also illustrates the impossibility of differentiating ICE from ICH based on HU measurements.

with clinical imaging and procedural variables, and its association with any radiologic type of ICH and clinical outcome.

MATERIALS AND METHODS

Study Sample

We retrospectively reviewed data from patients with ischemic stroke who underwent EVT between January 2019 and June 2020 and had a control DECT 24 hours later, at our University Hospital Center, a tertiary care academic center.

Patients with posterior circulation ischemic stroke, single-energy CT control, or without control CT were excluded from this study (Online Supplemental Data). The reporting of this study conforms to the Strengthening the Reporting of Observational Studies in Epidemiology (STROBE) Statement standards.¹⁷

Ethics Statement

In accordance with French legislation, a commitment to compliance was filed to the French National Commission for Information Technology and Civil Liberties, Health Data Hub before data centralization of both retrospective cohorts, in respect to the General Data Protection Regulation CMR004. Written informed consent was waived, but patients or their proxies were informed that they could oppose the use of their deidentified health-related data for the purpose of research.

Clinical Data

Using electronic health records, we retrospectively collected clinical data for each included patient, encompassing demographics, baseline treatments, past medical history, NIHSS index stroke severity (assessed by admission NIHSS and 24 hour-NIHSS),¹⁸ treatment variables, and clinical outcome at 6 months. A good clinical outcome was defined as an mRS score of ≤ 2 at 6 months.¹⁹

Endovascular Treatment Data

The following parameters were recorded: anesthesia technique, time to recanalization, delay between onset or last

seen well and groin puncture as well as maximal modified Thrombolysis in Cerebral Infarction score.²⁰ Procedural parameters, including blood pressure during procedure, EVT first intent technique (stent/aspiration/combined technique), number of device passes, and final modified Thrombolysis in Cerebral Infarction score were recorded.

Image Acquisition and Postprocessing

The initial diagnosis of AIS was directly obtained by MR imaging, without preceding CT (1.5T Magnetom Aera or 3T Magnetom Prisma, both Siemens). MRI protocol comprised systematic DWI, FLAIR, susceptibility-weighted imaging, time-of-flight MRA, and optional perfusion, and/or gadolinium-enhanced supra-aortic MRA (Online Supplemental Data).

We collected the following acute imaging parameters: occlusion site (middle cerebral artery and its segment [ie, M1, M2 or M3], internal carotid artery, or other), baseline ASPECTS (manually assessed, taking the whole brain into account),²¹ and positivity of FLAIR in correspondence with ischemia, semiautomated ischemic volume assessed with Carestream Vue PACS Lesion Management (version 12.2, Carestream-Health). For ischemia volume measurements, the semiautomated process was conducted in 2 steps, relying on the ischemia visible in the DWI $b = 1000 \text{ mm}^2/\text{s}^2$ sequence (for details, see Online Supplemental Data).

The follow-up at 24–48 h after EVT was obtained with a DECT Discovery-750HD (GE Healthcare), by using the fast kVp-switching technique. The standard practice in our center is to conduct DECT 24 h after endovascular thrombectomy (time of groin puncture), with a potential variation of ± 6 h depending on the clinical status and the practical imperatives. DECT acquisition and reconstruction parameters were as follows: caudocranial-scan direction tube A/B: 80/140 kV tube voltage with a 0.25 ms alternance, mAs-reference x/Y, CTDIvol_{16cm} value of 48 mGy \times cm, helical beam mono-detector collimation of 20 mm \times 0.625, 0.8 second rotation time, pitch = 0.531. The raw spiral data were reconstructed in three different series by a dedicated algorithm, iodine overlay map (IOM) images, virtual noncontrast (VNC) images, and a reconstructed conventional CT by using commercially available software Advantage-ADW-server (GE Healthcare). VNC images were at a 70Ke-V level. Based on the energy-dependent attenuation varying for each material, IOM images map iodine material, whereas blood, which is a substance close to water, is mapped on VNC images. Thus, ICE and ICH diagnoses are made, respectively, on IOM (formal ICE) and VNC (formal ICH) images, with the possibility of association of both (Fig 1).

We focused on a radiologic perspective, without distinguishing between symptomatic or asymptomatic ICH, as our research is primarily rooted in the analysis of imaging data related to ICE and ICH.

On follow-up imaging, we assessed the following: presence of mass effect, apparition of an ICH, or/and ICE with confidence index (from 0 to 5). For a more representative depiction of ICE and ICH cases within our population, we formed and analyzed 4 main groups (ICE and no-ICE groups, ICH and no-ICH groups), and 4 subgroups (eg, pure ICE group, ICE+ICH group, pure ICH group and no-ICE, no-ICH group).

Following DECT processing, we collected ICE attenuation value (Hounsfield unit [HU]) and localization as well as ICH attenuation value (HU), localization, and all type of ICH by using the Heidelberg classification²²; attenuation values are measurable on the reconstructed conventional images. Hyper attenuation areas were defined as areas with objective higher attenuation than the surrounding brain parenchyma (if doubtful, hyper attenuation of >20 HU compared with adjacent parenchyma). The absence of spontaneous hyper attenuation and formal conclusion for absence of ICE or ICH were recorded.

A double reading by 2 independent radiologists (an experienced neuroradiologist, C.C., 10 years of experience, and a junior radiologist, A.H., 4 years of experience) was performed for a subset of 110 patients' imaging data, a single reading was performed for the 87 remaining imagings (A.H.). All 197 patients' clinical and technical data were collected by a neurologist (C.H.) with 4 years of experience. Disagreement was resolved by consensus.

Statistical Analysis

The data were presented by using different measures depending on the variable type. For continuous variables, medians and interquartile ranges were reported. Categorical variables were expressed as counts and percentages. The normality of distributions was assessed by using histograms and the Shapiro-Wilk test. Interrater reliability was calculated by using the Cohen κ for nominal variables, and intraclass correlation coefficient (ICC) estimates and their 95% CIs for quantitative data. To evaluate the association between recorded variables and ICE, hemorrhagic transformation, and favorable outcome, we conducted univariable analyses by using appropriate tests as per variable types and distribution (categorical variables with Student *t* test and Mann-Whitney U test and continuous variables with the Pearson χ^2 test). For comparison of the 4 subgroups on continuous data, ANOVA or Kruskal-Wallis tests were performed according to data distribution. All variables with a significant association in the univariate analyses (predefined $P < .1$) were entered into multiple logistic regression models by using backward elimination to analyze potential predictors of ICE, ICH, and favorable outcome. In the model investigating clinical outcome, we forced adjustment for ICE and ICH. OR and their 95% CI were generated for each considered variable. Statistical significance was assessed at a 2-tailed α -level of .05. We calculated standard diagnostic accuracy parameters (ie, sensitivity, specificity, and positive and negative predictive values) for HU associated with ICE and an area under the receiver operating curve was generated. No correction for multiple testing was performed, as this study was inherently exploratory. Statistical analyses were performed by using JMP software, version Pro.14 (SAS Institute, 1989–2021).

RESULTS

We initially screened 350 patients through the prospective department database from January 2019 to June 2020. After application of exclusion criteria (Online Supplemental Data), 197 patients were included in the final analysis: we excluded 153 patients (3 due to missing 24–48 hours CT scan, 11 due to absence of initial imaging available, 123 who had a simple energy CT-control, 15 with a vertebralbasilar occlusion, and 1 patient without clinical information); for comparison between included and excluded population, see Online Supplemental Data.

Eighty-nine (45.4%) patients were women, with a median age of 72 IQR₂₅–IQR₇₅ (61–82) years (Online Supplemental Data). Median delay between EVT (hour of groin puncture) and control DECT was 23 h and 15 min, IQR₂₅–IQR₇₅ (21 h to 25 h 30 min).

On the basis of IOM and VNC images acquired by DECT, 88 (44.7%) patients had spontaneous hyper attenuation on the VNC images. Among them, 53 (26.9%) patients of the total population presented ICE and 58 (29.4%) presented ICH, corresponding in detail to 4 subgroups comprising 30 (15.2%) patients with pure ICE, 35 (17.8%) patients with pure ICH, 23 (11.7%) patients with both ICE and ICH (Fig 1), and 109 (55.3%) patients without ICE or ICH (Online Supplemental Data).

There was a good agreement for HU attenuation for ICE (ICC = 0.89; 95% CI, 0.763–0.946; $P < .001$); ASPECTS diffusion (ICC = 0.80; 95% CI, 0.726–0.854; $P < .001$); ICH diagnosis ($\kappa = 0.778$); ICE diagnosis ($\kappa = 0.772$); and moderate agreement for lowest ADC (ICC = 0.66; 95% CI, 0.528–0.761; $P < .001$).

Predictive Factors for Iodine Contrast Extravasation

Univariate analysis showed that patients who presented ICE had more per-procedural iodine contrast volume injected (200 IQR₂₅–IQR₇₅ [150–300] versus 100 IQR₂₅–IQR₇₅ [100–200], $P = .047$), higher glycemia at admission (1.38 IQR₂₅–IQR₇₅ [1.20–1.82] g/l versus 1.27 IQR₂₅–IQR₇₅ [1.09–1.48] g/l, $P = .016$), lower admission ASPECTS (6 IQR₂₅–IQR₇₅ [5–7] versus 7 IQR₂₅–IQR₇₅ [6–8], $P = .002$), more ICA occlusions than middle cerebral artery occlusions ($P = .036$), deeper territory ischemia ($P = .002$), lower minimal ADC ($P = .002$), and higher ischemic volume ($P < .001$). For the ICE group, EVT procedure duration was significantly longer ($P = .002$), the use combined-technique procedures and number of device passes to reach thrombectomy were higher ($P = .011$ and $P < .001$), with a lower recanalization rate ($P = .015$) (Table and Online Supplemental Data).

Details on main parameters for the 4 subgroups are given in Online Supplemental Data, summarizing univariate analysis comparing the pure ICE and ICE+ICH groups. A higher admission NIHSS was associated with pure ICE events compared with the 3 other subgroups ($P = .012$), and a lower admission ASPECTS was associated with pure ICE compared with ICE+ICH group ($P = .002$). No other factor was associated with ICE on univariate analysis (Online Supplemental Data).

Low initial ASPECTS, high contrast volume, and high admission glycemia were significantly associated with iodine extravasation in the multivariable analysis (respectively, OR = 0.43, 95% CI, 0.16–1.13, $P = .047$; OR = 1.02, 95% CI, 1.00–1.04, $P = .003$; OR = 8.92, 95% CI, 0.63–125.77, $P = .043$) (Table).

Multivariable analysis on ICE

	OR	95% CI	P Value
Data at admission			
Glycemia (g/l)	8.92	0.63–125.77	.043
NIHSS	0.77	0.56–1.06	.072
Imaging parameters			
Initial ASPECTS	0.43	0.16–1.13	.047
Initial lowest ADC	1.00	0.99–1.01	.783
EVT parameters			
Iodine-contrast volume injected during EVT (ml)	1.02	1.00–1.04	.003
Procedure duration (min)	0.99	0.96–1.01	.379
Number of device passes	1.14	0.55–2.37	.715

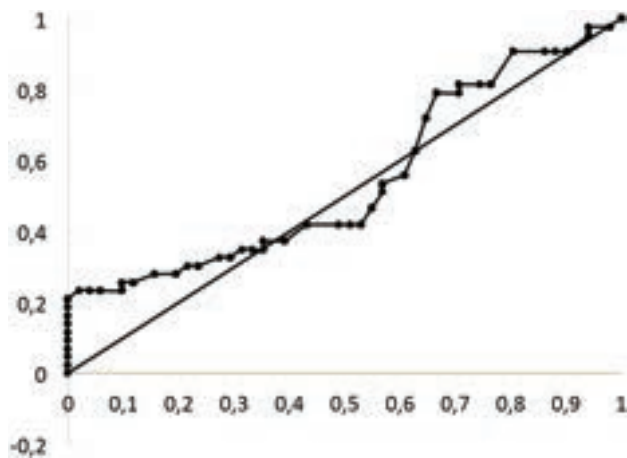


FIG 2. Receiver operating curve for mean HU in projection of ICE and ICH groups. Area under the curve = 0.546, illustrating the impossibility of differentiating ICE from ICH based on HU measurements.

Predictive Factors of ICH

Parameters significantly associated with ICH on the univariate analysis were as follows: ICH group versus no-ICH group: ICE ($n = 23$ [39.7%] versus 30 [23.6%], $P = .009$), ischemia volume (51 ml IQR₂₅–IQR₇₅ [20–83] versus 20 ml IQR₂₅–IQR₇₅ [8–45], $P = .012$), lower minimal-ADC (405.5×10^{-6} IQR₂₅–IQR₇₅ [346–459] versus 442×10^{-6} IQR₂₅–IQR₇₅ [390–495], $P = .006$), and more deep territory ischemia (22/55[40.0%] versus 36/125 [28.8%], $P = .017$) (Online Supplemental Data). Detailed information regarding the distribution of ICH types according to the Heidelberg classification and comparison for pure ICH versus ICH+ICE groups can be found in the Online Supplemental Data. It is worth noting that dyslipidemia posed a higher risk for pure ICH versus association of ICH and ICE ($P = .007$). Furthermore, during EVT, patients with pure ICH received a lower contrast volume injection, underwent fewer device passes, and achieved a higher recanalization compared with those with ICH+ICE (respective P -values of 0.024, 0.046, and 0.048).

Iodine contrast extravasation was independently associated with ICH on multivariable analysis ($P = .047$) (Online Supplemental Data).

Favorable Outcome

Patients without ICE had a better functional evolution (mRS ≤ 2) at 6 months than patients with ICE on univariate analysis (70/135

[51.9%] versus 16/49 [32.7%], $P = .029$). The pure ICE group was also associated with a poorer outcome ($P = .041$), contrary to the population presenting both ICE and ICH ($P = .267$) (Online Supplemental Data). Within the ICE population, pure ICE versus ICE+ICH patients did not demonstrate difference for outcome at 3 months ($P = .559$) (Online Supplemental Data). During EVT, both the global ICE population and the pure ICE group demonstrated a lower recanalization rate ($P = .015$ and $.010$, Online Supplemental Data).

ICH was not associated with less favorable outcomes: mRS ≤ 2 at 6 months for no-ICH-group versus ICH-group (63 [45.3%] versus 23 [39.7%], $P = .529$), and the pure ICH group did not demonstrate a poorer outcome ($P = .849$) (Online Supplemental Data).

Among patients without ICE or ICH, 55 (64.0%) achieved an mRS ≤ 2 at 6 months, while 40 (40.8%) experienced a poor outcome ($P = .002$).

In the multivariable analysis, 4 parameters were significantly associated with favorable outcome at 6 months (mRS ≤ 2): lower age ($P = .027$); higher baseline ASPECTS ($P = .015$); lower admission glycemia ($P = .032$); and lower admission NIHSS ($P = .004$) (Online Supplemental Data). Iodine contrast extravasation was not independently associated with functional outcome ($P = .223$).

Mean HU Value ICE versus ICH

There was no significant difference in the median attenuation values for the spontaneously hyperattenuated area on the reconstructed conventional images when comparing the ICE and ICH groups, which were previously identified on IOM and VNC maps ($P = .349$; 48.5 HU IQR₂₅–IQR₇₅ [40.5–64] versus 49HU IQR₂₅–IQR₇₅ [40–56]). This analysis was conducted separately for all locations of ICE ($n = 53$) and ICH ($n = 58$), with the understanding that patients with both ICE and ICH were included within each comparison group.

Area under the curve for HU distribution was not discriminative (0.026) (Fig 2). Consequently, we were unable to determine a discriminative threshold in HU sufficient to differentiate between ICE and ICH within the 30–70 HU range, encompassing the majority of our cases. Above 115 HU, all patients had an ICE ($n = 9$), associated with a 76.5% sensibility and a 18.6% specificity.

DISCUSSION

In this large retrospective cohort of patients treated with endovascular thrombectomy and with a DECT as part of early imaging follow-up, we showed ICE to be frequent, occurring in over one-fourth of our sample, with 15% of patients displaying pure ICE. While ICE was independently associated a higher frequency of ICH, we did not demonstrate an independent association with functional outcome at 3 months, even though the univariate analysis on global ICE and pure ICE groups indicated that extravasation was associated with a poorer outcome.

In this analysis, ICE was diagnosed by DECT, a recognized technique for the early cross-sectional differentiation between ICE and hemorrhage,^{10,12} providing relevant information on the determinants of ICE by comparison with previous works relying on longitudinal simple-energy CT controls,⁵ and most notably regarding the determinants of ICH and clinical outcome.

In line with previous literature, the incidence of any hyperattenuating lesions on follow-up CT was high in our cohort, found in 45% of our population after thrombectomy (32%–62% in previous works).^{7,23} In routine clinical practice, discerning whether these hyper attenuated lesions on control CT are ICE or ICH is important for the adjustment of medical care, and the stratification of hemorrhage risk.

Without DECT, identifying iodine extravasation requires repeated longitudinal control imaging to reveal iodine washout, while hemorrhage transformation persists for days to weeks.²⁴ Previous works proposed various thresholds to help discriminate ICE from ICH on cross-sectional CT, but the commonly used >90 HU cutoff, though sensitive for ICE, lacks sensitivity.^{24,25} The incidence of ICE on early (12–76 h) CT control widely varies in the literature (14%–81.8%),^{12,15,26–28} making the challenge not confirmation but rather clear differentiation from ICH.

In our sample, we could not establish a discriminative threshold in HU values to distinguish ICE from ICH, especially in the 30–70 HU range, which corresponds to most of our cases. While it is worth noting that all patients who presented attenuation >115 HU had an ICE, the accuracy for ICH in such attenuation ranges was not changed. The higher the attenuation, the higher the probability of contrast extravasation; while, as suggested by Bonatti et al,⁷ the higher the hyper attenuation value in early cases, the greater the risk of an ICH.

Quantitative assessment of iodine extravasation based on maximum iodine concentration measurements will possibly require a dedicated software,⁸ especially if postprocessing of IOM is not upgraded to calculate the iodine concentration from the increased HU values corresponding to ICE.

These data bring contrast extravasation diagnosis closer to the small-scale parenchymal analysis but are not always available on a routine practice.

Most publications on brain DECT applied to patients with AIS are based on the Siemens dual source technique^{10,11,27,29} or the Philips dual-layer principle.^{7,14} The fact that we used the fast kVp-switching technique proposed by GE Healthcare's technology, as Almqvist et al¹⁵ and Chrzan et al did,³⁰ contributed to broaden the spectrum of data on DECT. Indeed, its use is becoming more widespread, with variations in manufacturers depending on each imaging center.

Importantly, ICH and ICE are not independent, and they have been shown to co-occur in previous works, with ICE being independently linked to ICH. In the work by Chen et al,⁹ the odds for ICH more than doubled (OR = 2.150) in patients with ICE, and 49% of the ICE population experienced ICH. Similarly, 50% (28/56) of patients with ICE in the cohort of Baik et al⁸ showed ICH, a very disproportionately higher proportion than unselected cohorts. Their study design differs from ours, as they conducted DECT within 60 min after EVT and followed up with

MR imaging within 24 h. Given the higher sensitivity of MR imaging for detecting hemoglobin derivative products,³¹ it is likely that MR imaging will reveal a higher incidence of moderately extended hemorrhagic transformation, such as HI1 and HI2 according to the Heidelberg classification.

Another work, by Xu et al,⁵ also showed an association between ICE and ICH. In our sample, a lower initial ASPECTS, a high periprocedural volume of contrast media injection, and a high admission glycemia were independently associated with ICE, which was itself independently associated with ICH. Importantly, all the above-mentioned determinants of ICE are also directly or indirectly linked to the final infarct volume, the most important determinant for the risk of ICH following mechanical thrombectomy in the literature. Our findings plead for a strong interplay between the determinants of ICH and ICE. Whether these factors lead to BBB disruption to varying extents, which may translate as ICE and/or be responsible for ICH remains speculative. In our work, the fact that lower ADC values (a marker of ischemic process severity) were associated with higher risk for ICH, but also for the incidence of ICE, is an additional argument for such an interplay. Hemorrhagic transformation after endovascular treatment implies that the BBB is severely damaged. The disruption of the BBB soon after ischemia paves the way for reperfusion injuries and subsequent ICH. Both MR imaging and CT perfusion studies have aimed to assess disturbances in parenchymal permeability that result in BBB damages after AIS. This was done by analyzing parameters, such as increased time-to-peak or volume transfer constant (K^{trans}).^{32–35}

Conversely, iodine extravasation appears to enhance the permeability of the BBB without destroying the basal lamina, allowing the contrast agent to pass between the intravascular and extravascular spaces.^{32,36–38}

Importantly, the association between larger infarct volume (or its determinants) and ICE may explain why previous works have shown a univariable association between ICE and functional outcome, which was present in our work but was not maintained after multivariable adjustment.³⁹

Although we could not perform multivariable analysis for the pure ICE group (due to small sample size), this event was associated with a higher admission NIHSS, lower initial-ASPECTS, longer EVT duration, a higher number of device passes, and a lower recanalization rate compared with the other patients, encompassing mixed ICE+ICH, pure ICH, and cases without ICE or ICH.

The distribution of hemorrhagic transformation types according to the Heidelberg classification exhibited slight differences from recent literature,⁴⁰ showing a higher incidence of 1c/PH1 and a lower incidence of 1b/HI2. This variance could potentially be attributed to the relatively limited sample size examined.

Our study recommends that the neurologist consider low ASPECTS and high glycemia levels on admission to identify ICE-prone patients. This could prompt earlier CT monitoring, before 12 h post-EVT, as already practiced in some health care centers.^{8,27}

The strong association between per-procedural iodine contrast agent volume and ICE occurrence is expected. Reducing contrast agent volume is an ideal goal, but its feasibility depends on factors such as procedure complexity, patient-specific considerations, and

the interventional neuroradiologist's experience. Nevertheless, the concept of minimizing the usage of iodine contrast media in our diagnostic and interventional imaging procedures is gaining traction, driven by economic and environmental concerns.^{41,42}

The study's retrospective, single-center design poses a significant limitation, exposing to intractable inherent selection bias, though we aimed to minimize this bias by using prospectively collected data by using a stroke registry.

Contrast extravasation volume and localization were not detailed; this might be a confusion bias as brain areas have various functional implications. Nikoubashman et al⁴³ found predictive links between initial ischemia and ICE localization, while Song et al⁴⁴ demonstrated association between ICE volume and clinical outcome, without specifying the localization.

Radiomics development^{45,46} and computerized tools to differentiate hemorrhage from iodine extravasation may overcome quantitative imaging features and help in discovering new imaging biomarkers.

Collateral circulation's role in ICE and its impact on clinical outcomes warrant attention. We did not distinguish asymptomatic from symptomatic hemorrhagic transformation, which might explain that no association with clinical outcome was demonstrated.

Nonetheless, our study reveals significant ICE associations and novel imaging parameter findings. Neuroradiologists should heed these insights to identify ICE-prone patients, potentially averting hemorrhagic complications.

CONCLUSIONS

ICE evaluated by DECT occurred in 27% of post-EVT patients, with 15% of patients demonstrating pure ICE. Multivariable analysis showed association between ICE with low ASPECTS, high glycemia at admission and high contrast volume injected at the time of endovascular treatment, but not with clinical outcome. We have demonstrated an association between ICE and hemorrhage transformation, an indicator of BBB insult. Identification of patients with high contrast-extravasation and bleeding risks is crucial to improve their clinical management and potential outcome.

Disclosure forms provided by the authors are available with the full text and PDF of this article at www.ajnr.org.

REFERENCES

1. Yaghi S, Willey JZ, Cucchiara B, American Heart Association Stroke Council; Council on Cardiovascular and Stroke Nursing; Council on Clinical Cardiology; and Council on Quality of Care and Outcomes Research, et al. **Treatment and outcome of hemorrhagic transformation after intravenous alteplase in acute ischemic stroke: a scientific statement for healthcare professionals from the American Heart Association/American Stroke Association.** *Stroke* 2017;48:e343–61 CrossRef Medline
2. van Kranendonk KR, Treurniet KM, Boers AM, MR CLEAN Investigators, et al. **Hemorrhagic transformation is associated with poor functional outcome in patients with acute ischemic stroke due to a large vessel occlusion.** *J Neurointerv Surg* 2019;11:464–68 CrossRef Medline
3. Janvier P, Kerleroux B, Turc G, et al. **TAGE score for symptomatic intracranial hemorrhage prediction after successful endovascular**

- treatment in acute ischemic stroke.** *Stroke* 2022;53:2809–17 CrossRef Medline
4. Whitney E, Khan YR, Alastrá A, et al. **Contrast extravasation post thrombectomy in patients with acute cerebral stroke: a review and recommendations for future studies.** *Cureus* 2020;12:e10616 CrossRef Medline
5. Xu T, Wang Y, Yuan J, et al. **Contrast extravasation and outcome of endovascular therapy in acute ischaemic stroke: a systematic review and meta-analysis.** *BMJ Open* 2021;11:e044917 CrossRef Medline
6. Lummel N, Schulte-Altedorneburg G, Bernau C, et al. **Hyperattenuated intracerebral lesions after mechanical recanalization in acute stroke.** *AJNR Am J Neuroradiol* 2014;35:345–51 CrossRef Medline
7. Bonatti M, Lombardo F, Zamboni GA, et al. **Iodine extravasation quantification on dual-energy CT of the brain performed after mechanical thrombectomy for acute ischemic stroke can predict hemorrhagic complications.** *AJNR Am J Neuroradiol* 2018;39:441–47 CrossRef Medline
8. Baik M, Cha J, Ahn SS, et al. **Dual-energy computed tomography quantification of extravasated iodine and hemorrhagic transformation after thrombectomy.** *J Stroke* 2022;24:152–55 CrossRef Medline
9. Chen Z, Zhang Y, Su Y, et al. **Contrast extravasation is predictive of poor clinical outcomes in patients undergoing endovascular therapy for acute ischemic stroke in the anterior circulation.** *J Stroke Cerebrovasc Dis* 2020;29:104494 CrossRef Medline
10. Gupta R, Phan CM, Leidecker C, et al. **Evaluation of dual-energy CT for differentiating intracerebral hemorrhage from iodinated contrast material staining.** *Radiology* 2010;257:205–11 CrossRef Medline
11. Phan CM, Yoo AJ, Hirsch JA, et al. **Differentiation of hemorrhage from iodinated contrast in different intracranial compartments using dual-energy head CT.** *AJNR Am J Neuroradiol* 2012;33:1088–94 CrossRef Medline
12. Tijssen MP, Hofman PA, Stadler AA, et al. **The role of dual energy CT in differentiating between brain haemorrhage and contrast medium after mechanical revascularisation in acute ischaemic stroke.** *Eur Radiol* 2014;24:834–40 CrossRef Medline
13. Gabbai M, Leichter I, Mahgerefteh S, et al. **Spectral material characterization with dual-energy CT: comparison of commercial and investigative technologies in phantoms.** *Acta Radiol* 2015;56:960–69 CrossRef Medline
14. Hedent SV, Hokamp NG, Laukamp KR, et al. **Differentiation of hemorrhage from iodine using spectral detector CT: a phantom study.** *AJNR Am J Neuroradiol* 2018;39:2205–10 CrossRef Medline
15. Almqvist H, Holmin S, Mazya MV. **Dual energy CT after stroke thrombectomy alters assessment of hemorrhagic complications.** *Neurology* 2019;93:e1068–75 CrossRef Medline
16. Choi Y, Shin NY, Jang J, et al. **Dual-energy CT for differentiating acute intracranial hemorrhage from contrast staining or calcification: a meta-analysis.** *Neuroradiology* 2020;62:1617–26 CrossRef Medline
17. von Elm E, Altman DG, Egger M, STROBE Initiative, et al. **The Strengthening the Reporting of Observational Studies in Epidemiology (STROBE) Statement: guidelines for reporting observational studies.** *Int J Surg* 2014;12:1495–99 CrossRef Medline
18. Brott T, Adams HP, Olinger CP, et al. **Measurements of acute cerebral infarction: a clinical examination scale.** *Stroke* 1989;20:864–70 CrossRef Medline
19. Swieten JC, van Koudstaal PJ, Visser MC, et al. **Interobserver agreement for the assessment of handicap in stroke patients.** *Stroke* 1988;19:604–07 CrossRef Medline
20. Fugate JE, Klunder AM, Kallmes DF. **What is meant by “TICI?”** *AJNR Am J Neuroradiol* 2013;34:1792–97 CrossRef Medline
21. Barber PA, Demchuk AM, Zhang J, et al. **Validity and reliability of a quantitative computed tomography score in predicting outcome of hyperacute stroke before thrombolytic therapy. ASPECTS Study Group. Alberta Stroke Programme Early CT Score.** *Lancet* 2000;355:1670–74 CrossRef Medline
22. von Kummer R, Broderick JP, Campbell BC, et al. **The Heidelberg Bleeding Classification.** *Stroke* 2015;46:2981–86 CrossRef Medline

23. Parrilla G, García-Villalba B, de Rueda ME, et al. **Hemorrhage/contrast staining areas after mechanical intra-arterial thrombectomy in acute ischemic stroke: imaging findings and clinical significance.** *AJNR Am J Neuroradiol* 2012;33:1791–96 CrossRef Medline
24. Yedavalli V, Sammet S. **Contrast extravasation versus hemorrhage after thrombectomy in patients with acute stroke.** *J Neuroimaging* 2017;27:570–76 CrossRef Medline
25. Yoon W, Seo JJ, Kim JK, et al. **Contrast enhancement and contrast extravasation on computed tomography after intra-arterial thrombolysis in patients with acute ischemic stroke.** *Stroke* 2004;35:876–81 CrossRef Medline
26. Amans MR, Cooke DL, Vella M, et al. **Contrast staining on CT after DSA in ischemic stroke patients progresses to infarction and rarely hemorrhages.** *Interv Neuroradiol* 2014;20:106–15 CrossRef Medline
27. Pinckaers FM, Mentink MM, Boogaarts HD, et al. **Early post-endovascular treatment contrast extravasation on dual-energy CT is associated with clinical and radiological stroke outcomes: a 10-year single-centre experience.** *Eur Stroke J* 2023;8:508–16 CrossRef Medline
28. Ma C, Xu D, Hui Q, et al. **Quantitative intracerebral iodine extravasation in risk stratification for intracranial hemorrhage in patients with acute ischemic stroke.** *AJNR Am J Neuroradiol* 2022;43:1589–96
29. Renú A, Amaro S, Laredo C, et al. **Relevance of blood–brain barrier disruption after endovascular treatment of ischemic stroke.** *Stroke* 2015;46:673–79 CrossRef Medline
30. Chrzan R, Łasocha B, Brzegowy P, et al. **Dual energy computed tomography in differentiation of iodine contrast agent staining from secondary brain haemorrhage in patients with ischaemic stroke treated with thrombectomy.** *Neurol Neurochir Pol* 2022;56:68–74 CrossRef Medline
31. Arnould MC, Grandin CB, Peeters A, et al. **Comparison of CT and three MR sequences for detecting and categorizing early (48 hours) hemorrhagic transformation in hyperacute ischemic stroke.** *AJNR Am J Neuroradiol* 2004;25:939–44
32. Arba F, Piccardi B, Palumbo V, et al. **Blood–brain barrier leakage and hemorrhagic transformation: the Reperfusion Injury in Ischemic Stroke (RISK) study.** *Eur J Neurol* 2021;28:3147–54 CrossRef Medline
33. Bang OY, Saver JL, Alger JR, UCLA MRI Permeability Investigators, et al. **Patterns and predictors of blood–brain barrier permeability derangements in acute ischemic stroke.** *Stroke* 2009;40:454–61 CrossRef Medline
34. Donahue J, Wintermark M. **Perfusion CT and acute stroke imaging: foundations, applications, and literature review.** *J Neuroradiol* 2015;42:21–29 CrossRef Medline
35. Heye AK, Culling RD, Valdés Hernández MD, et al. **Assessment of blood–brain barrier disruption using dynamic contrast-enhanced MRI: a systematic review.** *Neuroimage Clin* 2014;6:262–74 CrossRef Medline
36. Desilles JP, Rouchaud A, Labreuche J, et al. **Blood–brain barrier disruption is associated with increased mortality after endovascular therapy.** *Neurology* 2013;80:844–51 CrossRef Medline
37. Avsenik J, Bisdas S, Popovic KS. **Blood–brain barrier permeability imaging using perfusion computed tomography.** *Radiol Oncol* 2015;49:107–14 CrossRef Medline
38. Hawkins BT, Davis TP. **The blood–brain barrier/neurovascular unit in health and disease.** *Pharmacol Rev* 2005;57:173–85 CrossRef Medline
39. An H, Zhao W, Wang J, et al. **Contrast staining may be associated with intracerebral hemorrhage but not functional outcome in acute ischemic stroke patients treated with endovascular thrombectomy.** *Aging Dis* 2019;10:784–92 CrossRef Medline
40. van der Steen W, van der Ende NA, Luijten SP, et al. **Type of intracranial hemorrhage after endovascular stroke treatment: association with functional outcome.** *J NeuroIntervent Surg* 2023;15:971–76 CrossRef
41. Zhang W, Fourcade F, Amrane A, et al. **Removal of iodine-containing X-ray contrast media from environment: the challenge of a total mineralization.** *Molecules* 2023;28:341 CrossRef
42. Dekker HM, Stroomberg GJ, Prokop M. **Tackling the increasing contamination of the water supply by iodinated contrast media.** *Insights Imaging* 2022;13:30 CrossRef Medline
43. Nikoubashman O, Reich A, Gindullis M, et al. **Clinical significance of post-interventional cerebral hyperdensities after endovascular mechanical thrombectomy in acute ischaemic stroke.** *Neuroradiology* 2014;56:41–50 CrossRef Medline
44. Song SY, Ahn SY, Rhee JJ, et al. **Extent of contrast enhancement on non-enhanced computed tomography after intra-arterial thrombectomy for acute infarction on anterior circulation: as a predictive value for malignant brain edema.** *J Korean Neurosurg Soc* 2015;58:321–27 CrossRef Medline
45. Wagner MW, Namdar K, Biswas A, et al. **Radiomics, machine learning, and artificial intelligence: what the neuroradiologist needs to know.** *Neuroradiology* 2021;63:1957–67 CrossRef Medline
46. Chen X, Li Y, Zhou Y, et al. **CT-based radiomics for differentiating intracranial contrast extravasation from intraparenchymal haemorrhage after mechanical thrombectomy.** *Eur Radiol* 2022;32:4771–79 CrossRef Medline

Assessing Perfusion in Steno-Occlusive Cerebrovascular Disease Using Transient Hypoxia-Induced Deoxyhemoglobin as a Dynamic Susceptibility Contrast Agent

Ece Su Sayin, James Duffin, Vittorio Stumpo, Jacopo Bellomo, Marco Piccirelli, Julien Poublanc, Vepeson Wijeya, Andrea Para, Athina Pangalu, Andrea Bink, Bence Nemeth, Zsolt Kulcsar, David J. Mikulis, Joseph A. Fisher, Olivia Sobczyk, and Jorn Fierstra



ABSTRACT

BACKGROUND AND PURPOSE: Resting brain tissue perfusion in cerebral steno-occlusive vascular disease can be assessed by MR imaging using gadolinium-based susceptibility contrast agents. Recently, transient hypoxia-induced deoxyhemoglobin has been investigated as a noninvasive MR imaging contrast agent. Here we present a comparison of resting perfusion metrics using transient hypoxia-induced deoxyhemoglobin and gadolinium-based contrast agents in patients with known cerebrovascular steno-occlusive disease.

MATERIALS AND METHODS: Twelve patients with steno-occlusive disease underwent DSC MR imaging using a standard bolus of gadolinium-based contrast agent compared with transient hypoxia-induced deoxyhemoglobin generated in the lungs using an automated gas blender. A conventional multi-slice 2D gradient echo sequence was used to acquire the perfusion data and analyzed using a standard tracer kinetic model. MTT, relative CBF, and relative CBV maps were generated and compared between contrast agents.

RESULTS: The spatial distributions of the perfusion metrics generated with both contrast agents were consistent. Perfusion metrics in GM and WM were not statistically different except for WM MTT.

CONCLUSIONS: Cerebral perfusion metrics generated with noninvasive transient hypoxia-induced changes in deoxyhemoglobin are very similar to those generated using a gadolinium-based contrast agent in patients with cerebrovascular steno-occlusive disease.

ABBREVIATIONS: BOLD = blood oxygen level–dependent; CNR = contrast-to-noise ratio; ΔS = BOLD signal change; dOHb = deoxyhemoglobin; GBCA = gadolinium-based contrast agents; $P_{ET}O_2$ = end-tidal partial pressure of oxygen; PO_2 = partial pressure of oxygen; rCBF = relative CBF; rCBV = relative CBV; THx-dOHb = transient hypoxia-induced deoxyhemoglobin

Angiography can characterize disease-related structural change in major cerebral arteries that can impede blood flow, but it has a limited ability to determine hemodynamic effects at the tissue level.¹ However, DSC MR imaging can measure resting perfusion metrics such as MTT, relative CBF (rCBF), and relative CBV

(rCBV) by tracing the passage of a susceptibility contrast agent through the cerebral vasculature.

Gadolinium-based contrast agents (GBCA) are commonly used because they are strongly paramagnetic and generate robust susceptibility signal changes. Nevertheless, possible long-term risks^{2,3} and measurement inaccuracies^{4,5} when using GBCA indicate the need for new alternative contrast agents.

Consequently, the paramagnetic properties of intrinsically generated changes in deoxyhemoglobin (dOHb)⁶ have recently been explored as an MR imaging contrast agent.^{7,8} Normally, breathing room air oxygenates the mixed venous blood, resulting in fully oxygenated blood returning in the pulmonary veins and into the systemic circulation. Reductions in dOHb in the arteries can be generated by administering a hypoxic inspired gas mixture. In this case, the mixed venous blood fails to fully oxygenate, allowing an increase in dOHb to pass into the arterial blood. Subsequent breathing of a normoxic gas mixture reoxygenates the hemoglobin in subsequent recirculation of the blood. The unsaturated blood generated during transient hypoxia acts as a transient change in

Received July 21, 2023; accepted after revision November 1.

From the Departments of Physiology (E.S.S., J.D., J.A.F.) and Medical Biophysics (D.J.M.), University of Toronto, Toronto, Ontario, Canada; Joint Department of Medical Imaging and the Functional Neuroimaging Lab (E.S.S., J.P., V.W., A. Para, D.J.M., O.S.), University Health Network, Toronto, Ontario, Canada; Department of Anesthesia and Pain Management (J.D., J.A.F.), University Health Network, University of Toronto, Toronto, Ontario, Canada; and Departments of Neurosurgery (V.S., J.B. J.F.) and Neuroradiology and Clinical Neuroscience Center (M.P., A. Pangalu, A.B., B.N., Z.K.), University Hospital Zurich, University of Zurich, Zurich, Switzerland.

Please address correspondence to Olivia Sobczyk, PhD, University Health Network, Toronto General Hospital, Toronto, Ontario, Canada, 200 Elizabeth St, Toronto, ON, Canada M5G 2C4, P: 647-255-1410; e-mail: olivia.sobczyk@uhn.ca

Indicates open access to non-subscribers at www.ajnr.org

Indicates article with online supplemental data.

<http://dx.doi.org/10.3174/ajnr.A8068>

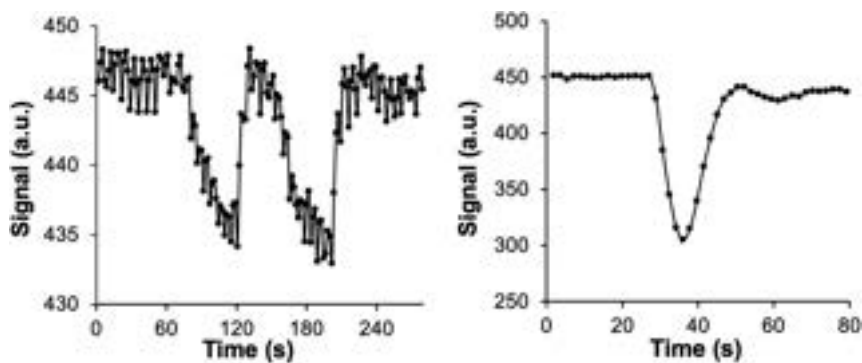


FIG 1. The 2 BOLD signal (a.u.) waveforms in a voxel over the MCA versus time in a representative participant for Thx-dOHb (A) and GBCA (B). A.u. indicates arbitrary units.

susceptibility contrast with pharmacokinetics similar to that of injected GBCA^{7,9-11} and thus lends itself to similar analysis for determining resting perfusion metrics. Indeed, in healthy volunteers, resting perfusion metrics generated with transient hypoxia-induced dOHb (THx-dOHb) have been shown to be similar in relative magnitudes and spatial distributions to those generated with GBCA.¹¹

The aim of this study was to evaluate the feasibility of examining cerebral resting perfusion metrics with THx-dOHb in patients with steno-occlusive cerebrovascular disease by comparing the metrics with those measured with GBCA. We hypothesized that resting MTT, rCBF, and rCBV obtained using GBCA and THx-dOHb would be comparable in the GM and WM of each participant and will likewise be able to distinguish flow deficits between affected and unaffected vascular territories.

MATERIALS AND METHODS

Participant and Ethics Approval

This study conformed to the standards set by the latest revision of the Declaration of Helsinki and was approved by the Ethics Committee of the Canton of Zurich (KEK Nr. 2020-02314), Zurich, Switzerland. All participants provided written, informed consent to partake in this study. We recruited 12 participants between the ages of 37 and 84 years with known large-vessel steno-occlusive disease through the neurosurgery outpatient clinic at University Hospital Zurich, Zurich, Switzerland. Ten participants completed the full experimental protocol, and 2 patients withdrew from the study during MR imaging due to discomfort during hypoxia. The ages, sex, and clinical profiles of those who completed the study and their MRAs are available in the Online Supplemental Data.

Experimental Protocol

The MR images were acquired using a 3T scanner (Magnetom Skyra VD13; Siemens) with a 32-channel head coil. The protocol consisted of a high-resolution T1-weighted structural scan followed by 2 identical blood oxygen level-dependent (BOLD) perfusion sequence scans. A high-resolution 3D T1-weighted spoiled gradient-echo volumetric sequence was acquired with the following parameters: TI = 942 ms, TR = 2400 ms, TE = 3.62 ms, flip angle = 12°, 176 slices, voxel size = 1.0 × 1.0 × 1.0 mm. The BOLD sequences consisted of a multi-slice 2D gradient-echo perfusion

sequence with the following parameters: TR = 1800 ms, TE = 30 ms, flip angle = 80°, 50 slices, voxel size = 2.5 × 2.5 × 2.5 mm. The first perfusion scan was acquired during end-tidal partial pressure of oxygen ($P_{ET}O_2$) manipulation while the second scan was acquired at normoxia following an IV injection of gadoterate meglumine (Dotarem; Guerbet).

Respiratory Protocol

All inspired gas was provided by a computerized gas blender running a prospective protocol^{12,13} to control end-tidal partial pressure of O_2 ($P_{ET}O_2$) and CO_2 independently of each other and of the pattern of breathing (RespirAct; Thornhill Medical). Patients breathed exclusively via a plastic face mask affixed to the face with skin tape (OpSite Flexifix; Smith & Nephew), making an airtight seal. The respiratory protocol consisted of a 60-second baseline $P_{ET}O_2$ of 95 mm Hg (normoxia), followed by a switch to $P_{ET}O_2$ of 40 mm Hg (hypoxia) for 60 seconds, and then a return to normoxia for 20 seconds, followed by repeat hypoxia for 60 seconds, followed by a return to normoxia (Fig 1A). Normocapnia was maintained throughout. After free breathing of room air for at least 5 minutes, gadoterate meglumine (0.1 mmol/kg) (Dotarem; Guerbet) was injected intravenously at a rate of 5 mL/s (with a baseline delay of 30 seconds before injection) followed by 30 mL of saline at a rate of 5 mL/s (Fig 1B).

Data Analysis Basics

The acquired BOLD images were volume-registered, slice-time corrected, and coregistered to the T1-weighted structural scans using Analysis of Functional Neuroimaging software (National Institutes of Health).¹⁴ The GBCA and THx-dOHb acquisitions were preprocessed in an identical manner to ensure that there was no bias toward any 1 scan. A 7-mm Gaussian spatial blur was applied to the data set. The T1-weighted structural scans were segmented into GM and WM and normalized to Montreal Neurological Institute coordinates using Statistical Parametric Mapping software (SPM8).^{15,16} The generated probability maps of GM and WM were thresholded at 70% probability. The MCA vascular territory was delineated manually on an anatomical Montreal Neurological Institute template (Online Supplemental Data). GM and WM masks were further divided into the left-hemisphere and right-hemisphere MCA.

Contrast-to-Noise Ratio and the BOLD Signal Change

The contrast-to-noise ratio (CNR) and BOLD signal change (ΔS) were calculated for GBCA and the THx-dOHb protocol, explained in additional detail by Poublanc et al.⁷ A 20-second continuous baseline signal at the beginning of each protocol was selected. A linear regression between the BOLD signal in each voxel and the average whole-brain signal (\bar{S} , see below) as the regressor was calculated with the slope determining the percentage signal change (ΔS). The whole-brain average signal (\bar{S}) was

Average measures of ΔS in percentages and the CNR calculated for GBCA and THx-dOHb for the 10 participants

	ΔS (%)		CNR	
	GM	WM	GM	WM
GBCA	25.20 (SD, 8.08)	14.78 (SD, 4.36)	11.21 (SD, 3.76)	8.17 (SD, 2.64)
THx-dOHb	5.71 (SD, 1.60)	2.87 (SD, 0.92)	6.33 (SD, 1.22)	6.41 (SD, 1.64)
P value	.002	.002	.004	.002

used as the regressor to ensure that both perfusion acquisitions could be compared, as summarized in Equation 1.

Equation 1
$$S = \alpha \times \bar{S} + \beta_1 \times t + \beta_2 + \varepsilon_t.$$

S is the scaled signal, α is the slope of the regression (parameter of interest), \bar{S} is the 1-dimensional time-series regressor, β_1 is the temporal linear signal drift component, β_2 is the signal baseline, and ε_t represents the residuals.

By means of the slope of the regression (α), ΔS was calculated as follows:

Equation 2
$$\Delta S = \alpha(\max(\bar{S}) - \min(\bar{S})).$$

Max (\bar{S}) and min (\bar{S}) are, respectively, the minimum and maximum of the \bar{S} time-series.

The noise was determined as the SD of the residuals from the linear regression, $std(\varepsilon_t)$. As shown in Equation 3, to obtain the CNR, we calculated the ratio of a signal difference (ΔS) to the noise.

Equation 3
$$CNR = \frac{\Delta S}{std(\varepsilon_t)}.$$

The GM and WM average CNR and ΔS values were calculated for each participant.

Resting Perfusion Metrics

For this study, perfusion metrics for GBCA and THx-dOHb were calculated in an identical manner. A standard tracer kinetic model was used to calculate MTT and rCBV, shown in Equation 4 and explained in additional detail by Poub Blanc et al.⁷

Equation 4
$$S_{c,t} = \frac{rCBV}{MTT} \times AIF_t \otimes R_t + \beta_1 \times t + \beta_2 + \varepsilon_t.$$

We assumed a linear relationship between the perfusion signal and the concentration of GBCA and dOHb. β_1 accounts for the signal drift, β_2 accounts for the baseline, and ε_t represents the residuals. For each contrast agent, the strongest signal change over the MCA was selected as the arterial input function (AIF_t). By means of a least-squares fitting procedure, rCBV and MTT metrics were determined. To account for the stronger signal decrease seen between GBCA and THx-dOHb during bolus transit through the vasculature, a scaling factor was needed to correct for this difference to compare rCBV maps. We used the ratio between the signal generated by GBCA and THx-dOHb as the scaling factor. The higher values obtained using GBCA were divided by the scaling factor rendering equivalence between GBCA and THx-dOHb.

By means of the central volume theorem, the rCBF was then calculated as rCBV/MTT.¹⁷ GM CBF is approximately 50 mL/100

g/min based on reliable measurements using PET,¹⁸ therefore, all participant CBF values were scaled by 50 arbitrary units on a voxelwise basis to obtain values within a familiar normative range. Perfusion metrics were overlaid onto their respective T1-weighted structural images using Analysis of Functional

Neuroimaging software (AFNI; <http://afni.nimh.nih.gov/afni>). Resting perfusion metrics were calculated in the supratentorial cortical GM and WM for GBCA and THx-dOHb. Resting perfusion metrics in GM and WM of each cerebral hemisphere were calculated using the previously created MCA vascular territory mask.

Statistical Analysis

The CNR, ΔS , calculated perfusion metrics, and their ratios of affected and unaffected vascular territories in GM and WM were compared between GBCA and THx-dOHb using a Wilcoxon matched-pairs signed-rank test (Prism 9 software; GraphPad). Using the calculated GM and WM averages, Bland-Altman plots were generated (Prism software; GraphPad).

RESULTS

Signal Comparison

The CNR and ΔS for GM and WM are presented in the Table. The GBCA signal was 4.41 times stronger in GM ($P = .002$) and 5.15 times stronger in WM ($P = .002$) than the THx-dOHb signal. However, the GBCA CNR was only 1.77 greater in GM ($P = .004$) and 1.27 times greater in WM ($P = .002$) than the THx-dOHb CNR.

Comparison of Resting Perfusion Metrics in GM and WM

A summary of perfusion metrics between GBCA and THx-dOHb are presented in the Online Supplemental Data. A Wilcoxon matched-pairs signed-rank test did not show statistically significant differences in resting perfusion metrics between GBCA and THx-dOHb in GM or WM ($P > .05$), except for WM MTT ($P < .05$) (Online Supplemental Data). Bland-Altman plots comparing the perfusion metrics from the GBCA and THx-dOHb are presented in Fig 2. A summary of the Bland-Altman plot analysis is presented in the Online Supplemental Data. The plots have negligible constant bias or proportional bias between techniques, except for WM MTT (Online Supplemental Data).

Comparison of Resting Perfusion Metrics in Affected and Unaffected Hemispheres

Of the 10 participants who completed the study, 8 had unilateral steno-occlusive disease, while 2 had bilateral lesions. The images of those with unilateral disease were divided into affected-versus-unaffected hemispheres. Figure 3 shows the line plots of MTT, rCBF, and rCBV in the affected and unaffected hemispheres in MCA GM and WM calculated using GBCA and THx-dOHb. The trends of hemodynamic metrics between hemispheres were very similar for both contrast agents. We compared the ratios of the affected and unaffected hemispheres in GM and WM between GBCA and THx-dOHb (Online Supplemental Data). A

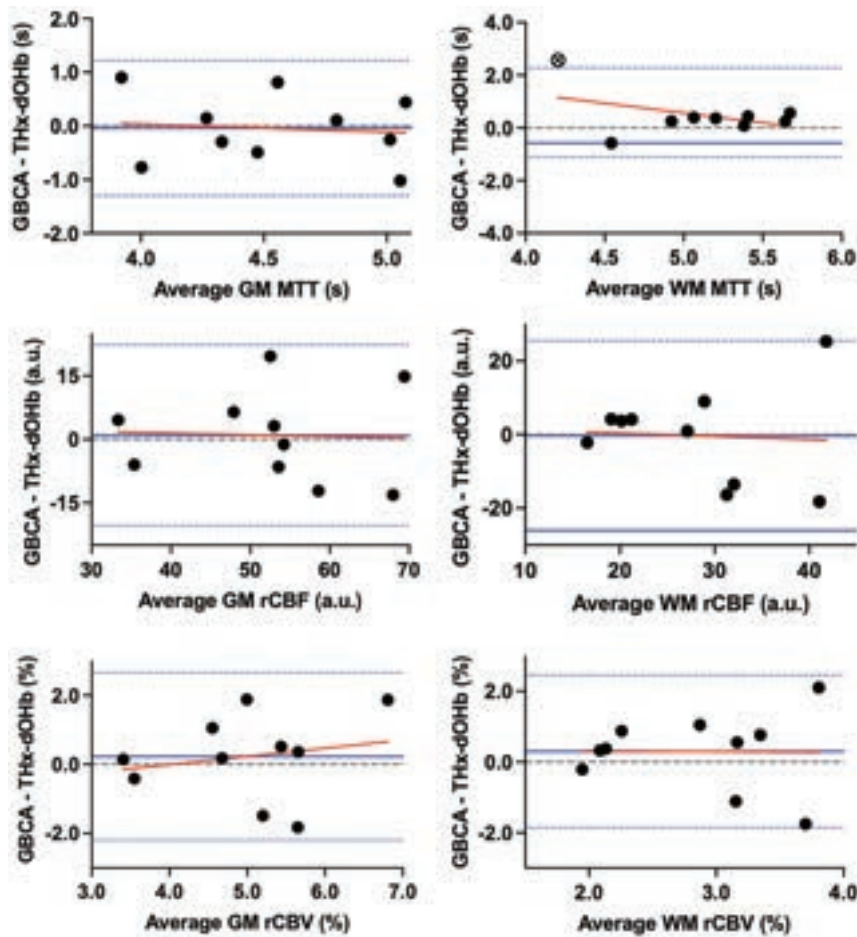


FIG 2. Bland-Altman plots comparing GBCA and THx-dOHb differences for perfusion metrics MTT, rCBF, and rCBV in GM and WM. The solid blue line depicts the mean, the dotted blue lines represent the 95% limits of agreement, and the red line represents the regression line.

Wilcoxon matched-pairs signed-rank test did not show a statistically significant difference in the ratios of affected and unaffected hemispheres between GBCA and THx-dOHb in GM or WM for all metrics ($P > .05$), except for WM rCBV (Online Supplemental Data).

Resting Perfusion Maps

Figure 4 shows perfusion maps for a representative participant (ID 1 as found in the Online Supplemental Data). This patient had a right ICA occlusion that led to a right ischemic stroke. The MTT, rCBF, and rCBV maps for the acquired images using GBCA and THx-dOHb have a high spatial similarity showing delayed MTT, slightly lower CBF, and higher CBV in the affected right hemisphere.

DISCUSSION

Main Findings

Resting cerebral perfusion metrics in patients with cerebrovascular steno-occlusive disease calculated with THx-dOHb contrast were similar to those generated with GBCA. In particular, the spatial distributions of the respective perfusion metrics MTT, rCBF, and rCBV were similar in both GM and WM. Both contrast agents were also similar, enabling the discrimination

between the affected and the unaffected hemispheres. Furthermore, the distributions of hemodynamic metrics between hemispheres were consistent with the locations of large-vessel pathology. We note that to eliminate any methodological, temporal, and disease variability, each participant was used as his or her own control. These findings, therefore, show that resting perfusion metrics obtained noninvasively with THx-dOHb can be of clinical value, particularly after considering the benefits and risks compared with GBCA.

Summary of Findings

Perfusion metrics MTT, rCBF, and rCBV were compared between GBCA and THx-dOHb in GM and WM. The perfusion metrics generated using the 2 contrast agents were not significantly different from one another, except for WM MTT. The WM MTT for THx-dOHb was significantly lower in comparison with GBCA ($P < .05$). Nevertheless, the individual participant perfusion maps are spatially very similar. Indeed, the results from the Bland-Altman plot analysis showed that the average discrepancy (constant bias) between the two agents is small for all perfusion metrics, with a narrow confidence interval, except for a constant bias for WM MTT in which the GBCA MTT is consistently greater than THx-dOHb. Furthermore, the differences between perfusion metrics in GM or WM have no proportional bias, with the slope of the regression line not significantly different from zero. The ratio of affected and unaffected hemispheres were the same for all subjects, with each contrast except for WM rCBV.

We suggest that these findings support the continued exploration of THx-dOHb for DSC imaging as (i) there is high agreement between metrics obtained using DSC imaging with GBCA and (ii) THx-dOHb is able to discriminate between affected and unaffected hemispheres in patients with steno-occlusive disease.

Advances over Current Knowledge

This study in patients with steno-occlusive disease follows previous investigations that demonstrated the utility of THx-dOHb as a contrast agent. Poublanc et al⁷ were the first to use THx-dOHb to calculate and map voxelwise resting perfusion metrics. The investigators applied sequential gas delivery¹³ and prospective end-tidal gas targeting¹² to generate abrupt transient isocapnic reductions in oxygen, to create pharmacokinetic profiles with dOHb that are similar to those obtained from an intravascular injection of GBCA, thereby enabling a similar approach to the calculation of perfusion metrics. Subsequently Sayin et al¹¹ found that the perfusion metrics generated by the 2 contrast agents were similar when

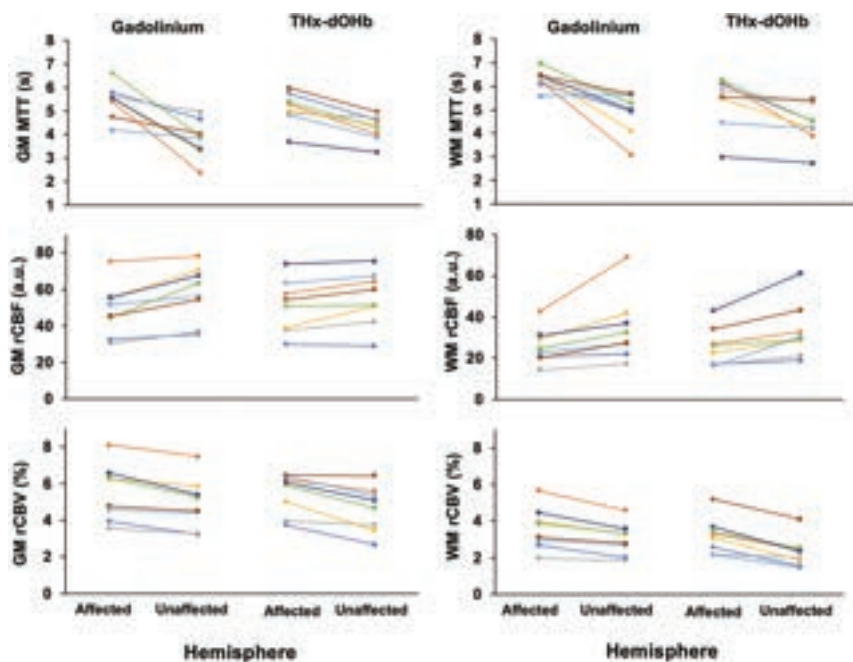


FIG 3. The affected-versus-nonaffected hemispheric perfusion metrics for GBCA and THx-dOHb for 8 participants who have unilateral steno-occlusive disease (patients 6 and 7 have bilateral disease and were excluded) in the MCA in the GM (*on the right*) and WM (*on the left*). The trends of affected-versus-unaffected hemispheres across both techniques are comparable. a.u. indicates arbitrary units.

assessed in the same healthy individuals. In this study, we extended these observations to show similarity in pattern as well as in the interpretation of perfusion metrics in patients with cerebrovascular pathology in the form of steno-occlusive disease.

THx-dOHb has several advantages over GBCAs as a contrast agent for DSC MR imaging. GBCA is an intravascular extracellular molecule. It can leak into the interstitial fluid¹⁹ in pathologic conditions when the BBB is disrupted and, therefore, requires leakage correction. By contrast, due to dOHb being contained in red cells, it remains intravascular regardless of the state of the BBB. This capacity may be a particularly useful advantage when the BBB is disrupted, provided that there is no active bleeding.²⁰ Furthermore, the analysis of the signal generated by GBCA can be affected during a second pass through the circulation, which will not occur with THx-dOHb unless there is a right-to-left cardiopulmonary shunt. On the contrary, THx-dOHb is cleared within 1 blood circulation time following pulmonary reoxygenation, enabling repeat measures as required. THx-dOHb may also be a suitable alternative contrast for patients with renal insufficiency who are at risk of nephrogenic systemic fibrosis if exposed to GBCA or at risk of worsening of renal function if exposed to iodinated contrast used for CTP.

During the past decade, there has been a drive to develop noninvasive techniques that are capable of identifying vascular dysfunction in individuals who are at risk. Arterial spin-labeling is a noninvasive MR imaging technique that provides quantitative measures of CBF. However, this technique has sensitivity to transit times and long collateral flow pathways associated with advanced cerebrovascular disease.²¹⁻²³ Currently, the only clinical standard for assessing perfusion metrics in patients with cerebrovascular steno-

occlusive disease is DSC imaging with GBCA. However, future work comparing CBF measured via Thx-dOHb with arterial spin-labeling may be beneficial.

Bolus Profile Comparison

The stimulus profile we used in this study was chosen to be consistent with its antecedent studies. The arterial input function profile of THx-dOHb differs from that of GBCA by having 2 susceptibility oxygen desaturations (Fig 1). Due to the strong paramagnetic properties of GBCA and the rapid IV injection, GBCA causes a very sharp decrease in the BOLD signal. In contrast, the rate of dOHb formation is limited by the rate of deoxygenation in the lungs. This process is one of breath-by-breath dilution of the oxygen in the lungs, over about 5–7 breaths taking about 20 seconds. Thus, the THx-dOHb performed a double 60-second hypoxic exposure targeting partial pressure of oxygen (PO₂) of 40 mmHg to improve the CNR. Previous studies have determined that the CNR increased marginally with repeat hypoxic stimuli. Although the susceptibility profiles of GBCA and Thx-dOHb differ, the arterial input functions can be used for both agents for the calculation of the respective perfusion metrics.^{7,11} Nevertheless, further changes in the hypoxic exposure profile may be considered for implementing strategies to shorten the time to reach target hypoxia.

Limitations

The tolerance of hypoxia in humans has been well-established. In formal studies, participants maintained a PO₂ at about 50 mm Hg for >20 minutes.²⁴⁻²⁶ In another study, a PO₂ of 55 mm Hg was maintained for 8 hours.²⁷ Hypoxia is experienced continuously by the millions who live at high altitudes, especially those with severe lung and heart disease, and intermittently by hundreds of millions throughout the world who have multiple episodes of obstructive sleep apnea nightly. Indeed, extended periods of intermittent hypoxia have even shown benefits of preconditioning against myocardial infarction,^{28,29} heart failure,³⁰ hypertension,^{30,31} and cognitive decline.³²

There is likely a range of sensitivity to hypoxia in humans and a range of its tolerability. In this study, 2 of 12 patients did not tolerate the hypoxia and aborted their study. Both participants who aborted the study did so during the second hypoxic exposure. It is possible that the low tolerance for hypoxia was related to the severity of the perfusion limitation, though there are no indications of this effect in people with severe steno-occlusive disease living at high altitudes or with concomitant severe pulmonary disease or severe, prolonged obstructive sleep apnea.

Another limitation of THx-dOHb is the issue of CBF increase in response to hypoxia, which could confound the measurement

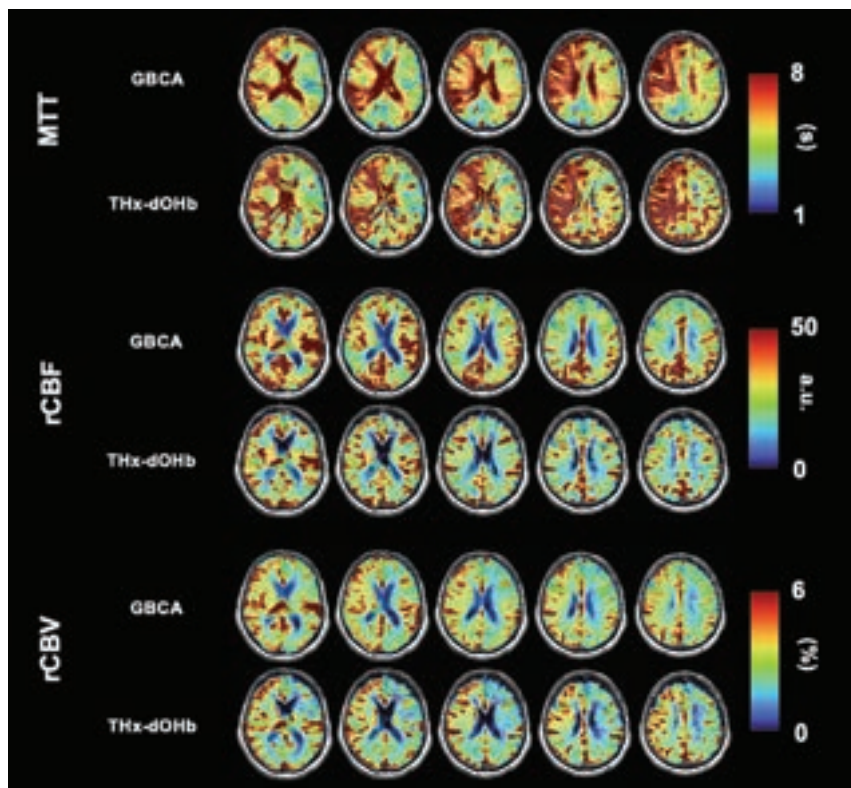


FIG 4. Perfusion maps of MTT, rCBF, and rCBV of a 71-year-old male participant (ID 1) with a right ICA occlusion comparing GBCA (A) and THx-dOHb (B). a.u. indicates arbitrary units.

of perfusion metrics. Ellingsen et al³³ had reported that a normocapnic reduction of PO₂ to 65 mm Hg resulted in an increase in carotid artery blood flow velocity over a period of about 10 minutes with a halftime of about 4 minutes. More recently, Harris et al²⁴ used pulsed arterial spin-labeling to measure the delay and time constant of a CBF increase in response to acute hypoxia. They found a delay to onset of flow change of about 3 minutes with a time constant of about 4.5 minutes. The duration of our hypoxic stimuli was only 60 seconds, repeated twice. However, the precise kinetics of CBF responses to acute severe hypoxia have not been rigorously documented.³⁴ If acute hyperemic responses do occur, reducing the extent of hypoxia or shortening the hypoxic interval may be feasible. These measures would also increase the tolerability of hypoxia.^{7,35,36} A further limitation may occur in areas of misery perfusion in which blood flow is low and the oxygen extraction fraction is high, resulting in a high baseline concentration of dOHb. With the initiation of THx-dOHb, the arterial oxygen delivery is further reduced, resulting in an exaggerated fall in the BOLD signal, perhaps marking the area of misery perfusion.

The presence of steno-occlusive disease or cerebral ischemia may itself result in dispersion of the bolus of contrast³⁷ and difficulty in accurately applying the input function. There are numerous ways to analyze perfusion data including, but not limited to, adopting a mono-/biexponential model from pharmacokinetics,³⁸ or using a vascular model³⁹ or a singular value decomposition.⁴⁰ However, these deconvolution techniques do not account for dispersion. For that, a complex model for the vasculature is required.⁴¹ When there is no correction for contrast dispersion, caution should

be used in interpreting the calculated MTT, rCBF, and rCBV metrics from either contrast. Similarly, if such peripheral late dispersion does exist, the deconvolution model would be equally offset with both GBCA and THx-dOHb profiles.

CONCLUSIONS

Cerebral perfusion metrics, including MTT, rCBF, and rCBV, using the novel contrast agent THx-dOHb show high spatial and scalar congruence with those generated by GBCA in subjects with known cerebrovascular steno-occlusive disease. In selected patients, THx-dOHb has the advantages of being needle-free and suitable for unlimited repeat examinations. These findings support the continued investigation of THx-dOHb as a noninvasive endogenous contrast agent to obtain cerebral perfusion metrics.

ACKNOWLEDGMENTS

All the authors thank University Hospital Zurich MR technologist Maria Sarioglou for all her help in acquiring the MR imaging data.

Disclosure forms provided by the authors are available with the full text and PDF of this article at www.ajnr.org.

REFERENCES

- Calamante F, Ganesan V, Kirkham FJ, et al. **MR perfusion imaging in moyamoya syndrome.** *Stroke* 2001;32:2810–16 CrossRef Medline
- Kanal E. **Gadolinium based contrast agents (GBCA): safety overview after 3 decades of clinical experience.** *Magn Reson Imaging* 2016;34:1341–45 CrossRef Medline
- Gulani V, Calamante F, Shellock FG, et al; International Society for Magnetic Resonance in Medicine. **Gadolinium deposition in the brain: summary of evidence and recommendations.** *Lancet Neurol* 2017;16:564–70 CrossRef Medline
- Cheng HL. **Investigation and optimization of parameter accuracy in dynamic contrast-enhanced MRI.** *J Magn Reson Imaging* 2008;28:736–43 CrossRef Medline
- Calamante F, Connelly A, van Osch MJ. **Nonlinear ΔR effects in perfusion quantification using bolus-tracking MRI.** *Magn Reson Med* 2009;61:486–92 CrossRef Medline
- Pauling L, Coryell CD. **The magnetic properties and structure of hemoglobin, oxyhemoglobin and carbonmonoxyhemoglobin.** *Proc Natl Acad Sci U S A* 1936;22:210–16 CrossRef Medline
- Poublanc J, Sobczyk O, Shafi R, et al. **Perfusion MRI using endogenous deoxyhemoglobin as a contrast agent: preliminary data.** *Magn Reson Med* 2021;86:3012–21 CrossRef Medline
- Vu C, Chai Y, Coloigner J, et al. **Quantitative perfusion mapping with induced transient hypoxia using BOLD MRI.** *Magn Reson Med* 2021;85:168–81 CrossRef Medline
- Bhogal AA, Sayin ES, Poublanc J, et al. **Quantifying cerebral blood arrival times using hypoxia-mediated arterial BOLD contrast.** *Neuroimage* 2022;261:119523 CrossRef Medline
- Schulman JB, Sayin ES, Manalac A, et al. **DSC MRI in the human brain using deoxyhemoglobin and gadolinium: simulations and**

- validations at 3T. *Front Neuroimaging* 2023;2:1048652 CrossRef Medline
11. Sayin ES, Schulman J, Poublanc J, et al. **Investigations of hypoxia-induced deoxyhemoglobin as a contrast agent for cerebral perfusion imaging.** *Hum Brain Mapp* 2023;44:1019–29 CrossRef Medline
 12. Slessarev M, Han J, Mardimae A, et al. **Prospective targeting and control of end-tidal CO₂ and O₂ concentrations.** *J Physiol* 2007;581:1207–19 CrossRef Medline
 13. Fisher JA, Iscoe S, Duffin J. **Sequential gas delivery provides precise control of alveolar gas exchange.** *Respir Physiol Neurobiol* 2016;225:60–69 CrossRef Medline
 14. Cox RW. **AFNI: software for analysis and visualization of functional magnetic resonance neuroimages.** *Comput Biomed Res* 1996;29:162–73 CrossRef Medline
 15. Ashburner J, Friston K. **Multimodal image coregistration and partitioning—a unified framework.** *Neuroimage* 1997;6:209–17 CrossRef Medline
 16. Ashburner J, Friston KJ. **Unified segmentation.** *Neuroimage* 2005;26:839–51 CrossRef Medline
 17. Ostergaard L. **Principles of cerebral perfusion imaging by bolus tracking.** *Magn Reson Imaging* 2005;22:710–17 CrossRef
 18. Fantini S, Sassaroli A, Tgavalekos KT, et al. **Cerebral blood flow and autoregulation: current measurement techniques and prospects for noninvasive optical methods.** *Neurophotonics* 2016;3:031411 CrossRef Medline
 19. Quarles CC, Bell LC, Stokes AM. **Imaging vascular and hemodynamic features of the brain using dynamic susceptibility contrast and dynamic contrast enhanced MRI.** *Neuroimage* 2019;187:32–55 CrossRef Medline
 20. Kanda T, Ishii K, Kawaguchi H, et al. **High signal intensity in the dentate nucleus and globus pallidus on unenhanced T1-weighted MR images: relationship with increasing cumulative dose of a gadolinium-based contrast material.** *Radiology* 2014;270:834–41 CrossRef Medline
 21. Buxton RB, Frank LR, Wong EC, et al. **A general kinetic model for quantitative perfusion imaging with arterial spin labeling.** *Magn Reson Med* 1998;40:383–96 CrossRef Medline
 22. Mandell DM, Han JS, Poublanc J, et al. **Selective reduction of blood flow to white matter during hypercapnia corresponds with leukoariosis.** *Stroke* 2008;39:1993–98 CrossRef Medline
 23. van Gelderen P, de Zwart JA, Duyn JH. **Pitfalls of MRI measurement of white matter perfusion based on arterial spin labeling.** *Magn Reson Med* 2008;59:788–95 CrossRef Medline
 24. Harris AD, Murphy K, Diaz CM, et al. **Cerebral blood flow response to acute hypoxic hypoxia.** *NMR Biomed* 2013;26:1844–52 CrossRef Medline
 25. Mahamed S, Duffin J. **Repeated hypoxic exposures change respiratory chemoreflex control in humans.** *J Physiol* 2001;534:595–603 CrossRef Medline
 26. Mahamed S, Cunningham DA, Duffin J. **Changes in respiratory control after three hours of isocapnic hypoxia in humans.** *J Physiol* 2003;547:271–81 CrossRef Medline
 27. Ren X, Dorrington KL, Robbins PA. **Respiratory control in humans after 8 h of lowered arterial PO₂, hemodilution, or carboxyhemoglobinemia.** *J Appl Physiol (1985)* 2001;90:1189–95 CrossRef Medline
 28. Nakada Y, Canseco DC, Thet S, et al. **Hypoxia induces heart regeneration in adult mice.** *Nature* 2017;541:222–27 CrossRef Medline
 29. Almendros I, Wang Y, Gozal D. **The polymorphic and contradictory aspects of intermittent hypoxia.** *Am J Physiol Lung Cell Mol Physiol* 2014;307:L129–40 CrossRef Medline
 30. Serebrovskaya TV, Manukhina EB, Smith ML, et al. **Intermittent hypoxia: cause of or therapy for systemic hypertension?** *Exp Biol Med (Maywood)* 2008;233:627–50 CrossRef Medline
 31. Ghofrani HA, Voswinkel R, Reichenberger F, et al. **Hypoxia- and non-hypoxia-related pulmonary hypertension: established and new therapies.** *Cardiovasc Res* 2006;72:30–40 CrossRef Medline
 32. Navarrete-Opazo A, Mitchell GS. **Therapeutic potential of intermittent hypoxia: a matter of dose.** *Am J Physiol Regul Integr Comp Physiol* 2014;307:R1181–97 CrossRef Medline
 33. Ellingsen I, Hauge A, Nicolaysen G, et al. **Changes in human cerebral blood flow due to step changes in PAO₂ and PACO₂.** *Acta Physiol Scand* 1987;129:157–63 CrossRef Medline
 34. Mardimae A, Balaban DY, Machina MA, et al. **The interaction of carbon dioxide and hypoxia in the control of cerebral blood flow.** *Pflugers Arch* 2012;464:345–51 CrossRef
 35. Balaban DY, Duffin J, Preiss D, et al. **The in-vivo oxyhaemoglobin dissociation curve at sea level and high altitude.** *Respir Physiol Neurobiol* 2013;186:45–52 CrossRef Medline
 36. Battisti-Charbonney A, Fisher JA, Duffin J. **Respiratory, cerebrovascular and cardiovascular responses to isocapnic hypoxia.** *Respir Physiol Neurobiol* 2011;179:259–68 CrossRef Medline
 37. Calamante F, Yim PJ, Cebral JR. **Estimation of bolus dispersion effects in perfusion MRI using image-based computational fluid dynamics.** *Neuroimage* 2003;19:341–53 CrossRef Medline
 38. Lassen NA, Andersen AR, Friberg L, et al. **The retention of [99mTc]-d,l-HM-PAO in the human brain after intracarotid bolus injection: a kinetic analysis.** *J Cereb Blood Flow Metab* 1988;8:S13–22 CrossRef Medline
 39. Mouridsen K, Friston K, Hjort N, et al. **Bayesian estimation of cerebral perfusion using a physiological model of microvasculature.** *Neuroimage* 2006;33:570–79 CrossRef Medline
 40. Ostergaard L, Weisskoff RM, Chesler DA, et al. **High resolution measurement of cerebral blood flow using intravascular tracer bolus passages, Part I: mathematical approach and statistical analysis.** *Magn Reson Med* 1996;36:715–25 CrossRef Medline
 41. Ostergaard L, Chesler DA, Weisskoff RM, et al. **Modeling cerebral blood flow and flow heterogeneity from magnetic resonance residue data.** *J Cereb Blood Flow Metab* 1999;19:690–99 CrossRef Medline

The Choroid Plexus as an Alternative Locus for the Identification of the Arterial Input Function for Calculating Cerebral Perfusion Metrics Using MRI

Olivia Sobczyk, Ece Su Sayin, Julien Poublanc, James Duffin, Andrea Para, Joseph A. Fisher, and David J. Mikulis



ABSTRACT

BACKGROUND AND PURPOSE: MR imaging-based cerebral perfusion metrics can be obtained by tracing the passage of a bolus of contrast through the microvasculature of the brain parenchyma. Thus, the temporal signal pattern of the contrast agent is typically measured over a large artery such as the MCA to generate the arterial input function. The largest intracranial arteries in the brain may not always be suitable for selecting the arterial input function due to skull base susceptibility artifacts or reduced size from steno-occlusive disease. Therefore, a suitable alternative arterial input function window would be useful. The choroid plexus is a highly vascular tissue composed essentially of arterialized blood vessels and acellular stroma with low metabolic requirements relative to its blood flow and may be a suitable alternative to identify the arterial input function.

MATERIALS AND METHODS: We studied 8 healthy participants and 7 patients with gliomas who were administered a bolus of gadolinium. We selected an arterial input function from both the left and right M1 segments of the MCA and both lateral ventricles of the choroid plexus for each participant. We compared the changes in the T2* signal and the calculated resting perfusion metrics using the arterial input functions selected from the MCA and choroid plexus.

RESULTS: We found no systematic difference between resting perfusion metrics in GM and WM when calculated using an arterial input function from the MCA or choroid plexus in the same participant.

CONCLUSIONS: The choroid plexus provides an alternative location from which an arterial input function may be sampled when a suitable measure over an MCA is not available.

ABBREVIATIONS: AIF = arterial input function; CNR = contrast-to-noise ratio; CP = choroid plexus; ΔS = voxelwise T2* signal changes; GBCA = gadolinium-based contrast agent; rCBF = relative CBF; rCBV = relative CBV

Resting perfusion metrics including MTT, relative CBF (rCBF), and relative CBV (rCBV) in the cerebral parenchyma as measured with MR imaging, require the introduction of a DSC agent as a tracer. The time course of the resulting T2*-weighted signal reduction measured in a major cerebral artery such as the MCA during the first pass of the contrast bolus is used to generate the required arterial input function (AIF). The resting perfusion


metrics are calculated from the resulting signal change as the contrast agent passes through the microvasculature of the brain parenchyma, by applying the principles of tracer kinetic modeling. The idealized model is one of instantaneous entry of the contrast bolus into a voxel, ie, an impulse function.¹ However, in practice, a gadolinium-based contrast agent (GBCA) injected IV as a tight bolus becomes increasingly dispersed at the confluence of veins during centripetal flow and in the passage through the cardiac chambers before it arrives in the cerebral arteries. Despite the dispersion of the bolus of contrast, reasonably accurate blood flow metrics can be achieved through deconvolution of the AIF with the bolus-induced signal changes at the tissue level.


The MCA is the largest intracranial artery measuring up to 3.5 mm in diameter² and is responsible for most hemispheric blood flow. It is, therefore, the obvious choice for sampling the AIF. However, there are 2 issues that can confound accurate measurement of the AIF. The first is that the signal induced by the contrast is quadratic within the blood vessel and linear in the tissue outside the vessel.³ It was therefore suggested that voxels for

Received September 26, 2023; accepted after revision November 2.

From the Joint Department of Medical Imaging and the Functional Neuroimaging Lab (O.S., E.S.S., J.P., J.D., A.P., J.A.F., D.J.M.), University Health Network, Toronto, Ontario, Canada; Department of Anaesthesia and Pain Management (O.S., J.A.F.), University Health Network, University of Toronto, Toronto, Ontario, Canada; and Department of Physiology (E.S.S., J.D., J.A.F.), University of Toronto, Toronto, Ontario, Canada.

Please address correspondence to Joseph Fisher, MD, University Health Network, Toronto General Hospital, 200 Elizabeth St, Toronto, ON, Canada M5G 2C4; e-mail: joe.fisher@utoronto.ca

 Indicates open access to non-subscribers at www.ajnr.org

 Indicates article with online supplemental data.

<http://dx.doi.org/10.3174/ajnr.A8099>

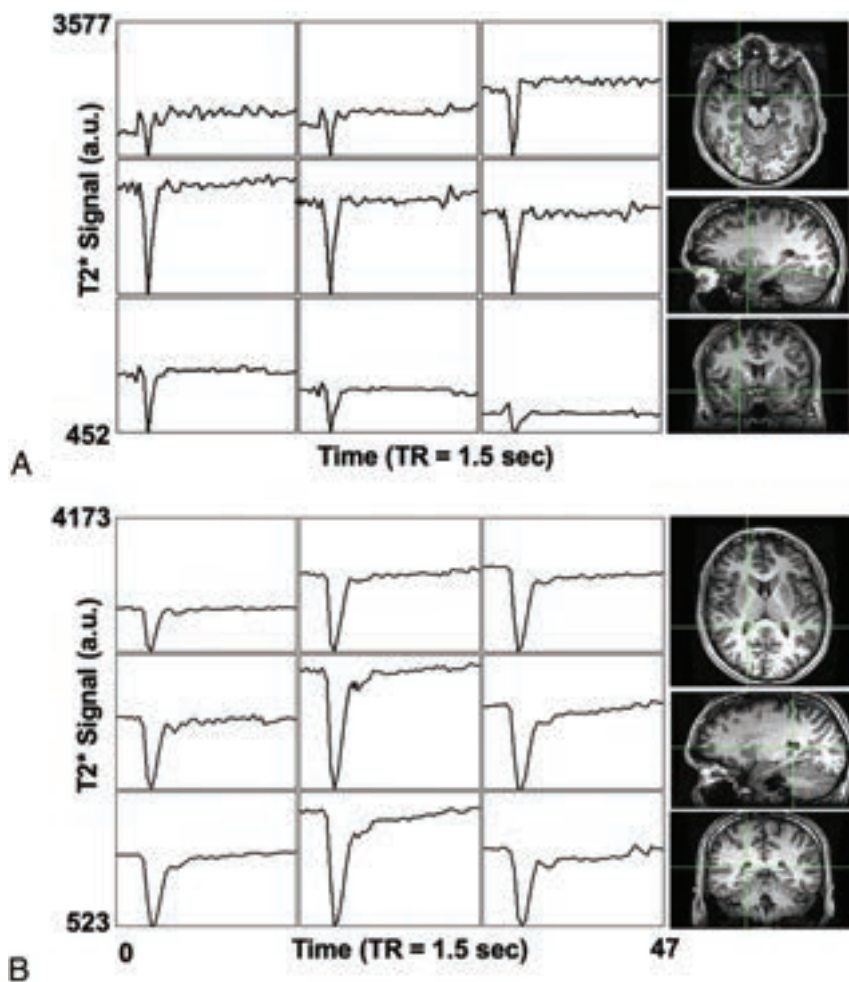


FIG 1. DSC voxel time-series in a representative healthy participant. The raw T2* signal time course in neighboring voxels adjacent to the MCA is shown in A and the CP in B. The green crosshairs in the T1 anatomical images show the corresponding locations of the center voxel in 3 planes for the MCA and CP AIF.

sampling the AIF should be immediately adjacent to, but not from within, the MCA.⁴ Voxel sizes are typically similar in size to the MCA, and maintaining placement proximity while avoiding signal averaging from IV extravascular signals can be difficult. The second issue is that in some instances, there are susceptibility effects at the skull base distorting the B₀ field homogeneity through which the major supply vessels must pass. The signal loss induced by these effects impairs accurate measurement of an AIF. As a result of these effects, it may not be possible to locate suitable voxels from which to obtain a reliable AIF in either MCA.

Here we explore a novel window from which to measure the AIF when MCAs are unsuitable for this purpose. In our experience of measuring increases of CBF in response to hypercapnia,⁵ we observed that there were no blood oxygen level-dependent signal changes in the choroid plexus (CP). This observation suggested that either the blood flow in the CP did not increase with hypercapnia (which is unlikely) or the CP did not contain venous blood that could be diluted by an increase in flow of arterial blood.^{6,7} The CP consists of small arteries embedded in an acellular matrix with an endothelium, which extracts little Oxygen relative to that available in the blood flow. We hypothesized that the

“arterialized” blood vessels in the CP would be well-suited to provide an AIF of similar quality to that of the MCA for measuring resting perfusion measures. To test this hypothesis, we compared the calculated resting relative perfusion metrics obtained from the CP with those obtained from the MCA in healthy participants and patients with gliomas.

MATERIALS AND METHODS

Participants and Ethics Approval

This study conformed to the standards set by the latest revision of the Declaration of Helsinki and was approved by the Research Ethics Board of the University Health Network. Eight healthy participants (6 men) between the ages of 23 and 60 (mean, 33.0 [SD, 15.34] years) and 7 patients (5 men) between the ages of 39 and 67 (mean, 46.29 [SD, 12.22] years) with gliomas were recruited. All healthy participants were nonsmokers, not taking any medications, and had no history of neurologic, cardiovascular, or kidney disease. All participants provided written, informed consent before scanning.

MR Imaging Protocol

Imaging in the healthy participants was acquired using a 3T HDx Signa system (GE Healthcare) with an 8-channel head coil. Patient images were acquired during their routine clinical scans and were obtained on the institution’s designated clinical scanner, a 3T Magnetom Vida system (Siemens) with a 32-channel head coil. Each participant underwent a protocol that consisted of a 3D T1-weighted sequence (~5.5 minutes) followed by a T2*-weighted sequence (~1.5 minutes) paired with an IV injection of GBCA. For the healthy participants, a 3D T1-weighted inversion recovery fast-spoiled gradient-recalled sequence was used with the following parameters: TI = 450 ms, TR = 7.88 ms, TE = 3.06 ms, flip angle = 12°, voxel size = 0.859 × 0.859 × 1 mm, matrix size = 256 × 256, 146 slices, FOV = 220 mm, no interslice gap. DSC data were acquired using a T2*-weighted gradient-echo echo-planar imaging sequence with the following parameters: TR = 1500 ms, TE = 30 ms, flip angle = 73°, 29 slices, voxel size = 3-mm isotropic, matrix size = 64 × 64. The patient group underwent a 3D T1-weighted MPRAGE (anatomical) sequence with the following parameters: TI = 900 ms, TR = 2200 ms, TE = 2.45 ms, flip angle = 8°, voxel size = 1 mm isotropic, matrix size = 256 × 256, 176 slices, FOV = 220 mm, no interslice gap. The DSC data for the patient group used T2*-weighted gradient EPI multiband sequence parameters: TR = 1750 ms, TE = 30 ms, flip angle = 80°, 56 slices, voxel size = 2.5 mm isotropic. During the DSC sequence for both groups, 5 mL

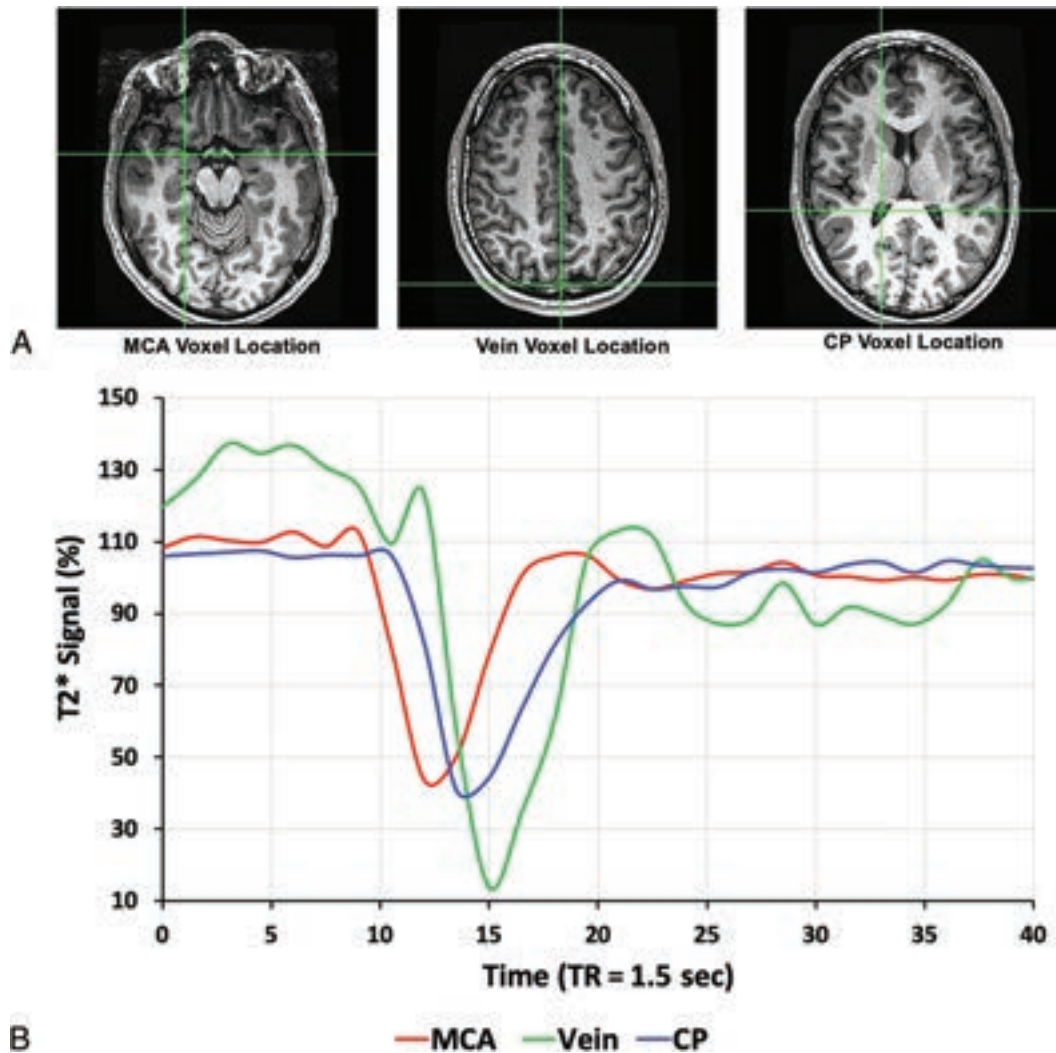


FIG 2. The scaled percentage signal changes across time after an injection of GBCA in the same healthy participant shown in Fig 1. A, The location of a voxel selected adjacent to the MCA, the superior sagittal sinus, and the CP. B, The scaled percentage signal change for each voxel as indicated in A.

of Gadovist (Bayer Schering Pharma) was injected IV at a rate of 5 mL/s (with no preload and a baseline delay of 30 seconds before injection) followed by 30 mL of saline at a rate of 5 mL/s.

Basic Data Analysis

The DSC images were first volume-registered, slice-time-corrected, and coregistered to their respective axial anatomical T1-weighted images using Analysis of Functional Neuroimaging software (National Institutes of Health).⁸ Analytic processing software (Statistical Parametric Mapping software [SPM8]) was used to segment the T1-weighted anatomical images into CSF, GM, and WM.⁹ The segmented masks for the patients with tumors included the nonenhancing tumor tissue and excluded the gadolinium-enhanced tissue.

AIF Selection

A cluster of 6–8 voxels from both the left and right M1 segments of the MCA (AIF-MCA) and both trigones of the lateral ventricles of the CP (AIF-CP) with the largest signal change were

selected manually. From this cluster of voxels, the lowest full width at half maximum signal was chosen as the AIF. A total of 4 suitable AIFs were selected from the left and right MCAs (AIF-MCA1, AIF-MCA2) and from the left and right CP (AIF-CP1, AIF-CP2) for subsequent DSC analysis. MCA and CP voxel locations were confirmed by a neuroradiologist (D.J.M.).

Calculation of Contrast

Voxelwise T2* signal changes (ΔS) were calculated as the ratio of the difference between the signal at each timepoint (S) minus the minimum intensity (min [S]) divided by the baseline mean (\bar{S}) (Equation 1):

$$1) \quad \Delta S = \left(\frac{S - \min(S)}{\bar{S}} \right) \times 100\%.$$

Signal variability in the MCA and CP AIFs was examined in the selected voxels. The percentage standard deviation (ΔSD) of the percentage signal changes (ΔS) was then calculated, and the

Table 1: ΔS , CNR, and coefficient of variation (mean \pm standard error of the mean) indices associated with the GBCA bolus time courses in the right-versus-left MCA and CP

	Factor	ΔS (%)	CNR
Mean coefficient of variation (%)	Between MCA AIFs	9 (SD, 3)	22 (SD, 3)
	Between CP AIFs	11 (SD, 3)	24 (SD, 5)

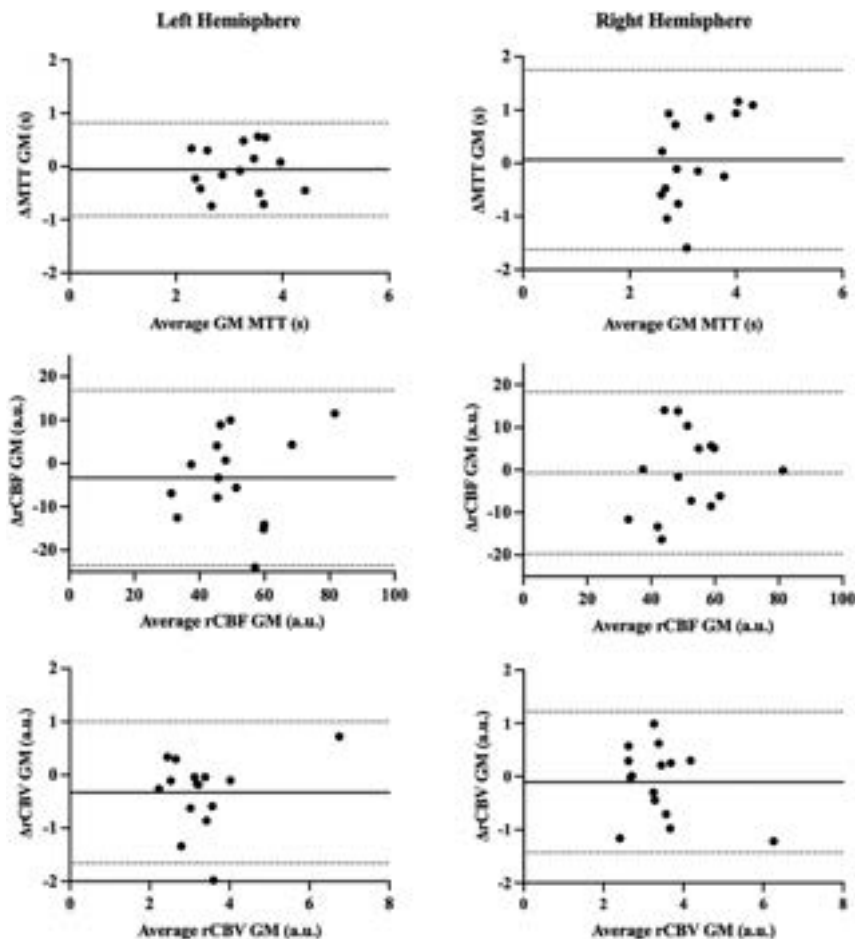


FIG 3. Bland-Altman plots comparing GM perfusion metrics (MTT, rCBF, and rCBV) calculated using the MCA AIF and CP AIF selected from the left and right hemispheres. Δ GM perfusion metrics (MTT, rCBF, and rCBV) = AIF MCA – AIF CP. The solid line depicts bias, and the dashed lines show the 95% upper and lower limits of agreement as the mean difference.

contrast to noise ratio (CNR) was determined for each of the selected AIFs using the following equation:

$$2) \quad CNR = \frac{\Delta S}{\Delta SD}.$$

Calculating Resting Perfusion Metrics

To account for arrival delay, we manually time-shifted the selected AIF-CP by approximately 1.4 seconds, the average time delay found between the T2* signal AIF-CP and AIF-MCA across all subjects. This step aligned the AIF-CP with the corresponding AIF-MCA. The T2* signal was converted to tissue concentration (R2*) as per Equation 3. Standard tracer kinetic modeling was used to calculate MTT and rCBV for both AIF selections, using the following parametrized method for deconvolving and fitting the residue function with an exponential as per Equation 4:

$$3) \quad C(t) \propto \Delta R2^* = \frac{1}{TE} \times \ln \frac{S(t)}{S_0},$$

$$4) \quad R2^* = \frac{rCBV}{MTT} \times C_{AIF} \otimes R_t.$$

$R_t = e^{-\frac{t}{MTT}}$ represents the residue function. MTT and rCBV were determined using a least squares fitting procedure with MTT bound between 1 and 8 seconds. This method is described in greater detail in Poublanc et al.¹⁰

rCBF was calculated using the central volume theorem according to the following equation:

$$5) \quad rCBF = \frac{rCBV}{MTT}.$$

DSC perfusion maps were generated and overlaid onto their respective anatomical images. Average values for MTT, rCBF, and rCBV were calculated for GM and WM excluding values of >3 SDs as outliers that are assumed to be from noise and partial volume effects (MTT from 1 to 8 seconds; rCBF from 0 to 120 a.u. and rCBV from 0 to 10 a.u.).

Statistical Analysis

Statistical comparisons were performed within the healthy volunteer and patient groups on the ΔS and CNR calculated for each selected voxel (AIF-MCA1, AIF-MCA2, AIF-CP1, AIF-CP2) using a 1-way analysis of variance with an all pair-wise multiple comparisons correction (Holm-Sidak method) and $\alpha = .05$ (Prism 9 software; GraphPad). Each of the selected AIFs were used to calculate MTT, rCBF, and rCBV. The coefficient

of variation, defined as the SD divided by the mean, was calculated among the ΔS , CNR, and perfusion metrics determined between the 2 AIFs chosen in the MCA and CP, independently. Statistical comparisons within each were performed on average MTT, rCBF, and rCBV values for GM and WM among the multiple locations in the MCA and CP using a 1-way analysis of variance with an all pair-wise multiple comparisons correction (Holm-Sidak method) with $\alpha = .05$. From the means of the calculated GM and WM perfusion averages, Bland-Altman plots were generated comparing the multiple locations in the MCA and CP.

RESULTS

AIF T2* Signals

The MCA and CP DSC signal magnitude and time course were similar in all subjects. Figure 1 illustrates signal changes in

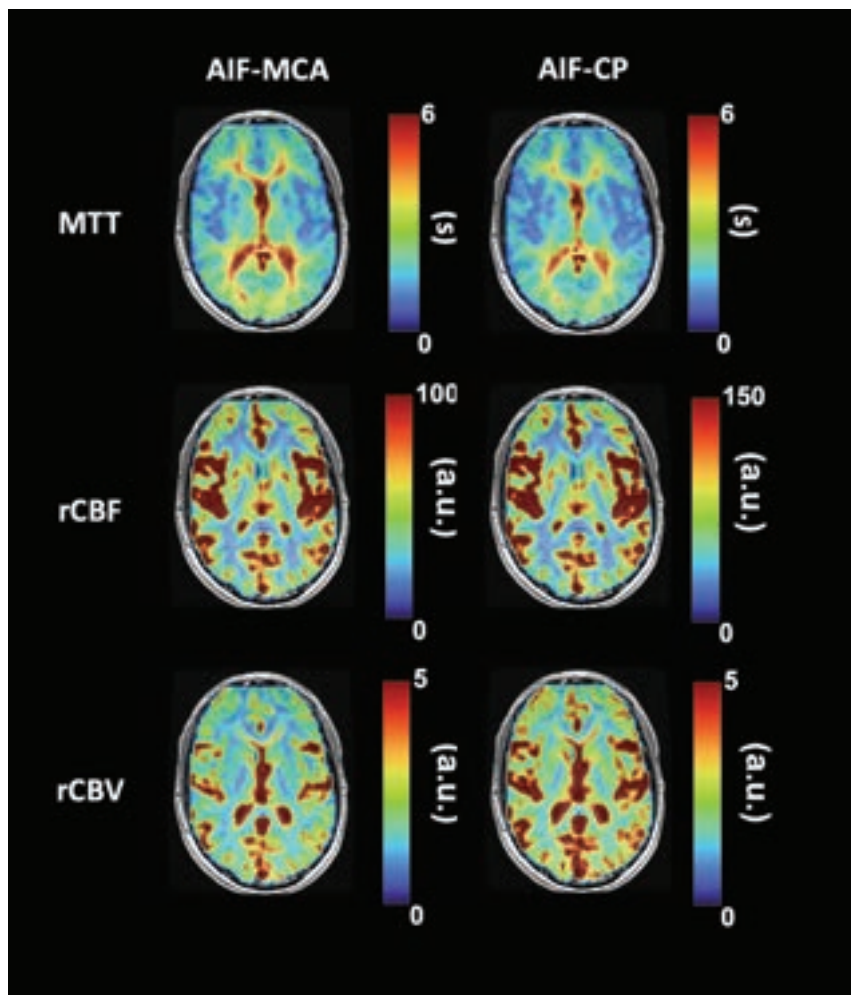


FIG 4. Maps of resting perfusion metrics for the healthy participant shown in Figs 1 and 2, calculated using an AIF from both the MCA and CP.

contiguous voxels in the vicinity of the MCA and from the CP in a representative healthy participant. The temporal signal change in the CP AIF followed that of the MCA AIF, preceding a voxel T2* signal change located in a vein (Fig 2).

AIF T2* Signal Comparisons

The T2* signal variability (percentage coefficient of variation) within and between the right and left MCA and CP AIF locations is presented in Table 1. The AIF 1-way analysis of variance factoring the AIF location (right and left MCA and CP) found no significant differences among any of these locations for ΔS and CNR in both groups. Each participant's ΔS and CNR for the 4 AIF locations are found in the Online Supplemental Data.

Resting Perfusion Metrics

The 1-way analysis of variance comparison of resting perfusion measures for GM and WM factoring the AIF location (right MCA AIF, left MCA AIF, right CP AIF, left CP AIF) found no significant differences among any of these locations for MTT, rCBF, and rCBV in both groups. Each participant's average perfusion measures for GM and WM for the 4 AIF locations are found in the Online Supplemental Data. Bland-Altman plot

analysis comparing the difference between perfusion metrics calculated using the MCA and CP (MCA1 versus CP1 and MCA2 versus CP2) in GM is presented in Fig 3 (WM plots are found in the Online Supplemental Data). Bland-Altman plot analysis comparing the variability between perfusion metrics using AIFs within the same location (MCA1 versus MCA2 and CP1 versus CP2) is presented in the Online Supplemental Data. The Bland-Altman plots have negligible constant bias or proportional bias among the AIF location choices.

Figures 4 and 5 illustrate the pattern and distribution of resting perfusion measures in a healthy volunteer and a patient with a glioma for an AIF selected in the MCA and CP. Each resting perfusion measure variability for GM and WM within and between the chosen AIF locations is summarized in Table 2.

DISCUSSION

Main Findings

The main finding of this study is that there were no systematic differences in resting cerebral perfusion metrics calculated from an AIF measured at either the MCA or CP. These findings suggest that an AIF chosen from within the CP is comparable with one chosen from the MCA and may, therefore, be a useful

alternative when there is no suitable MCA location to interrogate, for example, due to susceptibility artifacts at the skull base. An AIF selected from the CP is easier to acquire because of its larger size relative to the MCA and its location in a homogeneous magnetic environment. In addition, an AIF from the CP can be more consistently localized than the MCA as shown in Fig 1. It is therefore less sensitive to voxel placement for assessing signal changes induced by the passage of the contrast bolus.

AIF from the MCA versus the CP

Unlike CT perfusion in which a bolus of iodinated contrast agent shows a linear relationship between the concentration and x-ray attenuation, the signal intensity changes induced with GBCA are more complex. The pulse sequence used to acquire flow information following the administration of a bolus of GBCA measures the magnetic susceptibility effects of GBCA in the blood and in the adjacent tissue. The intravascular signal change with concentration is known to be quadratic,¹¹ whereas the extravascular signal effects are linear. Therefore, the signal changes in a voxel used to measure the AIF will depend on the percentage of arterial blood in the voxel. In an ideal setting, the susceptibility would arise from outside the voxel and remain linear

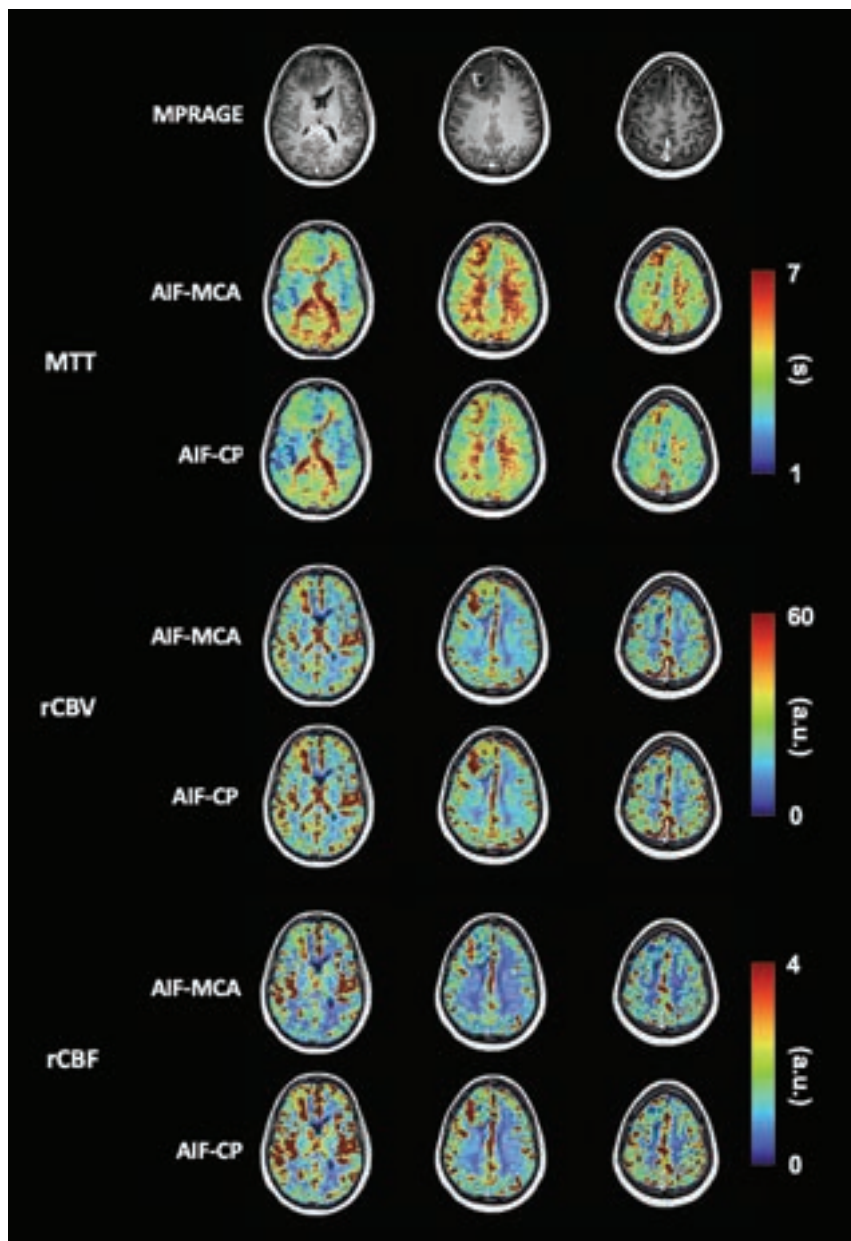


FIG 5. Perfusion maps calculated using an AIF selected from both the MCA and the CP for a patient with a right frontal high-grade glioblastoma. Also shown are the patient's T1-weighted MPRAGE images. Note that leakage correction was not used.

with GBCA concentration. The MCAs are located at the skull base where there are susceptibility effects generated by aerated paranasal sinuses that can obscure the vessels of interest. The position of the CP, on the other hand, is sufficiently distant from the skull base to be in a homogeneous B_0 magnetic environment and can provide optimal voxel selection for measuring an AIF (Fig 1).

Several features of the CP, nevertheless, require additional consideration. The high amplitude of the AIF obtained from the CP may be attributed to the CP vessels remaining highly arterialized throughout their course, having a high flow comparable with that of other arteries. Furthermore, the extensive arterialization of CP vessels also produces a uniform $T2^*$ signal change.¹² The pattern of contrast that is taken as the AIF is maintained (ie, not

disrupted or dispersed) with successive branching of the arteries. In the case of an upstream stenosis, there should be no disruption of the AIF unless there is also collateral blood flow, which would then distort the AIF. This principle would be true, and thus limiting, for intracranial perfusion patterns distal to the MCA as well. The CP AIF was identified from the glomus of the CP.

There is a slight delay of AIF in the CP compared with the MCA because the path to the CP is longer than that to the MCA (Fig 2B). The MCA is a primary supply artery as opposed to the CP, which is a branch vessel with inherently longer blood-arrival times. Time-shifting of the selected AIF CP signal curves was required to align with the signal curves from the MCA to account for this delay.

Resting Perfusion Metrics Maps

In the maps presented in Fig 4, the rCBF scales differ between those using an MCA AIF and those using a CP AIF. This scaling difference arises because the rCBF and rCBV were not scaled to actual values but to show the range of values and emphasize the similarity in the spatial pattern of contrast. Consequently, the resting perfusion metrics maps based on AIFs for either the MCA or the CP generate the same pattern of MTT and rCBV when compared. By contrast, rCBF is presented with the same scale for maps calculated with AIFs from the MCA or the CP because it is calculated as the ratio of rCBV/MTT.

Limitations

The use of the CP for an AIF can be compromised by large cysts, calcifications, and xanthogranulomas, which represent desquamated epithelium into choroid plexus cysts.¹³ Selecting a CP AIF with calcifications and cysts would decrease the amplitude of the AIF but would not prevent its application. We suspect that these histologic variations would not induce major changes in the homogeneity of B_0 to substantially alter the AIF calculation, but a larger series of subjects will be required for confirmation. Although there are other locations where the CP can be found, they are often not of sufficient size for selecting an AIF. CP-derived AIF may be confounded by partial volume effects. However, partial volume effects are less likely to occur in the CP because the structure is larger than the voxel size used, limiting the potential partial volume effects from adjacent CSF and/or

Table 2: Coefficient of variation between resting perfusion measures (MTT, rCBF, and rCBV) calculated using AIFs from the right-versus-left MCA and right-versus-left CP in the GM and WM

	Factor	MTT (s)		rCBF (a.u)		rCBV (a.u)	
		GM	WM	GM	WM	GM	WM
Mean coefficient of variation (%)	Between MCA AIFs	14 (SD, 2)	12 (SD, 2)	9 (SD, 2)	11 (SD, 2)	11 (SD, 2)	13 (SD, 3)
	Between CP AIFs	6 (SD, 2)	5 (SD, 1)	9 (SD, 2)	16 (SD, 5)	11 (SD, 2)	12 (SD, 2)

cerebral tissue. Finally, comparing MCA-versus-CP AIF perfusion metrics against CBF metrics acquired using the current criterion standard Oxygen-15 labeled water PET CBF would be informative in ranking the accuracy of the 2 AIF selection methods.

The segmented masks used to calculate perfusion metrics for the patients with tumors excluded the gadolinium-enhanced tumor tissue, where effects of contrast leakage would confound flow measures. However, if this method were to be implemented clinically, existing leakage-correction methodologies including a low-preload-dose gadolinium injection,¹⁵ low flip angle gradient-echo,¹⁴ or a tissue residue function correction¹⁶ should be applied. As an additional note, Fig 1 shows that the signal baseline in the CP before the GBCA bolus and after it did not change. Gadolinium leakage occurs over a longer time scale than the passage of an initial Gadovist preload dose and whatever leakage that did occur was insufficient to shorten the T1 relaxation and therefore will not influence the AIF.

CONCLUSIONS

The findings from this study demonstrates that the selection of an AIF from the CP yields hemodynamic measures similar to those when selecting an AIF from the MCA. A CP AIF may be a useful alternative when the MCA is unsuitable for this purpose.

Disclosure forms provided by the authors are available with the full text and PDF of this article at www.ajnr.org.

REFERENCES

- Lee D, Le TT, Im GH, et al. **Whole-brain perfusion mapping in mice by dynamic BOLD MRI with transient hypoxia.** *J Cereb Blood Flow Metab* 2022;42:2270–86 CrossRef Medline
- Idowu O, Shokunbi M, Malomo A, et al. **Size, course, distribution and anomalies of the middle cerebral artery in adult Nigerians.** *East Afr Med J* 2002;79:217–20 CrossRef Medline
- Bleeker EJ, van Buchem MA, van Osch MJ. **Optimal location for arterial input function measurements near the middle cerebral artery in first-pass perfusion MRI.** *J Cereb Blood Flow Metab* 2009;29:840–52 CrossRef Medline
- Calamante F. **Arterial input function in perfusion MRI: a comprehensive review.** *Prog Nucl Magn Reson Spectrosc* 2013;74:1–32 CrossRef Medline
- Hoiland RL, Fisher JA, Ainslie PN. **Regulation of the cerebral circulation by arterial carbon dioxide.** *Compr Physiol* 2019;9:1101–54 CrossRef Medline
- Hoge RD, Atkinson J, Gill B, et al. **Investigation of BOLD signal dependence on cerebral blood flow and oxygen consumption: the deoxyhemoglobin dilution model.** *Magn Reson Med* 1999;42:849–63 CrossRef Medline
- Davis MJ, Hill MA, Kuo L. **Local regulation of microvascular perfusion.** In: Tuma RF, Duran WN, Ley K. *Microcirculation*. 2nd ed. Academic Press, Wiley; 2008:161–284
- Cox RW. **AFNI: software for analysis and visualization of functional magnetic resonance neuroimages.** *Comput Biomed Res* 1996;29:162–73 CrossRef Medline
- Ashburner J, Friston KJ. **Unified segmentation.** *Neuroimage* 2005;26:839–51 CrossRef Medline
- Poublanc J, Sobczyk O, Shafi R, et al. **Perfusion MRI using endogenous deoxyhemoglobin as a contrast agent: preliminary data.** *Magn Reson Med* 2021;86:3012–21 CrossRef Medline
- Uludağ K, Müller-Bierl B, Uğurbil K. **An integrative model for neuronal activity-induced signal changes for gradient and spin echo functional imaging.** *Neuroimage* 2009;48:150–65 CrossRef
- Faraci FM, Heistad DD, Mayhan WG. **Role of large arteries in regulation of blood flow to brainstem in cats.** *J Physiol* 1987;387:115–23 CrossRef Medline
- Gaillard F, Anan R, Skandhan A. **Choroid plexus xanthogranuloma.** <https://radiopaedia.org/articles/choroid-plexus-xanthogranuloma>.
- Schminda KM, Prah MA, Hu LS, et al. **Moving toward a consensus DSC-MRI protocol: validation of a low-flip angle single-dose option as a reference standard for brain tumors.** *AJNR Am J Neuroradiol* 2019;40:626–33 CrossRef Medline
- Bell LC, Hu LS, Stokes AM, et al. **Characterizing the influence of preload dosing on percent signal recovery (PSR) and cerebral blood volume (CBV) measurements in a patient population with high-grade glioma using dynamic susceptibility contrast MRI.** *Tomography* 2017;3:89–95 CrossRef Medline
- Bjornerud A, Sorensen AG, Mouridsen K, et al. **T1- and T2*-dominant extravasation correction in DSC-MRI, Part I: theoretical considerations and implications for assessment of tumor hemodynamic properties.** *J Cereb Blood Flow Metab* 2011;31:2041–53 CrossRef Medline

CTA and CTP for Detecting Distal Medium Vessel Occlusions: A Systematic Review and Meta-analysis

João André Sousa, Anton Sondermann, Sara Bernardo-Castro, Ricardo Varela, Helena Donato, and João Sargento-Freitas



ABSTRACT

BACKGROUND: The optimal imaging method for detecting distal medium vessel occlusions (DMVOs) remains undefined.

PURPOSE: The objective of this study is to compare the diagnostic performance of CTA with CTP in detecting DMVOs.

DATA SOURCES: We searched PubMed, EMBASE, Web of Science Core Collection, and Cochrane Central Register of Controlled Trials up to March 31, 2023 (PROSPERO: CRD42022344006).

STUDY SELECTION: A total of 12 studies reporting accuracy values of CTA and/or CTP were included, comprising 2607 patients with 479 cases (18.3%) of DMVOs.

DATA ANALYSIS: Pooled sensitivity and specificity of both imaging methods were compared using a random-effects model. Subgroup analyses were performed based on the technique used in CTA (multi or single-phase) and the subtype of DMVOs (M2-only vs. M2 and other DMVOs). We applied Quality Assessment of Diagnostic Accuracy (QUADAS-2) tool and Grading of Recommendations, Assessment, Development and Evaluation (GRADE) quality assessment criteria.

DATA SYNTHESIS: CTA demonstrated significantly lower sensitivity compared to CTP in detecting DMVOs [0.74, 95%CI (0.63–0.82) vs. 0.89, 95% CI (0.82–0.93), $P < 0.01$]. When subgrouped into single-phase and multi-phase CTA, multi-phase CTA exhibited higher sensitivity for DMVO detection than single-phase CTA [0.91, 95%CI (0.85–0.94) vs. 0.64, 95%CI (0.56–0.71), $P < .01$], while reaching similar levels to CTP. The sensitivity of single-phase CTA substantially decreased when extending from M2 to other non-M2 DMVOs [0.74, 95%CI (0.63–0.83) vs. 0.61, 0.95%CI (0.53–0.68), $P = .02$].

LIMITATIONS: We identified an overall high risk of bias and low quality of evidence, attributable to the design and reference standards of most studies.

CONCLUSIONS: Our findings highlight a significantly lower sensitivity of single-phase CTA compared to multi-phase CTA and CTP in diagnosing DMVOs.

ABBREVIATIONS: DMVO = distal medium vessel occlusion; EVT = endovascular treatment; GRADE = Grading of Recommendations, Assessment, Development and Evaluation; mpCTA = multiphase CT angiography; QUADAS-2 = Quality Assessment of Diagnostic Accuracy; SCA = superior cerebellar artery; spCTA = single-phase CTA; Tmax = time-to-maximum

Distal medium vessel occlusions (DMVOs),¹ also known as medium vessel occlusions,² refer to the occlusion of arteries with diameters ranging from 0.75 to 2.0 mm. This term generally encompasses segments M2 to M4 of the MCA, A2 to A5 of the anterior cerebral artery, P2 to P5 of the posterior

cerebral artery, the PICA, AICA, and superior cerebellar artery (SCA).¹


Acute ischemic stroke imaging workflows have been designed to efficiently detect large-vessel occlusions suitable for endovascular treatment (EVT), which is increasingly being offered in DMVOs.³ Noncontrast CT and CTA, without advanced imaging techniques, have been used to identify candidates for EVT, even

Received August 3, 2023; accepted after revision October 31.

From the Neurology Department (J.A.S., S.B.-C., J.S.-F.) and Documentation and Scientific Information Service (H.D.), Centro Hospitalar e Universitário de Coimbra, Coimbra, Portugal; Neurogeriatrie Department (A.S.), Christian-Albrechts-Universität zu Kiel, Kiel, Germany; Faculdade de Medicina da Universidade de Coimbra (S.B.-C., J.S.-F.), Coimbra, Portugal; and Neurology Department (R.V.), Centro Hospitalar e Universitário de Santo António, Porto, Portugal.

J.A. Sousa and A. Sondermann contributed equally and should be listed as co-first authors.

Please address correspondence to João André Sousa, MD, Neurology Department, Centro Hospitalar e Universitário de Coimbra, Praceta Mota Pinto, 3000, Coimbra, Portugal; e-mail: sousajoaandre@gmail.com; @sousajoaandre

 Indicates article with online supplemental data.
<http://dx.doi.org/10.3174/ajnr.A8080>

in the late window.^{4,5} In contrast, CTP may be time-consuming and is not widely used, particularly in the early window and in primary stroke centers.⁶ However, incorporating CTP into imaging protocols could improve the detection and, therefore, the treatment of DMVOs, for which the optimal imaging approach is yet to be determined.

The aim of this study was to conduct a systematic review and meta-analysis of diagnostic test accuracy for CTA and CTP in the detection of DMVOs.

MATERIALS AND METHODS

This study was conducted in accordance with the Preferred Reporting Items for Systematic Reviews and Meta-Analyses (PRISMA) statement.⁷ We registered this study in PROSPERO (<https://www.crd.york.ac.uk/PROSPERO/>) (CRD42022344006) and published a comprehensive protocol detailing the methods.⁸ Because this a secondary study, no ethics approval was requested. We did not receive any funding or financial support. Aggregate data generated by this study will be available on reasonable request.

Search Strategy, Selection, and Data Collection

We conducted a systematic search of the PubMed (including MEDLINE), EMBASE, Web of Science Core Collection, and Cochrane Central Register of Controlled Trials to identify relevant primary studies reporting on the diagnostic accuracy of CTA and/or CTP (interpreted in conjunction with CTA or separately) for the detection of DMVOs. The search was performed from the inception of the databases until March 31, 2023. We used various combinations of the following terms: “acute ischemic stroke,” “distal vessel occlusion,” “medium vessel occlusion,” “distal medium vessel occlusion,” “M2,” “M3,” “M4,” “A2,” “A3,” “A4,” “A5,” “P2,” “P3,” “P4,” “P5,” “posterior inferior cerebellar artery,” “PICA,” “anterior inferior cerebellar artery,” “AICA,” “superior cerebellar artery” or “SCA” artery occlusions, “CT angiography,” “CT perfusion,” “perfusion imaging” and database-specific subject headings (eg, Medical Subject Headings [MeSH] terms). Detailed search strategies for each database can be found in the published protocol.⁸ We also scanned gray literature, references of selected studies, and reviews on the subject for missing articles.

Two authors (J.A.S. and A.S.) independently reviewed articles retrieved from the systematic search performed. We collected the following variables: study design, date, authors, index and reference tests, sample size, location of DMVOs, and either individual data or summary estimates of sensitivity, specificity and, when available, the number of true-positive, true-negative, false-positive, false-negative, positive predictive values, and negative predictive values of CTA and/or CTP. Data extracted were reviewed and validated by a third reviewer (S.B.C.).

Quality of Evidence and Risk of Bias

Two investigators assessed the risk of bias for each individual study independently (J.A.S. and A.S.) via the Quality Assessment of Diagnostic Accuracy (QUADAS-2) tool.⁹ We used Grading of Recommendations, Assessment, Development and Evaluation (GRADE) quality assessment criteria for diagnostic accuracy

studies.^{10,11} To assess publication bias, we performed a funnel plot and a complementary Deek test.¹²

Data Synthesis and Statistical Analysis

The statistical analysis was performed following the *Cochrane Handbook for Systematic Reviews of Interventions*.¹³ A bivariate model was used to combine sensitivity and specificity data and calculate 95% confidence regions around the summary operating points. The consistency and heterogeneity of the included studies were assessed using the Higgins I^2 statistic (low heterogeneity, $\leq 25\%$; moderate, between 25% and 50%; and high, $>75\%$). Data synthesis was performed using a random effects model to provide a more conservative estimate of the overall diagnostic performance.

Subgroup Analysis

We divided the studies on the basis of whether they used single-phase CTA (spCTA) or multiphase CTA (mpCTA). Additionally, we categorized the studies on the basis of the occlusion site composition of their study samples because 2 subgroups were clearly identified. The first included studies exclusively included M2 occlusions in their DMVO samples, while the second subgroup included studies with more heterogeneous samples, encompassing various types of DMVOs.

RESULTS

We identified 5378 unique studies. Twelve studies met the inclusion criteria for our analysis. The PRISMA flow chart is presented in Fig 1. The selected studies, summarized in the Online Supplemental Data, involved a total of 2607 patients, among whom 479 (18.3%) were identified as having DMVOs. The distribution of DMVOs is presented in the Table, with a predominance of M2 occlusions observed (312 patients, 65.1%). Eight studies¹⁴⁻²¹ included patients with acute ischemic stroke within 24 hours of symptom onset, two^{22,23} within 12 hours, and two^{24,25} within 9 hours. The evaluation of the images involved >79 different readers with varying levels of experience. All studies¹⁴⁻²⁵ provided information on CTA. Two studies investigated the combination of CTP and spCTA versus spCTA only;^{15,19,24} 1 study compared CTP with spCTA and separately tested the diagnostic accuracy of CTP alone.²⁰ Eleven studies^{14-22,24,25} provided data on spCTA, and 4 studies^{14,21-23} provided data on mpCTA. Between-study heterogeneity was observed in the sensitivity of the CTA studies ($I^2 = 70\%$, $P < .01$), while the heterogeneity was low in the CTP studies ($I^2 = 0\%$, $P = .81$).

QUADAS-2 and GRADE revealed an overall high risk of bias and a low quality of evidence (Online Supplemental Data). The funnel plot (Online Supplemental Data), along with Deek test, did not reveal any publication bias for the studies reporting on CTA (Deek: $t = -0.09$, $df = 13$, P value = .93). In the case of CTP studies, the Deek test could not be performed (<10 studies).

In all studies that used CTP, including one exclusively with an M2 occlusion sample,¹⁵ diagnostic accuracy in the detection of DMVOs was significantly higher compared with spCTA using either CTP alone through territorial time-to-maximum (Tmax) evaluation¹⁹ or CTP in a combination with spCTA (Online Supplemental Data).^{15,24} The specificity remained similar. Three studies directly compared the accuracy of DMVO detection in

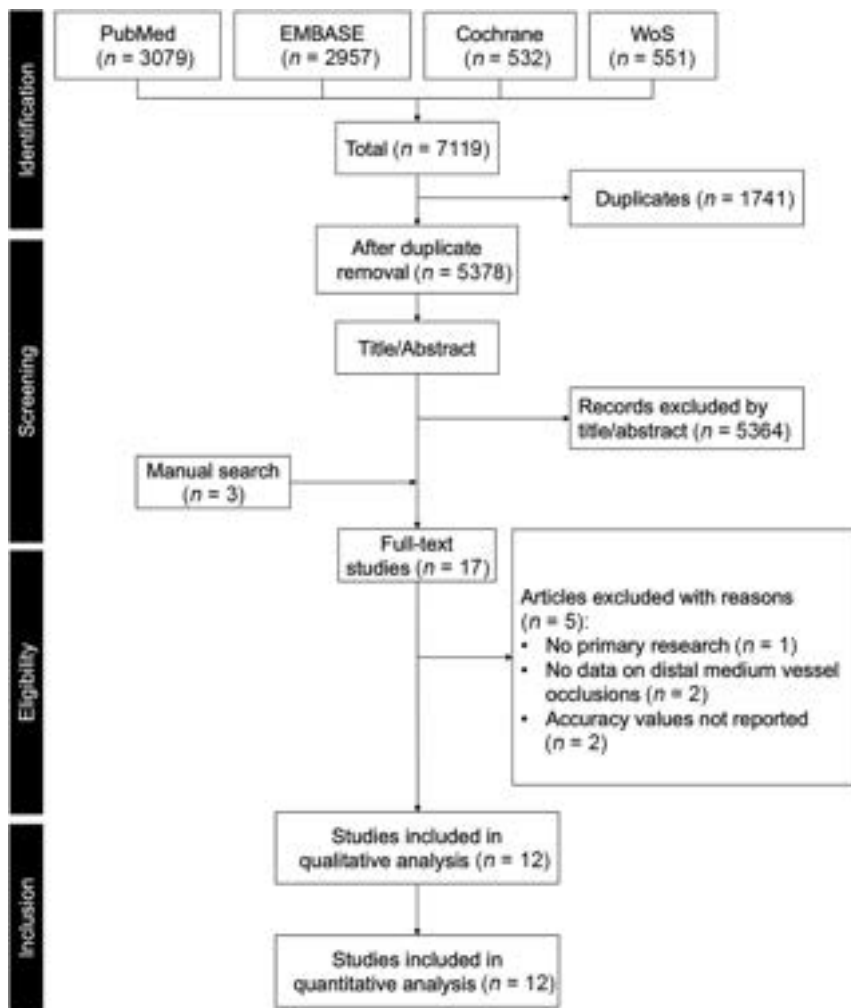


FIG 1. PRISMA flow chart.

Distribution of the DMVOs assessed in the selected studies

Characteristics	n = 2607
DMVOs (No.) (%)	479 (18.3)
Type of DMVO	
M2 (No.) (%)	312 (65.1)
M3/M4 (No.) (%)	52 (10.9)
A2/A3/A4 (No.) (%)	23 (4.8)
P2/P3/P4 (No.) (%)	42 (8.8)
PICA (No.) (%)	2 (0.42)
SCA (No.) (%)	1 (0.21)
Unspecified without M2 ^a	24 (5.0)
Unspecified with M2 ^b	23 (4.8)

^a M3, M4, anterior cerebral artery, A2, A3, posterior cerebral artery, P2, P3, P4, PICA, SCA.

^b M2, M3, A2, A3.

spCCTA versus mpCCTA. Of these, two^{14,22} reported improved accuracy as well as shorter detection times when mpCCTA was used. One that evaluated only M2 occlusions²¹ reported no differences (Online Supplemental Data).

In the meta-analysis, we observed that CTA had significantly lower sensitivity than CTP for the detection of DMVO (0.74; 95% CI, 0.63–0.82 versus 0.89; 95% CI, 0.82–0.93; $P < .01$) (Fig 2, part A). Subgroup analysis revealed that mpCCTA had significantly

higher sensitivity for DMVO detection compared with spCCTA (0.91; 95% CI, 0.85–0.94 versus 0.64; 95% CI, 0.56–0.71; $P < .01$) (Fig 2, part B), while achieving levels similar to those of CTP (0.91; 95% CI, 0.85–0.94 versus 0.89; 95% CI, 0.83–0.93; $P = .68$) (Fig 2, parts A and B). A pooled analysis including mpCCTA and CTP (Online Supplemental Data) studies showed high sensitivity (0.90; 95% CI, 0.86–0.93) compared with spCCTA (0.64; 95% CI, 0.56–0.71; $P < .01$). The specificity analysis did not reveal any differences except when comparing the specificity of CTA + CTP versus CTP-only (territorial Tmax) 0.98; (95% CI, 0.93–0.99) versus 0.88 (95% CI, 0.84–0.91; $P < .019$).

When comparing accuracy values provided by studies that included only M2 occlusions and those that included other DMVOs as well, we observed a significant decrease in sensitivity including non-M2 DMVO occlusions through spCCTA (0.74; 95% CI, 0.63–0.83 versus 0.61; 95% CI, 0.53–0.68; $P = .04$) (Fig 3 part A). This decline in sensitivity did not occur with either mpCCTA or the inclusion of CTP (Fig 3, parts B and C).

Also, the pooled sensitivity of the 3 spCCTA studies^{15,17,21} that included only M2 occlusions was 0.74 (95% CI, 0.63–0.83). In contrast, the sensitivity of the single M2-only CTP study¹⁵ was 0.91 (95% CI, 0.79–0.98; $P = .03$).

DISCUSSION

Our study provides consistent evidence for a higher sensitivity in detecting DMVO with mpCCTA or CTP compared with spCCTA (with or without cross-reference to spCCTA). This study represents the first systematic review specifically addressing the diagnosis of this subtype of acute ischemic stroke.

The pooled sensitivity of spCCTA from 4 studies that included only M2 occlusions^{15,18,21,25} was higher than the sensitivity of spCCTA retrieved from 8 studies^{14,16,17,19,20,22–24} that included other vessels within their DMVO sample. This finding indicates the challenge of detecting occlusions beyond the M2 territory using this imaging method. Most interesting, this decrease in sensitivity from M2-only to M2 + other DMVOs studies does not appear to occur in mpCCTA or CTP. However, it is important to exercise caution when interpreting these findings because there was a single M2-only study with CTP²¹ and only one with mpCCTA.¹⁵

Even when restricting the analysis to M2-only studies, the comparison among the pooled sensitivity of 3 studies with spCCTA with 1 CTP study favors the latter. This finding, while acknowledging the limitations imposed by the number of

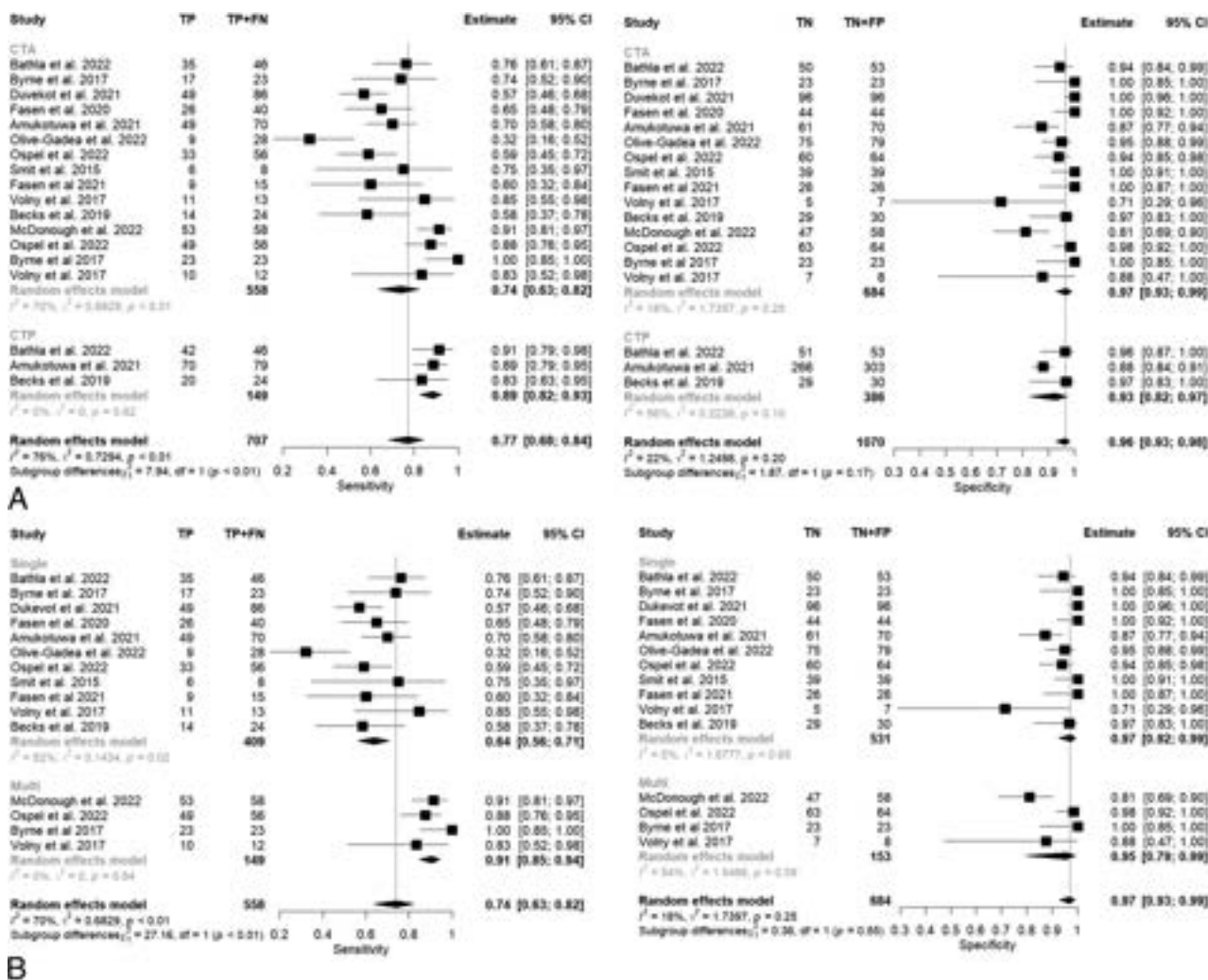


FIG 2. Forest plot of the pooled sensitivity and specificity of CTA and CTP (A) and CTA (spCTA) and mpCTA (B) in the diagnosis of DMVOs. TP indicates true positive; FN, false negative; TN, true negative; FP, false positive.

included studies in this subanalysis, highlights the potential limitations of single-phase CTA in a particular DMVO detection scenario in which there is a higher likelihood of a safe and effective thrombectomy, because it is already routinely performed.²⁶

No differences in terms of specificity were found, except for the higher specificity of CTA + CTP compared with CTP-only. However, only 1 study¹⁹ provided data for CTP-only. Relying solely on the territorial Tmax delay parameter, which was used to infer the presence of a DMVO, may result in false-positives.

No studies compared mpCTA with CTP. A between-study comparison yielded similar accuracy values. However, it is worth noting a slight difference in the included occlusions, because 2 CTP studies^{19,24} included M4, P4, PICA, AICA, and SCA that were not part of the occlusion sample in the mpCTA studies.

Our findings indicate that spCTA lacks sensitivity to reliably exclude DMVOs treatable by EVT, such as M2 occlusions, and imaging protocols should include either mpCTA or CTP because they offer the highest sensitivity. CTP should be complemented with CTA to increase specificity.

Future studies investigating the diagnostic accuracy in DMVOs should be performed on unselected patients, ideally

with a prospective design, and provide clear data on reference standards that should be standardized and preferably be DSA. With the aim of establishing the optimal DMVO imaging workflow, studies should also include data on stroke workflow metrics. Additionally, studies may explore information that can be extracted from imaging beyond diagnosis, such as assessing collateral status, given the growing interest in the assessment of collateral status to guide treatment.⁵ One study²⁷ has already demonstrated the relevance of quantitatively measuring collaterals with CTP in DMVO.

Strength of Evidence and Limitations

The overall strength of evidence was considered low (Online Supplemental Data) because it was downgraded in the risk of bias and indirectness categories. Between-study heterogeneity was substantial in the sensitivity values provided by CTA studies. This finding is attributed to the grouping of spCTA and mpCTA studies into the same category. Splitting spCTA and mpCTA studies reduces heterogeneity as shown in Fig 2. The risk of bias was considered high in the patient-selection domain due to study design and/or the reference standard in 8

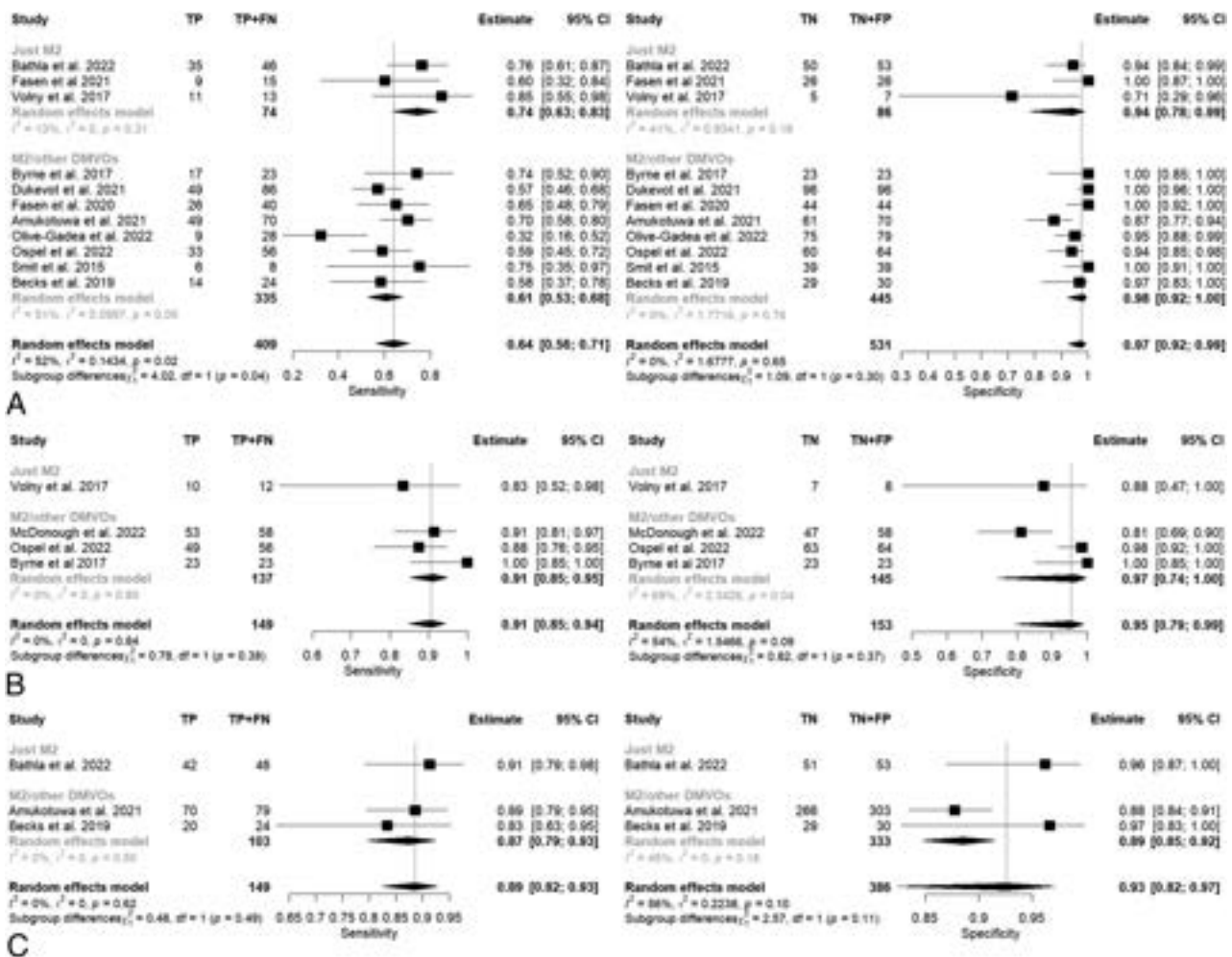


FIG 3. Forest plot of the pooled sensitivity and specificity of CTA (spCTA) (A), mpCTA (B), and CTP (C) in studies including only M2 occlusions versus others including other DMVOs. TP indicates true positive; FN, false negative; TN, true negative; FP, false positive.

studies^{14-18,21,23,25} as illustrated in the Online Supplemental Data. A notable limitation was the determination of the reference standard. Only 2^{15,20} of the 12 studies included DSA as part of the reference standard, as in the protocol developed by Sousa et al,⁸ because this examination is generally reserved for cases in which EVT is expected and to diagnose secondary DMVOs (ie, migration of a previous large-vessel occlusion). These 2 studies included a total of 437 patients and compared spCTA with CTP, and their findings were congruent with the remaining studies. Because DSA is considered the most sensitive technique for DMVO detection by consensus,¹ its unavailability as a reference standard in most of the studies may have overestimated the accuracy of CTA and/or CTP. In fact, hypo- and hyperperfusion in CTP may also occur in recently recanalized arteries.²⁸ Eight of the 12 studies used as a reference standard a combination of several imaging methods that included follow-up imaging in which it is unexpected that a DMVO goes unnoticed. Moreover, from a clinical perspective, the important aspect is not the exact accuracy values of each imaging technique but rather their comparative performance and the preferred diagnostic workflow. In this regard, this study provides consistent insights.

CONCLUSIONS

Imaging workflows incorporating multiphase CTA and CTP demonstrate significantly higher sensitivity in the diagnosis of DMVOs compared with single-phase CTA, particularly, but not exclusively, in arteries beyond the M2 segment of MCA.

Disclosure forms provided by the authors are available with the full text and PDF of this article at www.ajnr.org.

REFERENCES

- Saver JL, Chapot R, Agid R, et al; Distal Thrombectomy Summit Group. **Thrombectomy for distal, medium vessel occlusions.** *Stroke* 2020;51:2872–84 CrossRef Medline
- Goyal M, Ospel JM, Menon BK, et al. **MeVO: the next frontier?** *J Neurointerv Surg* 2020;12:545–47 CrossRef Medline
- Loh ED, Toh KZ, Kwok GY, et al. **Endovascular therapy for acute ischemic stroke with distal medium vessel occlusion: a systematic review and meta-analysis.** *J Neurointerv Surg* 2022 Dec 20 [Epub ahead of print] CrossRef Medline
- Nguyen TN, Abdalkader M, Nagel S, et al. **Noncontrast computed tomography vs computed tomography perfusion or magnetic resonance imaging selection in late presentation of stroke with large-vessel occlusion.** *JAMA Neurol* 2022;79:22–31 CrossRef Medline

5. Olthuis SG, Pirson FA, Pinckaers FM, et al; MR CLEAN-LATE Investigators. **Endovascular treatment versus no endovascular treatment after 6-24 h in patients with ischaemic stroke and collateral flow on CT angiography (MR CLEAN-LATE) in the Netherlands: a multicentre, open-label, blinded-endpoint, randomised, controlled, phase 3 trial.** *Lancet* 2023;401:1371–80 CrossRef Medline
6. Nogueira RG, Haussen DC, Liebeskind D, et al; Trevo Registry and DAWN Trial Investigators. **Stroke imaging selection modality and endovascular therapy outcomes in the early and extended time windows.** *Stroke* 2021;52:491–97 CrossRef Medline
7. McInnes MD, Moher D, Thoms BD, et al. **Preferred Reporting Items for a Systematic Review and Meta-analysis of Diagnostic Test Accuracy Studies: The PRISMA-DTA Statement.** *JAMA* 2018;319:388–96 CrossRef Medline
8. Sousa JA, Sondermann A, Bernardo-Castro S, et al. **Diagnostic accuracy of CT angiography and CT perfusion imaging for detecting distal medium vessel occlusions: protocol for a systematic review and meta-analysis.** *PLoS One* 2023;18:e0284116 CrossRef Medline
9. Whiting PF, Rutjes AS, Westwood M E, et al; QUADAS-2 Group. **QUADAS-2: a revised tool for the quality assessment of diagnostic accuracy studies.** *Ann Intern Med* 2011;155:529–36 CrossRef Medline
10. Schünemann HJ, Mustafa RA, Brozek J, et al; GRADE Working Group. **GRADE guidelines: 21, Part 1: study design, risk of bias, and indirectness in rating the certainty across a body of evidence for test accuracy.** *J Clin Epidemiol* 2020;122:129–41 CrossRef Medline
11. Schünemann HJ, Mustafa RA, Brozek J, et al; GRADE Working Group. **GRADE guidelines: 21, Part 2: test accuracy: inconsistency, imprecision, publication bias, and other domains for rating the certainty of evidence and presenting it in evidence profiles and summary of findings tables.** *J Clin Epidemiol* 2020;122:142–52 CrossRef Medline
12. van Enst WA, Ochodo E, Scholten RJ, et al. **Investigation of publication bias in meta-analyses of diagnostic test accuracy: a meta-epidemiological study.** *BMC Med Res Methodol* 2014;14:70 CrossRef Medline
13. Cumpston M, Li T, Page MJ, et al. **Updated guidance for trusted systematic reviews: a new edition of the Cochrane Handbook for Systematic Reviews of Interventions.** *Cochrane Database Syst Rev* 2019;10:ED000142 CrossRef Medline
14. Byrne D, Sugrue G, Stanley E, et al. **Improved detection of anterior circulation occlusions: the “delayed vessel sign” on multiphase CT angiography.** *AJNR Am J Neuroradiol* 2017;38:1911–16 CrossRef Medline
15. Bathla G, Pillenahalli Maheshwarappa R, Soni N, et al. **CT perfusion maps improve detection of M2-MCA occlusions in acute ischemic stroke.** *J Stroke Cerebrovasc Dis* 2022;31:106473 CrossRef Medline
16. Duvekot MH, van Es AC, Venema E, et al; PRESTO Investigators. **Accuracy of CTA evaluations in daily clinical practice for large and medium vessel occlusion detection in suspected stroke patients.** *Eur Stroke J* 2021;6:357–66 CrossRef Medline
17. Fassen BA, Borghans RA, Heijboer RJ, et al. **Reliability and accuracy of 3-mm and 2-mm maximum intensity projection CT angiography to detect intracranial large vessel occlusion in patients with acute anterior cerebral circulation stroke.** *Neuroradiology* 2021;63:1611–16 CrossRef Medline
18. Fassen BA, Heijboer RJ, Hulsmans FJ, et al. **CT angiography in evaluating large-vessel occlusion in acute anterior circulation ischemic stroke: factors associated with diagnostic error in clinical practice.** *AJNR Am J Neuroradiol* 2020;41:607–11 CrossRef Medline
19. Amukotuwa SA, Wu A, Zhou K, et al. **Distal medium vessel occlusions can be accurately and rapidly detected using Tmax maps.** *Stroke* 2021;52:3308–17 CrossRef Medline
20. Olive-Gadea M, Requena M, Diaz F, et al. **Systematic CT perfusion acquisition in acute stroke increases vascular occlusion detection and thrombectomy rates.** *J Neurointerv Surg* 2022;14:1270–73 CrossRef Medline
21. Volny O, Cimflova P, Kadlecova P, et al. **Single-phase versus multiphase CT angiography in middle cerebral artery clot detection—benefits for less experienced radiologists and neurologists.** *J Stroke Cerebrovasc Dis* 2017;26:19–24 CrossRef Medline
22. Ospel JM, Bala F, McDonough RV, et al. **Interrater agreement and detection accuracy for medium-vessel occlusions using single-phase and multiphase CT angiography.** *AJNR Am J Neuroradiol* 2022;43:93–97 CrossRef Medline
23. McDonough RV, Qiu W, Ospel JM, et al. **Multiphase CTA-derived tissue maps aid in detection of medium vessel occlusions.** *Neuroradiology* 2022;64:887–96 CrossRef Medline
24. Becks MJ, Manniesing R, Vister J, et al. **Brain CT perfusion improves intracranial vessel occlusion detection on CT angiography.** *J Neuroradiol* 2019;46:124–29 CrossRef Medline
25. Smit EJ, Vonken EJ, Meijer FJ, et al. **Timing-invariant CT angiography derived from CT perfusion imaging in acute stroke: a diagnostic performance study.** *AJNR Am J Neuroradiol* 2015;36:1834–38 CrossRef Medline
26. Kniep H, Meyer L, Broocks G, et al; German Stroke Registry-Endovascular Treatment (GSR-ET). **Thrombectomy for M2 occlusions: predictors of successful and futile recanalization.** *Stroke* 2023;54:2002–12 CrossRef Medline
27. Guenego A, Farouki Y, Mine B, et al. **Hypoperfusion intensity ratio predicts infarct growth after successful thrombectomy for distal medium vessel occlusion.** *Clin Neuroradiol* 2022;32:849–56 CrossRef Medline
28. Rubiera M, Garcia-Tornel A, Olivé-Gadea M, et al. **Computed tomography perfusion after thrombectomy.** *Stroke* 2020;51:1736–42 CrossRef Medline

Disconnection-Based Prediction of Poststroke Dysphagia

Kyung Jae Yoon, Chul-Hyun Park,  Myung-Ho Rho, and  Minchul Kim

ABSTRACT

BACKGROUND AND PURPOSE: Dysphagia is a common deficit after a stroke and is associated with serious complications. It is not yet fully clear which brain regions are directly related to swallowing. Previous lesion symptom mapping studies may have overlooked structural disconnections that could be responsible for poststroke dysphagia. Here, we aimed to predict and explain the relationship between poststroke dysphagia and the topologic distribution of structural disconnection via a multivariate predictive framework.

MATERIALS AND METHODS: We enrolled first-ever ischemic stroke patients classified as full per-oral nutrition (71 patients) and nonoral nutrition necessary (43 patients). After propensity score matching, 43 patients for each group were enrolled (full per-oral nutrition group with 17 women, 68 ± 15 years; nonoral nutrition necessary group with 13 women, 75 ± 11 years). The structural disconnectome was estimated by using the lesion segmented from acute phase diffusion-weighted images. The prediction of poststroke dysphagia by using the structural disconnectome and demographics was performed in a leave-one-out manner.

RESULTS: Using both direct and indirect disconnection matrices of the motor network, the disconnectome-based prediction model could predict poststroke dysphagia above the level of chance (accuracy = 68.6%, permutation $P = .001$). When combined with demographic data, the classification accuracy reached 72.1%. The edges connecting the right insula and left motor strip were the most informative in prediction.

CONCLUSIONS: Poststroke dysphagia could be predicted by using the structural disconnectome derived from acute phase diffusion-weighted images. Specifically, the direct and indirect disconnection within the motor network was the most informative in predicting poststroke dysphagia.

ABBREVIATIONS: CPM = connectome-based predictive modeling; DOSS = Dysphagia Outcome and Severity Scale; FA = fractional anisotropy; HCP = Human Connectome Project; LOOCV = leave-one subject-out cross-validation; MNI = Montreal Neurological Institute; SSPL = shortest structural path length; SVM = support vector machine; VFSS = videofluoroscopic swallowing study

Oropharyngeal dysphagia is a frequent symptom in stroke patients. More than 50% of patients with stroke have had swallowing difficulty.¹ Poststroke dysphagia is associated with complications, such as malnutrition, dehydration, or aspiration pneumonia. In particular, aspiration pneumonia can cause longer hospitalization, higher disability, or even death,² making early diagnosis of poststroke dysphagia critical to prevent these worse outcomes.

Poststroke dysphagia is diagnosed with various instrumental methods, such as videofluoroscopic swallowing study (VFSS) or fiberoptic endoscopic evaluation of swallowing.³ However, these tests can be performed only for patients who have sitting balance or good cooperation, which makes it difficult to effect early detection of poststroke dysphagia. The bedside swallowing test can be applied for those who cannot comply with VFSS for fiberoptic endoscopic evaluation of swallowing but still have the risk of aspiration pneumonia. Very early detection of poststroke dysphagia to avoid complications is essential and beneficial for the management of acute stroke since dysphagia improves significantly during the early days; after 2 weeks, most patients swallow safely.³ However, recent guidelines for dysphagia screening strategies for acute ischemic stroke have not yet provided reliable evidence,⁴ with one recent study reporting several patient characteristics predictive of poststroke dysphagia.⁵ In addition, the current body of evidence does not allow an exact relationship between acute focal brain lesions and related poststroke dysphagia, with some

Received April 27, 2023; accepted after revision October 24.

From the Department of Physical and Rehabilitation Medicine (K.J.Y., C.-H.P.), Medical Research Institute (K.J.Y., C.-H.P.), and Department of Radiology (M.-H.R., M.K.), Kangbuk Samsung Hospital, Sungkyunkwan University School of Medicine, Seoul, Korea.

K.J. Yoon and C.-H. Park contributed equally to this work.

Please address correspondence to Minchul Kim, MD, PhD, Department of Radiology, Kangbuk Samsung Hospital, Sungkyunkwan University School of Medicine, Seoul, Korea, 03181; e-mail: minchulusa@gmail.com



Indicates article with online supplemental data.

<http://dx.doi.org/10.3174/ajnr.A8074>

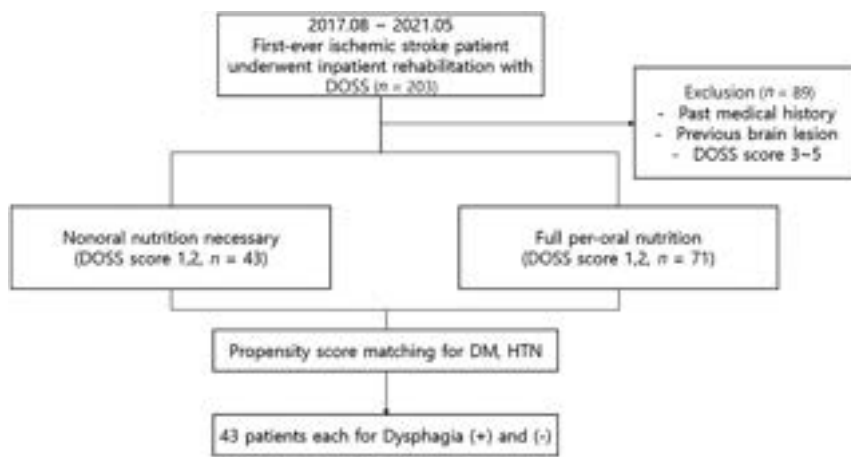


FIG 1. Flow chart of participants with poststroke dysphagia recruited for disconnectome analysis.

recent studies suggesting that white matter tract rather than focal cortical lesion involvement is crucial.^{6,7}

Previous voxel-based lesion symptom mapping studies reported poststroke dysphagia to be caused by distributed lesions in the swallowing network comprising the primary sensorimotor cortex, frontal operculum, insula, and associated white matter tracts.^{8,9} Recent data indicate that white matter disconnection might be a better predictor of brain dysfunction and recovery than the location of the lesion itself.¹⁰ Thus, we hypothesized that, rather than a focal lesion, a group of brain areas that is interconnected by the structural brain network is conjointly responsible for poststroke dysphagia. To investigate this possibility, we adapted a multivariate connectome-based symptom mapping approach combined with indirect estimation of structural disconnection to detect brain networks supporting swallowing.^{11,12} Multivariate predictive modeling aims to develop brain models that are tightly coupled with target outcomes by using pattern recognition techniques (or “machine learning”).¹³ In contrast to the mass-univariate approach, which focuses on permitting the inference that disconnection *C* is responsible, conditional on symptom *S* (ie, poststroke dysphagia), and assesses the probability $P(C|S)$, a new trend of predictive modeling has recently emerged to address the reverse inference that symptom *S* must have occurred given disconnection *C* being related to $P(S|C)$.¹³ Further, the indirect estimation of structural disconnection is a recently developed method that combines a patient’s structural lesion information and normative connectome data to estimate lesion-induced structural disconnection. This method involves embedding the patient’s lesion mask into normative connectome data obtained from healthy individuals to model the expected impact of a lesion on the typical white matter connectome, namely, the disconnectome (ie, the disruption of the network architecture of the brain) after a brain lesion.¹⁴

In this study, we aimed to achieve 2 objectives: 1) to develop an early prediction model of dysphagia in patients with ischemic stroke with clinically plausible acute phase diffusion-weighted brain MRI; and 2) to disclose the pattern of network

disconnections responsible for poststroke dysphagia, thereby deepening our understanding of pathophysiology.

MATERIALS AND METHODS

Patient Selection

We retrospectively reviewed the medical records of patients with ischemic stroke who underwent inpatient rehabilitation between August 2017 and May 2021. The inclusion criteria were 1) first-ever stroke confirmed by DWI within 7 days of symptom onset (because apparent diffusion coefficient maps may depict persistent darkening for ~7–10 days)¹⁵ and 2) Dysphagia Outcome and Severity Scale (DOSS) evaluation by using VFSS performed within 1 month after stroke

onset. The exclusion criteria were as follows: 1) prior imaging evidence of stroke and 2) other neurologic disorders causing oropharyngeal dysphagia, such as parkinsonism and dementia. The Institutional Review Board of Kangbuk Samsung Hospital approved the study protocols, which were in accordance with the Declaration of Helsinki, and informed consent was waived for retrospective study based on medical records. Among 180 patients with stroke with available DOSS scores, we enrolled those that received full per-oral nutrition (71 patients with DOSS scores 6 and 7) and others that received nonoral nutrition (43 patients with DOSS scores 1 and 2), based on DOSS scores.¹⁶

Because diabetes mellitus and hypertension were reported to be associated with dysphagia in ischemic patients,¹⁷ we used propensity score matching analysis to minimize the effects of these confounding factors.¹⁸ Propensity scores were matched by selecting the cases in the 2 groups, and the variables listed above were used as matching parameters by using the MatchIt R package (R Core Team, R Foundation for Statistical Computing).^{19,20} Figure 1 shows a flowchart of the participants included.

Image Acquisition

MRI data were acquired by using 1.5T and 3T scanners from Philips Healthcare (Intera, Ingenia, and Achieva), each with a standard head coil. The acute stroke MRI protocol for each patient included 6-direction DWI and FLAIR sequences. Fractional anisotropy (FA) and ADC maps were automatically created from DWI scans by using built-in software. DWI was acquired with a single-shot spin-echo echo-planar imaging sequence in alignment with the horizontal plane with the following parameters: diffusion-sensitizing gradients applied along 6 noncolinear directions with a *b*-value of 1000 seconds/mm², together with acquisition without diffusion weighting (*b* = 0 s/mm²); section thickness, 4 mm with no gap; repetition time, 5300 ms; echo time, 74 ms; number of averages, 2; flip angle, 90°; matrix size, 128 × 128.

Lesion Segmentation and Normalization

A schematic diagram of the procedure for lesion segmentation and normalization is shown in Figure 2A. The infarct cores were automatically segmented by using ADC maps and DWI by

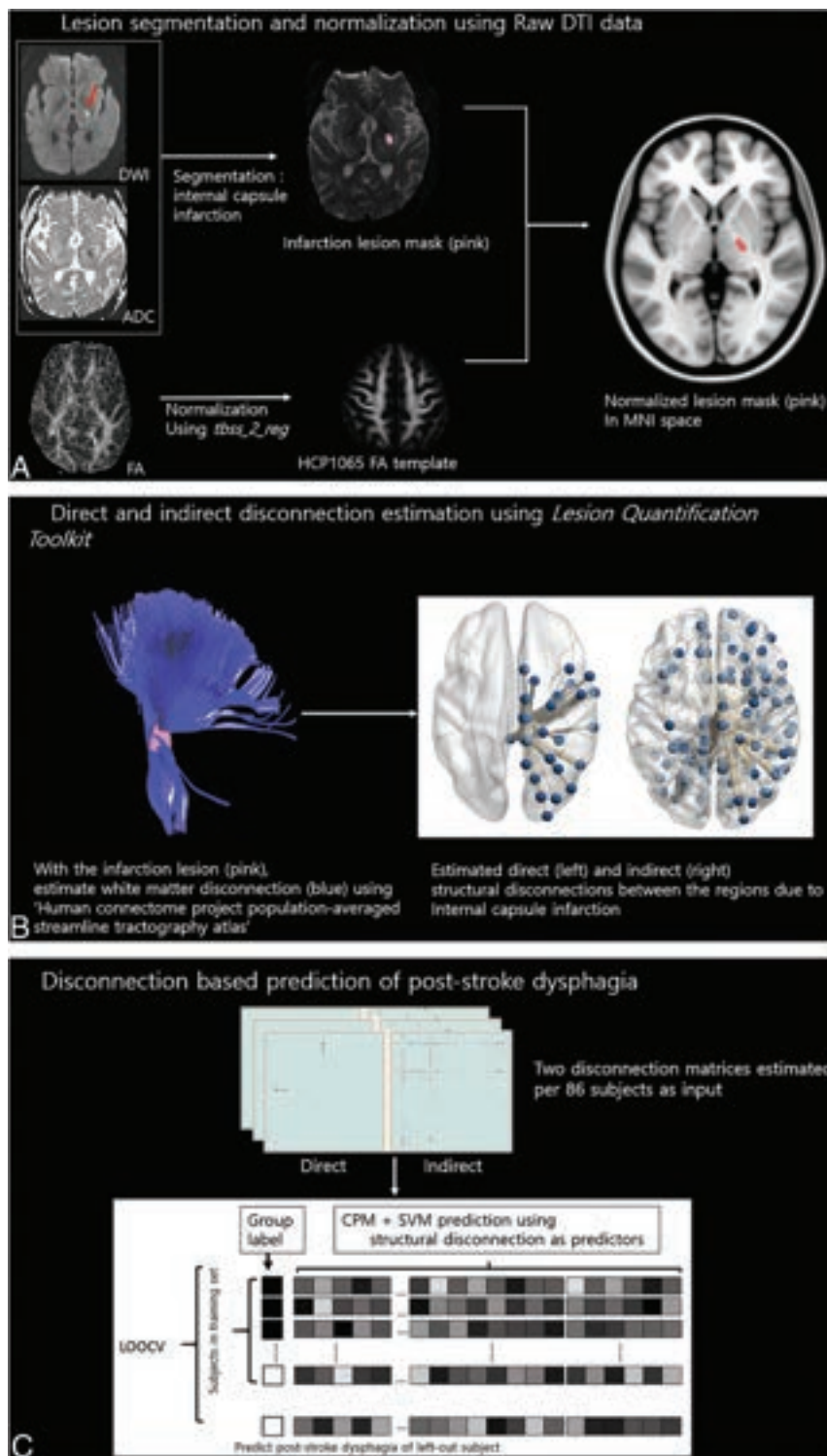


FIG 2. Schematic of using a CPM-SVM to predict poststroke dysphagia from the structural disconnectome. **A**, Processing scheme of a patient with internal capsule posterior limb infarction (red arrow). We segmented the infarct core using ADC maps and DWI. To normalize the lesion mask to the MNI space, we used warping results derived from the patient's FA map normalized to the FA template. In the end, we get the segmented lesion normalized in MNI space (pink in the image on the right). **B**, The Lesion Quantification Toolkit uses the lesion segmentation in **A** to estimate the structural disconnection using the HCP-842 population-averaged streamline tractography atlas. The blue tractography on the left is the tracts disconnected by the internal capsule posterior limb infarction, and the brain plotted on the right shows the distribution of direct and indirect disconnection due to infarction. The patient had poststroke dysphagia probably owing to disruption in the motor network. **C**, Using the disconnection derived from **B** as prediction features, we adopted the CPM-SVM model and LOOCV to predict poststroke dysphagia.

applying normalized absolute thresholding²¹ and minimally corrected by a board-certified neuroradiologist (M.K., code available at https://github.com/HyunnaLee/StrokeOnset/tree/master/1_InfarctSegmentation). We defined the infarct core as a lesion because the infarct core is considered irreversible tissue damage that cannot be recovered with treatment.²² Three patients had short-term follow-up imaging due to hyperacute infarction, and we used the image with a larger extent of infarct core.

After lesion segmentation, we performed FA map normalization to the Montreal Neurological Institute (MNI) template brain image by using the tract-based spatial statistics commands ('tbss_1_preproc' and 'tbss_2_reg') in the FMRIB Software Library toolbox (<http://www.fmrib.ox.ac.uk/fsl>), involving an established, carefully tuned non-linear registration of FA maps.²³ Then, the infarct core masks in the DWI space were transformed to the MNI space by using the 'applywarp' command, which is also a part of the FMRIB Software Library toolbox.²⁴

Estimating the Structural Disconnectome Using the Lesion Quantification Toolkit

A schematic diagram of the procedure for acquiring the disconnectome is shown in Figure 2B. The Lesion Quantification Toolkit, a publicly available MATLAB software package for quantifying the structural impacts of focal brain lesions implemented in MATLAB 2020b (MathWorks), was used to estimate the white matter disconnections.²⁵ In brief, the toolkit uses atlas-based approaches to estimate parcel-wise disconnection matrices. To estimate the degree of disconnection by using the Lesion Quantification Toolkit, 2 inputs are needed: 1) a binary lesion segmentation that is registered to the MNI template (ie, the infarction core in our case); and 2) a regional gray matter parcellation (ie, atlas) that is also registered to the MNI brain template space. We used the Shen 268-node atlas (available at https://www.nitrc.org/frs/?group_id=51), which has 8 specific functional networks (for details, see Online Supplemental Data), to test the hypothesis that certain brain

Clinical characteristics of the study population

	Full Per-Oral Nutrition (n = 43, 17 Women)	Nonoral Nutrition Necessary (n = 43, 13 Women)	P Value
Age (yr)	68.83 ± 15.69	75.09 ± 11.38	t = 2.264, P = .029 ^a
HTN	35	34	χ ² = 0.073, P = .786
DM	15	19	χ ² = 0.778, P = .377
Onset to VFSS interval (days)	11.67 ± 7.50	12.24 ± 7.64	t = 0.327, P = .745
MRI scanner	Intera = 35 Ingenia = 5 Achieva = 3	Intera = 37 Ingenia = 4 Achieva = 2	χ ² = 0.367, P = .832

Note:—DM indicates diabetes mellitus; HTN, hypertension.

^aP < .05.

networks contribute more to poststroke dysphagia than others.²⁶ The toolkit outputs several estimations based on the provided lesion and parcellation, including parcel-wise disconnection matrices and parcel-wise increases in shortest structural path length (SSPL) matrices (Fig 2B, brain images on the right). Parcel-wise disconnection matrices are estimated by using the Human Connectome Project (HCP)-842 population-averaged streamline tractography atlas.^{27,28} First, an atlas structural connectivity matrix is created by using the HCP-842 streamline tractography atlas and the provided Shen atlas. The structural connections between a parcel pair are defined as the number of atlas streamlines that bilaterally terminate within both parcels. Then, the lesion is embedded into the HCP-842 streamline tractography atlas, and the atlas is filtered to retain only the subset of streamlines whose trajectories intersect the volume occupied by the lesion (ie, disconnected streamlines, Fig 2B, tract image on the left) and terminate bilaterally within a parcel pair, creating a disconnection matrix. Finally, this raw disconnection matrix is converted to a “percent disconnection severity matrix” relative to the atlas structural connectivity matrix. The values for each cell (ie, parcel pair) in the final percent disconnection severity matrix correspond to the estimated disconnection severities for each pair of parcels.²⁵ Parcel-wise SSPL increases are also computed according to the same procedure used in a previous study.²⁸ The rationale for obtaining the matrix is that the white matter disconnections caused by focal brain lesions can disrupt communication between brain regions that are “indirectly” connected via a series of intermediary regions.²⁹

Disconnectome-Based Predictive Modeling

A schematic diagram of the procedure for predictive modeling is shown in Figure 2C. The code and data for replicating the predictive model are available at <https://osf.io/u4m5j/>. To predict poststroke dysphagia by using structural disconnection, we used connectome-based predictive modeling (CPM), a data-driven protocol for developing predictive models of brain-behavior relationships.¹² We modified the CPM approach by replacing its core learning algorithm with a support vector machine (SVM).³⁰

First, we separated the subjects into the 85-person training set and 1 test set in each iteration, implementing a leave-one-subject-

out cross-validation (LOOCV) process. LOOCV was performed to protect against overfitting.¹² Then, across all subjects in the training set, each edge in the disconnection matrices and SSPL increase matrices was correlated to the subjects’ group label (ie, whether 1 subject had poststroke dysphagia or not) as behavioral data by using the Spearman correlation.³⁰ Those edges that significantly correlated (below the threshold value of 0.05, which means severe disconnection in patients with severe dysphagia) were selected. Next, for each subject, the selected edges were summed into 2 predictive variables

(ie, disconnection matrix and SSPL increase matrix), and 3 SVM models (see Models 1–3 below) were trained and tested³¹:

- Model 1, Predicted group label = disconnection matrix
- Model 2, Predicted group label = SSPL increase matrix
- Model 3, Predicted group label = disconnection matrix + SSPL increase matrix

From the perspective of functional integration and segregation, whole-brain and 8 functional system analyses were conducted separately. Model performance (ie, correspondence between predicted and actual values) was assessed mainly by using classification accuracy, and we performed a permutation test to examine the significance of our model. For interpretation purposes, we identified those edges that appeared in every iteration of the leave-one-out process to yield “consensus edges” (edges appearing in 100% of the LOOCV iterations across all subjects).³²

In addition, for exploratory purposes, we calculated the diagnostic performance of the combined model incorporating the disconnection and demographic variables (age, sex, and lesion volume).

RESULTS

Demographics

The characteristics of the study samples are displayed in the Table. Contingency χ² tests and paired t-tests were used to examine group differences in demographics across the 2 groups. The statistical analyses were conducted in MATLAB 2020b. Using propensity matching, the incidence of diabetes mellitus and hypertension between the groups showed no significant difference (χ² = 0.073, P = .786 and χ² = 0.778, P = .377, respectively), though the full per-oral nutrition group showed a younger age (P = .029). There was no significant difference between the MRI scanners used between the 2 groups (χ² = 0.367, P = .832).

Disconnection-Based Prediction of Poststroke Dysphagia

Figure 3A summarizes the model performance of individual classification from whole-brain and network-based analyses. Notably, the best prediction model was the one that took the disconnection matrix and SSPL increase matrix of the motor

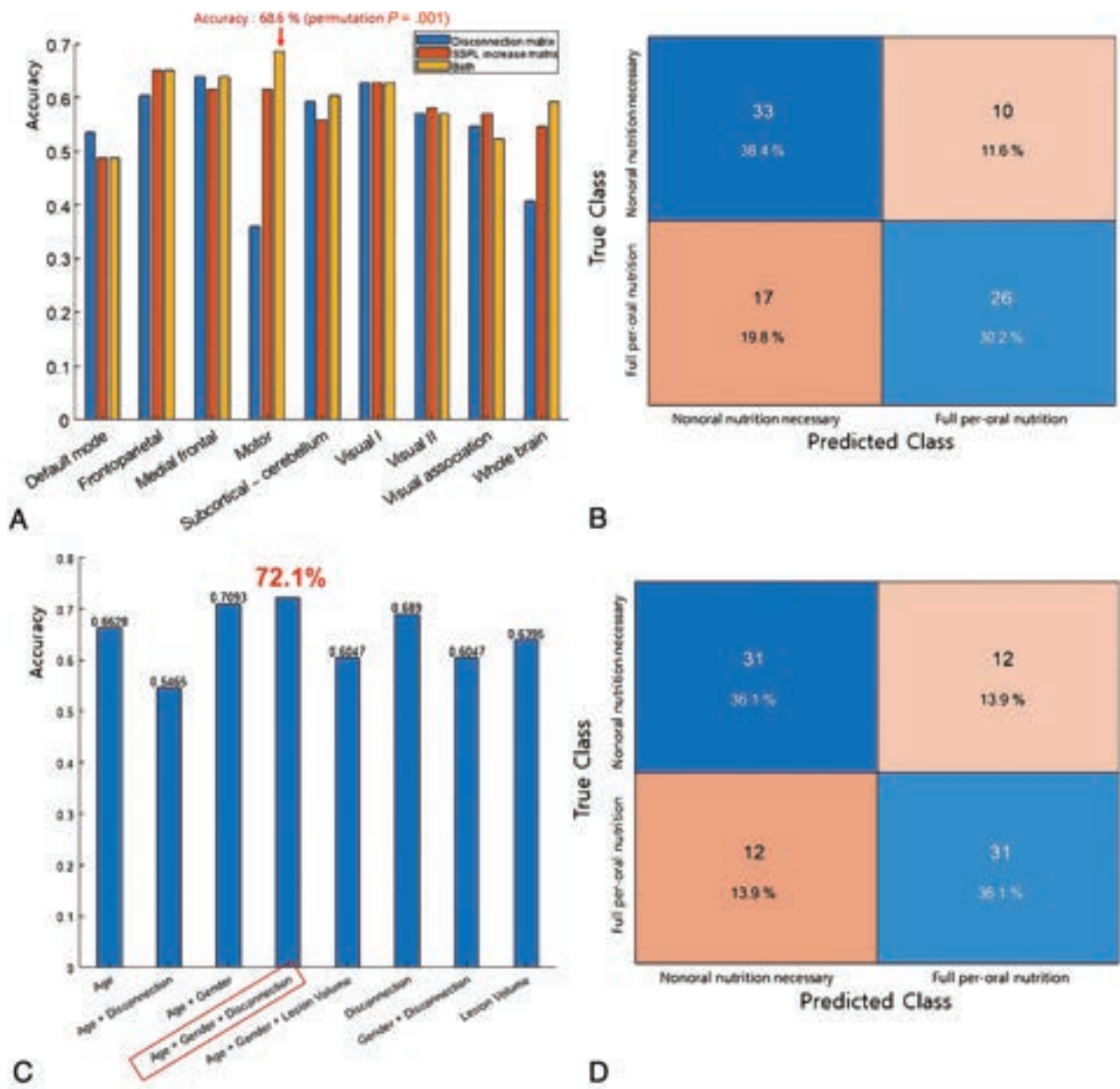


FIG 3. Leave-one-out classification result. *A*, Classification results in which, by using both the disconnection and SSPL, increased matrix of the motor network (red arrow) presented the highest accuracy. *B*, Confusion matrix of the motor network-based model, where the vertical axis is the true label of all patients. Blue boxes represent individuals correctly identified by the model. Orange boxes represent incorrect identification. Percentages in each box correspond to the proportions of subjects in the subgroup relative to the total subjects. *C* and *D*, Classification result when combined with demographic variables, indicating that the model, by using both disconnection and demographic features, shows the best prediction accuracy of 72.1%.

network into account (Model 3). The model accurately and relatively evenly identified individuals with dysphagia after stroke (accuracy = 68.6%, permutation testing, 1000 times, $P = .001$; sensitivity = 76.7%, specificity = 60.4%; Fig 3*B*). It is notable that disruption in the motor network contributes to the prediction of developing poststroke dysphagia. When we included the patient’s demographic variables of age and sex in the prediction model, the prediction accuracy rose to 72.1% (sensitivity = 72.1%, specificity = 72.1%; Fig 3*C*-, *D*), while the demographics could substantially predict poststroke dysphagia (eg, combination of “age + sex” achieved 70.9%).

The “consensus edges” of the disconnection matrix included 40 edges in which the highest-degree node (ie, the node with the most connections) was located in the left parietal lobe. The “consensus edges” in an SSPL increase matrix included 241 edges, and the highest-degree node in the SSPL increase matrix was located in the right insula, with the left motor strip being the location of the next highest (Fig 4).

DISCUSSION

In this study, we used a multivariate CPM to predict poststroke dysphagia and identify disconnections that are predictive of

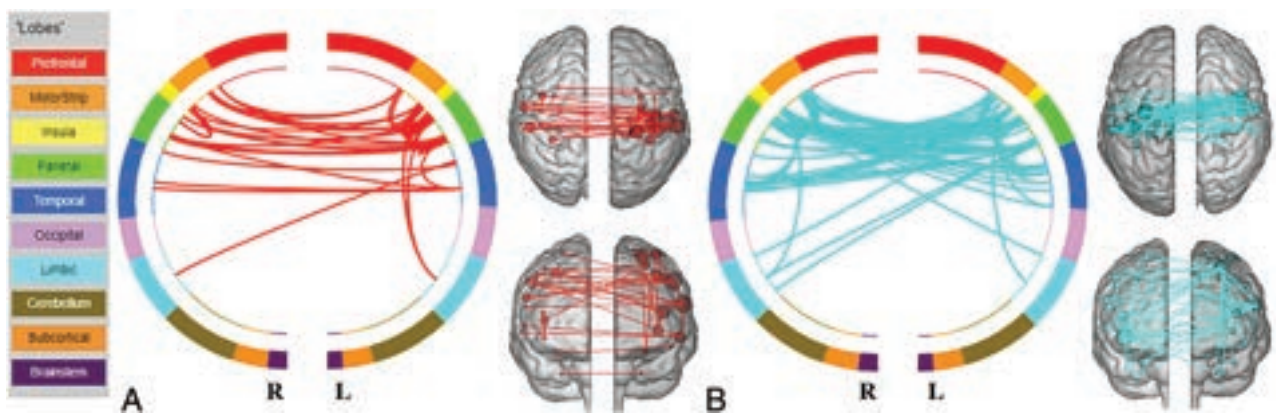


FIG 4. Spatial network anatomy of the motor network-based model. *A*, Spatial extent of the “consensus edges” from the disconnection network. In the circular plot, regions are organized according to their anatomic locations, with more anterior regions at the top and more ventral and posterior regions displayed toward the bottom. Node size in the brain represents the degree of the node (ie, the number of connections with the node). *B*, Summarization of “consensus edges” from the disconnection network. The nodes were filtered to have at least 20 edges for visualization purposes.

the disease. Across classification analyses, the motor network combining the information from both direct and indirect disconnections emerged as being the most informative in prediction.

There are 2 main advantages in our findings that we want to emphasize. First, we showed the potential of predicting poststroke dysphagia based only on clinically plausible acute-phase diffusion-weighted brain MRI. This is an advantage because no other advanced sequences, such as diffusion tractography, are needed. In addition, we conducted our study based on publicly available toolboxes, and we make our data and analysis code available to increase transparency and allow future researchers to replicate our findings (<https://osf.io/u4m5j/>). Clinically, our results can be utilized to predict whether a patient with stroke is at high risk of poststroke dysphagia at the time of symptom onset. If one is predicted to have a high risk of dysphagia, clinicians can postpone oral nutrition without any swallowing test, thus lowering the chance of aspiration in the acute phase.

Another important result is that the motor network emerged as being the most informative in predicting poststroke dysphagia. Figure 5 shows a representative case of infarction in the middle cerebellar peduncle without disconnection in the motor network, and the patient did not have poststroke dysphagia. This is in line with previous reports, which revealed that dysphagia secondary to stroke is associated with disruptive functional and structural integrity in the large-scale brain networks involved in motor control.³³ Specifically, the connection between the motor cortex and bulbar areas (corticobulbar tract) has been shown to be a potent neural pathway involved in swallowing, and any lesions disrupting this pathway can lead to dysphagia.⁹ Several recent studies utilizing advanced neuroimaging techniques support this by emphasizing the role of motor cortex connections to the bulbar area.^{34,35} In addition, our study is the first to point out that not only direct but also indirect disconnection (ie, SSPL increase) in the motor network is responsible for poststroke dysphagia. The increase in the shortest path length results in a decrease in network efficiency. It has also been reported that structural disconnections along the shortest structural paths linking indirectly

connected regions represent a general mechanism of stroke-induced functional connectivity disruptions.²⁸ On the contrary, some other networks, such as frontoparietal, reached similar prediction accuracy (65.1%), and the direct disconnection of the motor network had poor prediction (36.0%). This result implies networks other than the motor have a role in poststroke dysphagia. Together, we suggest that not only direct disconnection within the motor but also insufficient, including decreased, functional connectivity, may underlie the occurrence of poststroke dysphagia. In addition, our exploratory analysis by using the demographic variable as an additional predictor showed increased prediction accuracy with a decreased number of false-positives (17 → 12 in Fig 3*B, D*), giving the potential of a prediction model by using both brain-based and clinical features, and may be promising (Fig 6).

Although the prediction accuracy (Fig 3, 72.1%) we reported may seem modest, we suggest several reasons. To our knowledge, there is one paper investigated to predict acute stage poststroke dysphagia by using only clinical variables and can be a benchmark.⁵ The reported area under the receiver operating characteristic curve value was 0.86; however, this is a simple logistic regression result without cross-validation and thus cannot be directly compared with our LOOCV prediction accuracy, which provides a more conservative estimate.¹² It should also be mentioned that the combination of several demographic variables could substantially predict poststroke dysphagia. For example, “age + sex” alone had higher accuracy than the disconnection-based model (68.9%), and adding the disconnection to the “age + sex,” the accuracy only increased by 1.9%. It makes the disconnection seem somewhat trivial and the disconnection-model only was not very helpful. Interestingly, age and sex are included in our result and the prediction model of Zhang et al.⁵ As our study discovered that structural disconnection in the motor network has predictive information about poststroke dysphagia, future research could benefit from integrating larger demographic data.

Our study has a prominent limitation that the age was significantly younger in the full per-oral nutrition group, which may be a confounder. To see how much of the results were explained by

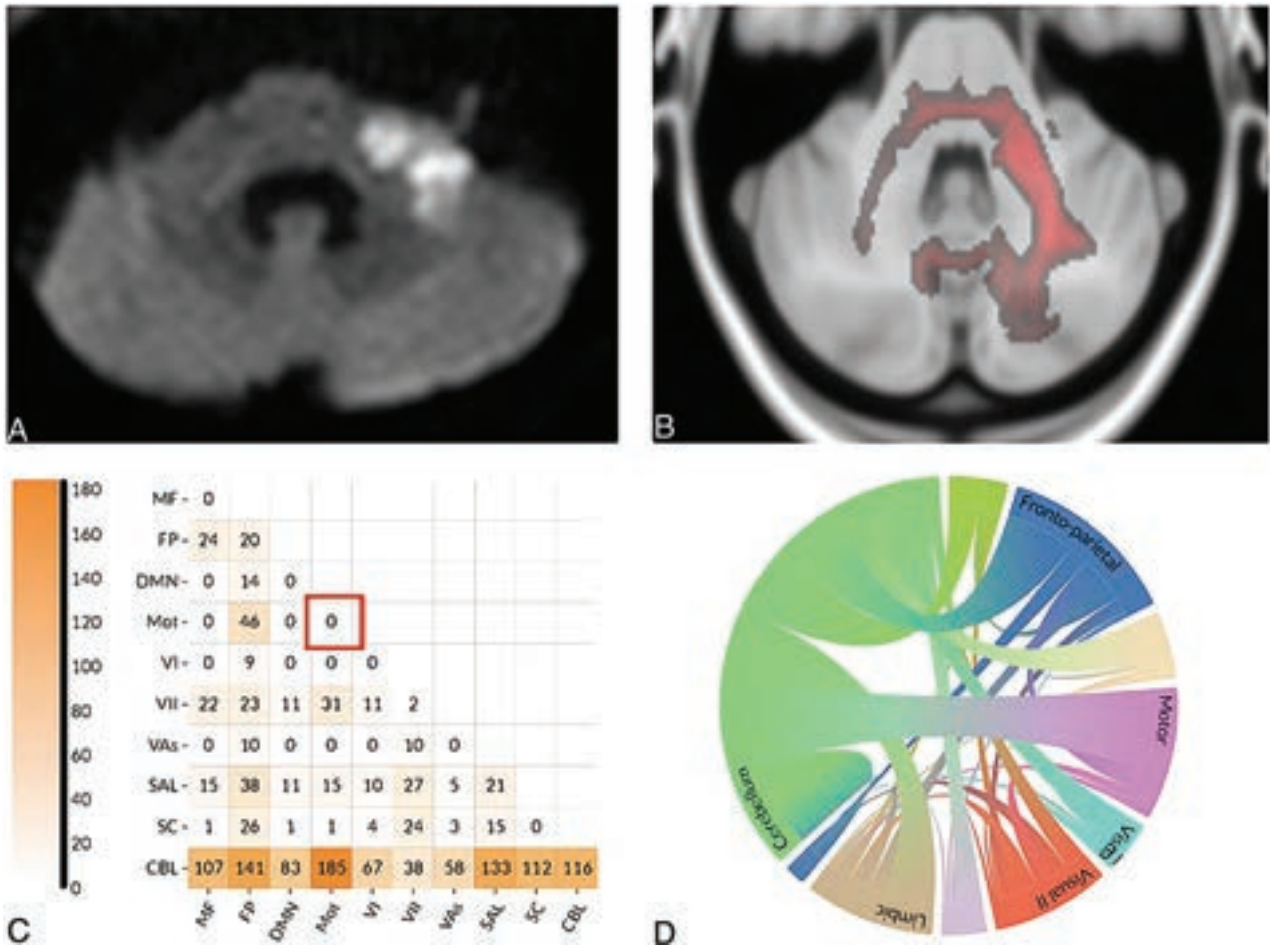


FIG 5. Representative case of a 62-year-old man with left middle cerebellar peduncle ischemic infarction. He did not have poststroke dysphagia, and the model also predicted negative results. *A*, Substantial infarction volume in DWI. *B*, Disconnected tract attenuation map (red) due to infarction. Nonetheless, the disconnection is mostly distributed in the cerebellar network, with no disconnection within the motor network (*C*, red square; *D*), which may be preventing the patient from poststroke dysphagia.

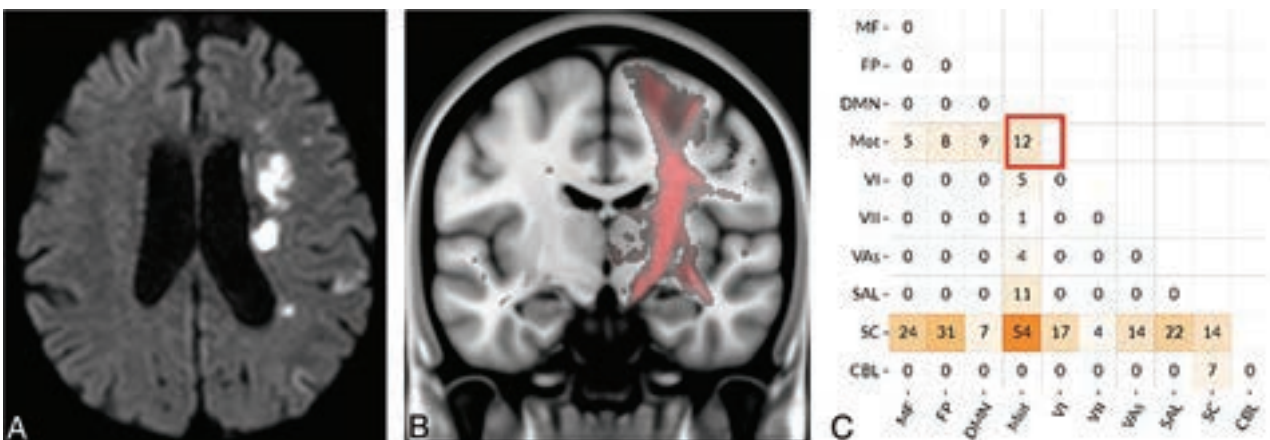


FIG 6. Representative case of a 39-year-old woman with left corona radiata ischemic infarction. The patient did not have poststroke dysphagia. She had disconnection in the motor network and not predicted correctly only by disconnection matrix (*C*, red square). However, the model incorporating both demographic variable and disconnection predicted correctly, maybe owing to the patient's relatively young age of 39. *A*, Left corona radiata infarction in DWI. *B*, Disconnected tract attenuation map (red) due to infarction. Substantial amount of the disconnection distributed in the motor network (*C*, red square); however, the prediction model incorporating both disconnection and age, sex could predict correctly.

age, we classified the groups only by using age and the result was 66.2% (Fig 3C). Age is indeed a protective factor for poststroke dysphagia as displayed in Figure 6.⁵ In addition, we tried to add age as a matching variable in the propensity score matching, and the significant difference remained, regardless of our effort. However, we showed that disconnection has additional information in the prediction of poststroke dysphagia.

There are several other limitations in this study. First, 3 different MRI scanners were used in our data set, which may bias the estimation of lesions. Second, this is a single-center retrospective study, which may limit the generalizability of the results. To compensate, we made our processed data and code available to increase reproducibility. Third, we did not include the cortical lesion in the analysis procedure because we wanted to focus on structural disconnection and reduce redundancy. Fourth, 3 patients with hyperacute infarction had follow-up MRI, and this may affect the generalizability of the study. Last, we used 6-direction DWI data to estimate the FA map in the normalization process. Although there are clear advantages in acquiring higher angular resolution data, several studies showed that 6-direction data provide diffusion measures with comparable robustness.³⁶

CONCLUSIONS

Although trivial, we show that structural disconnection as derived from acute phase stroke imaging is predictive of poststroke dysphagia. In addition, we suggest that not only direct but also indirect disconnection in the motor network is important in the prediction.
















Disclosure forms provided by the authors are available with the full text and PDF of this article at www.ajnr.org.

REFERENCES

- González-Fernández M, Ottenstein L, Atanelov L, et al. **Dysphagia after stroke: an overview.** *Curr Phys Med Rehabil Rep* 2013;1:187–96 CrossRef Medline
- Finlayson O, Kapral M, Hall R, Stroke Outcome Research Canada (SORCan) Working Group, et al. **Risk factors, inpatient care, and outcomes of pneumonia after ischemic stroke.** *Neurology* 2011;77:1338–45 CrossRef Medline
- Cohen DL, Roffe C, Beavan J, et al. **Post-stroke dysphagia: a review and design considerations for future trials.** *Int J Stroke* 2016;11:399–411 CrossRef Medline
- Smith EE, Kent DM, Bulsara KR, American Heart Association Stroke Council, et al. **Effect of dysphagia screening strategies on clinical outcomes after stroke: a systematic review for the 2018 Guidelines for the Early Management of Patients With Acute Ischemic Stroke.** *Stroke* 2018;49:e123–e28 CrossRef Medline
- Zhang L, Tang X, Wang C, et al. **Predictive model of dysphagia and brain lesion-symptom mapping in acute ischemic stroke.** *Front Aging Neurosci* 2021;13:753364 CrossRef Medline
- Wilmskoetter J, Bonilha L, Martin-Harris B, et al. **Mapping acute lesion locations to physiological swallow impairments after stroke.** *Neuroimage Clin* 2019;22:101685 CrossRef Medline
- Yang HE, Kang H, Kyeong S, et al. **Structural connectivity affecting aspiration after stroke.** *Dysphagia* 2022;37:1201–06 CrossRef Medline
- Galovic M, Leisi N, Müller M, et al. **Lesion location predicts transient and extended risk of aspiration after supratentorial ischemic stroke.** *Stroke* 2013;44:2760–67 CrossRef Medline
- Galovic M, Leisi N, Pastore-Wapp M, et al. **Diverging lesion and connectivity patterns influence early and late swallowing recovery after hemispheric stroke.** *Hum Brain Mapp* 2017;38:2165–76 CrossRef Medline
- Thiebaut de Schotten M, Foulon C, Nachev P. **Brain disconnections link structural connectivity with function and behaviour.** *Nat Commun* 2020;11:5094–98 CrossRef Medline
- Yourganov G, Fridriksson J, Rorden C, et al. **Multivariate connectome-based symptom mapping in post-stroke patients: networks supporting language and speech.** *J Neurosci* 2016;36:6668–79 CrossRef Medline
- Shen X, Finn ES, Scheinost D, et al. **Using connectome-based predictive modeling to predict individual behavior from brain connectivity.** *Nat Protoc* 2017;12:506–18 CrossRef Medline
- Woo CW, Chang LJ, Lindquist MA, et al. **Building better biomarkers: brain models in translational neuroimaging.** *Nat Neurosci* 2017;20:365–77 CrossRef Medline
- Sperber C, Griffis J, Kasties V. **Indirect structural disconnection-symptom mapping.** *Brain Struct Funct* 2022;227:3129–44 CrossRef Medline
- Allen LM, Hasso AN, Handwerker J, et al. **Sequence-specific MR imaging findings that are useful in dating ischemic stroke.** *Radiographics* 2012;32:1285–97 CrossRef Medline
- O’Neil KH, Purdy M, Falk J, et al. **The Dysphagia Outcome and Severity Scale.** *Dysphagia* 1999;14:139–45 CrossRef Medline
- Khedr EM, Abbas MA, Soliman RK, et al. **Post-stroke dysphagia. Frequency, risk factors, and topographic representation: hospital-based study.** *Egypt J Neurol Psychiatry Neurosurg* 2021;57:1–8 CrossRef Medline
- Morgan CJ. *Reducing Bias Using Propensity Score Matching.* New York: Springer-Verlag, 2018.
- Ho DE, Imai K, King G, et al. **MatchIt: nonparametric preprocessing for parametric causal inference.** *J Stat Soft* 2011;42:1–28
- R Core Team. **R: A Language and Environment for Statistical Computing.** *R Foundation for Statistical Computing, Vienna, Austria*; 2022. <https://www.R-project.org>. Accessed November 1, 2021
- Lee H, Jung K, Kang DW, et al. **Fully automated and real-time volumetric measurement of infarct core and penumbra in diffusion- and perfusion-weighted MRI of patients with hyper-acute stroke.** *J Digit Imaging* 2020;33:262–72 CrossRef Medline
- Bandera E, Botteri M, Minelli C, et al. **Cerebral blood flow threshold of ischemic penumbra and infarct core in acute ischemic stroke: a systematic review.** *Stroke* 2006;37:1334–39 CrossRef Medline
- Smith SM, Jenkinson M, Johansen-Berg H, et al. **Tract-based spatial statistics: voxelwise analysis of multi-subject diffusion data.** *Neuroimage* 2006;31:1487–505 CrossRef Medline
- Smith SM, Jenkinson M, Woolrich MW, et al. **Advances in functional and structural MR image analysis and implementation as FSL.** *Neuroimage* 2004;23 Suppl 1:S208–S19 CrossRef Medline
- Griffis JC, Metcalf NV, Corbetta M, et al. **Lesion Quantification Toolkit: a MATLAB software tool for estimating grey matter damage and white matter disconnections in patients with focal brain lesions.** *Neuroimage Clin* 2021;30:102639 CrossRef Medline
- Finn ES, Shen X, Scheinost D, et al. **Functional connectome fingerprinting: identifying individuals using patterns of brain connectivity.** *Nat Neurosci* 2015;18:1664–71 CrossRef Medline
- Yeh FC, Panesar S, Fernandes D, et al. **Population-averaged atlas of the macroscale human structural connectome and its network topology.** *Neuroimage* 2018;178:57–68 CrossRef Medline
- Griffis JC, Metcalf NV, Corbetta M, et al. **Damage to the shortest structural paths between brain regions is associated with disruptions of resting-state functional connectivity after stroke.** *Neuroimage* 2020;210:116589 CrossRef Medline
- Lu J, Liu H, Zhang M, et al. **Focal pontine lesions provide evidence that intrinsic functional connectivity reflects polysynaptic anatomical pathways.** *J Neurosci* 2011;31:15065–71 CrossRef Medline
- Song KR, Potenza MN, Fang XY, et al. **Resting-state connectome-based support-vector-machine predictive modeling of internet gaming disorder.** *Addict Biol* 2021;26:e12969 CrossRef Medline
- Yang FN, Hassanzadeh-Behbahani S, Bronshteyn M, et al. **Connectome-based prediction of global cognitive performance**

- in people with HIV.** *Neuroimage Clin* 2021;30:102677 CrossRef Medline
32. Ren Z, Daker RJ, Shi L, et al. **Connectome-based predictive modeling of creativity anxiety.** *Neuroimage* 2021;225:117469 CrossRef Medline
33. Li S, Ma Z, Tu S, et al. **Altered resting-state functional and white matter tract connectivity in stroke patients with dysphagia.** *Neurorehabil Neural Repair* 2014;28:260–72 CrossRef Medline
34. Dai M, Qiao J, Wei X, et al. **Increased cortical-medulla functional connectivity is correlated with swallowing in dysphagia patients with subacute infratentorial stroke.** *Neuroimage Clin* 2022;35:103104 CrossRef Medline
35. Kim Y, Han YJ, Park HY, et al. **Neural correlates in the development of and recovery from dysphagia after supratentorial stroke: a prospective tractography study.** *Neuroimage Clin* 2022;35:103103 CrossRef Medline
36. Lebel C, Benner T, Beaulieu C. **Six is enough? Comparison of diffusion parameters measured using six or more diffusion-encoding gradient directions with deterministic tractography.** *Magn Reson Med* 2012;68:474–83 CrossRef Medline

Glymphatic System Dysfunction in Myelin Oligodendrocyte Glycoprotein Immunoglobulin G Antibody–Associated Disorders: Association with Clinical Disability

 Akifumi Hagiwara,  Yuji Tomizawa,  Yasunobu Hoshino,  Kazumasa Yokoyama,  Koji Kamagata,  Towa Sekine,  Kaito Takabayashi,  Moto Nakaya,  Tomoko Maekawa,  Toshiaki Akashi,  Akihiko Wada,  Toshiaki Taoka,  Shinji Naganawa,  Nobutaka Hattori, and  Shigeki Aoki



ABSTRACT

BACKGROUND AND PURPOSE: Impaired glymphatic function has been suggested to be implicated in the pathophysiology of MS and aquaporin-4 immunoglobulin G-positive neuromyelitis optica spectrum disorder. This study aimed to investigate the interstitial fluid dynamics in the brain in patients with myelin oligodendrocyte glycoprotein antibody disorders (MOGAD), another demyelinating disorder, using a noninvasive imaging technique called the diffusivity along the perivascular space (ALPS) index.

MATERIALS AND METHODS: A prospective study was conducted on 16 patients with MOGAD in remission and 22 age- and sex-matched healthy control subjects. MR imaging was performed using a 3T scanner, and the ALPS index was calculated using diffusion MR imaging data with a b-value of 1000 s/mm². The ALPS index and gray matter volumes were compared between the 2 groups, and these parameters were correlated with the Expanded Disability Status Scale.

RESULTS: The mean ALPS index of patients with MOGAD was significantly lower than that of healthy controls (Cohen $d = 0.93$, false discovery rate–corrected $P = .02$). The lower mean ALPS index was significantly associated with a worse Expanded Disability Status Scale score (Spearman $\rho = -0.51$; 95% CI, -0.85 to -0.02 ; $P = .03$). However, cortical volume and deep gray matter volume were not significantly different between the 2 groups, and they were not correlated with the Expanded Disability Status Scale.

CONCLUSIONS: This study suggests that patients with MOGAD may have impaired glymphatic function, as measured by the ALPS index, which is associated with patient disability. Further study is warranted with a larger sample size.

ABBREVIATIONS: ALPS = diffusivity along the perivascular space; EDSS = Expanded Disability Status Scale; FA = fractional anisotropy; FDR = false discovery rate; IgG = immunoglobulin G; MOG = myelin oligodendrocyte glycoprotein; MOGAD = myelin oligodendrocyte glycoprotein antibody disorders; NMOSD = neuromyelitis optica spectrum disorder; QRAPMASTER = quantification of relaxation times and proton density by multiecho acquisition of a saturation-recovery by using turbo spin-echo readout

Myelin oligodendrocyte glycoprotein antibody disorders (MOGAD) is a newly recognized entity of demyelinating disorders of the CNS defined by the presence of serum immunoglobulin G (IgG) autoantibodies against myelin oligodendrocyte glycoprotein (MOG).^{1,2} MOGAD occurs in both children and

adults and is distinct from other neuroinflammatory and demyelinating diseases such as MS or aquaporin-4 IgG-positive neuromyelitis optica spectrum disorder (NMOSD).^{3,4} In MOGAD, similar to other demyelinating disorders, breakdown of the BBB and blood-CSF barrier occurs.^{5,6} The pathologic hallmark of MOGAD is coexisting perivenous and confluent demyelination with relatively preserved oligodendrocytes.^{4,7} A CD4-positive T-cell activation with cytokine release and granulocytic inflammation is typical,^{4,7,8} while humoral immunity with complement deposition is occasionally observed.^{4,7,9} In addition, the production of reactive oxygen species and the accumulation of iron in the CNS contribute to the disease burden observed in experimental animal models of demyelination.^{10,11} A waste-clearing system of the brain may be useful in avoiding further tissue damage due to the accumulation of neurotoxic waste products following inflammatory activity.


While the brain lacks a conventional lymphatic system, recent studies have shown evidence of the existence of a waste-clearance system called the “glymphatic system.”^{12,13} This system is highly

Received June 21, 2023; accepted after revision October 17.

From the Departments of Radiology (A.H., K.K., T.S., K.T., M.N., T.M., T.A., A.W., S.A.) and Neurology (Y.T., Y.H., N.H.), Juntendo University School of Medicine, Tokyo, Japan; Tousei Neurology Center (K.Y.), Shizuoka, Japan; Department of Radiology (M.N.), Graduate School of Medicine, The University of Tokyo, Tokyo, Japan; and Department of Radiology (T.T., S.N.), Nagoya University Graduate School of Medicine, Aichi, Japan.

This work was supported by JSPS KAKENHI grant Nos. 23K07189 and 22K20896 and the Juntendo Research Branding Project.

Please address correspondence to Akifumi Hagiwara, MD, Department of Radiology, Juntendo University School of Medicine, 1-2-1, Hongo, Bunkyo-ku, Tokyo, Japan, 113-8421; e-mail: a-hagiwara@juntendo.ac.jp; @Akifumi0314

 Indicates open access to non-subscribers at www.ajnr.org

<http://dx.doi.org/10.3174/ajnr.A8066>

organized and functions as a fluid transport system, where CSF enters the brain parenchyma and disperses throughout the interstitium via perivascular spaces created by the vascular end-feet of astrocytes. CSF mixes with interstitial fluid, including waste products, and flows through perivenous spaces toward the brain meninges, where it is collected and exported from the CNS via meningeal and cervical lymphatic vessels.¹⁴ The deposition of iron causes impairment of the lymphatic system,¹⁵ which, in turn, leads to the accumulation of reactive oxygen species.¹⁶ The lymphatic system also clears signaling molecules associated with neuroinflammation,¹⁷ and impaired lymphatic function in the presence of neuroinflammation may worsen inflammation by inhibiting the removal of cytokines from the brain.¹⁸

Despite the increasing interest in the lymphatic system, the lack of noninvasive techniques has hindered the *in vivo* assessment of its function. Recent studies have used MR imaging to assess lymphatic function, with most using a relatively invasive technique involving the administration of a gadolinium-based contrast agent via intrathecal or IV injection.¹⁹ However, a diffusion-weighted MR imaging technique called diffusivity along the perivascular space (ALPS) has been proposed as a promising noninvasive alternative that does not require the use of tracers.^{20,21} ALPS calculates the diffusivity along the deep medullary vein and perivascular space at the level of the lateral ventricle body, providing a measure of perivascular clearance activity in the human brain. A recent study validated the ALPS index as a measure of lymphatic function by correlating it with lymphatic function measurements based on MR imaging after intrathecal administration of a gadolinium-based contrast agent.²² The ALPS index was found to be lower in various neurologic disorders such as Alzheimer disease²³ and Parkinson disease²⁴ compared with healthy volunteers. In addition, the ALPS index was also lower in MS and NMO/D than in healthy controls, suggesting an impaired lymphatic system in these demyelinating disorders.^{25,26}

Therefore, we hypothesized that the lymphatic system is impaired in patients with MOGAD and contributes to clinical disability by indirectly worsening inflammatory and neurodegenerative processes due to the inefficient removal of soluble waste products, maintaining a proinflammatory state of the brain tissue. We investigated patients with MOGAD using ALPS and correlated the measurements with clinical disability.

MATERIALS AND METHODS

Study Participants

This study was approved by the institutional review board of Juntendo University Hospital, and written informed consent was obtained from all participants. We prospectively recruited 16 patients diagnosed with MOGAD (defined as MOG-antibody positivity using cell-based assays in the context of an acute demyelinating event in patients presenting with a MOGAD phenotype without red flags against a diagnosis of MOGAD, as previously described^{2,27}) from March 2018 to February 2022. Disability was assessed using the Expanded Disability Status Scale (EDSS).²⁸ Patients were consecutively recruited during the remission phase of the disease and had been on stable disease-modifying treatment, oral corticosteroids, or no treatment for at least 3 months and had been free of clinical relapse within the 3 months and IV corticosteroid use within 1 year before MR

imaging. As a control group, we also recruited 22 age- and sex-matched healthy subjects without neurologic and psychological symptoms or a history of neuropsychological disorders. Acquired images were confirmed not to include abnormalities such as moderate-to-severe WM ischemic lesions (Fazekas grade 2 or higher²⁹), brain infarction, or tumors.

Image Acquisition and Processing

MR imaging was performed using a 3T scanner (Discovery MR750w; GE Healthcare) with a 19-channel head coil. All participants underwent diffusion MR imaging, 3D T1-weighted imaging, and a 2D axial quantification of relaxation times and proton density by multiecho acquisition of a saturation-recovery by using turbo spin-echo readout (QRAPMASTER) pulse sequence.

Diffusion MR imaging was performed using a single-shot echo-planar imaging sequence along 30 motion-probing gradient directions with $b=1000/\text{mm}^2$. In addition, a volume of non-diffusion-weighted images was acquired. The other sequence parameters were the following: TR = 5000 ms, TE = 88.2 ms, FOV = 256×256 mm, matrix size = 256×256 , echo-train length = 128, bandwidth = 1953.12 kHz, section thickness/gap = 4.0/1.0 mm, slices = 30, and acquisition time = 2 minutes 37 seconds. All data sets were visually inspected for artifacts. We corrected in-plane and through-plane distortions of the DWIs caused by eddy currents and motion by using affine brain registration to the non-diffusion-weighted images.³⁰ Processed images were further denoised using position-orientation adaptive smoothing based on the propagation-separation approach.³¹ The fractional anisotropy (FA) map was computed using diffusion data with $b=0$ and 1000 s/mm^2 by fitting a tensor model. Postprocessing was performed with an in-house program in Matlab (release 2018a; MathWorks).

The acquisition parameters for the 3D T1-weighted images (inversion-recovery spoiled gradient-echo) were as follows: TR = 7.6 ms, TE = 3.09 ms, TI = 400 ms, bandwidth = 244 Hz/pixel, section thickness = 1 mm, FOV = 256×256 mm, matrix size = 256×256 , and acquisition time = 5 minutes 45 seconds.

The QRAPMASTER is a method of acquisition that uses a multislice, multiecho, multisaturation-delay saturation-recovery turbo spin-echo technique to collect images with combinations of 2 TEs and 4 saturation-delay times.³² We used TEs of 16.9 and 84.5 ms and delay times of 146, 546, 1879, and 3879 ms. The other parameters were as follows: TR = 4.0 seconds, FOV = 240×240 mm, matrix = 320×320 , echo-train length = 10, bandwidth = 31.25 kHz, section thickness/gap = 4.0/1.0 mm, slices = 30, and acquisition time = 7 minutes 12 seconds. The 8 complex images obtained per section were postprocessed using the SyMRI software (Version 8.0; SyntheticMR) to derive longitudinal R1 relaxation and transverse R2 relaxation rates and proton density. Synthetic FLAIR images were created using the R1, R2, and proton density maps with the following postprocessing parameters: TR = 15,000 ms, TE = 100 ms, TI = 3000 ms. An affine transformation was performed to register the acquired images using Statistical Parametric Mapping software (SPM12; <http://www.fil.ion.ucl.ac.uk/spm/software/spm12>).

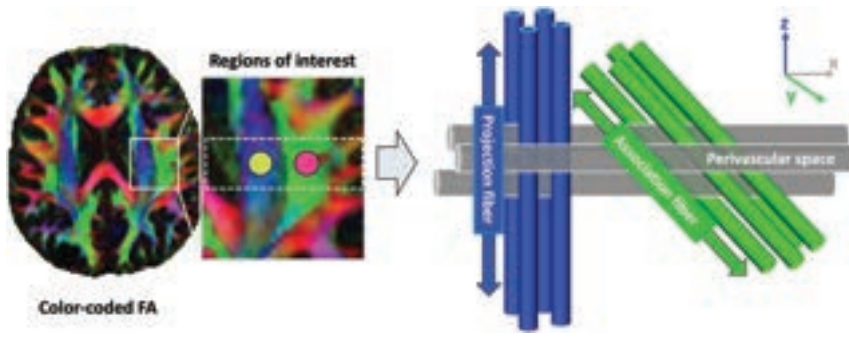


FIG 1. ROI placement for ALPS index calculation. A, A color-coded FA map shows the distribution of projection fibers (blue along z-axis) and association fibers (green along y-axis) at the lateral ventricle level. Spherical ROIs with a 5-mm diameter were placed in the projection and association areas. B, A schematic illustration of the relationship between the principal fiber and perivascular spaces, with the perivascular space running parallel to the medullary vein and perpendicular to the projection and association fibers.

Demographic characteristics of the participants

	Healthy Controls	MOGAD	P Value
No.	22	16	NA
Age (mean) (yr) ^a	44.77 (SD, 14.58)	44.19 (SD, 17.93)	.94
Sex (male/female) ^b	6/16	4/12	.88
Disease duration (mean) (yr)	NA	8.06 (SD, 11.86)	NA
EDSS (median) (range)	NA	0 (0–7)	NA
WM lesion, (mean) (mL)	NA	8.81 (SD, 7.67)	NA

Note:— NA indicates not applicable.

^a The statistical analysis was performed with a *t* test.

^b The statistical analysis was performed with a χ^2 test.

Lesion Maps

For all patients, hyperintense lesions were automatically segmented on synthetic FLAIR images by using the lesion-prediction algorithm³³ implemented in the Lesion Segmentation Toolbox (Version 2.0.15; <https://www.applied-statistics.de/lst.html>)³⁴ running in SPM12. All lesion maps were visually inspected and manually corrected by an expert neuroradiologist (A.H.) with 12 years of experience. The whole-brain WM lesion volume in each patient was calculated by multiplying the lesion area by the section thickness.

Brain Volumes

Before segmentation and volume calculation, the Lesion Segmentation Toolbox was used to fill the WM lesions detected on FLAIR images for the 3D T1-weighted images. The cortex and subcortical gray matter were segmented using FreeSurfer (Version 6.0; <http://surfer.nmr.mgh.harvard.edu>)³⁵ and the FMRIB Software Library (Version 6.0.0; <http://www.fmrib.ox.ac.uk/fsl/>)³⁶ respectively. These segmentation masks were used to calculate the cortical volume and subcortical gray matter volume for each participant.

Calculation of the ALPS Index

The ALPS index was calculated from the DWI data using a semi-automated pipeline developed and validated by Taoka et al.³⁷ The FA maps of all participants were registered to a FMRIB58_FA standard space image (https://fsl.fmrib.ox.ac.uk/fsl/fslwiki/FMRIB58_FA) through linear and nonlinear transformations. Spherical ROIs of 5-mm diameter were placed in the projection and association fiber areas at the level of the lateral ventricle bodies in both hemispheres using

the native color-coded FA map of the participant with the least warping (ie, the smallest sum of squared differences) (Fig 1). The ROIs were registered to the standard space image and then to the FA map of each participant. The position of the ROI was manually verified by referring to the lesion map. If the ROI overlapped with a lesion, the position of the ROI was manually shifted to avoid overlap while ensuring that the 2 ROIs were placed perpendicular to the lateral ventricles. This step is important because the perpendicular alignment between the perivascular space and nerve fiber direction adjacent to the lateral ventricles may be disrupted due to demyelination.²⁵

Finally, the ALPS index was calculated as the mean of the x-axis diffusivity in the projection area ($D_{xx,proj}$) and x-axis diffusivity in the association area ($D_{xx,assoc}$), divided by the mean of the y-axis diffusivity in the projection area ($D_{yy,proj}$) and the z-axis diffusivity in the association area ($D_{zz,assoc}$) as follows:

$$ALPS\ index = \frac{Mean(D_{xx,proj}, D_{xx,assoc})}{Mean(D_{yy,proj}, D_{zz,assoc})}$$

The left and right ALPS indices were then averaged and used for statistical analysis. An ALPS index close to 1.0 suggests minimal diffusivity along the perivascular space, while a higher value indicates increased diffusivity.

Statistical Analysis

Demographic variables for patients with MOGAD and healthy controls were compared using a *t* test or χ^2 test as appropriate. Structural MR imaging metrics and the mean ALPS index were compared between patients with MOGAD and healthy controls using a *t* test, with false discovery rate (FDR) correction applied to consider multiple comparisons of these MR imaging metrics. Cohen *d* effect sizes of the group differences were calculated. The Spearman rank correlation test was used to investigate the associations of MR imaging measurements in patients with MOGAD with EDSS scores and disease duration. Matlab was used for statistical analyses, with statistical significance set at $P < .05$.

RESULTS

The demographic characteristics of the healthy control group and patients with MOGAD are presented in the Table. There were no significant differences in age and sex between the 2 groups. Of the 16 patients with MOGAD, 14 were receiving chronic oral steroids, while none were on disease-modifying treatments.

Figure 2 displays violin and box plots comparing the MR imaging metrics of the MOGAD and healthy control groups. There was no patient with MOGAD who required manual correction of an ROI to avoid a WM lesion. The mean ALPS index

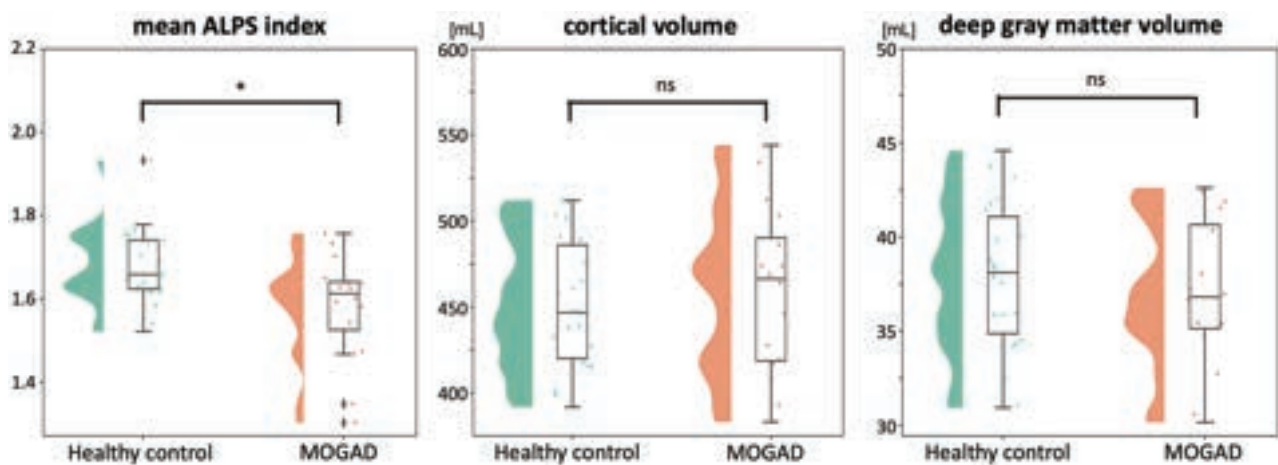


FIG 2. Violin and box plots of the MR imaging metrics compared between the MOGAD and healthy control groups. The asterisk indicates FDR-corrected $P < .05$; ns, indicates no significance.

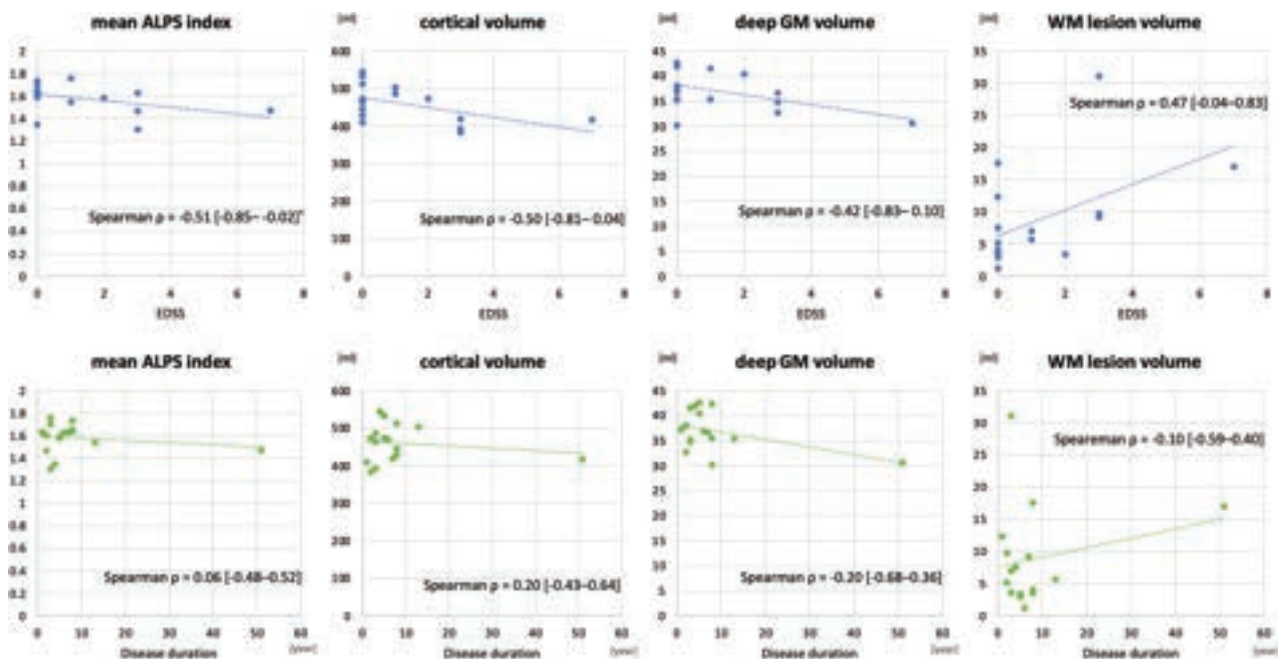


FIG 3. Scatterplots are presented to show the correlations between clinical characteristics and MR imaging metrics. An asterisk indicates statistical significance at $P < .05$.

of the patients with MOGAD was significantly lower than that of the control group (1.58 [SD, 0.13] versus 1.68 [SD, 0.09], FDR-corrected $P = .02$, Cohen $d = 0.93$). However, cortical volume and deep gray matter volume did not differ significantly between patients with MOGAD and healthy controls (459.68 [SD, 49.01] mL versus 451.73 [SD, 37.97] mL, FDR-corrected $P = .58$, Cohen $d = 0.19$; 37.00 [SD, 3.97] mL versus 37.86 [SD, 4.00] mL, FDR-corrected $P = .58$, Cohen $d = 0.21$). Moreover, the mean ALPS index of the patients with MOGAD was significantly negatively correlated with EDSS ($\rho = -0.51$; 95% CI, -0.85 to -0.02 ; $P = .03$) but not with disease duration ($\rho = 0.06$; 95% CI, -0.48 – 0.52 , $P = .67$) (Fig 3). Cortical volume and WM lesion volume were not significantly correlated with EDSS or disease duration.

DISCUSSION

In the current study, we investigated the function of the interstitial fluid dynamics in patients with MOGAD in remission, using a noninvasive MR imaging metric called the ALPS index, which measures diffusivity along the perivascular space. Our results showed that the ALPS index was significantly lower in patients with MOGAD compared with healthy controls, indicating reduced interstitial fluid dynamics, which may suggest impaired glymphatic system function in MOGAD. Additionally, we found a significant correlation between the ALPS index in patients with MOGAD and their clinical disability.

Impaired interstitial fluid dynamics, as indicated by a decreased ALPS index, has also been reported in other neuroinflammatory diseases, namely MS and NMO/DM. Like our study, these

previous studies investigated patients during their relapse-free phase. Neuroinflammation can impede the process of vascular polarization of aquaporin-4 from the astrocytic end-feet toward the soma due to abnormal localization of aquaporin-4, ultimately resulting in a reduction in glymphatic flow.¹⁷ Several studies have demonstrated that conditions associated with chronic neuroinflammation can sustain this decreased glymphatic flow.³⁸⁻⁴⁰ Additionally during inflammation, immune cells that infiltrate the perivascular spaces are known to accumulate, potentially obstructing the flow of fluid around the blood vessels and impeding the influx of CSF.⁴¹⁻⁴³ This disruption in glymphatic flow, along with the resulting buildup of cytokines and metabolic wastes, may contribute to a harmful cycle that perpetuates neuroinflammation.⁴⁴ Previous damage to the glymphatic system during the attack phase, ongoing inflammation and neurodegeneration, or both can be possible causes of the decreased ALPS index in demyelinating disorders, including MOGAD investigated in the current study.

A previous study demonstrated lower cortical and deep gray matter volumes in patients with MOGAD compared with healthy controls,⁴⁵ while the current study did not show a statistically significant difference. Additionally, the previous study showed a significant negative correlation between deep gray matter volume and the EDSS score, which was not observed in the current study. These discrepancies could be due to the smaller sample size of the current study. However, the current study found a significant difference in the ALPS index between patients with MOGAD and healthy controls, as well as a significant negative correlation between the index and EDSS scores. Therefore, the ALPS index may be a more sensitive biomarker for reflecting the disease process of MOGAD than brain volumes. The causative role of glymphatic dysfunction in patient disability should be investigated through longitudinal studies. Such studies may eventually evaluate the potential of glymphatic function assessment as a predictive marker of relapse and disease progression.

In MS, the ALPS index showed a correlation with disease duration, whereas in NMOSD and MOGAD, it did not. This finding may suggest an early glymphatic function impairment in NMOSD and MOGAD, which could be linked to the pathophysiology of the diseases, because these 2 disorders rarely have a progressive disease course.² In these disorders, the severity of clinical manifestations is likely to be influenced by the magnitude of the pathogenic mechanism, irrespective of the disease duration.

There are some limitations to the current study. First, the sample size was small. A further study is warranted with a larger sample size to confirm our findings. Second, the ALPS index is limited in its ability to assess glymphatic function throughout the entire brain due to its reliance on the geometric relationship between projection and association fibers and medullary arteries and veins in the lateral ventricle body.^{20,46} Therefore, the ALPS index can be evaluated only at the lateral ventricle body level. Additionally, the ALPS index does not exclusively measure the diffusivity of the perivenous space surrounding the deep medullary vein but is also affected by the surrounding WM microstructure within the ROI. Also, the timescale of the measurement by the ALPS index is much shorter than the actual rate of flow for glymphatic clearance.⁴⁷ Hence, careful interpretation and further investigation of the ALPS index are necessary. Furthermore, we

did not use gadolinium-based contrast agents to measure glymphatic function in our study. While the use of CSF tracers is rather invasive, it is currently considered the criterion standard for assessing glymphatic function.⁴⁶ However, the ALPS index has shown a high correlation with glymphatic function measures obtained through MR imaging with administration of an intrathecal gadolinium-based contrast agent.²²

CONCLUSIONS

We used the ALPS index, a noninvasive method, to assess the function of the glymphatic system. We demonstrated that patients with MOGAD exhibit impaired glymphatic function and that reduced glymphatic function is linked to patient disability. The findings of this study could potentially enhance our understanding of the pathophysiology of MOGAD and contribute to the development of new therapeutic strategies.

Disclosure forms provided by the authors are available with the full text and PDF of this article at www.ajnr.org.

REFERENCES

1. Reindl M, Schanda K, Woodhall M, et al. **International multicenter examination of MOG antibody assays.** *Neurol Neuroimmunol Neuroinflamm* 2020;7:e674 CrossRef Medline
2. Banwell B, Bennett JL, Marignier R, et al. **Diagnosis of myelin oligodendrocyte glycoprotein antibody-associated disease: International MOGAD Panel proposed criteria.** *Lancet Neurol* 2023;22:268–82 CrossRef Medline
3. Kim H, Lee EJ, Kim S, et al. **Serum biomarkers in myelin oligodendrocyte glycoprotein antibody-associated disease.** *Neurol Neuroimmunol Neuroinflamm* 2020;7:e708 CrossRef
4. Höftberger R, Guo Y, Flanagan EP, et al. **The pathology of central nervous system inflammatory demyelinating disease accompanying myelin oligodendrocyte glycoprotein autoantibody.** *Acta Neuropathol* 2020;139:875–92 CrossRef Medline
5. Tanaka S, Hashimoto B, Izaki S, et al. **Clinical and immunological differences between MOG associated disease and anti AQP4 antibody-positive neuromyelitis optica spectrum disorders: blood-brain barrier breakdown and peripheral plasmablasts.** *Mult Scler Relat Disord* 2020;41:102005 CrossRef Medline
6. Jarius S, Pellkofer H, Siebert N, et al; in cooperation with the Neuromyelitis Optica Study Group (NEMOS). **Cerebrospinal fluid findings in patients with myelin oligodendrocyte glycoprotein (MOG) antibodies, Part 1: results from 163 lumbar punctures in 100 adult patients.** *J Neuroinflammation* 2020;17:261 CrossRef Medline
7. Takai Y, Misu T, Kaneko K, et al; Japan MOG-antibody Disease Consortium. **Myelin oligodendrocyte glycoprotein antibody-associated disease: an immunopathological study.** *Brain* 2020;143:1431–46 CrossRef Medline
8. Kaneko K, Sato DK, Nakashima I, et al. **CSF cytokine profile in MOG-IgG neurological disease is similar to AQP4-IgG NMOSD but distinct from MS: a cross-sectional study and potential therapeutic implications.** *J Neurol Neurosurg Psychiatry* 2018;89:927–36 CrossRef Medline
9. Jarius S, Metz I, König FB, et al. **Screening for MOG-IgG and 27 other anti-gial and anti-neuronal autoantibodies in 'pattern II multiple sclerosis' and brain biopsy findings in a MOG-IgG-positive case.** *Mult Scler* 2016;22:1541–49 CrossRef Medline
10. Zarruk JG, Berard JL, Passos dos Santos R, et al. **Expression of iron homeostasis proteins in the spinal cord in experimental autoimmune encephalomyelitis and their implications for iron accumulation.** *Neurobiol Dis* 2015;81:93–107 CrossRef Medline

11. Ruuls SR, Bauer J, Sontrop K, et al. **Reactive oxygen species are involved in the pathogenesis of experimental allergic encephalomyelitis in Lewis rats.** *J Neuroimmunol* 1995;56:207–17 CrossRef Medline
12. Iliff JJ, Wang M, Liao Y, et al. **A paravascular pathway facilitates CSF flow through the brain parenchyma and the clearance of interstitial solutes, including amyloid β .** *Sci Transl Med* 2012;4:147ra111 CrossRef Medline
13. Lohela TJ, Lilius TO, Nedergaard M. **The glymphatic system: implications for drugs for central nervous system diseases.** *Nat Rev Drug Discov* 2022;21:763–79 CrossRef Medline
14. Nedergaard M, Goldman SA. **Glymphatic failure as a final common pathway to dementia.** *Science* 2020;370:50–56 CrossRef Medline
15. Liang S, Lu Y, Li Z, et al. **Iron aggravates the depressive phenotype of stressed mice by compromising the glymphatic system.** *Neurosci Bull* 2020;36:1542–46 CrossRef Medline
16. Gu S, Li Y, Jiang Y, et al. **Glymphatic dysfunction induced oxidative stress and neuro-inflammation in major depression disorders.** *Antioxidants (Basel)* 2022;11:2296 CrossRef Medline
17. Mogensen FL, Delle C, Nedergaard M. **The glymphatic system (en) during inflammation.** *Int J Mol Sci* 2021;22:7491 CrossRef Medline
18. Filiano AJ, Gadani SP, Kipnis J. **How and why do T cells and their derived cytokines affect the injured and healthy brain?** *Nat Rev Neurosci* 2017;18:375–84 CrossRef Medline
19. Naganawa S, Taoka T. **The glymphatic system: a review of the challenges in visualizing its structure and function with MR imaging.** *Magn Reson Med Sci* 2022;21:182–94 CrossRef Medline
20. Taoka T, Masutani Y, Kawai H, et al. **Evaluation of glymphatic system activity with the diffusion MR technique: diffusion tensor image analysis along the perivascular space (DTI-ALPS) in Alzheimer's disease cases.** *Jpn J Radiol* 2017;35:172–78 CrossRef Medline
21. Taoka T, Ito R, Nakamichi R, et al. **Diffusion-weighted image analysis along the perivascular space (DWI-ALPS) for evaluating interstitial fluid status: age dependence in normal subjects.** *Jpn J Radiol* 2022;40:894–902 CrossRef Medline
22. Zhang W, Zhou Y, Wang J, et al. **Glymphatic clearance function in patients with cerebral small vessel disease.** *NeuroImage* 2021;238:118257 CrossRef Medline
23. Kamagata K, Andica C, Takabayashi K, et al; for the Alzheimer's Disease Neuroimaging Initiative. **Association of MRI indices of glymphatic system with amyloid deposition and cognition in mild cognitive impairment and Alzheimer disease.** *Neurology* 2022;99:e2648–60 CrossRef Medline
24. Chen HL, Chen PC, Lu CH, et al. **Associations among cognitive functions, plasma DNA, and diffusion tensor image along the perivascular space (DTI-ALPS) in patients with Parkinson's disease.** *Oxidative Medicine and Cellular Longevity* 2021;2021:1–10.
25. Carotenuto A, Cacciaguerra L, Pagani E, et al. **Glymphatic system impairment in multiple sclerosis: relation with brain damage and disability.** *Brain* 2022;145:2785–95 CrossRef Medline
26. Cacciaguerra L, Carotenuto A, Pagani E, et al. **Magnetic resonance imaging evaluation of perivascular space abnormalities in neuro-myelitis optica.** *Ann Neurol* 2022;92:173–83 CrossRef Medline
27. Marignier R, Hachon Y, Cobo-Calvo A, et al. **Myelin-oligodendrocyte glycoprotein antibody-associated disease.** *Lancet Neurol* 2021;20:762–72 CrossRef Medline
28. Kurtzke JF. **A new scale for evaluating disability in multiple sclerosis.** *Neurology* 1955;5:580–83 CrossRef Medline
29. Fazekas F, Chalwilk JB, Alavi A, et al. **MR signal abnormalities at 1.5 T in Alzheimer's dementia and normal aging.** *AJR Am J Roentgenol* 1987;149:351–56 CrossRef Medline
30. Mohammadi S, Möller HE, Kugel H, et al. **Correcting eddy current and motion effects by affine whole-brain registrations: evaluation of three-dimensional distortions and comparison with slice-wise correction.** *Magn Reson Med* 2010;64:1047–56 CrossRef Medline
31. Becker SM, Tabelow K, Voss HU, et al. **Position-orientation adaptive smoothing of diffusion weighted magnetic resonance data (POAS).** *Med Image Anal* 2012;16:1142–55 CrossRef Medline
32. Hagiwara A, Warntjes M, Hori M, et al. **SyMRI of the brain: rapid quantification of relaxation rates and proton density, with synthetic MRI, automatic brain segmentation, and myelin measurement.** *Invest Radiol* 2017;52:647–57 CrossRef Medline
33. Egger C, Opfer R, Wang C, et al. **MRI FLAIR lesion segmentation in multiple sclerosis: does automated segmentation hold up with manual annotation?** *Neuroimage Clin* 2017;13:264–70 CrossRef Medline
34. Schmidt P, Gaser C, Arsic M, et al. **An automated tool for detection of FLAIR-hyperintense white-matter lesions in multiple sclerosis.** *Neuroimage* 2012;59:3774–83 CrossRef Medline
35. Fischl B. **FreeSurfer.** *Neuroimage* 2012;62:774–81 CrossRef Medline
36. Patenaude B, Smith SM, Kennedy DN, et al. **A Bayesian model of shape and appearance for subcortical brain segmentation.** *Neuroimage* 2011;56:907–22 CrossRef Medline
37. Taoka T, Ito R, Nakamichi R, et al. **Reproducibility of diffusion tensor image analysis along the perivascular space (DTI-ALPS) for evaluating interstitial fluid diffusivity and glymphatic function: CHanges in Alps index on Multiple condition acquisition eXperiment (CHAMONIX) study.** *Jpn J Radiol* 2022;40:147–58 CrossRef Medline
38. Kress BT, Iliff JJ, Xia M, et al. **Impairment of paravascular clearance pathways in the aging brain.** *Ann Neurol* 2014;76:845–61 CrossRef Medline
39. Ren Z, Iliff JJ, Yang L, et al. **'Hit & Run' model of closed-skull traumatic brain injury (TBI) reveals complex patterns of post-traumatic AQP4 dysregulation.** *J Cereb Blood Flow Metab* 2013;33:834–45 CrossRef Medline
40. Wang M, Iliff JJ, Liao Y, et al. **Cognitive deficits and delayed neuronal loss in a mouse model of multiple microinfarcts.** *J Neurosci* 2012;32:17948–60 CrossRef Medline
41. Rustenhoven J, Drieu A, Mamuladze T, et al. **Functional characterization of the dural sinuses as a neuroimmune interface.** *Cell* 2021;184:1000–16.e27 CrossRef Medline
42. Ivan DC, Walthert S, Berve K, et al. **Dwellers and trespassers: mononuclear phagocytes at the borders of the central nervous system.** *Front Immunol* 2020;11:609921 CrossRef Medline
43. Zhou H, Andonegui G, Wong CHY, et al. **Role of endothelial TLR4 for neutrophil recruitment into central nervous system microvessels in systemic inflammation.** *J Immunol* 2009;183:5244–50 CrossRef Medline
44. Salvador AF, de Lima KA, Kipnis J. **Neuromodulation by the immune system: a focus on cytokines.** *Nat Rev Immunol* 2021;21:526–41 CrossRef Medline
45. Duan Y, Zhuo Z, Li H, et al. **Brain structural alterations in MOG antibody diseases: a comparative study with AQP4 seropositive NMOSD and MS.** *J Neurol Neurosurg Psychiatry* 2021;92:709–16 CrossRef Medline
46. Naganawa S, Taoka T, Ito R, et al. **The glymphatic system in humans: investigations with magnetic resonance imaging.** *Invest Radiol* 2023 Mar 13 [Epub ahead of print] CrossRef
47. Pla V, Bork P, Harnpramukkul A, et al. **A real-time in vivo clearance assay for quantification of glymphatic efflux.** *Cell Rep* 2022;40:111320 CrossRef Medline

Prevalence of Developmental Venous Anomalies in Association with Sporadic Cavernous Malformations on 7T MRI

✉ Petrice M. Cogswell, ✉ Jay J. Pillai, ✉ Giuseppe Lanzino, and ✉ Kelly D. Flemming

ABSTRACT

BACKGROUND AND PURPOSE: The etiology of sporadic cavernous malformations is not well-understood. However, recent evidence suggests that they may arise from a developmental venous anomaly. The goal of this study was to evaluate the prevalence of developmental venous anomalies associated with sporadic cavernous malformations using 7T MR imaging.

MATERIALS AND METHODS: We retrospectively identified patients with a sporadic cavernous malformation imaged with 7T MR imaging between August 2019 and July 2022. Two raters determined whether a developmental venous anomaly was associated with each malformation.

RESULTS: The study included 59 patients with a total of 61 cavernous malformations. Of the sixty-one, 44 (72%) had an associated developmental venous anomaly. An associated anomaly was most common for cavernous malformations in the brainstem (88%) compared with the cerebral hemispheres or cerebellum (60%–67%).

CONCLUSIONS: By means of high-quality 7T imaging, most patients with a sporadic cavernous malformation were found to have an associated developmental venous anomaly. These findings support the hypothesis that cavernous malformations may arise secondary to hemodynamic abnormalities.

ABBREVIATIONS: CM = cavernous malformation; DVA = developmental venous anomaly; VM = venous malformation

Cavernous malformations (CMs) are vascular malformations identified in <1% of the population that may occur in sporadic or familial forms.¹ Sporadic CMs most commonly occur as a single lesion, and multiple CMs are more commonly found in patients with familial multiple CM syndrome.^{1,2} Familial CMs are thought to arise secondary to mutations in 1 of 3 known cerebral CM genes that lead to increased vascular permeability. The etiology of sporadic CMs is less well-understood, but recent studies have helped elucidate implicated somatic gene mutations. Sporadic CMs require either 2 somatic CM gene mutations in the same cell or a single gain-of-function mutation in the gene mitogen activated protein kinase 3 (*MAP3K3*). Mutations of the gene phosphatidylinositol-4,5-bisphosphate 3-kinase catalytic subunit alpha (*PIK3CA*) have also been implicated in sporadic CM genesis and symptomatic disease.³ An analysis in a limited number of patients demonstrated *PIK3CA* mutations in adjacent developmental venous anomalies

(DVAs), suggesting that sporadic CMs may be derived from cells of the DVA.³

DVAs may be visualized on postcontrast T1WI as well as T2*-WI, which are sensitive to heme products based on the susceptibility effects. In large cohorts, approximately 20%–40% of sporadic CMs will have a DVA detected on gradient-echo MR imaging, bringing into question the theory that the CM arises from a DVA in every sporadic CM.⁴ More recently, however, SWI has been developed and has improved detection of venous structures. SWI combines phase and magnitude information to create images that are sensitive to local susceptibility changes. On the basis of higher signal and improved spatial resolution, SWI is more sensitive than standard T2* gradient-echo sequences for the detection of heme products, including those associated with CMs.^{5,6} SWI also allows improved depiction of venous structures, including DVAs.

In addition to the choice of imaging sequences, higher MR imaging field strength may provide improved detection of lesions such as DVAs. Specifically, high-field imaging (>3T) has become more prevalent during the past several years, with human 7T MR imaging available at many academic institutions. High-field (7T) MR imaging provides improved signal relative to 3T and 1.5T and may support improved spatial resolution. Prior studies have

Received August 28, 2023; accepted after revision October 25.

From the Departments of Radiology (P.M.C., J.J.P., G.L.), Neurosurgery (G.L.), and Neurology (K.D.F.), Mayo Clinic, Rochester, Minnesota.

Please address correspondence to Petrice M. Cogswell MD, PhD, Mayo Clinic, 200 First St SW, Rochester, MN 55905; e-mail: Cogswell.petrice@mayo.edu

<http://dx.doi.org/10.3174/ajnr.A8072>

Frequency of CMs and associated DVAs by location^a

	Cerebral	Basal Ganglia	Brainstem	Cerebellum	Total
All CMs	36	5	17	3	61
Associated DVA	24 (67%)	3 (60%)	15 (88%)	2 (67%)	44 (72%)
Solitary CM	31	5	16	3	55
Associated DVA	20 (65%)	3 (60%)	14 (88%)	2 (67%)	39 (71%)
Clustered CM	5	0	1	0	6
Associated DVA	4 (80%)	0	1 (100%)	0	5 (83%)

^a A cluster of CMs in a single region was considered a single CM incidence.

shown the potential benefits of high-field-strength imaging for detection of DVAs associated with CMs.⁷⁻⁹ With improved imaging technology, a higher number of sporadic CMs have been found to be associated with a DVA, and a 2017 study by Dammann et al⁷ suggested that all sporadic CMs are associated with a venous malformation (VM), either a typical VM (DVA) or an atypical VM (dilated draining vein or asymmetric venous structure). The purpose of this study was to test the hypothesis that most sporadic CMs are associated with a DVA when evaluated using SWI and postcontrast T1WI at 7T.

MATERIALS AND METHODS

Patients

This study included patients with sporadic CMs and no prior intracranial intervention who underwent 7T brain MR imaging between August 2019 and July 2022 and had research authorization. Patients with presumed familial CMs, as identified by familial history, numerous widespread CMs on brain MR imaging and/or genetics were excluded. Patients with multiple CMs in 1 location (clustered CMs) were included. The clinical presentation in each patient was recorded from medical records as per standard guidelines.¹⁰

Imaging

All subjects underwent 7T MR imaging using a standardized protocol that included T2 FSE, SWI, and MPRAGE performed before and after IV gadolinium contrast administration. The T2 FSE parameters were the following: TR/TE = 5790/56 ms, flip angle = 150°, FOV = 171 × 200 mm, matrix = 784 × 504, and section thickness = 2 mm. The SWI parameters were the following: TR/TE = 22/15 ms, flip angle = 15°, FOV = 165 × 200 mm, matrix = 640 × 480, and section thickness = 1.2 mm. The MPRAGE parameters were the following: TR/TE = 2240/3.05 ms, TI = 1050 ms, flip angle = 7°, FOV = 224 × 224 mm, matrix = 320 × 320 mm, and section thickness = 0.7 mm. In 2 patients no postcontrast imaging was performed.

Image Review

First, 1 rater (P.M.C.) identified all CMs using the SWI, T2 FSE, and precontrast MPRAGE sequences. The SWI was used to detect foci of susceptibility, and the T2 FSE and MPRAGE, to verify the presence of a discrete lesion compatible with a CM. Punctate foci of susceptibility, which were too small to characterize on T2 FSE (1–2 mm), were not included. The CM number, location, and size were evaluated. Location was specified as cerebral white matter (frontal, parietal, temporal, or occipital), basal ganglia, brainstem, or cerebellum. For patients with multiple CMs, the distribution

was characterized as a multifocal solitary CM (a single CM in one of the above regions) or clustered (multiple CMs in a single region). The CM size was measured as the greatest transverse dimension on the T2 FSE sequence; in patients with multiple CMs, the largest one in each region was measured.

Next, 2 readers (P.M.C. and J.J.P.) reviewed each case to evaluate the presence or absence of a DVA in association

with each CM or cluster of CMs using SWI and postcontrast MPRAGE sequences. An associated DVA was defined as a venous structure with a branching pattern (caput medusa) that terminated near the margin or immediately adjacent to the CM. If a DVA was present, it was characterized as having deep-versus-superficial venous drainage. The 2 readers independently reviewed a subset of 12 cases to evaluate for the presence or absence of a DVA; this subset was used to determine interrater agreement. The remaining cases were reviewed in consensus. Image review was performed using the multiplanar reformatting tool in Visage Imaging (Version 7.1; <https://visageimaging.com/>).

Statistical Analyses

Interrater agreement for the presence or absence of a DVA was evaluated use the κ statistic. Descriptive statistics were used to summarize CM and DVA characteristics.

RESULTS

The study included 59 patients with a mean age of 47 (SD, 15) years at the time of imaging; 27 (46%) were women. The initial clinical presentation was intracranial hemorrhage in 25 (42.4%) patients, seizure (no hemorrhage) in 8 (13.5%), and focal neurologic deficit without hemorrhage in 5 (8.5%), and 21 (35.6%) patients presented with incidental findings. The 7T MR imaging was completed an average of 34.8 months after the initial diagnostic MR imaging.

The prevalence of CMs and associated DVAs is presented in the Table. Of the 59 patients, 51 (86%) had a single CM, and 8 (14%) had >1. Of the 8 cases with multiple CMs, 6 had multiple CMs that were clustered in 1 region. The other 2 patients had single CMs in 2 different brain regions: 1 patient had a CM in the pons and another CM in the parietal cortex; a different patient had a CM in the temporal cortex and another CM in the caudate head. Therefore, there were 55 solitary CMs in 53 patients, and 6 CM clusters in 6 patients. CMs were most frequently located in the cerebral white matter (36/61, 59%) and brainstem (17/61, 29%), with only a few found in the basal ganglia or cerebellum (Table). The average CM size on the T2 FSE sequence was 16 (SD, 8) mm, with a range of 4–33 mm.

Of the 55 solitary CMs, 39 (71%) had an associated DVA (Fig 1). Of the 6 CM clusters, 5 (83%) had an associated DVA (Fig 2). Overall, CMs in the brainstem were more likely to have an associated DVA (88%) than CMs in the cerebellum (67%), cerebral white matter (65%), and basal ganglia (60%). Of the 44 DVAs present, more than half, 25 (56%) had deep venous drainage (Fig 3).

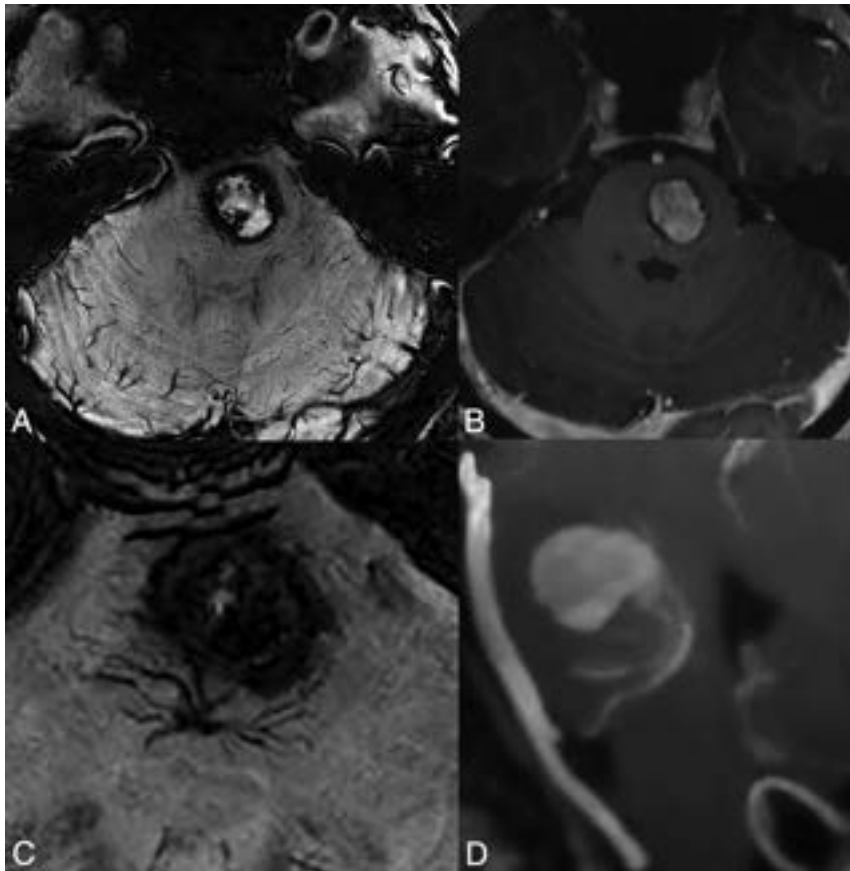


FIG 1. Representative CM with an associated DVA. Axial SWI (A and C) and postgadolinium MPRAGE (B and D) of a CM in the left aspect of the pons (A and B). Magnified axial-section SWI just inferior to the CM shows the caput medusa of the DVA (C). Sagittal MIP of a postgadolinium MPRAGE shows the DVA abutting the CM (D).

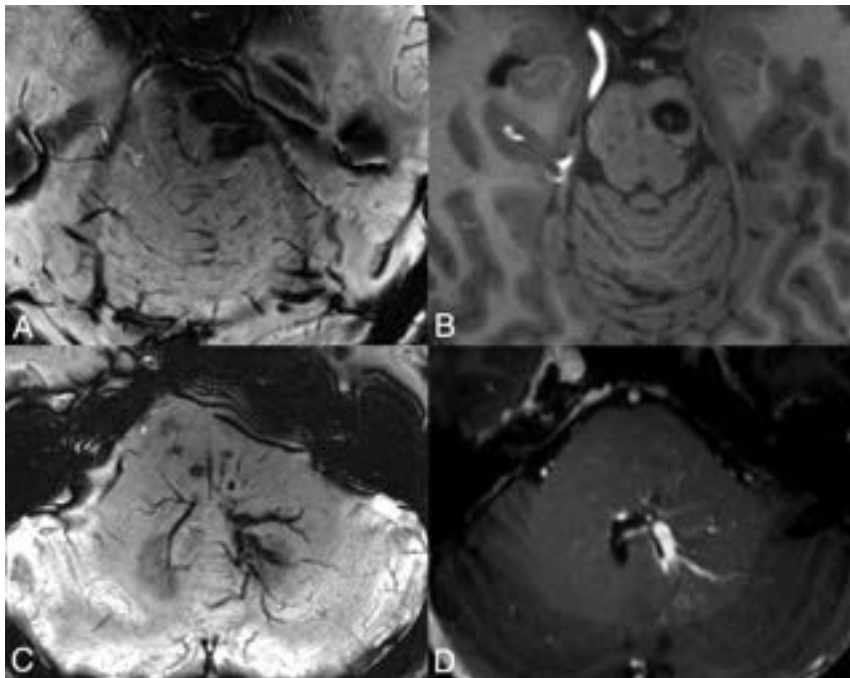


FIG 2. Representative example of clustered CMs with an associated DVA. Axial SWI (A and C) and pre- and postgadolinium MPRAGE (B and D) of adjacent slices show a dominant left cerebral peduncle CM (A and B) and a DVA with additional small CMs (C and D).

The 2 raters agreed on the presence or absence of a DVA in 11/12 (92%) CM locations with a κ statistic of 0.82 (near perfect agreement). On consensus review, it was determined that the 1 case in which the raters disagreed did have a DVA.

DISCUSSION

We found that most, but not all, sporadic CMs are associated with a DVA when evaluated on 7T MR imaging. The frequency of a DVA varied with location, with CMs in the brainstem being most likely to have an associated DVA.

Compared with the prior literature, we must consider the criteria and the imaging technique used to determine the presence or absence of a CM-associated VM. In this study, we focused on the prevalence of a DVA associated with CMs because DVAs have a well-defined and recognized appearance (caput medusa) leading to a definitive assessment of their presence or absence. The percentage of sporadic CMs with an associated DVA/typical VM in this study (72%) was greater than that found in some prior studies, including a study based on 1.5 and 3T imaging with T2* gradient recalled-echo or SWI sequences (8/18, 44%)⁴ and a 7T study with the use of SWI (7/20, 35%),⁸ though less than that reported at 7T by Dammann et al,⁷ in 2017 (11/13, 85%). A limited body of literature exists on the association of DVAs and CMs as studied with high-field MR imaging. This work adds to the literature by validating the results of prior work in a larger sample size, which supports generalizability of these findings.

Prior studies have considered the presence of a DVA as well as atypical VMs when concluding that all sporadic CMs are associated with a VM. Because atypical VMs are not well-defined structures that can be reliably differentiated from normal variations in the vasculature, we did not report their prevalence in this study.

It has been proposed that changes in the DVA angioarchitecture cause local venous hypertension that contributes to recurrent microhemorrhages and CM formation,¹¹ in part on the basis of a comparison of imaging features

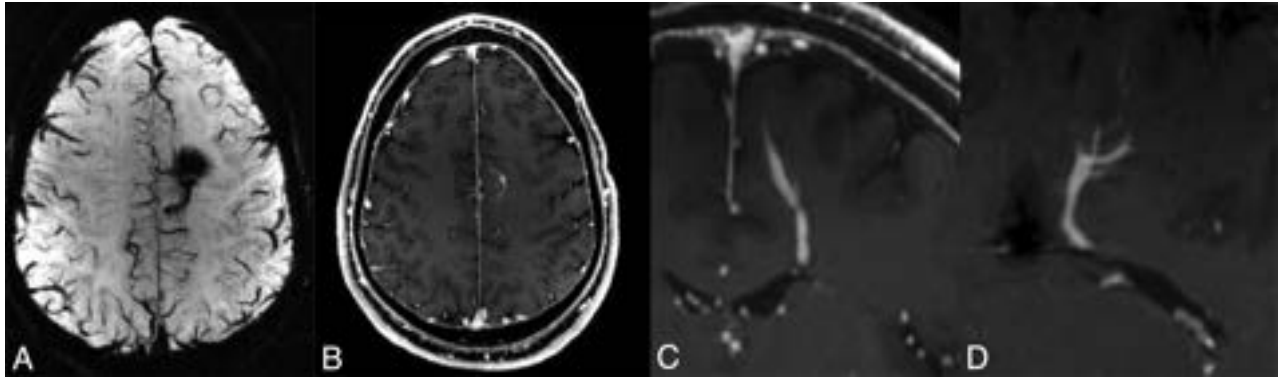


FIG 3. Sample of a left frontal CM (A, SWI) with an associated DVA (B, postcontrast MPRAGE) that has both superficial (C) and deep (D) venous drainage.

of DVAs with-versus-without an associated CM.^{12,13} Another study of a large number of patients with DVAs showed that the percentage of DVAs with an associated CM increases with age, further supporting CMs being acquired lesions.¹⁴ Our findings support the hypothesis that sporadic CMs may arise secondary to hemodynamic abnormalities in association with a DVA. Although a DVA was not visualized in association with all CMs, it is possible that there were regional venous/outflow abnormalities not visible on high-quality MR imaging or that the DVA could not be differentiated from normal vasculature.

There are limitations to this study. Evaluation of the frequency of DVAs with CMs in the basal ganglia and cerebellum was limited in this analysis due to low numbers of CMs in those regions. Some patients in our cohort were referred to our institution on the basis of an indeterminate interpretation of imaging findings elsewhere; therefore, our sample may be biased toward inclusion of cases without an obvious DVA. Finally, this is a single-center study. Future evaluation in a multicenter study with a larger sample size would provide additional support for these findings.

CONCLUSIONS

We found that when using high-quality 7T imaging, most (72%) patients with a sporadic CM had an associated DVA. These findings support the hypothesis that sporadic CMs may arise secondary to hemodynamic abnormalities.

ACKNOWLEDGMENTS

The authors thank Desiree Lanzino, PhD, and Sonia Watson, PhD, for their assistance in editing the manuscript.

Disclosure forms provided by the authors are available with the full text and PDF of this article at www.ajnr.org.

REFERENCES

- Zabramski JM, Wascher TM, Spetzler RF, et al. **The natural history of familial cavernous malformations: results of an ongoing study.** *J Neurosurg* 1994;80:422–32 CrossRef Medline
- Kattapong VJ, Hart BL, Davis LE. **Familial cerebral cavernous angiomas: clinical and radiologic studies.** *Neurology* 1995;45:492–97 CrossRef Medline
- Snellings DA, Girard R, Lightle R, et al. **Developmental venous anomalies are a genetic primer for cerebral cavernous malformations.** *Nat Cardiovasc Res* 2022;1:246–52 CrossRef Medline
- Petersen TA, Morrison LA, Schrader RM, et al. **Familial versus sporadic cavernous malformations: differences in developmental venous anomaly association and lesion phenotype.** *AJNR Am J Neuroradiol* 2010;31:377–82 CrossRef Medline
- de Champfleury NM, Langlois C, Ankenbrandt WJ, et al. **Magnetic resonance imaging evaluation of cerebral cavernous malformations with susceptibility-weighted imaging.** *Neurosurgery* 2011;68:641–47; discussion 647–48 CrossRef Medline
- Sparacia G, Speciale C, Banco A, et al. **Accuracy of SWI sequences compared to T2*-weighted gradient echo sequences in the detection of cerebral cavernous malformations in the familial form.** *Neuroradiol J* 2016;29:326–35 CrossRef Medline
- Dammann P, Wrede K, Zhu Y, et al. **Correlation of the venous angioarchitecture of multiple cerebral cavernous malformations with familial or sporadic disease: a susceptibility-weighted imaging study with 7-Tesla MRI.** *J Neurosurg* 2017;126:570–77 CrossRef Medline
- Dammann P, Wrede KH, Maderwald S, et al. **The venous angioarchitecture of sporadic cerebral cavernous malformations: a susceptibility weighted imaging study at 7 T MRI.** *J Neurol Neurosurg Psychiatry* 2013;84:194–200 CrossRef Medline
- Frischer JM, Göd S, Gruber A, et al. **Susceptibility-weighted imaging at 7 T: improved diagnosis of cerebral cavernous malformations and associated developmental venous anomalies.** *Neuroimage Clin* 2012;1:116–20 CrossRef Medline
- Al-Shahi Salman R, Berg MJ, Morrison L, et al; Angioma Alliance Scientific Advisory Board. **Hemorrhage from cavernous malformations of the brain.** *Stroke* 2008;39:3222–30 CrossRef Medline
- Perrini P, Lanzino G. **The association of venous developmental anomalies and cavernous malformations: pathophysiological, diagnostic, and surgical considerations.** *Neurosurg Focus* 2006;21:e5 CrossRef Medline
- Hong YJ, Chung TS, Suh SH, et al. **The angioarchitectural factors of the cerebral developmental venous anomaly; can they be the causes of concurrent sporadic cavernous malformation?** *Neuroradiology* 2010;52:883–91 CrossRef Medline
- Sharma A, Zipfel GJ, Hildebolt C, et al. **Hemodynamic effects of developmental venous anomalies with and without cavernous malformations.** *AJNR Am J Neuroradiol* 2013;34:1746–51 CrossRef Medline
- Brinjikji W, El-Masri AE, Wald JT, et al. **Prevalence of cerebral cavernous malformations associated with developmental venous anomalies increases with age.** *Childs Nerv Syst* 2017;33:1539–43 CrossRef Medline

Central Vein Sign in Multiple Sclerosis: A Comparison Study of the Diagnostic Performance of 3T versus 7T MRI

Lela Okromelidze, Vishal Patel, Rahul B. Singh, Alfonso S. Lopez Chiriboga, Shengzhen Tao, Xiangzhi Zhou, Sina Straub, Erin M. Westerhold, Vivek Gupta, Amit K. Agarwal, John V. Murray, Amit Desai, S.J.S. Sandhu, I. Vanessa Marin Collazo, and Erik H. Middlebrooks



ABSTRACT

BACKGROUND AND PURPOSE: An early and accurate diagnosis of multiple sclerosis remains challenging in clinical neurology. Established diagnostic methods have less than desirable sensitivity and specificity. An accurate, noninvasive diagnostic test for MS could have a major impact on diagnostic criteria. We compared the frequency of detection of the central vein sign (CVS) in white matter lesions of MS and controls on 7T T2*-weighted and SWI to 3T SWI. Additionally, we assessed the diagnostic performance of 7T T2*, 7T SWI, and 3T SWI for MS.

MATERIALS AND METHODS: A retrospective case-control study was performed of patients with MS having both 7T MRI and 3T MRI. A control group of patients without MS was selected. Diagnosis of MS was established by board-certified neurologists with fellowship training in autoimmune neurology in line with the 2017 McDonald criteria. Percentage of lesions with a CVS was blindly measured for each technique. Diagnostic performance was computed by sensitivity, specificity, and positive and negative likelihood ratios (LRs).

RESULTS: Sixty-one patients with MS (903 lesions) and 39 controls (1088 lesions) were included. 7T T2* showed significantly more CVS (87%) than both 7T SWI (73%) and 3T SWI (31%) (all $P < .001$). CVS was identified in the control group in $\leq 6\%$ of lesions on all sequences. Using a threshold of $>40\%$ of lesions with CVS on 7T T2* and $>15\%$ on 7T SWI, both sequences had an accuracy = 100%, sensitivity = 100%, specificity = 100%, infinite positive LR, and zero negative LR. Using an optimal threshold of $>12\%$, 3T SWI had an accuracy = 96.0%, sensitivity = 93.4%, specificity = 100%, infinite positive LR, and negative LR = 0.066.

CONCLUSIONS: 7T MRI had 100% sensitivity and specificity for the diagnosis of MS and is superior to 3T. Future revisions to MS diagnostic criteria may consider recommendations for 7T MRI and inclusion of CVS as a biomarker.

ABBREVIATIONS: AUC = area under the curve; CVS = central vein sign; DIR = double inversion recovery; ROC = receiver operating characteristic; T2*WI = T2*-weighted imaging

Multiple sclerosis is one of the most common and debilitating autoimmune conditions of the central nervous system.¹ With continued evolution of biomarkers, the ability to accurately diagnose MS has improved, yet there remains a gap in early diagnosis for subsets of patients.¹ MRI is one of the primary diagnostic tools, as outlined in the McDonald criteria of the International Panel on Diagnosis of MS,² but many patients may lack the fully defined MRI features for diagnosis, particularly at initial presentation or early in the disease course.

Nonspecific, nonenhancing WM lesions are frequently the only finding, which have broad overlap with other causes, such as small-vessel ischemic demyelination, migraine, or other etiologies. Unfortunately, this overlap also commonly leads to the erroneous diagnosis of MS, highlighting the need for a biomarker with both high negative and positive predictive value. One of the more commonly studied imaging biomarkers has been the central vein sign (CVS). Given the promise of CVS in MS, the North American Imaging in Multiple Sclerosis Cooperative recently issued a consensus statement calling for further research on this topic.³

The perivenular relationship of MS demyelinating plaques has been known from histologic literature for decades⁴ and is thought to represent one of the most histologically specific features of MS. The identification of CVS on MRI would therefore be a potentially powerful biomarker for the diagnosis of MS. Recent studies have reported the potential value of CVS to differentiate MS from other WM lesions, with a recent meta-analysis showing a pooled

Received September 14, 2023; accepted after revision October 30.

From the Departments of Radiology (L.O., V.P., R.B.S., S.T., X.Z., S.S., E.M.W., V.G., A.K.A., J.V.M., A.D., S.J.S.S., E.H.M.), and Neurology (A.S.L.C., I.V.M.C.), Mayo Clinic, Jacksonville, Florida.

L. Okromelidze and V. Patel contributed equally to this work.

Please address correspondence to Erik H. Middlebrooks, MD, Department of Radiology, Mayo Clinic, 4500 San Pablo Rd, Jacksonville, FL 32224; e-mail: middlebrooks.erik@mayo.edu; @EMiddlebrooksMD

<http://dx.doi.org/10.3174/ajnr.A8083>

Table 1: 7T and 3T sequence parameters

	TR/TE (ms)	T1 (ms)	FA (degree)	Voxel Size (mm ³)	iPAT	BW (Hz/Pix)	TA (m:s)	Dimension
7T T2*WI	1040/20.8	NA	52	0.1 × 0.1 × 1.5	3	50	8:03	2D
7T SWI	21/14	NA	15	0.2 × 0.2 × 1.2	3	140	5:11	3D
7T DIR	8000/408	3400 (T1) 620 (T2)	T2 VFA	0.4 × 0.4 × 0.9	3 (PE) 2 (SE)	698	7:22	3D
3T SWI	25/18	NA	15	0.9 × 0.9 × 2	2	120	4:32	3D
3T FLAIR	4800/440	1550	T2 VFA	0.9 × 0.9 × 1.0	2	781	5:38	3D

Note:—FA indicates flip angle; iPAT, integrated parallel acquisition techniques; BW, bandwidth; TA, time of acquisition; VFA, variable flip angle; PE, phase encoding direction; SE, section encoding direction.

sensitivity and specificity of 95% and 92%, respectively.⁵ However, there was a wide range of reported sensitivity and specificity, with variations in definitions, MRI sequences, MRI field strength, and many other factors. While 3T MRI was significantly better at identifying CVS compared with 1.5T,⁵ there has been increased interest in even higher field MRI, such as 7T. To date, several smaller studies have shown the ability of 7T to detect CVS in MS lesions;⁶⁻¹⁵ however, a meta-analysis failed to show a significant advantage over 3T.⁵ Additionally, only a few, small studies have compared MS to other WM lesions to determine the accuracy of 7T in diagnosing MS.^{8,11,15} There are also very limited data directly comparing the accuracy of 3T to 7T and only in a small number of patients.^{10,16}

There have also been a variety of sequences used in identification of CVS. At 1.5 and 3T, SWI has been the most commonly reported study due to its sensitivity to susceptibility with increased visibility of veins.⁵ At 7T, T2*-weighted imaging (T2*WI) has also been frequently reported and offers some advantages at 7T.^{7,12,14} While no 7T studies have directly compared these approaches, studies using these sequences have reported mixed results with varying percentages of lesions with CVS.⁶⁻¹⁵ To date, there is no clear consensus on the optimal imaging sequence for CVS detection at 7T.

In this retrospective study, we directly compare the utility of 3T SWI, 7T SWI, and T2*WI in detecting CVS. In addition, we assess the ability of CVS to differentiate MS from nonspecific WM lesions in patients without MS (presumed vascular origin) in a large cohort of patients. We hypothesize that 7T is superior to 3T in detecting CVS and has greater accuracy in diagnosing MS. We also hypothesize that 7T T2*WI, configured with a higher in-plane resolution and longer TE, is superior to 7T SWI in detecting CVS and diagnosing MS.

MATERIALS AND METHODS

Patient Selection

This retrospective study was approved by Mayo Clinic Institutional Review Board. Search of an institutional database was performed covering the period from 2021–2023 to identify patients who had undergone a 7T brain MRI imaging with both 3D SWI and 2D gradient-echo T2*WI sequences.

The MS group was retrospectively selected from consecutive patients >18 years of age who were evaluated at the Mayo Clinic neurology department for possible MS. Patients were included if they were determined to have a final diagnosis of MS after evaluation by 1 of 2 board-certified neurologists who specialize in MS and completed fellowship training in autoimmune neurology. The patient's clinical history, physical examination, and results of

standard testing were all used to arrive at a final diagnosis in line with the 2017 revisions to the McDonald criteria.² Inclusion criteria also included having a 3T MRI with SWI, which is the most commonly utilized clinical sequence in the literature. A control group was selected from patients who had no history, physical examination, or laboratory findings that suggested an inflammatory demyelinating disorder and had WM lesions of presumed vascular origin (eg, patients imaged with a wide range of non-MS disorders, including migraine, small-vessel vascular disease, epilepsy, etc). Images were manually assessed for quality, and patients were excluded if any of the 3 sequences had excessive motion artifacts. Pertinent clinical data were collected.

MRI Data Acquisition

The 7T 3D SWI and double inversion recovery (DIR) scans and 2D T2*WI scans were performed on a Magnetom Terra (Siemens) equipped with a 8-channel transmit 32-channel receive head coil (Nova Medical) under “TrueForm” B1 transmit mode. The 3T SWI and FLAIR scans were performed on Prisma, Vida or Skyra (Siemens) machines equipped with a 64-, 32-, or 20-channel receive head coil. Sequence parameters are listed in Table 1. The product SWI sequence and inline processing were used to create SWI, with 4 times of phase mask multiplication, consistent with standard reported practice.¹⁷

Image Analysis

All SWI was independently reviewed in conjunction with coregistered (affine registration with 6 degrees of freedom) DIR for 7T or FLAIR images for 3T to identify WM lesions. The T2*WI allowed adequate visualization of lesions due to its greater T2 weighting. Only lesions that were present on both the 7T and 3T examinations were evaluated for CVS. Lesions were counted for subcortical (<5 mm from cortex), deep (>5 mm from cortex and not contacting the ventricle margin), and periventricular locations and assessed for the presence or absence of CVS.³ Lesions in the posterior fossa and cortical lesions were excluded from the analysis. We excluded confluent periventricular WM lesions where round/ovoid borders of individual lesions were not discriminated, which limits determination of CVS. In contrast to prior guidelines derived for 1.5 and 3T MRI,³ all lesions were included with no restrictions on minimum lesion size. The images were retrospectively reviewed by a board-certified neuro-radiologist (8 years of experience and >2 years of experience reading a high volume of clinical 7T MRI cases) who was blinded to the clinical diagnosis.

To assess interrater reliability, 3 board-certified neuroradiologists (13 and 14 years of experience) with clinical 7T MRI

experience each rated 60 randomly selected lesions (randomization constrained to select 30 lesions from patients with MS and 30 from controls, with 20 lesions each from 3T SWI, 7T SWI, and 7T T2*WI sequences).

Statistical Analysis

We refer to each combination of magnetic field strength and imaging sequence as a “technique”; these are 3T SWI, 7T SWI, and 7T T2*WI and serve as the independent variables in our analyses. In each subject, for each technique, we computed the fraction of lesions exhibiting the CVS, and this served as the dependent variable in our analyses. We first examined the ability of each technique to distinguish between patients with MS and controls by using independent-samples *t*-tests (the Mann-Whitney *U* test was substituted when analyzing the 3T SWI technique because the outcome variable was found to be not normally distributed in control subjects). We then evaluated whether the 3 techniques were equivalent in their ability to detect the CVS in

the MS population by using 1-way repeated-measures ANOVA. As that null hypothesis was rejected, we further compared the 3 techniques pair-wise by using paired *t*-tests to determine exactly which techniques were significantly different (corrected $P < .05$).

To evaluate the performance of the techniques in evaluating MS cases, we plotted receiver operating characteristic (ROC) curves generated by computationally varying the diagnostic threshold for the fraction of lesions exhibiting CVS. We computed the area under the curve (AUC) for each ROC plot. For the point on each ROC curve corresponding to the highest test accuracy, we also computed the test sensitivity, specificity, and positive and negative likelihood ratios. AUCs were statistically compared by using the DeLong nonparametric technique. Interrater reliability was calculated as Fleiss κ statistic. The statistic was computed for all lesions in aggregate as well as stratified by imaging technique.

RESULTS

Clinical Data

Of 161 screened patients, we identified 61 patients with MS meeting inclusion criteria. A control group of 39 patients was also identified meeting inclusion criteria. A total of 903 lesions were detected in patients with MS versus 1088 in the control group. Demographic and lesion data are shown in Table 2.

Identification of CVS by MRI Field Strength

One-way repeated-measures ANOVA established nonequivalence of the 3 techniques with regards to the fraction of lesions exhibiting CVS in patients with MS ($P < .001$; Fig 1). Further pair-wise testing revealed that 7T SWI demonstrated CVS significantly more often than 3T SWI (73% versus 31% of lesions, respectively; $P < .001$). 7T T2*WI showed the CVS even more frequently than 3T SWI (87% versus 31%, respectively; $P < .001$). In contrast,

CVS was not commonly identified in the control group, with only 2%, 5%, and 6% of lesions having CVS on 3T SWI, 7T SWI, and 7T T2*WI, respectively (Figs 1 and 2).

CVS in WM Lesions of Patients with MS versus Controls

For all techniques, we found that a statistically greater fraction of WM lesions demonstrated a CVS in patients with MS relative to controls ($P < .001$ in each case) (Figs 2 and 3). ROC curves for each technique are provided in Figure 4. The ROC curve for the 3T SWI technique had an AUC = 0.975. The best diagnostic accuracy for the 3T SWI technique was achieved by using a threshold of >12% of lesions demonstrating CVS. At this threshold, the 3T SWI technique provided an accuracy of 96.0%, sensitivity of 93.4%, specificity of 100%, infinite positive likelihood ratio, and negative likelihood ratio of 0.066. ROC curves for both the 7T SWI

Table 2: Study group demographic and lesion data

	MS	Control	P Value
Age			.02
Mean (SD)	46.0 (11.8)	52.2 (13.7)	
Median (Q1, Q3)	47 (35, 55)	53 (42, 63)	
Sex			
Female	48	36	
Male	13	3	
Mean lesion number			
Subcortical (SD)	4.2 (2.9)	17.3 (20.6)	<.001
Deep (SD)	5.0 (4.4)	8.2 (7.4)	.03
Periventricular (SD)	5.6 (5.6)	2.4 (3.7)	<.001
Total (SD)	27.9 (27.9)	14.8 (11.2)	.04
Subjects with ≤ 5 lesions, <i>n</i> (%)	16 (26.2%)	5 (12.8%)	

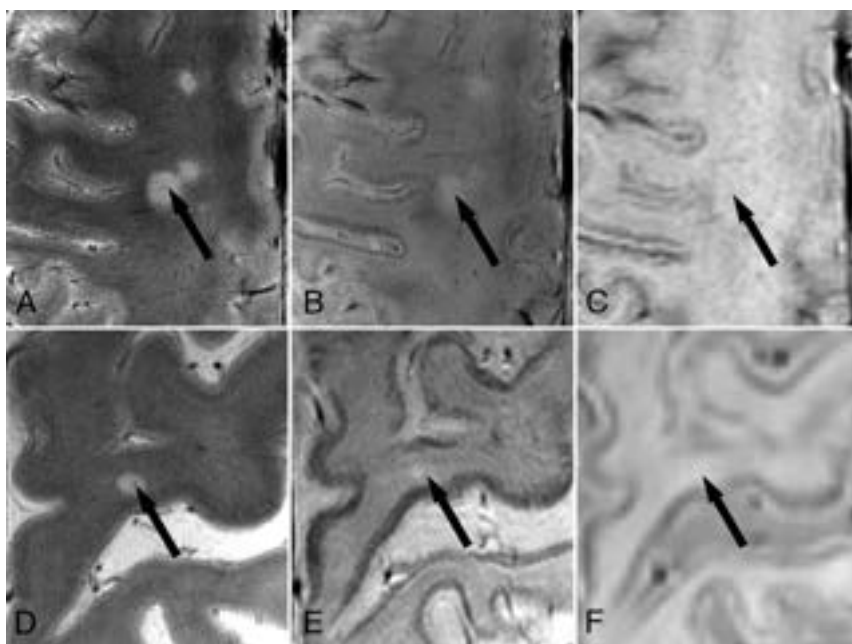


FIG 1. CVS by MRI field strength. A, 7T T2* shows a subtle central vein (arrow) that is not well seen on (B) 7T SWI or (C) 3T SWI. D, 7T T2* shows a central vein (arrow) in a small subcortical lesion that is not well seen on (E) 7T SWI or (F) 3T SWI.

and 7T T2*WI techniques had an AUC = 1.0, indicating the presence of perfect discrimination thresholds for the separation of our population of MS and control cases based on the fraction of lesions demonstrating the CVS. The best diagnostic accuracy for the 7T SWI technique was achieved by using a threshold of >15% of lesions demonstrating CVS, while a cutoff of >40%

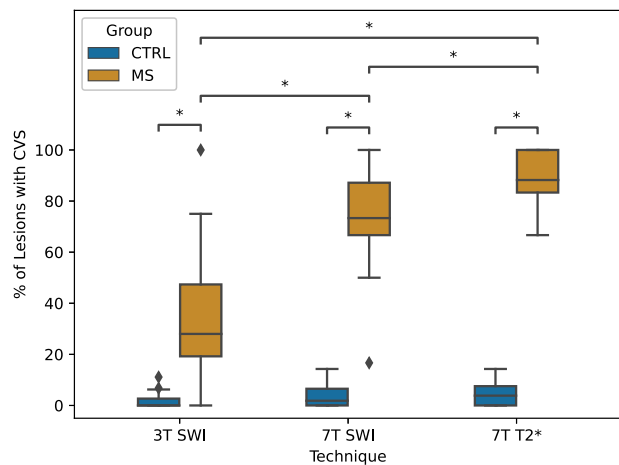


FIG 2. Fraction of WM lesions exhibiting the CVS by MR technique. Regardless of MR technique, a significantly greater proportion of lesions in patients with MS exhibit the CVS compared with those in control subjects. Additionally, in patients with MS, the 7T T2* technique reveals a greater proportion of lesions with CVS compared with 7T SWI, which in turn depicts the CVS more often than 3T SWI.

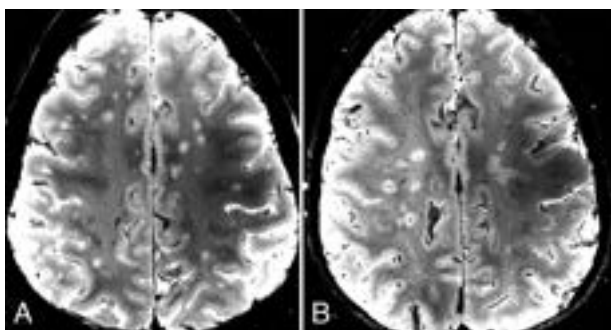


FIG 3. A, Axial 7T T2* in a patient with WM lesions of presumed vascular origin shows no CVS in any of the lesions. B, Axial 7T T2* image in a patient with MS showing CVS in all visible lesions.

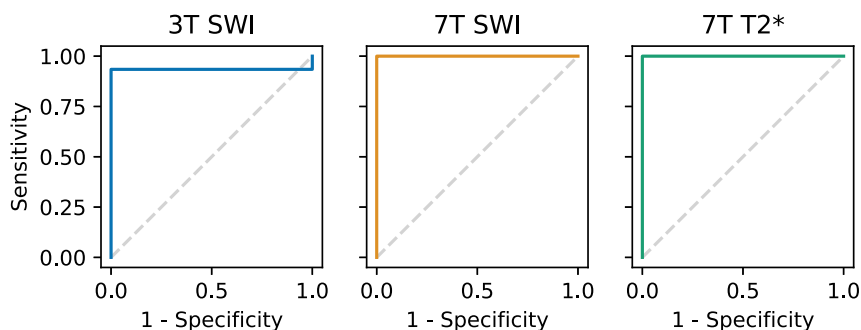


FIG 4. ROC curves for discriminating MS from non-MS cases based on fraction of lesions exhibiting the CVS. In our cohort, 3T SWI achieved accuracy of 96% at the optimal threshold, while both 7T SWI and 7T T2* techniques provided perfect separation of MS and non-MS cases.

provided the greatest separation for the 7T T2*WI technique. As expected from the ROC analysis, at these thresholds, the ultra-high-field methods had accuracies, sensitivities, and specificities of 100%, infinite positive likelihood ratios, and zero negative likelihood ratios. AUCs for both the 7T SWI and 7T T2*WI techniques were statistically greater than the AUC for 3T SWI ($P = .0415$ in both cases).

Performance of 7T SWI versus 7T T2*WI

The 7T T2*WI was significantly superior to 7T SWI for detection of CVS, with 87% of lesions having CVS on T2*WI versus 73% on 7T SWI ($P < .001$). The difference in CVS detection rates between 7T T2*WI and 7T SWI for both MS and control groups led to differences in the optimal cutoff threshold of >40% versus >15%, respectively. Nevertheless, the diagnostic performance for both sequences was identical with an AUC = 1.0, accuracy = 100%, sensitivity = 100%, specificity = 100%, infinite positive likelihood ratios, and zero negative likelihood ratios.

Impact of Lesion Location on CVS

In the MS group, lesions were most commonly periventricular in location with subcortical lesions being least common (Table 3). In contrast, the control group most frequently had deep lesions with periventricular lesions being least common. Percentages of lesions with CVS for each region are shown in Table 3. For the MS group, the percentage of lesions with CVS was greatest in periventricular lesions followed by deep then subcortical lesions across all techniques.

Interrater Reliability in CVS Detection

Interrater reliability for CVS detection between 3 neuroradiologists was very high in our data set. Across all assessed lesions, Fleiss κ for CVS presence was 0.887. Agreement remained high when each imaging technique was considered separately, with Fleiss κ 1.000 for 3T SWI, 0.794 for 7T SWI, and 0.859 for 7T T2*WI ($P < .001$ in all cases).

DISCUSSION

To our knowledge, our study is the largest cohort of patients with MS versus controls that have been evaluated for CVS at 7T. Likewise, our study is unique in directly comparing 2 of the most common 7T imaging sequences, SWI and T2*WI. Our results show that 7T SWI and T2* (73% and 87% of lesions, respectively) showed significantly more CVSs than 3T (31%). Additionally, comparing the T2*WI and SWI sequences used in this study, we found that the T2*WI sequence was superior to the SWI sequence in detecting CVS at 7T, as configured in our study. Despite the increased detection of CVS, both 7T techniques were 100% accurate (AUC = 1.0) for diagnosing MS from WM lesions of presumed vascular origin, which was superior to 3T (AUC = 0.975). CVS is a useful biomarker for the diagnosis or exclusion

Table 3: Number of WM lesions with CVS for each technique relative to lesion location

Study Groups	Imaging Technique	Periventricular [CVS/total (%)]	Deep [CVS/total (%)]	Subcortical [CVS/total (%)]	Total [CVS/total (%)]
MS	3T SWI	139/340 (41)	100/305 (33)	42/258 (16)	281/903 (31)
	7T SWI	286/340 (84)	241/305 (79)	132/258 (51)	659/903 (73)
	7T T2*WI	320/340 (94)	274/305 (90)	188/258 (73)	782/903 (87)
Control group	3T SWI	5/93 (5)	15/320 (5)	5/675 (1)	25/1088 (2)
	7T SWI	6/93 (6)	27/320 (8)	17/675 (3)	50/1088 (5)
	7T T2*WI	6/93 (6)	31/320 (10)	29/675 (4)	66/1088 (6)

of MS. While 3T had good sensitivity, 7T was superior in both detection of CVS and in accuracy of identifying patients with MS.

Despite advances in laboratory biomarkers and multiple revisions to diagnostic criteria, the diagnosis or exclusion of MS remains a frequent clinical challenge. Compared with the 2010 version, the revised McDonald criteria in 2017 were shown to have a higher sensitivity (increased from 41% to 85%), but lower specificity (decreased from 85% to 63%).¹⁸ Additionally, common laboratory biomarkers also have trade-offs in diagnostic accuracy, such as κ free light chain index (88% sensitivity; 83% specificity) and oligoclonal bands (82% sensitivity; 92% specificity).¹⁹ Given the need for better biomarkers, there has been increasing interest in MRI morphologic characteristics. Among these, CVS has been one of the more promising biomarkers, with a recent meta-analysis showing a pooled sensitivity of 95% and specificity of 92%.⁵ However, small 7T studies in this pooled analysis were major drivers of the increased performance, with many 3T studies showing poorer sensitivity and specificity. Despite this, the meta-analysis failed to show a significant advantage of 7T over 3T in detecting CVS, which likely reflects a lack of power or lack of direct comparison studies.⁵ However, there are a number of inherent biases in the studies included in the meta-analysis. Many 3T studies that reported a wide range of CVS limited their assessment of CVS to only larger lesions, which likely inflated the percentage of lesions reported to have CVS at 3T.⁵ Such size criteria have been arbitrarily applied based on expert opinion, but largely from data at 1.5T or 3T. While CVS detection is higher in larger lesions, this does not equate to histopathology where small lesions possess a CVS. Indeed, more than one-half of lesions with no CVS identified on ultra-high-resolution ex vivo scanning had a CVS histologically, and these lesions had a smaller mean lesion size.²⁰ When not reporting a size limit, CVS detection at 3T was similar to our results suggesting that many studies have an overestimation of CVS by restricting to only larger lesions.⁷ By directly comparing 3T and 7T, we show that 7T is not only superior in detecting CVS but also outperforms 3T in diagnosing MS from WM lesions of presumed vascular origin. In our ROC analysis, at the optimal CVS prevalence threshold, up to 6.6% of patients with MS were classified as false-negatives with 3T imaging. Given the potential for disease progression and disability associated with untreated MS, we believe it is worthwhile to pursue 7T imaging in uncertain cases with negative 3T MRI, or even as the initial imaging if local availability permits.

Interestingly, we found an identical optimal threshold value (>40% of lesions with CVS) for 100% sensitivity and specificity in the 7T T2*WI as one of the few prior studies assessing CVS in diagnosing MS in a cohort of 28 patients with MS.¹¹ In a smaller

cohort of 13 patients, Mistry et al⁸ attempted to replicate this threshold value of >40% of lesions having CVS by using T2*WI and also found 100% sensitivity and specificity. However, Kilsdonk et al¹⁵ used T2*WI in a cohort of 16 patients with MS and found a cutoff of >52% of lesions with CVS with a sensitivity and specificity of only 88%. Notably, their CVS detection rate was much lower (74%) than our cohort and the studies by Tallantyre et al¹¹ and Mistry et al,⁸ suggesting that the imaging methods may vary. The cutoff of >40% was also independently found in a pooled meta-analysis of 3T and 7T T2*WI.⁵ There are limited data on optimal cutoffs for 7T SWI, and we show that these optimal values differ depending on the technique used. While >40% of lesions with CVS appears to be optimal for T2*WI in multiple studies, the SWI threshold was lower at >15% for 7T and >12% for 3T. The difference in cutoff thresholds between T2*WI and SWI techniques at 7T could be related to the differences in pulse sequence parameters. Dixon et al¹⁶ have shown that vessel orientation and various acquisition settings (eg, spatial resolution, TE, and application of phase mask) can affect the sensitivity to smaller veins. The higher cutoff with T2*WI sequence suggests a higher sensitivity to small veins compared with SWI used in this study for the given imaging parameters.

Our results also show that the ability to detect CVS varies by lesion location, with all techniques showing a fewer percentage of subcortical lesions with CVS. There were a greater number of lesions with CVS on T2*WI versus SWI, which may be in part due to technique, such as the longer TE for the T2*WI sequence, higher in-plane spatial resolution, lower pixel bandwidth, and smaller imaging slab. Nevertheless, there were fewer subcortical lesions with CVS even on 7T T2*WI compared with deep and periventricular lesions. Tallantyre et al¹² and Hosseini et al¹⁴ also found similar results with subcortical lesions being least likely to have CVS on T2*WI. It is possible that even at 7T with higher in-plane resolution, the more peripheral medullary veins remain too small to visualize. Alternatively, because there is a higher incidence of WM lesions of presumed vascular origin in the subcortical regions,^{21,22} there may be a coexistence of MS-related demyelinating plaques and other causes of WM lesions in patients with MS. Hosseini et al¹⁴ suggested that their multiecho SWI technique with a maximum TE of 26.22 ms and an in-plane resolution of 0.5 mm was superior to prior T2*WI studies at 7T in detecting small CVS. Meanwhile, in this study, the 7T T2*WI sequence with a TE of 20.8 ms and higher in-plane resolution was superior to the 7T SWI (TE=14 ms) as well as the results reported by Hosseini et al,¹⁴ with CVS detected in 94% of periventricular, 90% of deep, and 73% of subcortical lesions. This highlights the role of higher in-plane spatial resolution and better T2* weighting in detecting CVS.

The detection of CVS in these small subcortical lesions is critical because smaller lesions are significantly less likely to have a central vein detected on MRI.¹⁰ Because many studies at 1.5T and 3T MRI restricted their analysis only to large lesions (often >3 mm) due to limited sensitivity and specificity at lower field strength, the sensitivity may be reduced because many patients with MS may present with only smaller lesions.⁵

We suggest that 7T should be preferred for evaluation of MS, particularly when combined with other advantages, such as increased prevalence of paramagnetic rim sign²³ and improved detection of cortical lesions.²⁴ In this study, the used T2*WI was preferable to SWI due to better CVS detection, but both were 100% accurate. However, the used T2*WI protocol was advantageous by its better inherent depiction of the WM lesion compared with SWI due to the longer TE and better in-plane resolution. To enhance lesion visibility, others have proposed fused techniques, such as FLAIR*;¹⁵ however, this approach is dependent on additional image processing and may be vulnerable to inaccuracies in registration at 7T due to differences in susceptibility-induced distortions between T2*WI/SWI and 3D turbo spin-echo sequences, such as FLAIR. 7T T2*WI has also been shown to be a highly reliable technique with perfect interrater agreement (mean [SE] Cohen κ coefficient, 1.000 [0.000]).⁸

Our study does have several limitations. First, we restricted the analysis to patients with a confirmed diagnosis of MS, which may have excluded patients with less typical presentations or other autoimmune demyelinating conditions. Further studies will be needed to assess the role of 7T in differentiating other autoimmune demyelinating disorders. Second, due to the retrospective nature of the study, a direct comparison with various other biomarkers is difficult due to the heterogeneity of available data.

CONCLUSIONS

In a large cohort of patients with MS, we show that 7T is superior to 3T in the detection of CVS and more accurate in diagnosing patients with MS. With 100% sensitivity and specificity for the diagnosis of MS, 7T is a powerful biomarker in the evaluation of patients with possible MS. In addition, we show that the 7T T2*WI sequence with higher in-plane resolution and T2* weighting is superior to the 7T SWI sequence used in this study in detecting CVS; however, both sequences had 100% accuracy in diagnosing MS. Optimal thresholds for the diagnosis of MS varied by technique, with 3T SWI, 7T SWI, and 7T T2*WI having optimal thresholds of CVS lesions of >12%, >15%, and >40%, respectively.

Disclosure forms provided by the authors are available with the full text and PDF of this article at www.ajnr.org.

REFERENCES

1. Reich DS, Lucchinetti CF, Calabresi PA. **Multiple sclerosis.** *N Engl J Med* 2018;378:169–80 CrossRef Medline
2. Thompson AJ, Banwell BL, Barkhof F, et al. **Diagnosis of multiple sclerosis: 2017 revisions of the McDonald criteria.** *Lancet Neurol* 2018;17:162–73 CrossRef Medline
3. Sati P, Oh J, Constable RT, NAIMS Cooperative, et al. **The central vein sign and its clinical evaluation for the diagnosis of multiple sclerosis: a consensus statement from the North American Imaging**

- in Multiple Sclerosis Cooperative. *Nat Rev Neurol* 2016;12:714–22 CrossRef Medline
4. Fog T. **On the vessel-plaque relationships in the brain in multiple sclerosis.** *Acta Neurol Scand Suppl* 1964;40:9–15 CrossRef
5. Castellaro M, Tamanti A, Pisani AI, et al. **The use of the central vein sign in the diagnosis of multiple sclerosis: a systematic review and meta-analysis.** *Diagnostics (Basel)* 2020;10:1025 CrossRef
6. Gaitan MI, Sati P, Inati SJ, et al. **Initial investigation of the blood-brain barrier in MS lesions at 7 Tesla.** *Mult Scler* 2013;19:1068–73 CrossRef Medline
7. Grabner G, Dal-Bianco A, Scherthaner M, et al. **Analysis of multiple sclerosis lesions using a fusion of 3.0 T FLAIR and 7.0 T SWI phase: FLAIR SWI.** *J Magn Reson Imaging* 2011;33:543–49 CrossRef Medline
8. Mistry N, Dixon J, Tallantyre E, et al. **Central veins in brain lesions visualized with high-field magnetic resonance imaging: a pathologically specific diagnostic biomarker for inflammatory demyelination in the brain.** *JAMA Neurol* 2013;70:623–28 CrossRef Medline
9. Sinnecker T, Dorr J, Pfueller CF, et al. **Distinct lesion morphology at 7-T MRI differentiates neuromyelitis optica from multiple sclerosis.** *Neurology* 2012;79:708–14 CrossRef Medline
10. Tallantyre EC, Morgan PS, Dixon JE, et al. **A comparison of 3T and 7T in the detection of small parenchymal veins within MS lesions.** *Invest Radiol* 2009;44:491–94 CrossRef Medline
11. Tallantyre EC, Dixon JE, Donaldson I, et al. **Ultra-high-field imaging distinguishes MS lesions from asymptomatic white matter lesions.** *Neurology* 2011;76:534–39 CrossRef Medline
12. Tallantyre EC, Brookes MJ, Dixon JE, et al. **Demonstrating the perivascular distribution of MS lesions in vivo with 7-Tesla MRI.** *Neurology* 2008;70:2076–78 CrossRef Medline
13. Wuerfel J, Sinnecker T, Ringelstein EB, et al. **Lesion morphology at 7 Tesla MRI differentiates Susac syndrome from multiple sclerosis.** *Mult Scler* 2012;18:1592–99 CrossRef Medline
14. Hosseini Z, Matusinec J, Rudko DA, et al. **Morphology-specific discrimination between MS white matter lesions and benign white matter hyperintensities using ultra-high-field MRI.** *AJNR Am J Neuroradiol* 2018;39:1473–79 CrossRef Medline
15. Kilsdonk ID, Wattjes MP, Lopez-Soriano A, et al. **Improved differentiation between MS and vascular brain lesions using FLAIR* at 7 Tesla.** *Eur Radiol* 2014;24:841–49 CrossRef Medline
16. Dixon JE, Simpson A, Mistry N, et al. **Optimization of T(2)*-weighted MRI for the detection of small veins in multiple sclerosis at 3 T and 7 T.** *Eur J Radiol* 2013;82:719–27 CrossRef Medline
17. Haacke EM, Mittal S, Wu Z, et al. **Susceptibility-weighted imaging: technical aspects and clinical applications, part 1.** *AJNR Am J Neuroradiol* 2009;30:19–30 CrossRef Medline
18. Habek M, Pavicic T, Ruska B, et al. **Establishing the diagnosis of multiple sclerosis in Croatian patients with clinically isolated syndrome: 2010 versus 2017 McDonald criteria.** *Mult Scler Relat Disord* 2018;25:99–103 CrossRef Medline
19. Leurs CE, Twaalfhoven H, Lissenberg-Witte BI, et al. **Kappa free light chains is a valid tool in the diagnostics of MS: A large multicenter study.** *Mult Scler* 2020;26:912–23 CrossRef Medline
20. Al-Louzi O, Manukyan S, Donadieu M, et al. **Lesion size and shape in central vein sign assessment for multiple sclerosis diagnosis: an in vivo and postmortem MRI study.** *Mult Scler* 2022;28:1891–902 CrossRef Medline
21. Wu X, Ya J, Zhou D, et al. **Pathogenesis and imaging features of cerebral white matter lesions of vascular origins.** *Aging Dis* 2021;12:2031–51 CrossRef Medline
22. Absinta M, Rocca MA, Colombo B, et al. **Patients with migraine do not have MRI-visible cortical lesions.** *J Neurol* 2012;259:2695–98 CrossRef Medline
23. Ng Kee Kwong KC, Mollison D, Meijboom R, et al. **The prevalence of paramagnetic rim lesions in multiple sclerosis: a systematic review and meta-analysis.** *PLoS One* 2021;16:e0256845 CrossRef Medline
24. Madsen MA, Wiggermann V, Bramow S, et al. **Imaging cortical multiple sclerosis lesions with ultra-high field MRI.** *Neuroimage Clin* 2021;32:102847 CrossRef Medline

Cortical Thin Patch Fraction Reflects Disease Burden in MS: The Mosaic Approach

Marlene Tahedl, Tun Wiltgen, Cui Ci Voon, Achim Berthele, Jan S. Kirschke, Bernhard Hemmer, Mark Mühlau, Claus Zimmer, and Benedikt Wiestler



ABSTRACT

BACKGROUND AND PURPOSE: GM pathology plays an essential role in MS disability progression, emphasizing the importance of neuroradiologic biomarkers to capture the heterogeneity of cortical disease burden. This study aimed to assess the validity of a patch-wise, individual interpretation of cortical thickness data to identify GM pathology, the “mosaic approach,” which was previously suggested as a biomarker for assessing and localizing atrophy.

MATERIALS AND METHODS: We investigated the mosaic approach in a cohort of 501 patients with MS with respect to 89 internal and 651 external controls. The resulting metric of the mosaic approach is the so-called thin patch fraction, which is an estimate of overall cortical disease burden per patient. We evaluated the mosaic approach with respect to the following: 1) discrimination between patients with MS and controls, 2) classification between different MS phenotypes, and 3) association with established biomarkers reflecting MS disease burden, using general linear modeling.

RESULTS: The thin patch fraction varied significantly between patients with MS and healthy controls and discriminated among MS phenotypes. Furthermore, the thin patch fraction was associated with disease burden, including the Expanded Disability Status Scale, cognitive and fatigue scores, and lesion volume.

CONCLUSIONS: This study demonstrates the validity of the mosaic approach as a neuroradiologic biomarker in MS. The output of the mosaic approach, namely the thin patch fraction, is a candidate biomarker for assessing and localizing cortical GM pathology. The mosaic approach can furthermore enhance the development of a personalized cortical MS biomarker, given that the thin patch fraction provides a feature on which artificial intelligence methods can be trained. Most important, we showed the validity of the mosaic approach when referencing data with respect to external control MR imaging repositories.

ABBREVIATIONS: AI = artificial intelligence; CamCAN = Cambridge Center for Ageing and Neuroscience; CIS = clinically isolated syndrome; CT = cortical thickness; EDSS = Expanded Disability Status Scale; HC = healthy controls; IQR = interquartile range; MAP = mosaic approach; MuSIC = Multiple Sclerosis Inventory of Cognition; PMS = progressive MS; RRMS = relapsing-remitting MS; TPF = thin patch fraction; TUM = Technical University of Munich

MS is a chronic disease of the CNS, which is characterized by a complex interplay of inflammatory and neurodegenerative processes.^{1,2} The significance of MR imaging for MS diagnosis and disease monitoring has increased during the past decades

and has ultimately allowed the diagnosis of MS based on a single MR imaging assessment along a clinical symptoms.³

One problem in early and accurate patient management is the vast heterogeneity of the disease and the severity, which cannot be

Received August 4, 2023; accepted after revision October 18.

From the Departments of Neuroradiology (M.T., J.S.K., C.Z., B.W.) and Neurology (T.W., C.C.V., A.B., B.H., M.M.), School of Medicine, Technical University of Munich, Munich, Germany; and Munich Cluster for Systems Neurology (B.H.), Munich, Germany.

A.B. has received consulting and/or speaker fees from Alexion, Biogen, Celgene, Horizon, Novartis, Roche, and Sandoz/Hexal, and his institution has received compensation for clinical trials from Alexion, Biogen, Merck, Novartis, Roche, and Sanofi Genzyme, all outside the current work. J.S.K. has received speaker fees from Novartis. B.H. has served on scientific advisory boards for Novartis; he has served as data safety monitoring board member for AllergyCare, Sandoz, Polpharma, Biocon, and TG Therapeutics; his institution received research grants from Roche for MS research. He has received honoraria for counseling (Gerson Lehmann Group). He holds part of 2 patents; one for the detection of antibodies against KIR4.1 in a subpopulation of patients with MS and one for genetic determinants of

neutralizing antibodies to interferon. B.H. is associated with Data Integration for Future Medicine (DIFUTURE) (BMBF 01ZZ1804[A-I]) and received funding for the study by the European Union's Horizon 2020 Research and Innovation Program (grant MultipleMS, EU RIA 733161) and the Deutsche Forschungsgemeinschaft (DFG, German Research Foundation) under Germany's Excellence Strategy within the framework of the Munich Cluster for Systems Neurology (EXC 2145 SyNergy; ID 390857198). All conflicts are not relevant to the topic of the study.

Please address correspondence to Marlene Tahedl, MD, Department of Neuroradiology, School of Medicine, Technical University of Munich, Ismaninger Strasse 22, Munich, 81675, Germany; e-mail: marlene.tahedl@tum.de

Indicates article with online supplemental data.

<http://dx.doi.org/10.3174/ajnr.A8064>

Demographic details of the study population

	MS Clinical Profiles			All Patients with MS	HC Subgroups		T Test (W) ^a /χ ² Test (C2) ^b	T Test (W) ^a /χ ² Test (C2) ^b
	CIS	RRMS	PMS		CamCAN (External)	TUM (Internal)		
No. subjects	19	465	17	501	651	89	NA	NA
Age (mean) (yr)	58.73 (SD, 12.06)	40.14 (SD, 9.94)	55.58 (SD, 5.23)	40.56 (SD, 10.22)	54.26 (SD, 18.58)	37.36 (SD, 15.06)	W: $t(150.61) = 9.78$, $P < .001$	W: $t(102.87) = -1.92$, $P = .056$
Sex (female/male)	13:6	305:160	10:7	328:173	330:321	59:30	C2: $\chi^2(1, N = 740)$ $= 7.03, P = .008$	C2: $\chi^2(1, N = 590)$ $< 0.001, P = .976$
Dominant hand (R/L)	19/0	415/50	16/1	450/51	NA	NA	NA	NA
EDSS (median) (IQR)	0.0 (1.0)	1.5 (2.0)	4.25 (1.75)	1.5 (2.0)	NA	NA	NA	NA
Cognition MuSIC (mean)	28.05 (SD, 3.01)	27.10 (SD, 3.66)	25.82 (SD, 4.05)	27.09 (SD, 3.66)	NA	NA	NA	NA
Fatigue MuSIC (mean)	6.21 (SD, 2.64)	7.58 (SD, 4.59)	11.65 (SD, 3.32)	7.67 (SD, 4.56)	NA	NA	NA	NA
Lesion volume, (mean) (mL)	0.98 (SD, 1.23)	5.39 (SD, 8.41)	11.78 (SD, 9.01)	5.45 (SD, 8.40)	NA	NA	NA	NA

Note.—R indicates right; L, left.

^a Welch 2-sample *t* tests were performed to test differences in age between all patients with MS versus TUM (ie, internal) HC.

^b χ^2 tests were performed to test differences in sex frequencies between all patients with MS versus TUM (ie, internal) HC.

predicted at onset; moreover, highly individualized neuroradiologic and clinical patterns are observed.^{4,5} As a consequence of this diversity, the quest for a personalized approach to MS therapy has evolved, which requires biomarkers that can be assessed on a single-patient basis.⁶

Existing MR imaging biomarkers traditionally focus on the quantification of WM lesions, given their well-established association with disease burden.⁷⁻⁹ However, the role of progressive GM pathology for the clinical course is increasingly recognized.¹⁰⁻¹³ Thus, the acquisition of 3D T1WI gradient recalled-echo sequences (inversion recovery or MPRAGE) has been optionally recommended for monitoring GM pathology in the latest consensus guidelines by the Consortium for Magnetic Resonance Imaging in MS (MAGNIMS).¹⁴

However, individualized assessment of subcortical and cortical GM atrophy is an ongoing-but-urgent challenge.¹⁵ One problem is the lack of a common standard on which GM can be rated. During the past years, increasingly large-scale MR imaging databases have been more freely available to the community,^{16,17} some of which are population-representative such as the UK Biobank.¹⁸ Such resources provide the exciting opportunity to define population-based reference standards on which an individual patient's GM can be assessed for signs of atrophy or even hypertrophy.¹⁹

Following this strategy, using external big data resources has been suggested to define age- and sex-matched reference standards for the assessment of cortical thickness (CTH) suggestive of atrophy.²⁰ This strategy included a high-resolution parcellation of the cortex into roughly equal-sized “patches” or “mosaics”—hence referred to as the “mosaic-approach” (MAP)—and performing nonparametric statistical significance testing for CTH normality at each patch. This strategy allows precise anatomic allocation of individual cortical disease burden and has been shown to be clinically relevant in primary neurodegenerative disorders, including amyotrophic lateral sclerosis,²⁰ progressive lateral sclerosis,²¹ and frontotemporal dementia.²²

In this investigation, we examined the validity of MAP as a cortical biomarker for MS. Specifically, we tested the 3 following applications of MAP in MS: 1) discrimination between patients with MS and controls, 2) classification among different MS clinical phenotypes, and 3) association with established biomarkers

and disease burden in MS, including the Expanded Disability Status Scale (EDSS), cognitive and fatigue scores, as well as WM lesion volume. If the MAP can be validated for these applications, it might be a useful method for monitoring GM cortical burden in MS clinical practice. Furthermore, the MAP could serve as a feature for artificial intelligence (AI) applications, allowing personalized interpretation of single-subject GM pathology.

MATERIALS AND METHODS

Study Cohort and Data Acquisition

We included cross-sectional data from 501 patients with MS (328 women) and 89 healthy controls (HC, 59 women) from a prospective, monocentric observational cohort for this study, acquired at the Technical University of Munich (TUM, Table). We focused our analysis on patients with relapsing-remitting MS (RRMS) ($n = 465$) and additionally included smaller patient subgroups, namely clinically isolated syndrome (CIS) ($n = 19$) and progressive MS (PMS) ($n = 17$, both primary and secondary PMS) to probe the MAP differences among phenotypes. Patients were diagnosed by a certified neurologist in accordance with the 2017 revisions of the McDonald criteria.³ Structural T1WI MPRAGE data were acquired at the Klinikum Rechts der Isar of the TUM on 1 of two 3T Philips Healthcare MR imaging systems: Achieva dStream and Ingenia with identical scanning parameters: 267 sagittal slices, FOV = 240 × 252 mm, spatial resolution = 1.00 mm isotropic, TR = 9 ms, TE = 4 ms, flip angle = 8°, no parallel imaging. Additionally, a 3D FLAIR sequence was acquired, which we used to calculate WM lesion volume using the LST toolbox (<https://www.appliedstatistics.de/lst.html>).²³ Demographic and clinical details, including age, sex, EDSS, and dominant hand (for patients) were obtained from our hospital's Neurology Department. Additionally, the Multiple Sclerosis Inventory of Cognition (MuSIC) was available for patients, evaluating neuropsychological function specifically in MS.^{24,25} For the present study, we used the MuSIC to quantify cognition (with a score ranging from 0 to 30) and fatigue (ranging from 3 to 21). We tested differences in mean age between all patients with MS and HC using Welch 2-sample tests and sex distributions using a χ^2 test with a Yates continuity correction, correcting for age and sex.

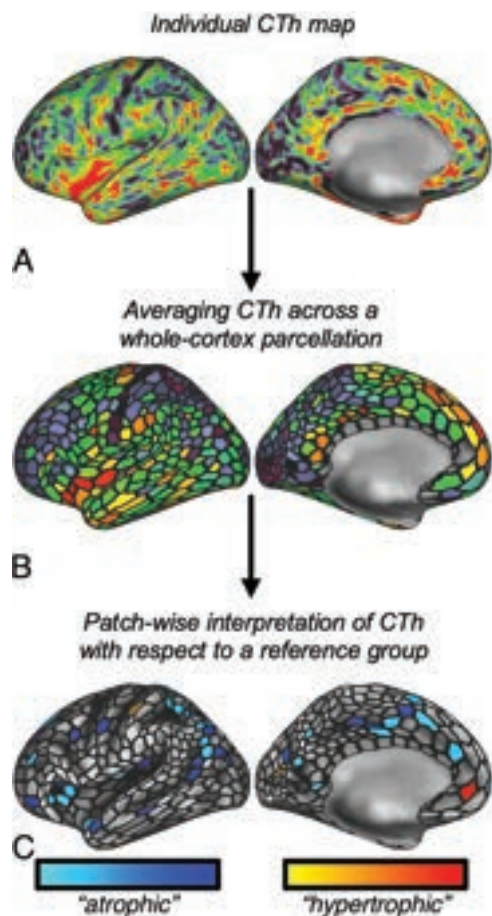


FIG 1. In the proposed MAP, atrophy (hypertrophy) was estimated on the basis of CTh maps (A). The cortical surface was subparcellated into 1000 “patches” (black lines in B), and the average CTh for each parcel was calculated (B). By referencing the value of each parcel to an age-/sex-matched control group, P maps can be calculated (C) so that the lower end of the spectrum is suggestive of “atrophy” (cool colors) and the higher end of “hypertrophy” (hot colors). MAP uses the fraction of any “atrophic” patches, ie, the TPF, as a metric to estimate cortical disease burden.

The study was approved by the local ethics committee of the TUM and was in accord with the Declaration of Helsinki, and informed consent was collected from all subjects.

In addition, we considered external reference T1WI data from an open-source repository by the Cambridge Center for Ageing and Neuroscience (CamCAN).¹⁶ We refer to this external HC group as “CamCAN-HC” as opposed to the internally acquired “TUM-HC.” The CamCAN-HC repository shares 651 MPRAGE images (330 women) collected from a 3T Magnetom TrioTrim (Siemens) system at the University of Cambridge with the following sequence parameters: 256 sagittal slices, FOV = 240 × 192 mm, spatial resolution = 1 mm isotropic, TR = 2250 ms, TE = 2.99 ms, flip angle = 9°, and generalized autocalibrating partially parallel acquisition (GRAPPA) factor = 2. We tested differences in mean age between CamCAN-HC and TUM-HC using the Welch 2-sample *t* test and sex distributions using a χ^2 test with a Yates continuity correction, correcting for age and sex.

Neuroimaging Data Analysis

T1-weighted data were preprocessed using the fully-automated recon-all pipeline from the software FreeSurfer²⁶⁻²⁸ ([\[surfer.nmr.mgh.harvard.edu/fswiki/recon-all\]\(https://surfer.nmr.mgh.harvard.edu/fswiki/recon-all\)\) and the Ciftify package \(<https://github.com/edickie/ciftify>\),²⁹ which outputs surface-based CTh maps \(“standard” CTh maps\). Before FreeSurfer preprocessing, lesion filling was performed on the basis of T1WI and FLAIR data using the LST toolbox.²³ The MAP approach evaluates regional CTh by a *z* score-based approach \(Fig 1\): Standard CTh maps¹⁹⁻²² of individual patients are subdivided into 1000 equal-sized mosaics³⁰ and rated as significantly “thin” or “thick” with respect to a demographically matched HC group using nonparametric permutation testing.³¹ To account for the physiologic effects of sex and aging, subject-specific reference groups for each patient were generated \(same sex, \$\pm 2\$ years\)²⁰ from the collapsed TUM-/CamCAN-HC groups. The thin patch fraction \(TPF\) is calculated as the fraction of all significantly thin patches of a single subject from the total of 1000 patches \(“whole-brain TPF”\). Thick patch fractions were calculated analogously. In addition to whole-brain TPF, the TPF was also calculated for distinct brain lobes, including the frontal, parietal, insular, temporal, and visual cortices, as well as the motor cortex, which we refer to as super-ROIs. Further details on the parcellation-based estimation of individual atrophy, definition of reference groups, and definition of super-ROIs are provided in the Online Supplemental Data.](https://</p>
</div>
<div data-bbox=)

Statistics

The goal of this study was to validate MAP as a biomarker of several applications in MS using externally acquired MR imaging data. We followed a 3-fold strategy for this validation process:

First, we wanted to know whether MAP differentiates between patients with MS and HC. Therefore, we calculated the thin (thick) patch fraction for each patient with MS and HC and used a 1-way ANOVA to test for the main effect of the binary variable “MS diagnosis: yes/no” (notice that we did not differentiate among MS clinical phenotypes in this analysis). We included age, sex, and lesion volume as variables-of-no-interest into our model, and the α -level was set to $P \leq .05$.

Second, we evaluated whether MAP discriminates among MS clinical phenotypes. We used 1-way ANOVA to compare differences of thin/thick patch fractions among 3 phenotypes (CIS, RRMS, PMS) and HC, testing for the main effect of phenotype. Age, sex, and lesion volume were modeled as variables-of-no-interest. When the ANOVA reached significance at $P \leq .05$, we conducted post hoc pair-wise comparisons using Tukey Honestly Significant Difference testing, which outputs *P* values adjusted for multiple comparisons (P_{adj}).

Third, we investigated whether MAP is associated with established measures reflecting disease burden in MS, including EDSS, cognition and fatigues scores (both from the MuSIC inventory), and lesion volume. Associations were tested using general linear modeling, in which the thin (thick) patch fractions across all patients were modeled as the dependent and the respective clinical measures as the independent variable. We tested for the main effect of the independent variable, setting the α level to $P \leq .05$. Age, sex, and lesion volumes (except for the testing for the main effect, lesion volume) were included as variables-of-no-interest in the model.

Control Analysis: Standard Approach and Comparison with MAP

Given that we probed a novel biomarker in this study to quantify MS cortical disease burden on the basis of parcelled CTh, we also

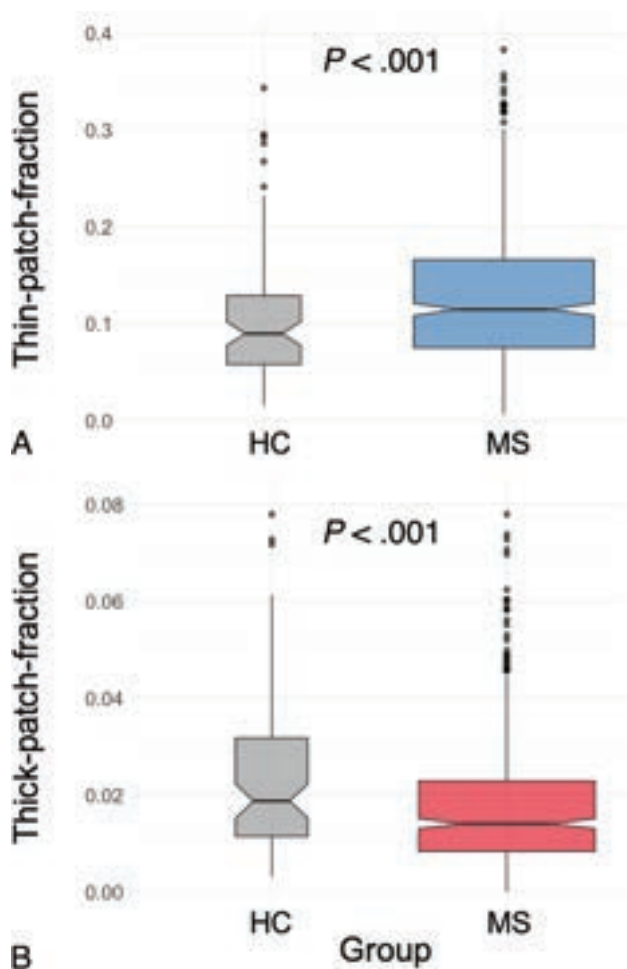


FIG 2. We investigated whether MAP differentiates patients with MS from HC. We found that both the primary outcome of MAP, ie, the TPF (A), as well as its opposite, the thick patch fraction (B), significantly discriminate MS from HC. Notice the opposed directionality: MS yields more thin but fewer thick patches. Boxplots show median (notched), IQRs, and outliers (dots); boxplot width reflects square root of sample sizes.

included a control analysis in which we considered unparcellated CTh data. We refer to this approach as a “standard approach.” We repeated all statistical comparisons for unparcellated CTh data, ie, using raw CTh values in millimeters, averaged across the cortex.

Given that we found a significant correlation between EDSS scores and MAP—but not the standard approach—we probed this difference formally in a post hoc analysis. We probed using bootstrapping, in which we first resampled the observed correlations for each method (with replacement, 999 replicates) and then calculated the respective bootstrapped correlation coefficients (r^* _{Standard}/ r^* _{Mosaic}) and assessed their difference (Δr^*). Notice that we flipped the sign of the standard approach to achieve comparability (given that atrophy corresponds to less but CTh to more thin patches). We calculated the 95% CI for Δr^* and rejected the null hypothesis of no difference in correlations if $\Delta r^* = 0.00$ was not included in the CI. Additionally, we ran another formal test comparing the correlation coefficients by using the cocor package in R (<https://cran.r-project.org/web/packages/cocor/index.html>),³² which offers various methods for comparing correlation differences. We

chose a Monte Carlo testing scheme developed for comparing dependent correlations.³³

Quantile Comparisons

In this study, we calculated TPFs using a mixed HC control data set, consisting of a smaller subset that was acquired at the same center as the MS patient cohort (TUM-HC) and a larger subset from an external center (CamCAN-HC). To estimate the effects of the different origins of the 2 HC data sets, we ran quantile (Q) analyses comparing the whole-brain TPF between TUM-HC and TUM-MS. We inspected QQ-plots between the 2 data sets and compared quantile ranks between the 2 groups for some exemplary quantile scores (corresponding to the 50%, 80%, and 95% quantile ranks in the TUM-HC group).

RESULTS

Demographics

The demographic profiles of the study populations are summarized in the Table. Adequate age-matching between all patients with MS (mean, 40.56 [SD, 10.22] years) and TUM-HC (mean, 37.36 [SD, 15.06] years) was suggested by a nonsignificant t test ($t = -1.92, P = .056$). Furthermore, χ^2 testing confirmed comparable sex distributions between the study groups ($\chi^2 < 0.001, P = .976$). The clinical scores suggested relatively mild disease burden of the MS study group, as evidenced by a median EDSS score of 1.5 (interquartile range [IQR] = 2.0), a mean cognitive MuSIC score of 27.09 (SD, 3.66), a mean MuSIC fatigue score of 7.67 (SD, 4.56), and mean lesion volume of 5.45 (SD, 8.40) mL. TUM-HC differed from CamCAN-HC, both in terms of age ($t = 9.78, P < .001$) and sex distributions ($\chi^2 = 7.03, P = .008$). The control group sizes for each individual were roughly equal, with a median of $n = 30.0$ (IQR = 6.0).

MAP Differentiates Patients with MS from HC

First, we tested whether MAP differentiates patients with MS from HC (Fig 2, note that thin and thick patches were found for MS as well as HC). T tests revealed that both thin (Fig 2A) as well as thick patch counts (Fig 2B) were significantly different between the study groups. Note that patients with MS had more thin patches ($P < .001$) but fewer thick patches ($P = .002$) than HC. Also, the standard approach showed thinner mean CTh in patients with MS versus HC ($P < .001$). See the Online Supplemental Data for further statistical details.

MAP Discriminates between MS Phenotypes

Second, we tested whether MAP discriminates among MS phenotypes (Fig 3): One-way ANOVAs suggested significantly different thin ($F [4558] = 13.84, P < .001$, Fig 3A) as well as thick ($F [4558] = 7.663, P < .001$, Fig 3B) patch fractions among the MS clinical phenotypes. Post hoc Tukey Honestly Significant Difference testing suggested that the TPFs yielded higher differential power compared with the thick patch fraction, given that more MS clinical phenotypes could be pair-wise differentiated (PMS had more thin patches versus HC ($P_{\text{adj}} < .001$), CIS ($P_{\text{adj}} < .001$), and RRMS ($P_{\text{adj}} < .001$) and also demonstrated more thin patches in RRMS versus HC ($P_{\text{adj}} < .001$). In terms of thick patches, only the pair-wise comparisons between RRMS versus

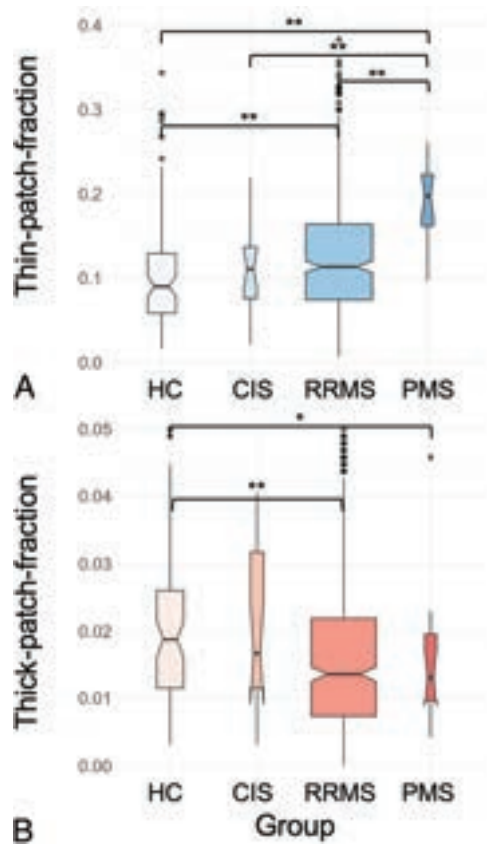


FIG 3. We investigated whether MAP discriminates among MS clinical phenotypes: Especially, the TPF (A) yielded high potential for classifying among MS clinical phenotypes because it was significantly different between PMS and HC/CIS/RRMS and, moreover, discriminated RRMS from HC. The thick patch count (B) was less sensitive and only differentiated SPMS and RRMS from HC. Boxplots show median (notched), IQRs, and outliers (dots); boxplot width reflects the square root of sample sizes. The asterisk denotes statistical significance at $P < .05$; double asterisks, $P < .001$ in post hoc testing.

HC ($P_{\text{adj}} < .001$) and PMS versus HC ($P_{\text{adj}} = .009$) were significant, suggesting fewer thick patches in the respective patient groups. Note that the standard approach also suggested different average CTh among the clinical phenotypes ($F [4564] = 35.24$, $P < .001$), but see the Online Supplemental Data for the statistical details.

MAP Is Associated with Established Scores Reflecting MS Disease Burden

Third, we tested whether MAP is associated with established scores reflecting MS disease burden (Fig 4): General linear modeling suggested significant correlations of all analyzed metrics with the TPF, including EDSS ($P = .0151$), the cognitive MuSIC score ($P = .035$), the fatigue MuSIC score ($P = .017$), and lesion volume ($P < .001$). Of note, the standard approach, ie, raw averaged CTh values, did not show significant associations with the EDSS score ($P = .132$). Bootstrapping suggested that the differences in correlations between EDSS and TPF versus EDSS and the standard approach were significantly different, given that the 95% CI interval did not include 0.00 (Online Supplemental Data). Correspondingly, Monte Carlo resampling demonstrated

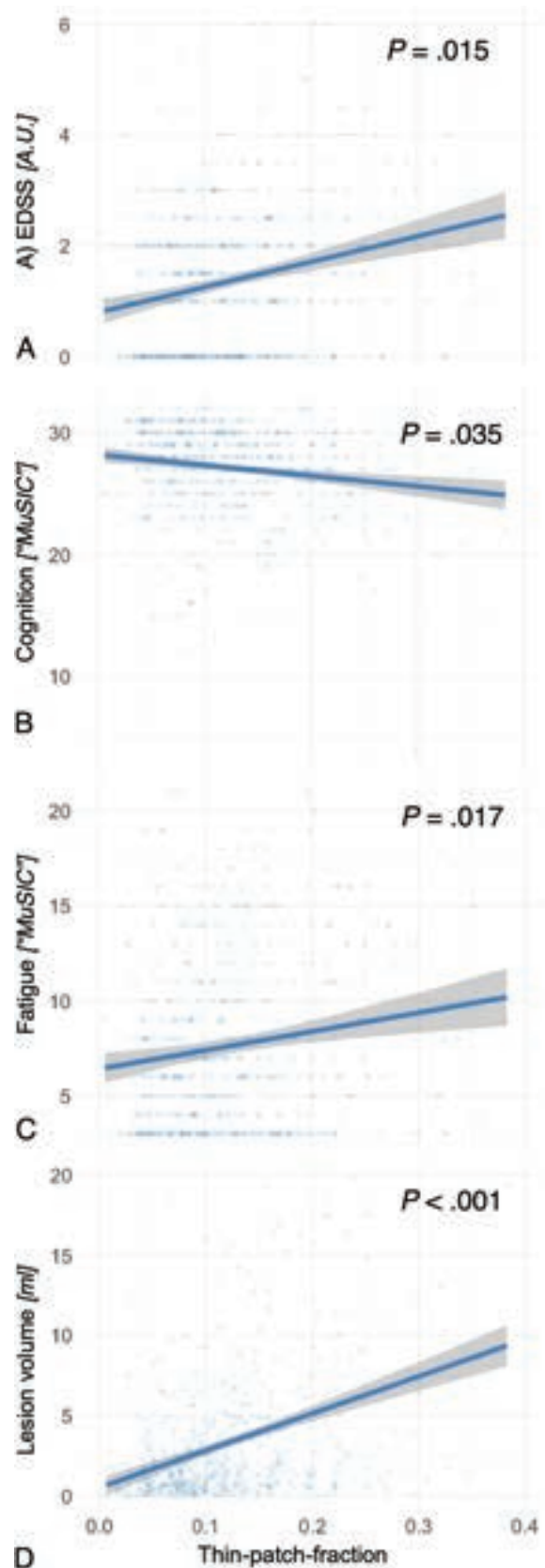


FIG 4. We tested associations of MAP with established scores of MS disease burden: We found that the primary outcome of MAP, ie, the TPF, was significantly associated with EDSS scores (A), the cognitive MuSIC score (B), the fatigue MuSIC score (C), and lesion volume (D).

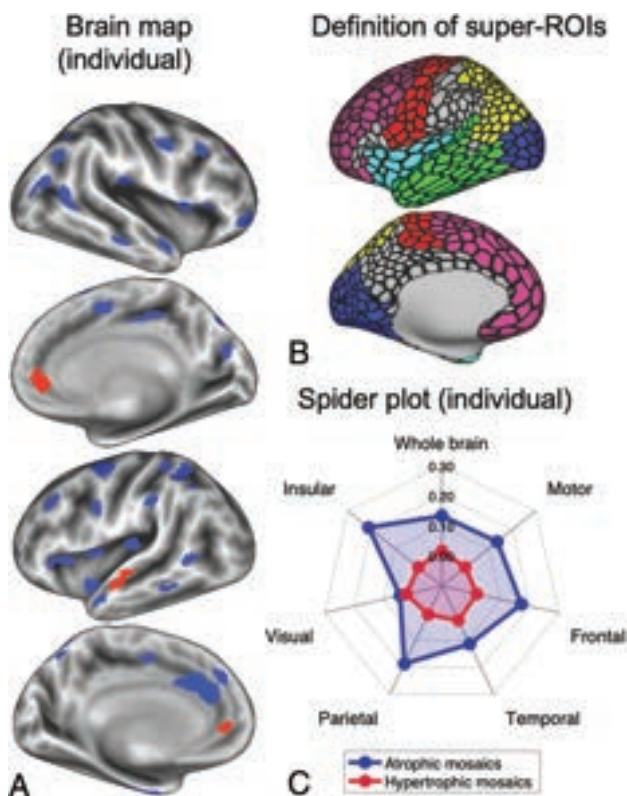


FIG 5. MAP allows visualizing individual brain maps with regionally specific estimations of atrophy (blue) or hypertrophy (red) based on comparisons with a matched reference group (A). This method may be further refined anatomically; for example, instead of summing thin patches across the entire cortex, one can specify super-ROIs (B) such as motor (red), frontal (purple), parietal (yellow), insular (light blue), temporal (green), and visual (dark blue) cortices. Thin/thick patch fractions can then be calculated for each of these super-ROIs and used for an individual and regionally specific illustration, eg, in a spider plot (C).

this significance formally ($z = 3.413$, $P = .0006$). Statistical details of the ANOVAs can be found in the Online Supplemental Data.

MAP Allows Straightforward Visualization of Region-Wise Atrophy

In Fig 5, we demonstrate the potential of MAP for straightforward visualization of individualized atrophy (or hypertrophy). Figure 5A shows a brain map from a single patient with RRMS, whereas blue patches indicate significantly “atrophic,” and red, significantly “hypertrophic” areas. Furthermore, the method allows further anatomic refinement: For example, in Fig 5B, we defined 6 super-ROIs, ie, anatomically labeled accumulations of patches around the motor, frontal, parietal, insular, temporal, and visual cortices. With this partitioning, one can assess the TPF per super-ROI instead of across the whole cortex. This information can be visualized straightforward, eg, using spider plots, such as the one shown in Fig 5C, which shows patient yields of relatively high disease burden in the insular and temporal cortices but relatively little involvement of the visual cortices.

Quantile Analyses

To estimate the effects of different data sources of HC (TUM versus CamCAN), we ran quantile comparisons (Online Supplemental

Data). We found that TUM-MS had consistently higher TPF quantile scores compared with TUM-HC (Online Supplemental Data). Moreover, we found that the quantile rank of the 50% (80%/95%) TUM-HC quantile score (TPF = 0.089/0.149/0.263) corresponded to the 36% (67%/90%) TUM-MS quantile rank (Online Supplemental Data), suggesting that TUM-MS yielded more TPFs.

DISCUSSION

In this study, we tested the validity of a relatively novel biomarker for assessing cortical disease burden in patients with MS. This strategy is based on averaging CTh across a high-resolution parcellation (No. of patches = 1000) and testing each of those patches for significantly different CTh with reference to an age-/sex-matched HC group. The method was hence dubbed MAP, and its primary outcome measure is the thin (thick) patch fraction, which indicates the fraction of significantly atrophic (hypertrophic) patches. We tested 3 potential clinical applications of MAP for MS, demonstrating the following: 1) both thin and thick patch fractions successfully differentiate patients with MS from HC, 2) TPF discriminates among MS clinical phenotypes, and 3) TPF is significantly associated with established measures reflecting MS disease burden, including EDSS, cognition and fatigue scores, as well as lesion volume. Of note, the standard approach did not show a significant correlation to EDSS. Post hoc testing using resampling approaches demonstrated the superiority of MAP versus the standard approach with respect to the association with EDSS. Finally, MAP can also be used for visualizing localized atrophy in a single-subject manner, as demonstrated in Fig 5.

Potential of MAP for Care of Patients with MS, Clinical Trials, and AI Applications

This study provides evidence that MAP, a cortical biomarker constructed from T1WI data, can provide clinically relevant information regarding GM pathology in MS. MAP is a software-supported MR imaging evaluation system that assesses T1WI data of single patients with respect to a control group to detect deviations from normality. Of particular importance, we considered reference data from open-source MR imaging repositories (ie, the CamCAN database) so that our results suggest the general validity of rating individual data with respect to externally acquired HC. Furthermore, our findings suggest that although GM estimation is known to be affected by differences in MR imaging hardware and sequence parameters such as TI,^{34,35} such a system has diagnostic value. This is of particular importance given the emerging need for quantification of GM for precision medicine in MS.¹⁵ Provided that increasing open-source population-based MR imaging data sets become available, our findings suggest that such resources can be used as adequate reference standards for personalized interpretation of MR imaging data.³⁶

Of note, MAP allows straightforward visualization of the topography of probable disease burden for single patients (Fig 5A), which may prove invaluable for MS diagnosis, given the vast heterogeneity of GM atrophy patterns.^{37,38} As we showed before investigating patients from the motor neuron disease spectrum, MAP can readily be used for monitoring atrophy progression in individual patients.^{20,21} Although we focused our investigation on a variant of MAP that estimates disease burden across the

entire cortex, we have also shown that further anatomic refinement of the method can be implemented easily so that disease burden can be specified for distinct anatomic areas of interest such as the motor cortex or frontal lobe. Such anatomic refinement is likely to have even more information for the care of patients with MS, given the demonstrated clinical relevance of the topography of atrophy patterns in MS.³⁹⁻⁴¹

Another potential application of MAP for MS is its implementation as an outcome variable in clinical trials. Whereas numerous outcome measures have been defined for MS,⁴² a personalized outcome measure to quantify cortical GM disease burden has not yet been established. Given that neurodegeneration plays a crucial role in controlling disability progression in MS,^{43,44} this is a gap that needs to be filled. We believe that MAP, via its primary outcome measure, TPF, can provide a feature for enhancing personalized detection of cortical abnormality using AI-based applications.

Limits

The current study has limitations that need to be further evaluated before any potential clinical translation of MAP into MS clinical practice. Currently, the main drawback of the here-proposed strategy is the overall small sample size of the reference group. Although we have included >700 HC from both externally and locally acquired data resources in our investigation, the size of this reference group was considerably smaller for an individually assessed patient due to age- and sex-matched selection. This feature results in discrete reference distributions and, hence, *P* values in permutation testing, which might, in turn, hamper statistical power.³¹ It might also explain why both thin and thick patches were found for our internal HC group, whereas one would expect to find no such differences for a perfect external reference population. Nevertheless, thin patches being significantly higher in MS demonstrates the discriminative power of MAP. As increasingly large-scale population-representative MR imaging databases are becoming available, this availability provides a promising opportunity for boosting the sizes of reference data, which is essential for further statistical refinement of MAP and thus an ongoing effort in our lab.

Another limitation is that the age and sex distributions from the 2 HC groups differed. The externally acquired CamCAN-HC were, on average, markedly older than the internally acquired TUM-HC. Notice, however, that the difference was expected, provided CamCAN-HC were recruited to match uniform sex and age distributions throughout the ages (spanning from ~20 years to ~90 years) and TUM-HC were recruited to match patients with MS from TUM. Note, however, that we constructed age- and sex-matched “personalized” control cohorts for each individual (see the Online Supplemental Data for details). Furthermore, both age and sex were included in all statistical assessments as variables-of-no-interest. Notice, however, that within linear regression modeling, this feature can reduce potential confounding effects but not fully eliminate them.⁴⁵

Even with such further statistical refinement, MAP as presented herein can only be 1 component of a biomarker for MS. Despite the established significance of cortical atrophy for clinical manifestation,^{46,47} MS is a multidimensional disorder that affects a vast range of functional systems.⁴⁸ Therefore, a comprehensive MS biomarker

requires multivariate construction, also taking into account, beyond MR imaging metrics, molecular measures such as neurofilaments, metabolites, and microbiomes.⁴⁹ In terms of neuroradiologic markers, tools reflecting individual subthalamic GM atrophy and WM microstructure will provide further important insight for precise assessment of overall CNS disease burden and will, thus, allow more accurate personalized patient management in MS.⁵⁰

Finally, although MAP is calculated and can be visualized for single patients, the present validation was based on group-level statistics. Therefore, we cannot claim MAP as a personalized cortical biomarker in its current form. A truly individualized assessment would typically rely on AI-based methods. However, MAP and TPF provide a validated feature with which AI-algorithms can be trained.

Despite its limitations, the MAP method, even in its current form, offers a neuroradiologic tool for software-supported assessment of cortical disease burden in MS. It can be readily collected on a regular basis in a timesaving, digital way and be visualized for individuals to localize potential cortical disease burden. Thus, MAP provides an objective, reliable, automatized, and digital solution for MS diagnostics, monitoring cortical disease progression, and may ultimately serve as an outcome measure in clinical trials, given its demonstrated relevance for neurologic impairment.

CONCLUSIONS

This study demonstrates the validity of using external T1WI data for referencing single-patient data to detect signs of abnormal CTh in MS (MAP). MAP had previously been shown to yield relevant diagnostic information in primary neurodegenerative disorders including ALS, PLS, and FTD. Here, we showed that the primary outcome measure of MAP, the TPF, differentiates MS from HC, discriminates among MS phenotypes, and is associated with established scores of MS disease burden, including EDSS, cognitive and fatigue scores, as well as lesion volume. Provided this evidence, we believe that MAP can contribute to a neuroradiologic biomarker for MS diagnostics. Furthermore, MAP can accelerate the development of a personalized MS biomarker since it provides a feature on which AI-based algorithms can be trained. Such individual features can enhance precision medicine in this highly heterogeneous disorder.

Disclosure forms provided by the authors are available with the full text and PDF of this article at www.ajnr.org.

REFERENCES

1. Lassmann H. **Multiple sclerosis pathology.** *Cold Spring Harb Perspect Med* 2018;8:a028936 CrossRef Medline
2. Friese MA, Schattling B, Fugger L. **Mechanisms of neurodegeneration and axonal dysfunction in multiple sclerosis.** *Nat Rev Neurol* 2014;10:225–38 CrossRef Medline
3. Thompson AJ, Banwell BL, Barkhof F, et al. **Diagnosis of multiple sclerosis: 2017 revisions of the McDonald criteria.** *Lancet Neurol* 2018;17:162–73 CrossRef Medline
4. Klineova S, Lublin FD. **Clinical course of multiple sclerosis.** *Cold Spring Harb Perspect Med* 2018;8:a028928 CrossRef Medline
5. Lublin FD. **New multiple sclerosis phenotypic classification.** *Eur Neurol* 2014;72(Suppl 1):1–5 CrossRef Medline
6. Rotstein D, Montalban X. **Reaching an evidence-based prognosis for personalized treatment of multiple sclerosis.** *Nat Rev Neurol* 2019;15:287–300 CrossRef Medline
7. Todea RA, Lu PJ, Fartaria MJ, et al. **Evolution of cortical and white matter lesion load in early-stage multiple sclerosis: correlation with**

- neuroaxonal damage and clinical changes. *Front Neurol* 2020;11:973 CrossRef Medline
8. Engl C, Tiemann L, Grahl S, et al. **Cognitive impairment in early MS: contribution of white matter lesions, deep grey matter atrophy, and cortical atrophy.** *J Neurol* 2020;267:2307–18 CrossRef Medline
 9. Mollison D, Sellar R, Bastin M, et al. **The clinico-radiological paradox of cognitive function and MRI burden of white matter lesions in people with multiple sclerosis: a systematic review and meta-analysis.** *PLoS One* 2017;12:e0177727–16 CrossRef Medline
 10. Cortese R, Collorone S, Ciccarelli O, et al. **Advances in brain imaging in multiple sclerosis.** *Ther Adv Neurol Disord* 2019;12:1756286419859722 CrossRef Medline
 11. Uher T, Vaneckova M, Krasensky J, et al. **Pathological cut-offs of global and regional brain volume loss in multiple sclerosis.** *Mult Scler* 2019;25:541–53 CrossRef Medline
 12. De Stefano N, Giorgio A, Battaglini M, et al. **Assessing brain atrophy rates in a large population of untreated multiple sclerosis subtypes.** *Neurology* 2010;74:1868–76 CrossRef Medline
 13. Eshaghi A, Prados F, Brownlee WJ, et al; MAGNIMS Study Group. **Deep gray matter volume loss drives disability worsening in multiple sclerosis.** *Ann Neurol* 2018;83:210–22 CrossRef Medline
 14. Wattjes MP, Ciccarelli O, Reich DS, et al; North American Imaging in Multiple Sclerosis Cooperative MRI guidelines working group. **2021 MAGNIMS-CMSC-NAIMS consensus recommendations on the use of MRI in patients with multiple sclerosis.** *Lancet Neurol* 2021;20:653–70 CrossRef Medline
 15. Amiri H, de Sitter A, Bendfeldt K, et al; MAGNIMS Study Group. **Urgent challenges in quantification and interpretation of brain grey matter atrophy in individual patients with MS using MRI.** *Neuroimage Clin* 2018;19:466–75 CrossRef Medline
 16. Shafto M, Tyler LK, Dixon M, et al; Cam-CAN. **The Cambridge Centre for Ageing and Neuroscience (Cam-CAN) study protocol: a cross-sectional, lifespan, multidisciplinary examination of healthy cognitive ageing.** *BMC Neurol* 2014;14:204 CrossRef Medline
 17. Van Essen DC, Smith SM, Barch DM, et al; WU-Minn HCP Consortium. **The WU-Minn Human Connectome Project: an overview.** *Neuroimage* 2013;80:62–79 CrossRef Medline
 18. Alfaro-Almagro F, Jenkinson M, Bangerter NK, et al. **Image processing and quality control for the first 10,000 brain imaging datasets from UK Biobank.** *Neuroimage* 2018;166:400–24 CrossRef Medline
 19. Tahedl M. **Towards individualized cortical thickness assessment for clinical routine.** *J Transl Med* 2020;18:151 CrossRef Medline
 20. Tahedl M, Chipika RH, Lope J, et al. **Cortical progression patterns in individual ALS patients across multiple timepoints: a mosaic-based approach for clinical use.** *J Neurol* 2021;268:1913–26 CrossRef Medline
 21. Tahedl M, Shing SL, Finegan E, et al. **Propagation patterns in motor neuron diseases: Individual and phenotype-associated disease-burden trajectories across the UMN-LMN spectrum of MNDs.** *Neurobiol Aging* 2022;109:78–87 CrossRef Medline
 22. McKenna MC, Tahedl M, Lope J, et al. **Mapping cortical disease-burden at individual-level in frontotemporal dementia: implications for clinical care and pharmacological trials.** *Brain Imaging Behav* 2022;16:1196–207 CrossRef Medline
 23. Schmidt P, Gaser C, Arsic M, et al. **An automated tool for detection of FLAIR-hyperintense white-matter lesions in multiple sclerosis.** *Neuroimage* 2012;59:3774–83 CrossRef Medline
 24. Yaldizli Ö, Penner IK, Frontzek K, et al. **The relationship between total and regional corpus callosum atrophy, cognitive impairment and fatigue in multiple sclerosis patients.** *Mult Scler* 2014;20:356–64 CrossRef Medline
 25. Calabrese P, Kalbe E, Kessler J. **Ein neuropsychologisches Screening zur Erfassung kognitiver Störungen bei MS-Patienten: Das Multiple Sklerose Inventarium Cognition (MUSIC).** *Psychoneuro* 2004;30:384–88 CrossRef
 26. Fischl B. **FreeSurfer.** *Neuroimage* 2012;62:774–81 CrossRef Medline
 27. Dale AM, Fischl B, Sereno MI. **Cortical surface-based analysis. I: segmentation and surface reconstruction.** *Neuroimage* 1999;9:179–94 CrossRef Medline
 28. Fischl B, Sereno MI, Dale AM. **Cortical surface-based analysis. II: Inflation, flattening, and a surface-based coordinate system.** *Neuroimage* 1999;9:195–207 CrossRef Medline
 29. Dickie EW, Anticevic A, Smith DE, et al. **Ciftify: a framework for surface-based analysis of legacy MR acquisitions.** *Neuroimage* 2019;197:818–26 CrossRef Medline
 30. Schaefer A, Kong R, Gordon EM, et al. **Local-global parcellation of the human cerebral cortex from intrinsic functional connectivity MRI.** *Cereb Cortex* 2018;28:3095–114 CrossRef Medline
 31. Nichols TE, Holmes AP. **Nonparametric permutation tests for functional neuroimaging: A primer with examples.** *Hum Brain Mapp* 2002;15:1–25 CrossRef Medline
 32. Diedenhofen B, Musch J. **cocor: a comprehensive solution for the statistical comparison of correlations.** *PLoS One* 2015;10:e0121945 CrossRef Medline
 33. Hittner JB, May K, Silver NC. **A Monte Carlo evaluation of tests for comparing dependent correlations.** *J Gen Psychol* 2003;130:149–68 CrossRef Medline
 34. Durand-Dubief F, Belaroussi B, Armspach JP, et al. **Reliability of longitudinal brain volume loss measurements between 2 sites in patients with multiple sclerosis: comparison of 7 quantification techniques.** *AJNR Am J Neuroradiol* 2012;33:1918–24 CrossRef Medline
 35. Biberacher V, Schmidt P, Keshavan A, et al. **Intra- and interscanner variability of magnetic resonance imaging based volumetry in multiple sclerosis.** *Neuroimage* 2016;142:188–97 CrossRef Medline
 36. Bethlehem RA, Seidlitz J, White SR, et al; VETSA. **Brain charts for the human lifespan.** *Nature* 2022;604:525–33 CrossRef Medline
 37. Tsagkas C, Parmar K, Pezold S, et al. **Classification of multiple sclerosis based on patterns of regional atrophy covariance.** *Hum Brain Mapp* 2021;42:2399–415 CrossRef Medline
 38. Tsagkas C, Chakravarty MM, Gaetano L, et al. **Longitudinal patterns of cortical thinning in multiple sclerosis.** *Hum Brain Mapp* 2020;41:2198–215 CrossRef Medline
 39. Steenwijk MD, Geurts JJ, Daams M, et al. **Cortical atrophy patterns in multiple sclerosis are non-random and clinically relevant.** *Brain* 2016;139:115–26 CrossRef Medline
 40. Rocca MA, Valsasina P, Meani A, et al; MAGNIMS Study Group. **Association of gray matter atrophy patterns with clinical phenotype and progression in multiple sclerosis.** *Neurology* 2021;96:e1561–73 CrossRef Medline
 41. Eijlers AJ, Dekker I, Steenwijk MD, et al. **Cortical atrophy accelerates as cognitive decline worsens in multiple sclerosis.** *Neurology* 2019;93:e1348–59 CrossRef Medline
 42. Munster CV, Uitdehaag BM. **Outcome measures in clinical trials for multiple sclerosis.** *CNS Drugs* 2017;31:217–36 CrossRef Medline
 43. Vaughn CB, Jakimovski D, Kavak KS, et al. **Epidemiology and treatment of multiple sclerosis in elderly populations.** *Nat Rev Neurol* 2019;15:329–42 CrossRef Medline
 44. Sorensen PS, Sellebjerg F, Hartung HP, et al. **The apparently milder course of multiple sclerosis: changes in the diagnostic criteria, therapy and natural history.** *Brain* 2020;143:2637–52 CrossRef Medline
 45. Pourhoseingholi MA, Baghestani AR, Vahedi M. **How to control confounding effects by statistical analysis.** *Gastroenterol Hepatol Bed Bench* 2012;5:79–83 Medline
 46. Charil A, Dagher A, Lerch JP, et al. **Focal cortical atrophy in multiple sclerosis: relation to lesion load and disability.** *Neuroimage* 2007;34:509–17 CrossRef Medline
 47. Schoonheim MM, Pinter D, Prouskas SE, et al. **Disability in multiple sclerosis is related to thalamic connectivity and cortical network atrophy.** *Mult Scler* 2022;28:61–70 CrossRef Medline
 48. Dillenseger A, Weidemann ML, Trentzsch K, et al. **Digital biomarkers in multiple sclerosis.** *Brain Sci* 2021;11:1519 CrossRef Medline
 49. Yang J, Hamade M, Wu Q, et al. **Current and future biomarkers in multiple sclerosis.** *Int J Mol Sci* 2022;23:5877 CrossRef Medline
 50. Filippi M, Agosta F. **Imaging biomarkers in multiple sclerosis.** *J Magn Reson Imaging* 2010;31:770–88 CrossRef Medline

Delayed Gadolinium Leakage in Ocular Structures on Brain MR Imaging: Prevalence and Associated Factors

Richard Olatunji, Timothy Reynold Lim, Blair Jones, Monica Tafur, Shobhit Mathur, Amy W. Lin, Aditya Bharatha, and Suradech Suthiphosuwana



ABSTRACT

BACKGROUND AND PURPOSE: Gadolinium leakage in ocular structures (GLOS) is characterized by hyperintense signal in the chambers of the eye on FLAIR and has been reported in association with blood-ocular barrier breakdown in patients with ischemic strokes. The underlying mechanism of GLOS remains poorly understood; however, some studies suggest it may be part of a physiologic excretion pathway of gadolinium. This study aimed to determine the prevalence of GLOS in an unselected patient population.

MATERIALS AND METHODS: A retrospective analysis was conducted on 439 patients who underwent brain MR imaging within 7 days of receiving a gadolinium-based contrast agent injection for a prior MR imaging study. Clinical, imaging, and laboratory data were collected. Descriptive and logistic regression analyses were performed.

RESULTS: GLOS was observed in 26 of 439 patients (6%). The occurrence of GLOS varied with time, with 3 (12%), 14 (54%), 8 (31%), and 1 (4%) patient showing GLOS within 24, 25–72, 73–120, and >120 hours after gadolinium-based contrast agent injection, respectively. Patients with GLOS were older (median age: 72 versus 55 years, $P = .001$) and had higher median serum creatinine levels (73 versus $64 \mu\text{mol/L}$, $P = .005$) and a lower median estimated glomerular filtration rate (84 versus $101 \text{ mL/min/1.73 m}^2$, $P < .001$). A shorter median time interval between gadolinium-based contrast agent injection and the index brain MR imaging was observed in the group positive for GLOS (62 versus 91 hours, $P = .003$). Multivariable regression analysis identified the estimated glomerular filtration rate (OR = 0.970; 95% CI, 0.049–0.992; $P = .008$) and time interval since gadolinium-based contrast agent injection (OR = 0.987; 95% CI, 0.977–0.997; $P = .012$) as independent factors associated with GLOS.

CONCLUSIONS: GLOS was observed in only a small percentage of patients receiving gadolinium-based contrast agent within 7 days before brain MR imaging. This phenomenon was noted in patients with normal findings on brain MR imaging and those with various CNS pathologies, and it was associated with lower estimated glomerular filtration rates and shorter time intervals after gadolinium-based contrast agent injection. While GLOS may be a physiologic gadolinium-based contrast agent excretion pathway, the presence of ocular disease was not formally evaluated in the included population. Awareness of GLOS is nonetheless useful for appropriate radiologic interpretation.

ABBREVIATIONS: eGFR = estimated glomerular filtration rate; GBCA = gadolinium-based contrast agent; GLOS = gadolinium leakage in ocular structures; IQR = interquartile range

Gadolinium leakage in ocular structures (GLOS) is a recently identified but inadequately understood phenomenon that refers to the enhancement of intraocular fluid compartments and structures following the intravascular administration of IV gadolinium-based contrast agents (GBCAs).¹ Although primarily documented in cerebrovascular disorders, such as large-vessel strokes and small-vessel

disease,^{1–5} transient global amnesia,⁶ and posterior reversible encephalopathy syndrome,⁷ GLOS has also been observed in various ocular abnormalities affecting both the anterior and posterior eye compartments,^{8–10} including central retinal artery occlusion¹¹ and optic neuritis.¹² These observations have suggested a possible mechanism involving the breakdown of the brain-ocular barrier.

Received July 28, 2023; accepted after revision October 25.

From the Division of Diagnostic Neuroradiology (R.O., T.R.L., S.M., A.W.L., A.B., S.S.), Department of Medical Imaging, Department of Data Science (B.J.), and Division of Abdominal and Breast Imaging (M.T.), Department of Medical Imaging, St. Michael's Hospital, Unity Health Toronto, University of Toronto, Toronto, Ontario, Canada; Department of Radiology (R.O.), University College Hospital, University of Ibadan, Ibadan, Nigeria; and Medical Imaging Office of Research & Innovation (S.M.), Li Ka Shing Knowledge Institute, Toronto, Ontario, Canada.

Please address correspondence to Suradech Suthiphosuwana, MD, FRCR, Division of Diagnostic Neuroradiology, Department of Medical Imaging, St. Michael's Hospital, Unity Health Toronto, University of Toronto, 30 Bond St, Toronto, ON, M5B 1W8, Canada; e-mail: suradech.suthiphosuwana@unityhealth.to

Indicates article with online supplemental data.

<http://dx.doi.org/10.3174/ajnr.A8073>

Most interesting, GLOS has also been noted in the anterior eye chamber of healthy infants¹³ and adults,¹⁴ indicating a natural excretion pathway of chelated GBCA via the blood-aqueous barrier as a physiologic event. Other possible physiologic excretion pathways in the eyes include the extraocular lymphatic pathway (through which CSF enters the optic nerve sheath complex), ocular lymphatic system (comprising the aquaporin-4-expressing retinal glial Müller cells in the inner nuclear layer of the retina), and a lymphatic drainage system that ultimately connects to the submandibular nodes.¹⁵ Numerous questions surrounding GLOS persist, however, such as its occurrence in a broader spectrum of neurologic disorders, predisposing factors, and implications for ophthalmic health or comorbid conditions.¹⁶ Thus, achieving a more complete understanding of this phenomenon is important.

In recent years, a variety of gadolinium-deposition phenomena have been recognized, ranging from asymptomatic gadolinium deposition in patients with normal renal function, termed “gadolinium storage condition,” to the more severe nephrogenic systemic fibrosis at the other end of the spectrum.^{17,18} These phenomena have had notable consequences for clinicians, patients, and the imaging industry, impacting the medical, medicolegal, and commercial perspectives. Regarding GLOS, however, whether there are short-term or long-term clinical implications associated with its occurrence remains unknown.

Given the immune-privileged status of the eyes and the uncertainty of the consequences of GLOS, the radiologist should recognize and document leakage of GBCA into this protected compartment. The sanctuary status of the eyes is maintained by 2 highly effective blood-ocular barriers, namely the blood-aqueous and blood-retinal barriers. Briefly, the blood-aqueous barrier consists of epithelial and endothelial tight junctions, respectively, in the ciliary body and iris, which are the gatekeepers for the aqueous chamber.¹⁹ The blood-retinal barrier has an outer retinal vascular endothelial barrier and an inner retinal pigment epithelial barrier working together to keep unwanted molecules out of the vitreous chamber.²⁰ Why, how, and when the blood-ocular barriers become permeable to GBCA remains a focus of contemporary research.

The time window for the onset of GLOS continues to evolve. Before Deike-Hofmann et al¹⁴ explored the pathway of GBCA through the lymphatic system up to 24 hours postinjection, there was little interest in extending the window beyond the usual 10 minutes postinjection. Other authors exploring GLOS extended the observation window up to 72 hours postinjection in prospective studies.¹⁵ The possibility of GLOS occurring after 72 hours has not yet been explored.

The primary objective of this study was to investigate the prevalence of GLOS in routine brain MR imaging performed within 7 days after prior gadolinium-enhanced MR imaging on a heterogeneous population of patients encountered in routine neuroradiology practice and to identify factors associated with the occurrence of GLOS. We also aimed to explore the possibility of GLOS as a potential physiologic process, further contributing to the understanding of this intriguing phenomenon.

MATERIALS AND METHODS

This study was approved by the institutional research ethics board of St. Michael's Hospital, Unity Health Toronto. The patient consent form was waived.

Patient Population

The MR imaging report database was used to retrospectively identify patients who had undergone brain MR imaging within 0–168 hours (7 days) of any type of GBCA injection for any contrast-enhanced MR imaging procedure (regardless of body part) between January 1, 2011, and December 31, 2020. Patients were excluded if there were severe artifacts in the orbits on brain MR images, no available axial FLAIR sequence, ocular blood products present on the index brain MR imaging study (if the baseline study was of the brain) as evidenced by abnormal susceptibility on SWI or intrinsic high signal on T1-weighted images, or incomplete laboratory data. The FLAIR sequence with fat saturation was excluded from the analysis because of frequent incomplete fluid signal suppression in the orbits and its proneness to motion-related artifacts.

Demographic and clinical data were extracted from the electronic medical records, including age and sex, indications for brain MR imaging, prior cataract surgery, serum creatinine level at the time of index brain MR imaging, and the corresponding estimated glomerular filtration rate (eGFR) calculated using an online calculator on the basis of the National Kidney Foundation and the American Society of Nephrology Task Force recommendations.²¹

MR Imaging Protocol

All patients had at least 1 initial gadolinium-enhanced MR imaging, regardless of the body part or clinical indications, performed following IV administration of any of the following GBCAs: gadobenate dimeglumine (MultiHance, 529 mg/mL; Bracco); gadoteriol (ProHance, 279.3 mg/mL; Bracco); and gadobutrol (Gadovist, 604 mg/mL; Bayer) at a dose of 0.1 mL/kg body weight.

Within 0–168 hours after the initial gadolinium-enhanced MR imaging, the patients included in the review underwent an index brain MR imaging performed on a 1.5T MR imaging scanner (Achieva DS; Philips Healthcare) using a 6-channel head coil. The axial 2D FLAIR sequences in the index brain MR imaging were acquired either without GBCA or concurrent with/immediately after GBCA injection before the acquisition of the postgadolinium T1-weighted sequence (if the index brain MR imaging protocol included a GBCA injection, as per our institution's protocol). All included axial 2D FLAIR images were acquired without fat saturation with the following sequence parameters: TR/TE/TI/flip angle = 11,000 ms/140 ms/2800 ms/90°, section thickness = 5 mm, section spacing = 6 mm, number of excitations = 1, matrix size = 240 × 240, FOV = 200 mm.

The dose and type of GBCAs injected on the initial gadolinium-enhanced MR images and the time interval between the prior gadolinium-enhanced MR imaging scan and the index brain MR imaging were recorded.

Image Analysis

The MR imaging examinations of the patients who fulfilled all eligibility criteria were electronically anonymized and placed in a designated folder on the institutional PACS. Two readers (R.O. and T.R.L.) independently reviewed the images in a random order, blinded to the antecedent imaging and clinical and

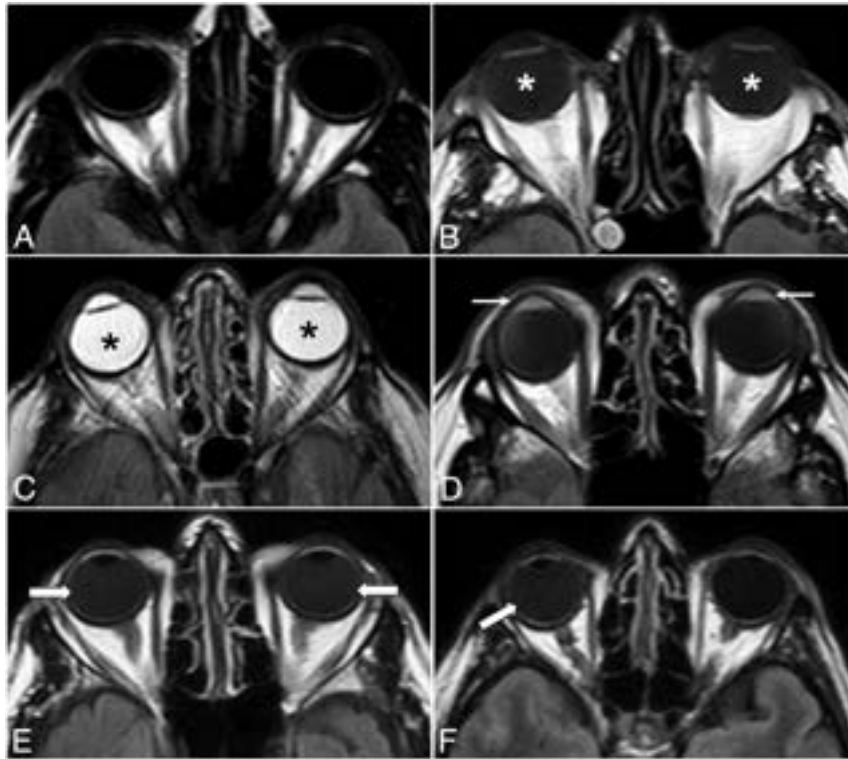


FIG 1. Illustrative examples of different GLOS patterns. Axial FLAIR images show normal globes (A), mild bilateral GLOS (asterisks in B), strong bilateral GLOS (asterisks in C), GLOS in the aqueous (arrows in D) and vitreous chambers (arrows in E), and unilateral GLOS involving the right globe (arrow in F).

laboratory data of the patients. If there was discordance between the 2 readers, a third senior reviewer (S.S.) assessed the findings and a consensus was reached. The presence or absence of GLOS, unilateral or bilateral ocular involvement, and involvement of the aqueous and/or vitreous chamber on the index brain MR imaging scan were documented. GLOS was defined as a lack of or incomplete suppression of fluid signal in the fluid-containing structures of the globes on the axial FLAIR sequence without fat saturation. Specifically, findings were considered mildly positive for GLOS if ocular fluid showed at least a higher signal intensity relative to the normal CSF but less than that of normal white matter on the same section; and they were intensely positive for GLOS if the signal intensity was greater than that of the normal white matter, approximating or equivalent to that of unsuppressed fat signal on the same section (Fig 1). The studies were visually inspected for GLOS to simulate routine clinical practice in this observational, qualitative study. Subsequently, post hoc analyses used ROIs to confirm that the signal was indeed higher than that of normal CSF or normal white matter for mild and intense GLOS, respectively.

Statistical Analysis

The baseline and demographic characteristics were summarized using descriptive statistics and compared using a χ^2 or Fisher exact test for categorical variables and Mann-Whitney *U* tests for continuous variables. The Kolmogorov-Smirnov test of normality showed that data were not normally distributed with $P < .05$. Univariable and multivariable logistic regression analyses were performed to determine which factors were associated with the presence of GLOS. The variables of interest from the univariable

analyses (age, sex, eGFR, time interval since GBCA injection, and the presence of prior cataract surgery) were included in the multivariable model using the enter method. A P value $< .05$ was considered statistically significant. Data were analyzed using SPSS Statistics for Windows, Version 25 (IBM).

RESULTS

A total of 439 patients (242 women [55.1%]; median age, 55 years; interquartile range [IQR], 45–67 years) fulfilled all inclusion criteria. Clinical indications for MR imaging included brain tumors ($n = 150$, 34.2%), intracranial hemorrhage ($n = 29$, 6.6%), ischemic stroke ($n = 24$, 5.5%), baseline assessment post-endovascular treatment ($n = 83$, 18.9%), infection/inflammation ($n = 39$, 8.9%), and others ($n = 81$, 18.5%). Thirteen (3%) patients had prior gadobutrol injection; 270 (61.5%), gadobenate dimeglumine; 152 (34.6%), gadoteridol; and 4 (0.9%) had injections using 2 different GBCAs. The index brain MR imaging was acquired without GBCA in 260 (59.2%) and was concurrent with GBCA injection in 179 (40.8%) patients. In terms of renal function, 320 (72.9%) patients were classified as G1, 102 (23.2%) as G2, and only 17 (3.9%) as G3 (Online Supplemental Data).

GLOS Prevalence and Spatiotemporal Distribution

There was imaging evidence of GLOS in 26/439 (5.9%) patients (14 women [53.8%]; median age, 71.5 years; IQR = 51.0–77.5 years). Among the patients with GLOS ($n = 26$), the index MR imaging was acquired without GBCA in 19 (73.1%) and concurrent with GBCA injection in 7 (26.9%). MR imaging showed brain tumors in 9 (34.6%), normal brain findings in 4 (15.4%), acute infarcts in 2 (7.7%), and hemorrhage in 2 (7.7%) (Online Supplemental Data). GLOS was bilateral in 22 (84.6%) and unilateral in 4 (15.4%). It involved the aqueous chamber only in 1 (3.8%), the vitreous chamber only in 18 (69.2%), and both aqueous and vitreous chambers in 7 (26.9%). GLOS was mildly positive in 21 (80.8%) and intensely positive in 5 instances (19.2%). Of the patients with intensely-positive GLOS, all 5 cases (100%) involved the aqueous chamber, while 2 cases (40%) involved both the aqueous and vitreous chambers (Table 1 and the Online Supplemental Data). GLOS was seen in 3 (11.5%), 14 (53.8%), 8 (30.8%), and 1 (3.8%) patients who underwent the index brain MR imaging within 24 hours, 25–72 hours, 73–120 hours, and >120 hours of the prior gadolinium-enhanced MR imaging, respectively (Fig 2).

Comparison of Patients with and without GLOS

Patients with GLOS were older (median age, 71.5 [IQR = 51–75.5] versus 55 [IQR = 44–66] years, $P = .001$), had higher median

serum creatinine levels (72.5 [IQR = 67.8–98] versus 64 [IQR = 44–77] $\mu\text{mol/L}$, $P = .005$), a lower median eGFR (84 [IQR = 61.5–99.5] versus 101 [IQR = 89–113] mL/min/1.73 m^2 , $P < .001$), and a shorter median time interval between the injection of GBCA and the index brain MR imaging (62 [IQR = 35–85.3] versus 91 [IQR = 51.5–133] hours, $P = .003$) compared with those without GLOS. The median dose of GBCA (16 [IQR = 10–26.5] versus 16 [IQR = 10–20] mL , $P = .9$) was not significantly different between the 2 groups. There was no association between GLOS and the type of GBCAs used ($P = .9$, Fisher exact test) (Online Supplemental Data).

Predictors of GLOS

Univariable logistic regression showed that GLOS was significantly associated with older age (OR = 1.051; 95% CI, 1.020–1.083; $P = .001$), higher serum creatinine levels (OR = 1.026; 95% CI, 1.010–1.041; $P = .001$), a lower eGFR (OR = 0.961; 95% CI, 0.943–0.979; $P = < .001$), a shorter time interval between the GBCA injection and the index brain MR imaging (OR = 0.986; 95% CI, 0.976–0.996; $P = .005$), and the presence of prior cataract surgery (OR = 3.744; 95% CI, 1.477–9.490; $P = .005$). Multivariable analysis showed that only a lower eGFR (OR = 0.970; 95% CI, 0.049–0.992; $P = .008$) and a shorter time interval between GBCA injection and the index brain MR imaging (OR = 0.987; 95% CI, 0.977–0.997; $P = .012$) were found to

be statistically significant independent predictors of GLOS; however, the magnitude of OR is small (Table 2).

DISCUSSION

In our study, GLOS was demonstrated on MR imaging in 5.9% of patients imaged for a broad range of clinical indications. Its occurrence was not limited to patients with neurovascular conditions but was also seen in those with other various pathologies and even in patients without any identified abnormality of the brain and orbits on MR imaging. This expanded distribution of GLOS underscores the importance of considering it as a potential physiologic phenomenon in a diverse cohort of patients undergoing gadolinium-enhanced MR imaging.

Our findings showed that most (around 64%) GLOS occurred within 72 hours of prior IV GBCA administration, while 36% of GLOS occurred after the usual 72-hour time window. Univariable regression analysis revealed associations between GLOS and older age, lower eGFR, prior cataract surgery, and a shorter time interval from the initial gadolinium-enhanced MR imaging scan to the index brain MR imaging. In multivariable regression analysis, however, only lower eGFR levels and a shorter time interval from prior GBCA injection to the index brain MR imaging were identified as statistically significant independent predictors of GLOS, though the effect sizes were relatively small. The dose, frequency, and type of GBCAs administered had no impact on the occurrence of GLOS.

Distinct from the general diffusion of GBCAs into extravascular spaces seen commonly in patients with chronic renal disease,²² GLOS was recently recognized in a cohort of patients with stroke at the US National Institutes of Health.¹ Subsequent work on GLOS by other authors has mainly focused on strokes and TIAs, leading to the prevailing perception of GLOS as a manifestation of ischemic insult.^{1–7} However, a recent study from a stroke unit showed that the occurrence of GLOS is not specific to stroke but rather possibly represents blood-retinal barrier dysfunction related to small-vessel disease.⁵ In our study, which included a heterogeneous group of different neurologic conditions not limited to patients with stroke, we observed

the occurrence of GLOS in patients with other entities such as brain tumors, intracranial hemorrhage, infectious/inflammatory processes, post-intracranial aneurysm coiling, and even in those with normal brain MR imaging findings. Our findings are consistent with those in prior studies showing an association between GLOS and older age.^{1,3,5} Additionally, we observed an association with lower eGFR, similar to findings of Galmiche et al,⁵ but we did not find any association with the dose of GBCA administered.

The 5.9% prevalence of GLOS in our study is much lower than the previously reported rates of 30%–76% in the setting of acute-onset permanent or reversible brain ischemia.^{1–3,5–7} Galmiche

Table 1: Spatiotemporal distribution of GLOS

GLOS Involvement (n = 26)	Count (%)
Unilateral vs bilateral involvement	
Unilateral	4 (15.4%)
Bilateral	22 (84.6%)
Aqueous and vitreous chamber involvement	
Aqueous chamber only	1 (3.8%)
Vitreous chamber only	18 (69.2%)
Both chambers	7 (26.9%)
GLOS intensity	
Mild	21 (80.8%)
Intense	5 (19.2%)

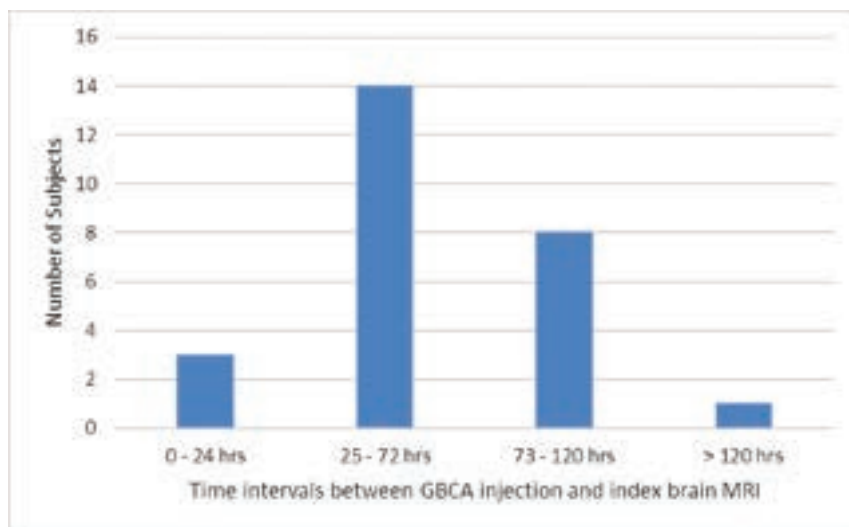


FIG 2. Bar chart showing the number of subjects positive for GLOS at different time intervals between the administration of gadolinium-based contrast agent and the index brain MR imaging.

Table 2: Associations of selected features with occurrence of GLOS

Features	Univariable Analysis		Multivariable Analysis	
	OR (95% CI)	P Value	OR (95% CI)	P Value
Age (yr)	1.051 (1.020–1.083)	.001	1.025 (0.988–1.064)	.189
Sex	0.947 (0.427–2.096)	.892	0.679 (0.290–1.586)	.679
Creatinine ($\mu\text{mol/L}$)	1.026 (1.010–1.041)	.001		
eGFR (mL/min/1.73 m^2)	0.961 (0.943–0.979)	<.001	0.970 (0.049–0.992)	.008
Time interval between GBCA injection and index brain MR imaging (hr)	0.986 (0.976–0.996)	.005	0.987 (0.977–0.997)	.012
Frequency of GBCA injections	1.268 (0.338–4.753)	.725		
GBCA doses (mL)	1.025 (0.968–1.085)	.572		
GBCA types	1.190 (0.582–2.433)	.633		
Prior cataract surgery	3.744 (1.477–9.490)	.005	1.284 (0.431–3.823)	.653

et al⁵ also sought to understand GLOS beyond stroke, reporting a prevalence of approximately 30% in their study subjects with proved ischemic stroke or TIA. In contrast, only 5.5% of our study subjects had ischemic stroke or TIA. Several factors may have contributed to our lower GLOS prevalence, including the extension of the time interval between the GBCA injection and the index brain MR imaging beyond 72 hours, the younger age of our patients, and fewer patients with impaired renal function. Other authors who reported a higher prevalence of GLOS reviewed MR imaging performed only within 24–72 hours after GBCA injection.^{1,5} In our study, most documented GLOS (14/26, 53.8%) also manifested between 24 and 72 hours after GBCA administration. Furthermore, only 3.9% of our subjects had an eGFR between 30 and 60 mL/min/1.73 m², and none had an eGFR <30 mL/min/1.73 m², representing better renal function than found in the population included in previous studies. The interplay of a more heterogeneous, relatively younger, healthier population, at least from the renal function perspective, likely resulted in the low prevalence of GLOS in our study.

On the basis of our observations, we hypothesize that GLOS might represent the physiologic excretion of GBCAs into the ocular globes via the blood-aqueous barrier, with accumulation in the vitreous chamber, which was captured at a specific time delay after GBCA injection. A recent study using delayed heavily T2-weighted and fat-suppressed FLAIR at 3 and 24 hours post-GBCA injection demonstrated physiologic excretion of GBCA into the aqueous chamber of the eye via the ciliary body even in patients without blood-brain barrier disruption or renal impairment. Excreted GBCA was observed to migrate from the aqueous chambers and accumulate in the vitreous chambers.¹⁴ Similar increased signal intensity in the aqueous chamber after GBCA administration with subsequent migration to the vitreous chamber has also been shown in healthy infantile eyes and healthy controls.^{10,13} Most interesting, in previous studies evaluating GLOS in patients with stroke, isolated aqueous chamber involvement was more commonly seen on scans with shorter time intervals between the initial and follow-up MR imaging,^{1,2} possibly, to some extent, also related to this physiologic pathway. We found evidence of GLOS in 4/26 (15.4%) patients with normal MR imaging findings of the brain and orbits, only one of whom had impaired renal function. In addition, while GLOS was significantly associated with a lower eGFR in our study, many patients positive for GLOS on MR imaging did not have marked renal impairment. These findings indicate that GLOS may be a form of

physiologic distribution or excretion of GBCA in the eye, particularly in the absence of any identifiable medical cause to explain its occurrences.

Although prior cataract surgery and age were found to be statistically associated with the presence of GLOS on univariable regression analysis, no statistical significance was noted when controlling for eGFR levels. While ocular enhancement on the postcontrast FLAIR sequence after ocular surgery has been previously demonstrated²³ and it is known that blood-ocular barrier dysregulation may persist even several years after cataract surgery,^{24,25} there has been no previous study showing a direct association of prior cataract surgery with GLOS, to the best of our knowledge. In addition, several studies have also demonstrated GLOS in various ophthalmologic pathologies involving the anterior and posterior eye compartments, including optic neuritis.^{9–12,23} Therefore, locoregional alterations in the structural and functional integrity of the blood-aqueous and blood-retinal barriers from ocular diseases and post-surgical causes should be considered in the differential diagnosis and overall assessment of GLOS.

Our study has 3 main areas of strength. First, our retrospective study is one of the largest clinical investigations on GLOS and is also among the few conducted on a heterogeneous group of patients not limited to those having neurovascular conditions, representing a real-world clinical setting. Second, we also report 2 potential independent predictors of GLOS (lower renal functional status and short time interval from GBCA injection to index brain MR imaging). Last, we report the occurrence of GLOS beyond the previously reported usual 72-hour time window post-GBCA administration.^{1,5} Delayed physiologic excretion might account for the occurrence of GLOS later during the first week in more than one-third of the patients who were positive for GLOS.

Our study has some limitations as well. First, this study is a single-center retrospective observational study in a heterogeneous population with a relatively small number of patients with GLOS. Larger prospective studies are needed to validate our findings and gain a more comprehensive understanding of the GLOS incidence and risk factors and to evaluate the impact of ophthalmologic disease on GLOS. On the basis of our study, the association between ocular diseases and the occurrence of GLOS also cannot be determined. Next, exclusion of patients with an eGFR <30 mL/min/1.73m² as per our institutional protocol during the period of data collection precludes evaluation of this cohort. Regarding our available index MR imaging studies, when performed with gadolinium, they included a 2D FLAIR sequence

acquired concurrently with GBCA injection, which could potentially affect our results. While GLOS has been found to occur as early as 12–20 minutes post-GBCA injection, however, this occurrence was documented in infantile eyes with immature blood-aqueous barriers or with a heavily T2-weighted FLAIR sequence, which is more sensitive to GBCA compared with a routine 2D FLAIR sequence.¹⁰ In addition, our imaging studies were performed at 1.5T, did not have fat suppression on FLAIR imaging, and used 2D FLAIR sequences with 5-mm section thicknesses, which could limit our ability to detect GLOS. Finally, our retrospective data derived from a routine MR imaging database precludes direct comparison with prospective data obtained with dedicated orbit surface coils and/or a heavily T2-weighted FLAIR sequence, and our rate of subjects positive for GLOS might have been understated. Despite these limitations, our study contributes data regarding the prevalence, predictors, and distribution of GLOS in patients undergoing brain MR imaging for various clinical indications.

CONCLUSIONS

Our study found GLOS in a small percentage of brain MR imaging studies in an unselected population of patients who received GBCA injections within 7 days before the index brain MR imaging. GLOS may result from the physiologic excretion of GBCAs, and its occurrence is not limited to neurovascular conditions. Lower eGFR and a shorter time interval between GBCA injection and the index brain MR imaging were found to be independently associated with GLOS. Additional research is needed to further understand the mechanism and assess the clinical significance of GLOS. Awareness of GLOS would be useful for appropriate radiologic interpretation and patient counseling when encountering this phenomenon in routine clinical practice.

Disclosure forms provided by the authors are available with the full text and PDF of this article at www.ajnr.org.

REFERENCES

- Hitomi E, Simpkins AN, Luby M, et al. **Blood-ocular barrier disruption in patients with acute stroke.** *Neurology* 2018;90:e915–23 CrossRef Medline
- Förster A, Al-Zghloul M, Wenz H, et al. **Gadolinium leakage in ocular structures is common in lacunar infarction.** *Stroke* 2019;50:193–95 CrossRef Medline
- Förster A, Ramos A, Wenz H, et al. **GLOS and HARM in patients with transient neurovascular symptoms with and without ischemic infarction.** *J Neuroradiol* 2022;49:244–49 CrossRef Medline
- Förster A, Wenz H, Böhme J, et al. **Asymmetrical gadolinium leakage in ocular structures in stroke due to internal carotid artery stenosis or occlusion.** *Clin Neuroradiol* 2020;30:221–28 CrossRef Medline
- Galmiche C, Moal B, Marnat G, et al. **Delayed gadolinium leakage in ocular structures: a potential marker for age- and vascular risk factor-related small vessel disease?** *Invest Radiol* 2021;56:425–32 CrossRef Medline
- Förster A, Wenz H, Böhme J, et al. **Gadolinium leakage in ocular structures: a novel MRI finding in transient global amnesia.** *J Neurol Sci* 2019;404:63–65 CrossRef Medline
- Ozkan E, Gocmen R, Topcuoglu MA, et al. **Blood–retina-barrier disruption accompanying blood–brain-barrier dysfunction in posterior reversible encephalopathy syndrome.** *J Neurol Sci* 2014;346:315–17 CrossRef Medline
- Manfrè L, Midiri M, Giuffrè G, et al. **Blood-ocular barrier damage: use of contrast-enhanced MRI.** *Eur Radiol* 1997;7:110–14 CrossRef Medline
- Herrera DA, Franco S, Bustamante S, et al. **Contrast-enhanced T2-FLAIR MR imaging in patients with uveitis.** *Int Ophthalmol* 2017;37:507–12 CrossRef Medline
- Manava P, Eckrich C, Luciani F, et al. **Glymphatic system in ocular diseases: evaluation of MRI findings.** *AJNR Am J Neuroradiol* 2022;43:1012–17 CrossRef Medline
- Hamel J, Fiebich JB, Villringer K. **Ocular hyperintense acute reperfusion marker.** *Neurology* 2012;79:1622–23 CrossRef Medline
- Förster A, Böhme J, Groden C, et al. **Gadolinium leakage in ocular structures in optic neuritis.** *J Clin Neurosci* 2019;68:268–70 CrossRef Medline
- Deike-Hofmann K, von Lampe P, Schlemmer HP, et al. **The anterior eye chamber: entry of the natural excretion pathway of gadolinium contrast agents?** *Eur Radiol* 2020;30:4633–40 CrossRef Medline
- Deike-Hofmann K, Reuter J, Haase R, et al. **Glymphatic pathway of gadolinium-based contrast agents through the brain.** *Invest Radiol* 2019;54:229–37 CrossRef Medline
- Deng W, Liu C, Parra C, et al. **Quantitative imaging of the clearance systems in the eye and the brain.** *Quant Imaging Med Surg* 2020;10:1–14 CrossRef Medline
- Förster A, Groden C, Alonso A. **Response by Förster et al to letter regarding article, “Gadolinium Leakage in Ocular Structures Is Common in Lacunar Infarction.”** *Stroke* 2019;50:e115 CrossRef Medline
- Harvey HB, Gowda V, Cheng G. **Gadolinium deposition disease: a new risk management threat.** *J Am Coll Radiol* 2020;17:546–50 CrossRef Medline
- Boehm IB. **Gadolinium deposition disease (GDD): does the missing link exist—a suggested pathologic model.** *Eur J Intern Med* 2022;105:118–20 CrossRef Medline
- Coca-Prados M. **The blood-aqueous barrier in health and disease.** *J Glaucoma* 2014;23:S36–38 CrossRef Medline
- Cunha-Vaz J, Bernardes R, Lobo C. **Blood-retinal barrier.** *Eur J Ophthalmol* 2011;21(Suppl 6):S3–9 CrossRef Medline
- Delgado C, Baweja M, Crews DC, et al. **A unifying approach for GFR estimation: recommendations of the NKF-ASN Task Force on reassessing the inclusion of race in diagnosing kidney disease.** *Am J Kidney Dis* 2022;79:268–88.e1 CrossRef Medline
- Kanamalla US, Boyko OB. **Gadolinium diffusion into orbital vitreous and aqueous humor, perivascular space, and ventricles in patients with chronic renal disease.** *AJR Am J Roentgenol* 2002;179:1350–52 CrossRef Medline
- Mathews VP, Caldemeyer KS, Lowe MJ, et al. **Brain: gadolinium-enhanced fast fluid-attenuated inversion-recovery MR imaging.** *Radiology* 1999;211:257–63 CrossRef Medline
- Schauersberger J, Kruger A, Müllner-Eidenböck A, et al. **Long-term disorders of the blood-aqueous barrier after small-incision cataract surgery.** *Eye (Lond)* 2000;14(Pt 1):61–63 CrossRef Medline
- Miyake K. **Blood-retinal barrier in long-standing aphakic eyes after extra- and intracapsular lens extractions.** *Graefes Arch Clin Exp Ophthalmol* 1985;222:232–33 CrossRef

Application of a Denoising High-Resolution Deep Convolutional Neural Network to Improve Conspicuity of CSF-Venous Fistulas on Photon-Counting CT Myelography

Ajay A. Madhavan, Jeremy K. Cutsforth-Gregory, Waleed Brinjikji, John C. Benson, Felix E. Diehn, Ian T. Mark, Jared T. Verdoorn, Zhongxing Zhou, and Lifeng Yu

ABSTRACT

SUMMARY: Photon-counting detector CT myelography is a recently described technique that has several advantages for the detection of CSF-venous fistulas, one of which is improved spatial resolution. To maximally leverage the high spatial resolution of photon-counting detector CT, a sharp kernel and a thin section reconstruction are needed. Sharp kernels and thin slices often result in increased noise, degrading image quality. Here, we describe a novel deep-learning-based algorithm used to denoise photon-counting detector CT myelographic images, allowing the sharpest and thinnest quantitative reconstruction available on the scanner to be used to enhance diagnostic image quality. Currently, the algorithm requires 4–6 hours to create diagnostic, denoised images. This algorithm has the potential to increase the sensitivity of photon-counting detector CT myelography for detecting CSF-venous fistulas, and the technique may be valuable for institutions attempting to optimize photon-counting detector CT myelography imaging protocols.

ABBREVIATIONS: CVF = CSF-venous fistula; CTM = CT myelography; HR-CNN = high-resolution deep convolutional neural network; PCCT = photon-counting detector CT; PC-CTM = photon-counting CT myelography; QIR = quantum iterative reconstruction; T3D = low-energy threshold

Photon-counting detector CT (PCCT) is an increasingly used imaging technology that has numerous benefits compared with traditional energy-integrating detector CT.^{1,2} Some of the advantages of PCCT include improved spatial resolution, increased signal of contrast media, improved radiation dose efficiency, and inherent spectral imaging capabilities. These features result in improved diagnostic capabilities, reduction in radiation dose, and the ability to reduce doses of contrast media for some examinations.³ Recently, PCCT myelography (PC-CTM) with the patient in the decubitus position was described as a technique to improve detection of CSF-venous fistulas (CVFs), a common cause of spontaneous intracranial hypotension.^{2,4-6}

The improved spatial resolution conferred by PCCT is particularly helpful for detecting CVFs. PCCT has the capability of reconstructing images at a section thickness of 0.2 mm, whereas most modern energy-integrating detector CT scanners have a minimum section thickness of 0.5–0.6 mm or more. Because draining veins associated with CVFs are often near other densely opacified structures such as the thecal sac or meningeal

diverticula, high spatial resolution is sometimes necessary to make the diagnosis or increase diagnostic confidence.⁶ To maximally leverage the high spatial resolution of PCCT, one must reconstruct images with a sharp kernel. If smoother kernels are used, spatial resolution is impaired. However, sharper-kernel reconstructions tend to introduce noise into the images, ultimately limiting the sharpness of the kernel that can be used without creating excessive noise. Here, we describe a novel deep-learning-based denoising algorithm used to improve the conspicuity of CVFs on PC-CTM. To our knowledge, this is the first application of such an algorithm in the realm of CT myelography, with prior algorithms having been used for chest imaging, CT angiography, and other applications.⁷⁻⁹

Technical Report

Background. The imaging protocol and technique for PC-CTM have been previously detailed.⁶ Briefly, patients are placed in the decubitus Trendelenburg position on the PCCT table (NAEOTOM Alpha; Siemens), and 3–6 scans of the spine are obtained during active injection of 5 mL of Omnipaque 300 (GE Healthcare) after a lumbar puncture with a 22- or 20-ga spinal needle. Two of these scans are obtained in an ultra-high-resolution mode, permitting 0.2-mm section thickness reconstructions. The needle is removed, and the process is repeated with the patient in the contralateral decubitus position after placing a new spinal needle. Initially, we reconstructed images using a low-energy threshold (T3D) and a

Received September 21, 2023; accepted after revision October 30.

From the Departments of Radiology (A.A.M., W.B., J.C.B., F.E.D., I.T.M., J.T.V., Z.Z., L.Y.), and Neurology (J.K.C.-G.), Mayo Clinic, Rochester, Minnesota.

Please address correspondence to Ajay Madhavan, MD, Division of Neuroradiology, Department of Radiology, Mayo Clinic, 200 First St SW, Rochester, MN 55905; e-mail: madhavan.ajay@mayo.edu

<http://dx.doi.org/10.3174/ajnr.A8097>

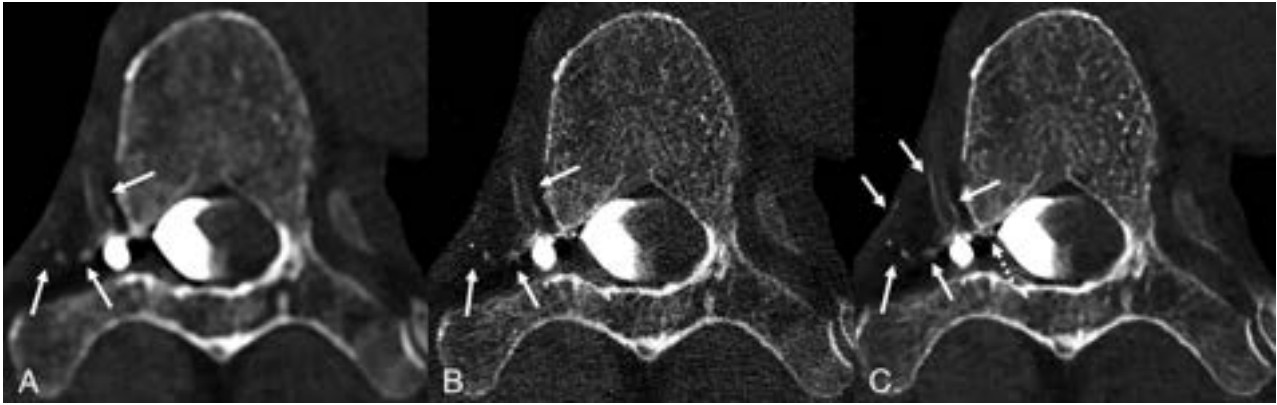


FIG 1. Axial low-energy thresholded (T3D) images in a 70-year-old man with a right T6 CVF. Images were reconstructed using a Br56 kernel (A), a sharper Qr89 kernel (B), and a Qr89 kernel after denoising with the trained model (C), all presented at the same section and window/level settings. Hazy opacification of the external vertebral venous plexus is evident using the smoother Br56 kernel (A, arrows). These external vertebral veins are poorly visualized using the Qr89 kernel secondary to noise (B, arrows). The denoised Qr89 image most clearly delineates all the involved veins, including multiple veins of the external vertebral venous plexus (C, solid arrows), and definite involvement of the internal vertebral venous plexus (C, dashed arrow).



FIG 2. Axial low-energy thresholded (T3D) images in a 70-year-old woman with a right T7 CVF. Images were reconstructed using a Br56 kernel (A), a sharper Qr89 kernel (B), and a Qr89 kernel after denoising with the trained model (C), all presented at the same section and window/level settings. The Br56 kernel demonstrates ill-defined contrast lateral to a right T7 diverticulum (A, arrow), which was thought to be suspicious but not definitive for a CVF. The Qr89 kernel more clearly delineates this finding as likely venous opacification (B, arrows), though substantial noise degrades the overall image quality and results in uncertainty in the findings. The denoised Qr89 image clearly characterizes these structures as tiny veins, (C, arrows), confirming the presence of a CVF.

Br56 kernel at a quantum iterative reconstruction (QIR) strength of 4 (Figs 1A, 2A, and 3A). When a sharper Qr89 kernel was used, the resulting images were too noisy, impairing diagnostic performance (Figs 1B, 2B, and 3B).

Implementation of the Denoising Algorithm. Subsequently, we applied a deep-learning-based algorithm to denoise the Qr89 reconstructions. The denoising model was a dedicated high-resolution deep convolutional neural network (HR-CNN) that was trained using existing patient CT myelography (CTM) examinations acquired at a high-resolution mode and reconstructed with the Qr89 kernel and 0.2-mm section thickness.^{8,9} Patient images were allocated into training/validation (7 patients) and testing (12 patients) data sets. The training/validation data set contained 11,115 routine-dose ultra-high-resolution spine CTM images reconstructed using both filtered back-projection and

QIR with strength 4 (QIR VA40; Siemens), which was split into training and validation sets using a 9:1 ratio. All images were reconstructed with the sharpest quantitative kernel (Qr89) and a pixel size of 0.15 mm (150-mm FOV and 1024 matrix) to fully use the high spatial resolution.

The following steps were used to generate paired input and target images for training the network. Noise maps were generated by taking the difference of thin-section filtered back-projection and iterative reconstruction images with section thickness/increment of 0.2/0.2 mm at the same anatomic location. Then the noise maps were scaled and random-translated with the range of -15 to +15 pixels. Iterative reconstruction images (0.4/0.2 mm) were reconstructed as the target images, while the input of the model was generated by adding the noise map to the corresponding target images.

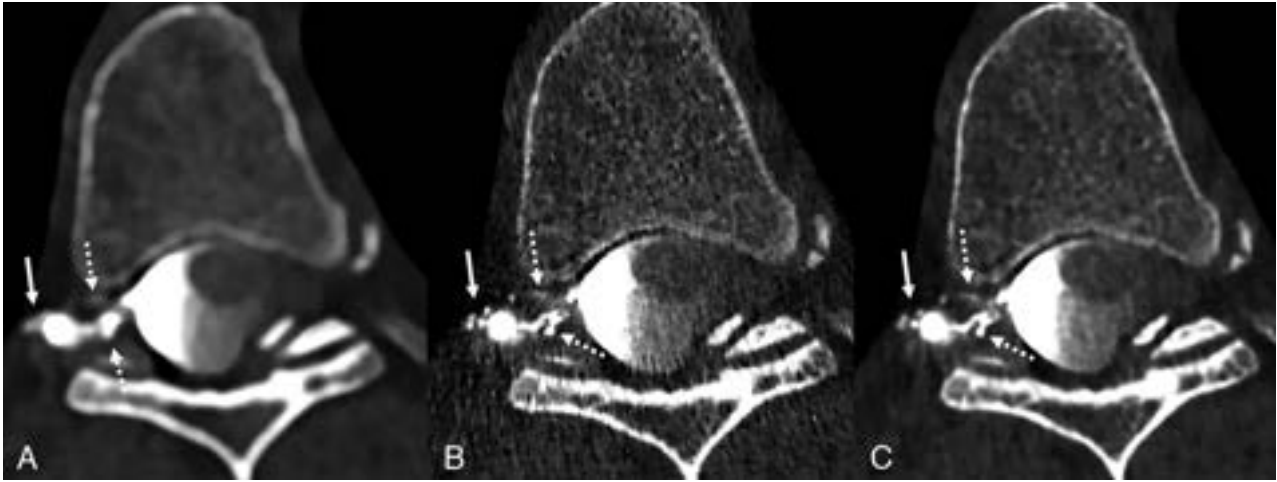


FIG 3. Axial low-energy thresholded (T3D) images in a 50-year-old woman with a right T6 CVF. Images were reconstructed using a Br56 kernel (A), a sharper Qr89 kernel (B), and a Qr89 kernel after denoising with the trained model (C), all presented at the same section and window/level settings. The Br56 kernel demonstrates amorphous opacification around a right T6 diverticulum (A, *solid arrow*) and possible venous opacification in the internal vertebral venous plexus (A, *dashed arrows*). The Qr89 kernel more clearly delineates individual external vertebral veins (B, *solid arrow*), though the image is overall degraded secondary to noise (B, *dashed arrows*). The denoised Qr89 image clearly identifies all the involved veins, including the external vertebral veins (C, *solid arrow*) and ventral/dorsal internal vertebral venous plexus (C, *dashed arrows*).

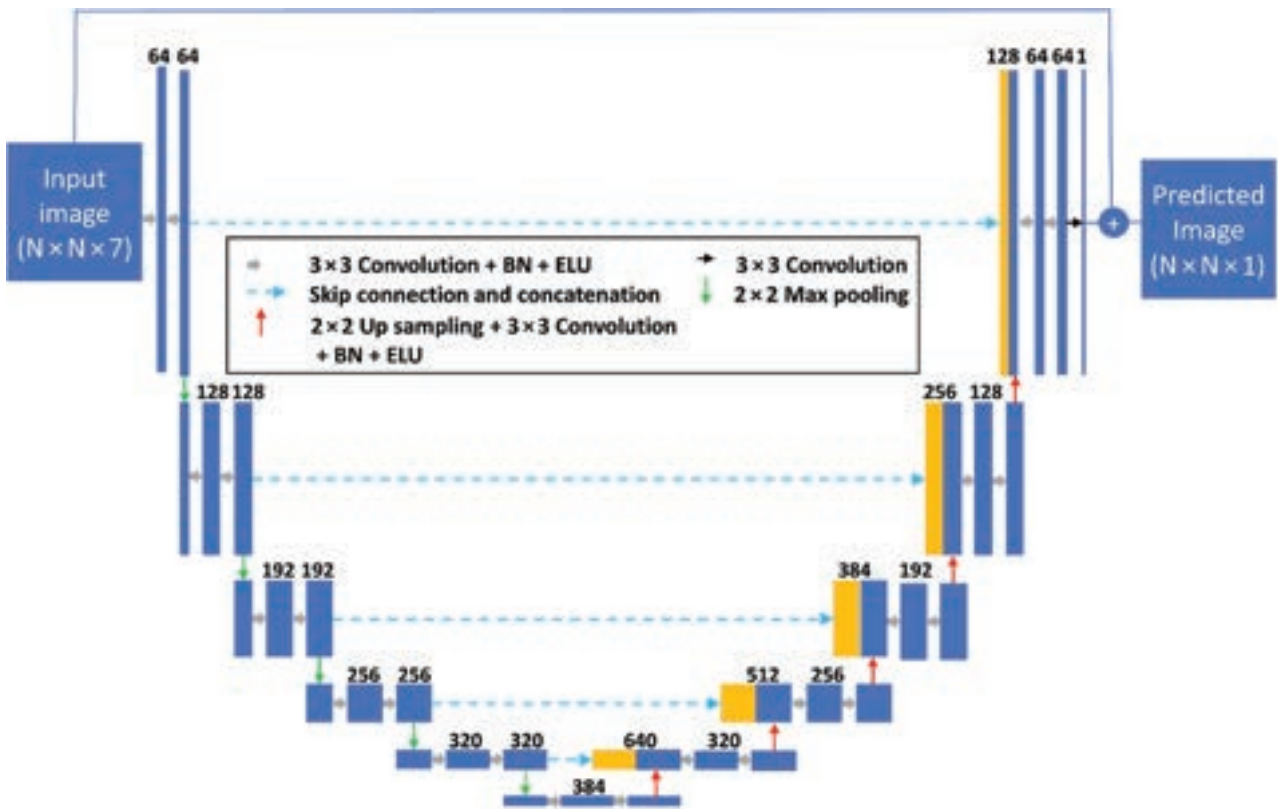


FIG 4. Schematic of the modified U-Net architecture used for this study. BN indicates batch normalization; ELU, exponential linear unit; N, arbitrary image size.

The proposed HR-CNN used a modified 6-layer residual U-Net as the architecture, (Fig 4). The architecture consists of 5 max pooling and up-convolutional layers, 64 filters with the number of filters increased by 64 at each pooling layer, and exponential linear unit activation. To optimize the performance of the HR-CNN

model, we used 7 adjacent CT slices as the channel input of the model. The network was trained for 200 epochs using the Adam optimizer with a descending learning rate from 0.001 to 0.00001, and a minibatch of 16 image patches for each iteration. We used pixel-wise mean-squared-error between the HR-CNN

Characteristics of patients and CVFs to which the fully trained denoising algorithm was applied

Characteristics	
Total patients	12
No. female	8
Total number of CVFs	10 (1 CVF in each positive case)
No. right-sided CVFs	7
Levels of CVFs (No.)	T3 (2), T6 (2), T7 (1), T8 (3), T10 (1), T12 (1)
No. CVFs only visible on denoised images (occult on smooth B656 kernel or noisy Qr89 images)	5
No. CVFs visible on all series (Br56, Qr89, Qr89 denoised) but with improved diagnostic confidence and best visualization on denoised Qr89 images	5
No CVFs present	2

output and ground truth as the loss function during optimization. The training was performed on a Tesla M40 GPU (NVIDIA) with 12-GB memory. Training was performed by a CT physicist with special expertise in PCCT and 17 years of practice experience (L.Y.), as well as a postdoctoral fellow with subspecialty training in CT physics (Z.Z.).

With the fully trained model, we were able to input a 0.2-mm section thickness T3D series with a Qr89 kernel, resulting in an output series with the same spatial resolution but substantially decreased noise (Figs 1C, 2C, and 3C). The output series takes 4–6 hours to generate. In our early experience, the use of a sharp Qr89 kernel with denoising for PC-CTM has the potential to improve the conspicuity of veins draining CVFs. To date, the algorithm has been used in 12 patients. Specific preliminary data regarding the diagnostic utility of the algorithm in these 12 cases, on case review by a single neuroradiologist (A.A.M.), are available in the Table. The mean dose-length product for these 12 patients was 4572 mGy × cm for the full examinations, and 1242 mGy × cm for the ultra-high-resolution scans used to obtain the sharp kernel, denoised images.

DISCUSSION

Application of a deep-learning-based denoising algorithm resulted in substantial image-quality improvement on the sharpest quantitative kernel (Qr89) and thinnest section-thickness (0.2 mm) reconstructions during PC-CTM. The algorithm was successfully trained with 7 clinical PC-CTM ultra-high-resolution scans, with the potential for further improvement with more training data. On the basis of our preliminary experience, this algorithm has the potential to optimize the benefits of high spatial resolution on PC-CTM, which may lead to improved sensitivity and increased diagnostic confidence. Institutions using PC-CTM may benefit from using a denoising algorithm to permit image reconstruction with the sharpest kernel possible. Since this algorithm was developed, it is not currently publicly available, though ours or similar algorithms will likely become available in the near future. Further details regarding the specific algorithm, which can be used to denoise PC-CTM examinations and other examination types, are pending publication.⁹

Limitations of this preliminary technical report include the small number of examinations to which the algorithm has been applied ($n = 12$), the computer time taken to generate the denoised images with the algorithm (4–6 hours per examination), the potential cost for institutions seeking to incorporate similar algorithms (physicist time and computing resources), and the additional images requiring review (mean of 4020 added images per case requiring approximately 20 minutes to review in our patients). Furthermore, the clinical benefit of this algorithm remains to be demonstrated.

CONCLUSIONS

Specifically, future studies should focus on identifying how frequently the algorithm improves diagnostic confidence of CVFs on image review by neuroradiologists. Nonetheless, on the basis of our current experience, we believe that the algorithm will improve conspicuity of CVFs on PC-CTM and potentially even facilitate the diagnosis of otherwise missed CVFs.

Disclosure forms provided by the authors are available with the full text and PDF of this article at www.ajnr.org.

REFERENCES

1. McCollough CH, Rajendran K, Leng S, et al. **The technical development of photon-counting detector CT.** *Eur Radiol* 2023;33:5321–30 CrossRef Medline
2. Schwartz FR, Malinzak MD, Amrhein TJ. **Photon-counting computed tomography scan of a cerebrospinal fluid venous fistula.** *JAMA Neurol* 2022;79:628–29 CrossRef Medline
3. Cundari G, Deilmann P, Mergen V, et al. **Saving contrast media in coronary CT angiography with photon-counting detector CT.** *Acad Radiol* 2023 July 31 [Epub ahead of print] CrossRef Medline
4. Schievink WI, Moser FG, Maya MM. **CSF-venous fistula in spontaneous intracranial hypotension.** *Neurology* 2014;83:472–73 CrossRef Medline
5. Pradeep A, Madhavan AA, Brinjikji W, et al. **Incidence of spontaneous intracranial hypotension in Olmsted County, Minnesota: 2019-2021.** *Interv Neuroradiol* 2023 Mar 22 [Epub ahead of print] CrossRef Medline
6. Madhavan AA, Yu L, Brinjikji W, et al. **Utility of photon-counting detector CT myelography for the detection of CSF-venous fistulas.** *AJNR Am J Neuroradiol* 2023;44:740–44 CrossRef Medline
7. VanMeter P, Marsh J Jr, Rajendran K, et al. **Quantification of coronary calcification using high-resolution photon-counting-detector CT and an image domain denoising algorithm.** *Proc SPIE Int Soc Opt Eng* 2022;12031:120311R CrossRef Medline
8. Huber NR, Ferrero A, Rajendran K, et al. **Dedicated convolutional neural network for noise reduction in ultra-high-resolution photon-counting detector computed tomography.** *Phys Med Biol* 2022;67 CrossRef Medline
9. Zhongxing Zhou AB, Chi Wan K, Kelly H, et al. **Pushing the limits of spatial resolution in clinical photon-counting-detector (PCD) CT using a dedicated high-resolution convolutional neural network (HR-CNN).** In: *Proceedings of the Annual Meeting of the Radiological Society of North America.* November 26–30, 2023. Chicago, Illinois

Temporal Characteristics of CSF-Venous Fistulas on Dynamic Decubitus CT Myelography: A Retrospective Multi-Institution Cohort Study

Andrew L. Callen, Mo Fakhri, Vincent M. Timpone, Ashesh A. Thaker, William P. Dillon, and Vinil N. Shah



ABSTRACT

BACKGROUND AND PURPOSE: CSF-venous fistula can be diagnosed with dynamic decubitus CT myelography. This study aimed to analyze the temporal characteristics of CSF-venous fistula visualization on multiphase decubitus CT myelography.

MATERIALS AND METHODS: A retrospective, multisite study was conducted on patients diagnosed with CSF-venous fistula at 2 institutions between June 2017 and February 2023. Both institutions perform decubitus CT myelography with imaging immediately following injection and usually with at least 1 delayed scan. The conspicuity of CSF-venous fistula was assessed on each phase of imaging.

RESULTS: Forty-eight patients with CSF-venous fistula were analyzed. CSF-venous fistulas were better visualized on the early pass in 25/48 cases (52.1%), the delayed pass in 6/48 cases (12.5%) and were seen equally on both passes in 15/48 cases (31.3%). Of 25 cases in which the CSF-venous fistula was better visualized on the early pass, 21/25 (84%) fistulas were still at least partially visible on a delayed pass. Of 6 cases in which the CSF-venous fistula was better visualized on a delayed pass, 4/6 (67%) were partially visible on the earlier pass. Six of 48 (12.5%) CSF-venous fistulas were visible only on a single pass. Of these, 4/6 (66.7%) were seen only on the first pass, and 2/6 (33.3%) were seen only on a delayed pass. One fistula was found with one pass only, and one fistula was discovered upon contralateral decubitus imaging without a dedicated second injection.

CONCLUSIONS: A dynamic decubitus CT myelography imaging protocol that includes an early and delayed phase, likely increases the sensitivity for CSF-venous fistula detection. Further studies are needed to ascertain the optimal timing and technique for CSF-venous fistula visualization on dynamic decubitus CT myelography and its impact on patient outcomes.

ABBREVIATIONS: CVF = CSF-venous fistula; dCTM = dynamic decubitus CT myelography; DSM = digital subtraction myelography; SIH = spontaneous intracranial hypotension

Spontaneous intracranial hypotension (SIH) is a neurologic syndrome characterized predominantly by a postural headache, which results from a reduction in CSF volume.¹ The 3 primary causes of spontaneous CSF leaks are dural tears, ruptured meningeal diverticula, and CSF-venous fistula (CVF).¹ The latter has garnered considerable attention recently as a treatable cause of SIH and now represents $\geq 25\%$ of cases referred to academic medical centers.² CVF refers to a direct communication between the spinal subarachnoid space and a paraspinal vein, which results in the loss of CSF volume.³ CVFs were first discovered and described

on digital subtraction myelography (DSM), followed shortly by both dynamic fluoroscopy without digital subtraction and dynamic decubitus CT myelography (dCTM).³⁻⁵ DSM benefits from excellent temporal resolution but has a limited FOV and superimposition of artifacts, often requiring general anesthesia for breath-holding to minimize lung motion artifact, while dCTM benefits from a whole-spine FOV and lacks superimposition of artifacts but often requires multiple phases to increase the temporal resolution and is associated with higher radiation doses.^{6,7} Which procedure is performed at a given institution generally depends on resource availability and technical expertise.

Recent studies have demonstrated that certain technical aspects of dCTM can increase detection of CVFs, including decubitus positioning, pressure augmentation, resisted inspiration, and rapid imaging after contrast administration.^{5,8-10} A recent study by Mark et al¹¹ investigated the temporal characteristics of CVFs using DSM. However, similar data have not been published regarding the optimal timing to detect CVF on dCTM. The purpose of this retrospective multi-institution cohort study was to analyze the temporal features of CVF visualization on dCTM.

Received August 17, 2023; accepted after revision October 6.

From the Department of Radiology (A.L.C., V.M.T., A.A.T.), Neuroradiology Section, University of Colorado Anschutz Medical Campus, Aurora, Colorado; and Department of Radiology and Biomedical Imaging (M.F., W.P.D., V.N.S.), Neuroradiology Section, University of California, San Francisco, San Francisco, California.

Please address correspondence to Andrew L. Callen, MD, 12401 E 17th Ave, Aurora, CO 80045, Mail Stop L954; e-mail: andrew.callen@cuanschutz.edu; @AndrewCallenMD

<http://dx.doi.org/10.3174/ajnr.A8078>

MATERIALS AND METHODS

Study Design

This was a retrospective, cross-sectional, multisite study of patients diagnosed with CVF at the University of California, San Francisco, and the University of Colorado School of Medicine. The study was approved by the institutional review board of each institution.

Patient Selection

All patients who underwent dCTM for suspected CVF between June 2017 and February 2023 at the University of California, San Francisco, or the University of Colorado School of Medicine were queried, and those studies that positively identified a CVF were included in the analysis. If >1 dCTM was performed for a patient, the study that first identified the fistula was included.

Dynamic Myelography Technique

Both institutions follow a similar procedural technique, which has been previously described.⁶ Briefly, all patients undergo lumbar puncture directly on the CT table. The puncture is performed between the L2 and S1 levels depending on patient anatomy using a 22- to 25-ga Quincke or Whitacre spinal needle (Medline Industries). Spinal opening pressure is measured using a digital manometer (Compass; Mirador Biomedical), and as long as pressure is either within the normal range or low, 5-mL aliquots of sterile saline are infused intrathecally and pressure remeasured incrementally until the pressure reaches approximately 20–25 cm H₂O. Subsequently, 10 mL of preservative-free 300-osmolar iodinated contrast material is infused, the needle is then removed, and a HoverMatt Air Transfer System (HoverTech International) is inflated for approximately 10 seconds to facilitate the cephalad movement of contrast. After deflation, 2–4 whole-spine acquisitions, or passes, are performed in rapid succession. In some cases, if imaging findings are equivocal for a CVF and clinical suspicion is high, delayed imaging up to 5 minutes is performed. In most cases, imaging is begun with the patients in the right lateral decubitus position, followed by delayed imaging with the patient in the left lateral decubitus position without a repeat injection.¹² If the findings of that initial study are negative, a dedicated contralateral dCTM is frequently performed in a different session.⁵ Imaging is performed using a multidetector row CT scanner (GoldSear Discovery CT750 HD, GE Healthcare, or Somatom Definition AS, Siemens) with the following scan parameters: detector configuration, 32 × 0.625; helical scan mode; rotation time, 800 ms; spiral pitch factor, 1.375; tube voltage, 140 kV(peak); automatic exposure control on; tube current, 300–800 mA; and section thickness, 0.625 mm.

Variables Studied

For all patients, all available imaging, including diagnostic MR imaging examinations of the brain (with and without contrast) as well as noncontrast total-spine MR imaging was reviewed at each institution. The spinal level and laterality of each CVF were recorded, as well as the number of phases performed (within a single decubitus examination) and on which phase the CVF was optimally visualized. Optimal visualization was defined as a quantitative binary variable and determined by a

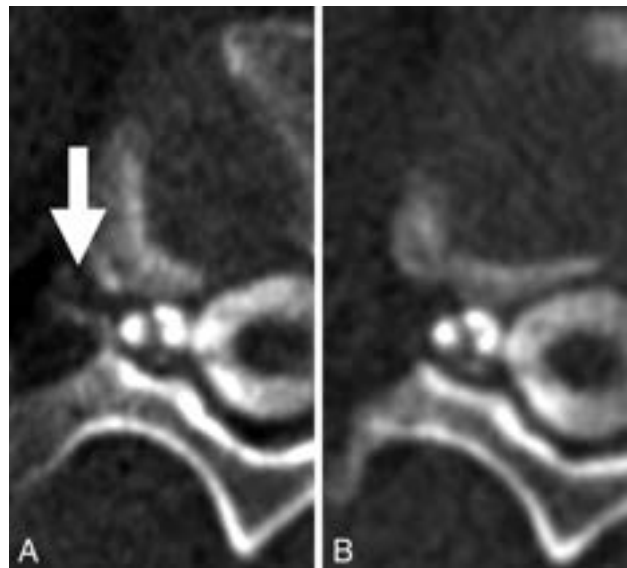


FIG 1. CVF most conspicuous on the early phase of imaging (A, arrow), which dissipates on the immediately acquired delayed phase (B).

board-certified subspecialty-trained neuroradiologist. In general, optimal visualization was designated if attenuation levels of the opacified paraspinal vein were similar to those of intrathecal contrast, with no more than a 20% difference in Hounsfield units. If the fistula could be partially-but-suboptimally visualized on a separate phase within the same decubitus examination, this result was also recorded. Figures 1 and 2 demonstrate examples of phase-specific CVF visualization, and Fig 3 demonstrates a CVF equally visible on both phases. The time between passes was calculated as the difference between the time stamps at the level of the CVF for a given phase.

If measured, the CSF opening pressure was recorded for all included patients. Binary variables such as the use of resisted inspiration and saline augmentation of CSF pressure were recorded. A Bern Score was assigned according to imaging features on each patient's preprocedural MR imaging brain examination.¹³

RESULTS

Patient Characteristics

The cohort consisted of 48 patients diagnosed with CVF, composed of 19 men (39.6%) and 29 women (60.4%) with a mean age of 58.7 (SD, 11.9) years. Twenty-one patients were from the University of Colorado, and 27 were from the University of California, San Francisco.

Imaging Characteristics of CVFs

The Table outlines patient and CVF characteristics. All except 3 CVFs were in the thoracic spine. One originated in the cervical spine, 1 originated in the lumbar spine, and 1 originated in the sacrum. CVFs were more common on the right side (34/48, 70.8%) compared with the left side (14/48, 29.2%). In this cohort, no patients had >1 CVF. For 39/48 patients (81.2%), saline pressure augmentation was performed. In 9/48 (18.8%) patients, resisted inspiration was used.

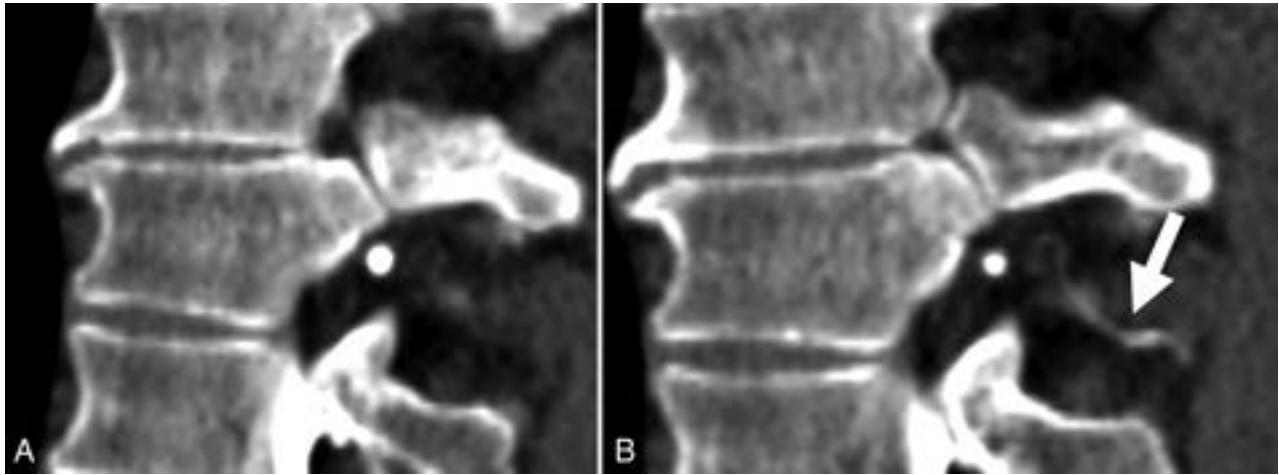


FIG 2. Early (A) and late (B) phases of dCTM, demonstrating a CVF, which is more apparent on the delayed phase (B, arrow).



FIG 3. CVFs (arrows in A and B) equally well seen on early (A) and delayed (B) phases. C, Volume-rendered CT image shows the CVF.

The number of full spine passes performed ranged from 1 to 4, with most of the cases (26/48, 57.8%) including 3 passes. The mean radiation dose per pass was 12.0 mGy (volume CT dose index) and 803.3 mGy × cm (dose-length product). The mean time between the first and second pass (calculated as the difference between the time stamps at the image displaying the fistula and the same location on the subsequent pass) was 37.7 (SD, 57.51) seconds.

The fistula origin was better visualized on the first pass of imaging in 25/48 cases (52.1%), better visualized on a delayed phase of imaging in 6/48 cases (12.5%), and equally seen on both the first and subsequent phases in 15/48 cases (31.3%). Of 25 cases in which the fistula was better visualized on the first pass, 21/25 (84.0%) fistulas were still at least partially visible on a subsequent delayed pass. Of 6 cases in which the fistula was better visualized on a delayed pass, 4/6 (67%) were partially visible on the earlier pass. Six of 48 (12.5%) fistulas were visible only on a single pass of imaging. Of these, 4/6 (66.7%) were seen only on the first pass, and 2/6 (33.3%) were seen only on a delayed pass. One fistula was found with one pass only, and one fistula was discovered upon contralateral decubitus imaging without a dedicated second injection.

Of the CVFs seen better on the early pass, 18/25 (72%) were on the right and 7/25 (28%) were on the left. Of the CVFs better seen on the delayed pass, 5/6 (83%) were on the right and 1/6 (17%) was on the left.

Clinical and Imaging Findings

Spinal opening pressure was measured in all except 1 patient (47/48). The opening CSF pressure ranged from 4 to 26 cm H₂O, with mean and median values of 12.2 and 11.0 cm H₂O, respectively. Only 2/48 (4.2%) patients had opening pressure <6 cm H₂O.

Preprocedural brain MR imaging was available in 44/48 (91.7%) patients. Pachymeningeal enhancement was observed in 34 patients (77.2%); engorgement of the venous sinus in 32 patients (72.7%); effacement of the suprasellar cistern in 29 patients (65.9%); effacement of prepontine cistern in 30 patients (68.2%); and narrowing of the mamillopontine distance in 30 patients (68.2%). The Bern Score ranged from 0 to 9, with a mean value of 6.0. Four of 44 (9%) patients had a Bern Score of ≤2 (low probability), 5/44 (11.4%) patients had a Bern Score of 3 or 4 (intermediate probability), and 35/44 (79.5%) patients

Patient and CVF characteristics

Characteristics	Overall (n = 48)
Age (mean) (SD)	58.7 (11.9)
Sex	
Female	29 (60.4%)
Male	19 (39.6%)
CVF level	
Cervical	1/48 (2.1%)
Thoracic	45/48 (93.8%)
Lumbar	2/48 (4.2%)
CVF side	
Right	34/48 (70.8%)
Left	14/48 (29.2%)
CVF visualization	
Better visualized early	25/48 (52.1%)
Still partially visualized on delay	21/25 (84.0%)
Better visualized late	6/48 (12.5%)
Still partially visualized on early	4/6 (67%)
Equally visualized early and late	15/48 (31.3%)

had a Bern Score of ≥ 5 (high probability). One patient had a Bern Score of 0.

DISCUSSION

This retrospective multi-institutional study found that while most CVFs are visible on first or subsequent phases of dCTM, approximately 1 in 8 were only visible on either the early or delayed phase, but not both. This finding suggests that acquiring >1 phase of imaging increases the sensitivity of dCTM by increasing its temporal resolution. We found that most CVFs filled early, with better visualization in more than one-half of the cases (52.1%) on early-phase imaging. A plausible hypothesis for this finding is that CVF filling is likely a function of the pressure gradient between the subarachnoid space and the surrounding epidural venous plexus, as well as the density of subarachnoid contrast material, both of which are at their peak at the beginning of the procedure. We estimate that the time between injection and scan initiation is approximately 20–30 seconds, including inflation of the HoverMatt. Additionally, in our cohort, the average time between successive scans was 37.7 seconds. This observation aligns with the findings of Mark et al,¹¹ who reported an average time to CVF filling of approximately 9 seconds and average duration of filling of 48.1 seconds using DSM. Given this time to washout, by the second run on CT, many CVFs dissipate. Thus, we advocate for imaging to be performed shortly after contrast injection, with acquisition of at least 1 additional phase to maximize the chances of CVF detection.

Our study also found that CVFs were more common on the right side, which is consistent with prior literature.¹² This observation may be related to anatomic or physiologic differences between the normal presence of arachnoid villi or paraspinal veins on the right versus the left, though the exact reasons remain to be elucidated.¹⁴

Two of 48 (4.2%) patients in our cohort had an opening pressure of <6 cm H₂O, the lower limit used by the International Classification of Headache Disorders guidelines for the diagnosis of headache attributable to low CSF pressure.¹⁵ This finding is in keeping with several recent publications demonstrating that low opening pressure is uncommon in patients with SIH.^{16,17}

Finally, in this study, most patients with CVFs had high Bern Scores, a measure of the probability of localizing a CSF leak or CVF on the basis of brain MR imaging features. Specifically, 79.5% of patients had scores of ≥ 5 , and 20.5% of patients had scores of ≤ 4 . Given that our cohort consisted entirely of individuals with confirmed CVFs, the generalizability of this observation to broader populations may be limited due to selection bias.

This study has important limitations. First, resisted inspiration, a technique known to increase the detection of CVF, was performed in only about 19% of the patients because several patients were evaluated before this technique was published, raising the question of whether the use of resisted inspiration could have resulted in improved visualization or increased detection rates of CVFs. Another limitation is related to the inability to determine whether the fistulas would have refilled if the patients were left in the decubitus position and rescanned again after a longer delay. This information could potentially guide the optimal timing and frequency of imaging to maximize CVF detection.

CONCLUSIONS

This study highlights the importance of an imaging protocol in the detection of CVFs that includes early and delayed phases of imaging. Future studies should further investigate the optimal timing and technique for CVF visualization on dCTM and explore the implications of these findings for patient outcomes and clinical management.

Disclosure forms provided by the authors are available with the full text and PDF of this article at www.ajnr.org.

REFERENCES

1. Schievink WI. Spontaneous intracranial hypotension. *N Engl J Med* 2021;385:2173–78 CrossRef Medline
2. Mamlouk MD, Shen PY, Dahlin BC. Headache response after CT-guided fibrin glue occlusion of CSF-venous fistulas. *Headache* 2022;62:1007–18 CrossRef Medline
3. Kranz PG, Amrhein TJ, Gray L. CSF venous fistulas in spontaneous intracranial hypotension: imaging characteristics on dynamic and CT myelography. *AJR Am J Roentgenol* 2017;209:1360–66 CrossRef Medline
4. Schievink WI, Moser FG, Maya MM. CSF-venous fistula in spontaneous intracranial hypotension. *Neurology* 2014;83:472–73 CrossRef Medline
5. Mamlouk MD, Ochi RP, Jun P, et al. Decubitus CT myelography for CSF-venous fistulas: a procedural approach. *AJNR Am J Neuroradiol* 2021;42:32–36 CrossRef Medline
6. Callen AL, Timpone VM, Schwertner A, et al. Algorithmic multimodality approach to diagnosis and treatment of spinal CSF leak and venous fistula in patients with spontaneous intracranial hypotension. *AJR Am J Roentgenol* 2022;219:292–301 CrossRef Medline
7. Nicholson PJ, Guest WC, van Prooijen M, et al. Digital subtraction myelography is associated with less radiation dose than CT-based techniques. *Clin Neuroradiol* 2021;31:627–31 CrossRef Medline
8. Kranz PG, Gray L, Amrhein TJ. Decubitus CT myelography for detecting subtle CSF leaks in spontaneous intracranial hypotension. *AJNR Am J Neuroradiol* 2019;40:754–56 CrossRef Medline
9. Pope MC, Carr CM, Brinjikji W, et al. Safety of consecutive bilateral decubitus digital subtraction myelography in patients with spontaneous intracranial hypotension and occult CSF leak. *AJNR Am J Neuroradiol* 2020;41:1953–57 CrossRef Medline

10. Amrhein TJ, Gray L, Malinzak MD, et al. **Respiratory phase affects the conspicuity of CSF-venous fistulas in spontaneous intracranial hypotension.** *AJNR Am J Neuroradiol* 2020;41:1754–56 CrossRef Medline
11. Mark I, Madhavan A, Oien M, et al. **Temporal characteristics of CSF-venous fistulas on digital subtraction myelography.** *AJNR Am J Neuroradiol* 2023;44:492–95 CrossRef Medline
12. Mamlouk MD, Shen PY, Jun P, et al. **Spontaneous spinal CSF leaks stratified by age, body mass index, and spinal level.** *AJNR Am J Neuroradiol* 2022;43:1068–72 CrossRef Medline
13. Dobrocky T, Grunder L, Breiding PS, et al. **Assessing spinal cerebrospinal fluid leaks in spontaneous intracranial hypotension with a scoring system based on brain magnetic resonance imaging findings.** *JAMA Neurol* 2019;76:580–87 CrossRef Medline
14. Borg N, Cutsforth-Gregory J, Oushy S, et al. **Anatomy of spinal venous drainage for the neurointerventionalist: from puncture site to intervertebral foramen.** *AJNR Am J Neuroradiol* 2022;43:517–25 CrossRef Medline
15. Gobel H. **7.2 Headache attributed to low cerebrospinal fluid (CSF) pressure.** *HIS Classification ICHD-3.* <https://ichd-3.org/7-headache-attributed-to-non-vascular-intracranial-disorder/7-2-headache-attributed-to-low-cerebrospinal-fluid-pressure/>. Accessed July 15, 2023
16. Kranz PG, Tanpitukpongse TP, Choudhury KR, et al. **How common is normal cerebrospinal fluid pressure in spontaneous intracranial hypotension?** *Cephalalgia* 2016;36:1209–17 CrossRef Medline
17. Callen A, Pattee J, Thaker AA, et al. **Relationship of Bern Score, spinal elastance, and opening pressure in patients with spontaneous intracranial hypotension.** *Neurology* 2023;100:e2237–46 CrossRef Medline

Lateral Decubitus Dynamic CT Myelography with Real-Time Bolus Tracking (dCTM-BT) for Evaluation of CSF-Venous Fistulas: Diagnostic Yield Stratified by Brain Imaging Findings

Thien J. Huynh, Donna Parizadeh, Ahmed K. Ahmed, Christopher T. Gandia, Hal C. Davison, John V. Murray, Ian T. Mark, Ajay A. Madhavan, Darya Shlapak, Todd D. Rozen, Waleed Brinjikji, Prasanna Vibhute, Vivek Gupta, Kacie Brewer, and Olga Fermo

ABSTRACT

BACKGROUND AND PURPOSE: CSF-venous fistulas (CVFs) associated with spontaneous intracranial hypotension (SIH) may have a transient appearance, relative to contrast arrival, which may influence the diagnostic performance of lateral decubitus CT myelography (CTM). We developed a dynamic CTM protocol using real-time bolus-tracking (dCTM-BT) to improve the temporal resolution and standardize the timing of CTM acquisitions post-intrathecal contrast administration. The purpose of our study was to evaluate the feasibility of the dCTM-BT technique and evaluate its diagnostic yield for CVF detection, stratified by brain MRI SIH findings.

MATERIALS AND METHODS: Patients with suspected SIH without extradural fluid collection on spine MRI who underwent dCTM-BT were retrospectively reviewed. CT bolus monitoring was performed at the upper thoracic level. Following the visualization of dense intrathecal contrast, at least 3 CTM acquisitions of the spine were obtained and reviewed by 2 neuroradiologists. The Bern SIH score was calculated on the brain MRI. The diagnostic yield for CVF detection was evaluated, stratified by Bern score categories and a receiver operating characteristic (ROC) analysis.

RESULTS: Out of 48 patients, 23 (48%) had a CVF on dCTM-BT, located at T1–5 ($n = 4$), T6–12 ($n = 18$), L1 ($n = 1$), with 70% on the right. CVF was identified in 22/22 (100%) of patients who had a high Bern score, 1/7 (14%) of those who had an intermediate score, and 0/19 (0%) of those who had a low score. The area under the ROC curve was 0.99 (95% CI, 0.98–1.00). The optimal cutoff was a Bern score of ≥ 5 (96% sensitivity, 100% specificity).

CONCLUSIONS: dCTM-BT is feasible and has excellent diagnostic performance for CVF identification/localization. The Bern score is strongly associated with CVF detection and may help inform who will benefit from dCTM-BT.

ABBREVIATIONS: CTM = CT myelography; CVF = CSF-venous fistula; dCTM-BT = dynamic CT myelogram with bolus-tracking; DSM = digital subtraction myelogram; IQR = interquartile range; ROC = receiver operating characteristic; SD = standard deviation; SIH = spontaneous intracranial hypotension; SLEC = spinal longitudinal extradural CSF collection

Spinal CSF-venous fistulas (CVFs) are spontaneously occurring abnormal connections between a meningeal diverticulum or nerve root sleeve and an adjacent paraspinal vein that result in unregulated CSF egress and CSF volume depletion, commonly known as spontaneous intracranial hypotension (SIH).¹ The probability of identifying a spinal CSF leak source, including a CVF, is highly dependent on brain MRI findings that are systematically


incorporated into a 3-tier SIH score described by Dobrocky et al.² The identification and localization of a CVF are critical steps that are required for the successful treatment of SIH associated with CVF; however, these steps may be challenging, given absent findings on conventional myelography and that they require the use of specialized lateral decubitus myelographic techniques that are not routinely performed at many centers.³

Lateral decubitus digital subtraction myelography (DSM) is known to increase the yield of CVF detection by nearly 5-fold, compared to prone DSM.⁴ While several centers use DSM as a first-line modality for CVF identification, lateral decubitus CT myelography (CTM) is increasingly being used, as it provides excellent cross-sectional spatial resolution for CVF detection, is an overall easier procedure for most operators to perform, and does not require general anesthesia.^{5–7} However, a disadvantage of CTM, compared with DSM, is that its lack of temporal resolution potentially represents a significant limitation, as we have

Received May 17, 2023; accepted after revision October 29.

From the Departments of Radiology (T.J.H., D.P., A.K.A., C.T.G., H.C.D., J.V.M., P.V., V.G., K.B.), Neurology (T.D.R., O.F.), and Neurosurgery (T.J.H.), Mayo Clinic, Jacksonville, Florida; and Department of Radiology (I.T.M., A.A.M., D.S., W.B.), Mayo Clinic, Rochester, Minnesota.

Please address correspondence to Thien J Huynh, MD, MSc, Assistant Professor, Diagnostic and Interventional Neuroradiology, Departments of Radiology and Neurosurgery, Mayo Clinic, 4500 San Pablo Rd, Jacksonville, FL 32224; e-mail: huynh.thien@mayo.edu; @ThienHuynh15

 Indicates article with online supplemental data.

<http://dx.doi.org/10.3174/ajnr.A8082>

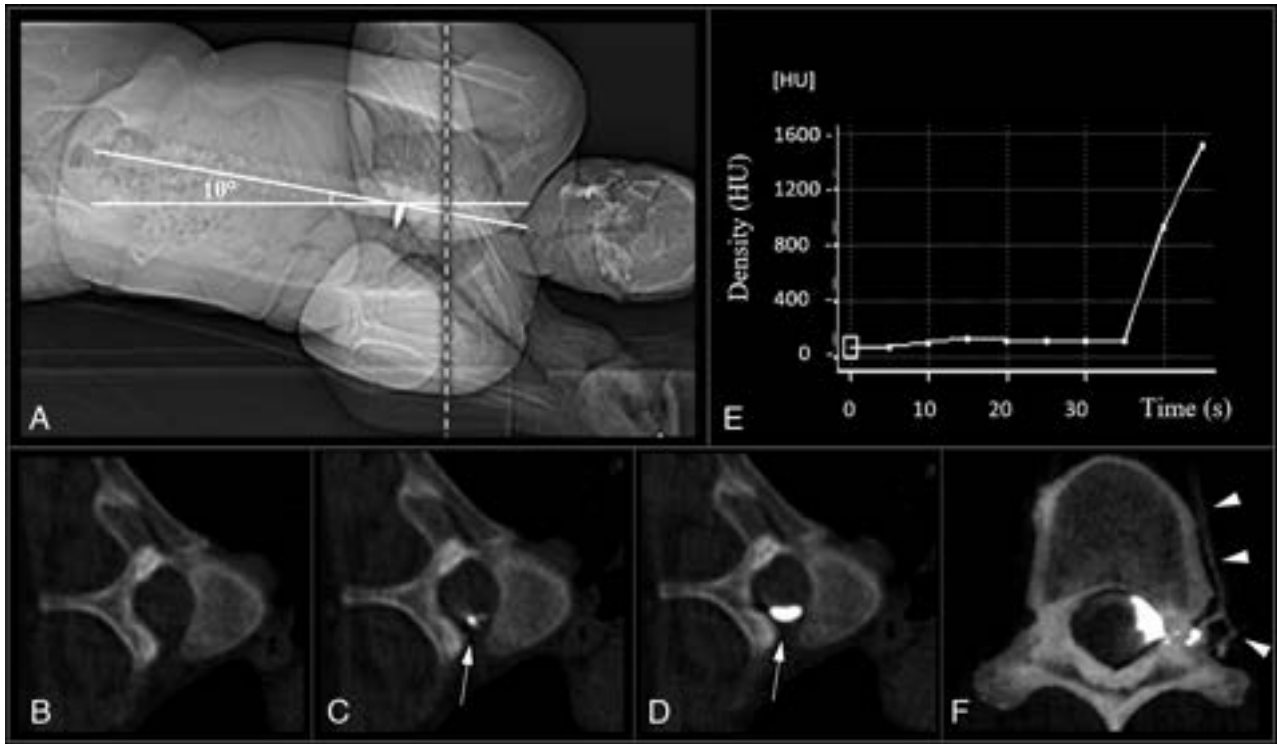


FIG 1. Lateral decubitus dynamic CT myelogram with real-time contrast bolus tracking (dCTM-BT): A, Frontal CT scout image shows patient in the left lateral decubitus position on the CT gantry table, with the hips placed at the apex of a custom firm foam wedge in the Trendelenburg position, at an angle of approximately 10°, to facilitate the caudocranial flow of contrast from the lumbar puncture towards the cervical spine. B–D, Real-time contrast bolus monitoring axial scans at the level of T5 (A, dashed line) with axial slices taken at 5-second intervals until the visualization of dense contrast (D, arrow). Note that dense contrast visualization is typically observed immediately after the initial appearance of contrast (C, arrow). E, Graph of density (Hounsfield units, HU) of monitored contrast bolus over time (region of interest placed at arrow in panels C and D; note that this graph is for illustrative purposes and is not utilized during the procedure). F, Axial CT myelogram showing the contrast enhancement of the paraspinous veins at the left T10, indicating a CSF-venous fistula (F, arrowheads).

anecdotally noted that several CVFs appear only transiently after contrast administration, which is a phenomenon that has recently been described using DSM⁸ and has also been noted on CTM.⁷

Given the importance of the timing of contrast arrival, relative to CVF opacification, we sought to standardize the timing of CTM acquisition post-intrathecal contrast administration and improve upon the temporal resolution of conventional CTM by developing a lateral decubitus dynamic CTM protocol using real-time bolus-tracking (dCTM-BT). This technique helps ensure the consistent and standardized timing of dense contrast opacification along the length of the spine, and the multiple acquisitions add temporal resolution for CVF detection. The purpose of our study was to evaluate the feasibility of the dCTM-BT technique and evaluate its diagnostic yield for CVF detection, stratified by brain MRI SIH findings.

MATERIALS AND METHODS

Patient Population

Institutional Review Board approval was obtained, and the requirement for signed informed consent was waived.

Consecutive patients who were evaluated with dCTM-BT between March 2021 and December 2022 were retrospectively reviewed. The inclusion criteria for suspected SIH were based on the clinical criteria of the International Classification of

Headache Disorders, 3rd edition⁹ and/or imaging findings on brain MRI. A spine T2-weighted MRI was performed on all patients as part of a systematic approach to SIH patient evaluation,¹⁰ and patients with spinal longitudinal extradural CSF collection (SLEC) were excluded. All included patient records were reviewed for age, sex, and presenting symptoms.

dCTM-BT Technique

A summary of the dCTM-BT protocol, including the effective dose estimates for each diagnostic CT acquisition, are listed in the Online Supplemental Data.

Patient Positioning and Lumbar Puncture. Lateral decubitus dCTM-BT was performed for all patients on 2 consecutive days, typically starting right side down on day 1 and followed by left side down on day 2. Two-day studies were performed, even if a CVF was found on the first day, to ensure a complete evaluation and exclude the possibility of multiple CVFs. The patient was positioned on the CT table in the lateral decubitus Trendelenburg position, with head downward and hips elevated, using angled foam wedges that place the patient at a 10–13° angle (Figure 1A). Pillows were placed under the patient's head and knees, and the arms were placed at or above the head, keeping the hands together for comfort to minimize motion artifacts. A frontal scout CT image of the patient was then reviewed to confirm Trendelenburg

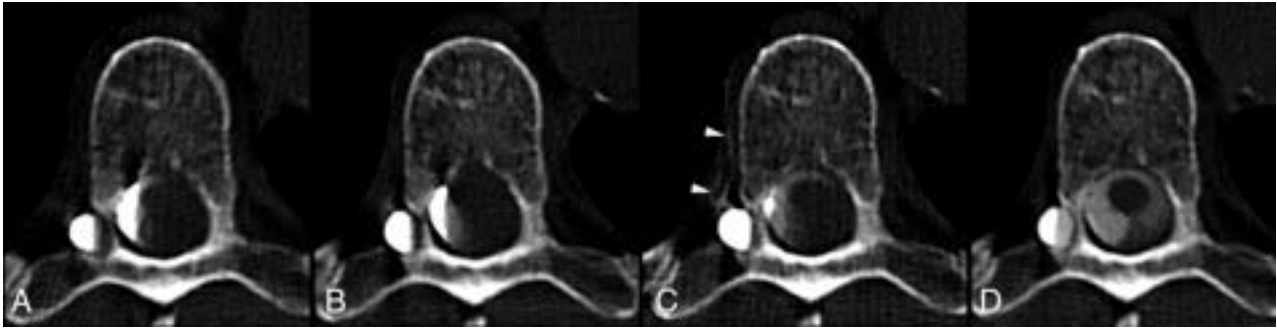


FIG 2. Axial images from a right lateral decubitus dynamic CT myelogram with bolus-tracking that were acquired at 30 seconds (A), 60 seconds (B), 2 minutes (C), and 4 minutes (D) after dense contrast was visualized on the bolus-tracking. A CSF-venous fistula is clearly identified on the image acquired at 2 minutes, with contrast visualized in a right T7 paraspinal vein (C, arrowheads). Note that the CVF only becomes more prominent after the adjacent diverticulum has nearly been completely filled with contrast.

spine angulation at a minimum of 5°, which will allow for the free cephalad flow of intrathecal contrast.⁵

Lumbar spine CT was then performed to guide needle access. A lumbar puncture was performed at or below the L2–3 level, using a 22-gauge spinal needle under CT fluoroscopy guidance. Intrathecal needle positioning was confirmed with CT fluoroscopy and with the return of CSF. If there was concern for needle placement, 0.5 mL of Omnipaque 300 (GE Healthcare) was injected to confirm positioning and avoid subdural injection. The specific equipment and injection techniques used, including the syringes and tubing, were similar to those described by Kim et al.⁵ for lateral decubitus myelography, though we used a single contrast syringe with 10 mL of preservative-free iohexol contrast (Omnipaque 300). We injected 5–10 mL of preservative-free 0.9% saline prior to the contrast injection to ensure that there was no resistance to the injection and also to empirically provide positive pressure to encourage CVF visualization. The patients were confirmed to have either low or normal opening pressure, based on a lumbar puncture in the neutral lateral decubitus position either immediately prior to the performance of the dCTM-BT or on a prior lumbar puncture.

Real-Time Bolus-Tracking and Dynamic/Multiphase CT Acquisitions. Bolus-tracking acquisitions are included in our CT software (Somatom Definition Flash; Siemens) and are widely used for contrast bolus monitoring for angiographic CT studies. The bolus-tracking pre-monitoring level was placed at the upper thoracic spine, typically T2 to T5, using the frontal and lateral CT scout images (Figure 1A). The bolus-monitoring intervals were set at 5 seconds per scan with manual triggering of the scan by the proceduralist. The rationale for placement in the upper thoracic spine was that due to the inherent delay from the time of bolus-tracking to the time of CTM acquisition, contrast would be expected to have just reached the cervical spine by the time of the first CTM acquisition. Initial pre-monitoring acquisition (Figure 1B) was performed and reviewed to ensure that the patient was not tilted either forward or backward, and, if needed, subtle patient adjustments were made. With the proceduralist in the room, bolus-tracking monitoring was then initiated, and 10 mL of iodinated contrast (Omnipaque 300) were hand-

injected at approximately 1 mL/second. During the injection, the proceduralist inspected the axial bolus-tracking acquisitions in real-time for confluent dense layering intrathecal contrast, which was typically >1500 HU in density and observed on the bolus-tracking scan immediately after the first appearance of contrast (Figure 1C-, D). Once dense contrast was visualized, the proceduralist signaled to the CT technician to trigger the CTM acquisition, which was performed in a cranial-caudal direction to minimize the time to move from the level of the monitoring to the start of the acquisition level. We performed manual triggering for the scan with a qualitative assessment of the dense contrast as subtle patient movement. Often, only approximately 6–7 mL of contrast were injected by the time of the acquisition. In the rare event that contrast was not visualized during the real-time bolus tracking, a saline chase bolus, similar to that performed for DSM, was given to further encourage the cephalad flow of contrast.⁵ At the time of the CTM acquisition, the proceduralist can either stay in the room or place the syringe setup in a sterile fashion on top of the patient and exit the room to reduce the radiation dose to the proceduralist. Following the initial CTM acquisition, which is typically acquired 15–30 seconds after the visualization of dense contrast on the bolus-tracking and thereby allows for the movement of the CT table, the remainder of the contrast was hand-injected. Additional CTM scans were performed 30–60 seconds (caudal-cranial acquisition direction) and 60–120 seconds (cranial-caudal acquisition direction) after the initial scan. The images were then reviewed for CVF visualization and the complete filling of the diverticulum, as we have anecdotally noted that a subset of CVFs only become visible after the complete filling of the adjacent diverticulum (Figure 2). Based on the diverticulum filling, additional scans were obtained at roughly 1–2 minute intervals. Each CTM acquisition was performed by covering the cervical, thoracic, and lumbar spine to the level of the lumbar puncture, with each acquisition lasting 10–20 seconds on a 128-slice CT scanner (Somatom Definition Flash). Each acquisition was also performed during instructed patient inspiration over 10–20 seconds to increase the conspicuity of the CVF.¹¹ Axial CT reconstruction was performed at a thickness of 0.6 mm, using bone and soft tissue kernels to allow for

Patient and imaging characteristics with and without CSF-venous fistula^a

	Total (n = 48)	CVF Absent (n = 25)	CVF Present (n = 23)	P Value
Patient characteristics				
Age, mean (SD)	54 (12.0)	48 (11.5)	60 (9.7)	<.001
Female	37 (77.1)	18 (72.0)	19 (83)	.38
Orthostatic/Valsalva headache	35 (72.9)	17 (68)	18 (78)	.42
CVF characteristics				
Right side			16 (70)	
CVF level				
T1–T5			4 (17%)	
T6–T12			18 (78%)	
L1			1 (4%)	
MRI brain SIH findings				
Engorgement of venous sinus	21 (44)	0 (0)	21 (91)	<.001
Pachymeningeal enhancement	21 (44)	0 (0)	21 (91)	<.001
Suprasellar cistern effacement	26 (54)	7 (28)	19 (83)	<.001
Subdural fluid collection	1 (2)	0 (0)	1 (4.3)	.48
Prepontine cistern effacement	35 (73)	13 (52)	22 (96)	<.001
Decreased mamillopontine distance	33 (69)	12 (48)	21 (91)	.001
Bern SIH Score	4 (1–8)	1 (0–3)	8 (6–8)	<.001
Bern SIH score category				
Low	19 (40)	19 (76)	0 (0)	
Intermediate	7 (15)	6 (24)	1 (4)	
High	22 (46)	0 (0)	22 (96)	

^aFor the categoric variables, the data are presented as n (%) and are compared between groups via χ^2 or Fisher exact tests. For the continuous variables, the age is reported as a mean (SD) and is compared between groups via an independent *t* test, and the other continuous variables are reported as a median (IQR) and are compared between groups via a Mann-Whitney *U* test. A *P* value of <.05 was considered to be indicative of a statistically significant result and is reported in bold.

the detection of subtle CVFs. An example of multiple dynamic images obtained from a dCTM-BT study is shown in Figure 2.

Imaging Review

All imaging was reviewed using a Visage viewer (v 7.1, Visage Imaging), using multiplanar reconstructions from the axial CTM source images, by 2 fellowship-trained, board-certified neuroradiologists. The presence and location of CVFs were identified by contrast in parasagittal veins, typically arising from the foramen venous plexus. Two neuroradiologists evaluated contrast-enhanced MRIs of the brain and dCTM-BTs. For each examination, the MRI readers were blinded to the dCTM-BT findings, and the dCTM-BT readers were blinded to the MRI findings. Discrepancies were resolved by consensus.

For dCTMs, the readers reported: 1) the presence or absence of a CVF, 2) the side of the CVF, and 3) the level of the CVF. A single reader documented additional dCTM-BT details, including 1) the Trendelenburg spine angle on the lateral CT scout image, 2) adequate contrast layering throughout the spine on the initial CTM, 3) the number of CTM acquisitions, and 4) the presence of early renal contrast excretion.

For the brain MRIs, the readers reported the features of SIH based on the Bern SIH score.² These include 3 major findings (2 points each): Smooth pachymeningeal enhancement, engorged venous sinuses, and suprasellar cistern ≤ 4.0 mm; and 3 minor findings (1 point each): subdural fluid collections, prepontine cistern ≤ 5.0 mm, and mamillopontine distance ≤ 6.5 mm. Bern SIH scores of ≤ 2 , 3–4, or ≥ 5 points represent a low, intermediate, or high probability of identifying a spinal CSF leak, respectively. Radiation exposure was recorded as the volume-weighted CT dose index and dose-length product for each acquisition.

Statistical Analysis

Continuous variables were reported as the mean (standard deviation [SD]) or median (interquartile range [IQR], 25–75) and compared between groups via an independent *t* test or Mann-Whitney *U* test, as appropriate for the data distribution. Categoric variables were reported as a frequency (percentage) and compared between groups via χ^2 or Fisher exact tests, as appropriate for the sample size. The interrater reliability for the Bern SIH Score and dCTM-BT evaluations were determined using weighted Cohen kappa (κ). Agreement was defined as fair ($\kappa = 0.21$ – 0.4), moderate ($\kappa = 0.41$ – 0.60), substantial ($\kappa = 0.61$ – 0.80), or nearly perfect ($\kappa = 0.81$ – 1).¹² The diagnostic yield of the dCTM-BT was assessed overall and stratified by Bern SIH score. A receiver operating characteristic (ROC) analysis was performed to assess the association of the Bern SIH score with the CVF diagnosis and determine the optimal cutoff for CVF detection on dCTM-

BT. All tests were 2-sided, and a *P* value of <.05 was considered to be indicative of a statistically significant result. The statistical analyses were performed using R v4.1.2 (<https://www.r-project.org/>).

RESULTS

Forty-eight patients with suspected SIH, with a mean age of 54 ± 12 years (37 female, 77%), were evaluated with bilateral lateral decubitus dCTM-BT. The patients presented with orthostatic and/or Valsalva-induced headaches (73%), impaired balance (38%), tinnitus (33%), cognitive impairment (25%), and vision impairment (19%).

A single CVF was found in 23 of 48 (48%) patients, and none of the patients had multiple CVFs. The patient and CVF characteristics are summarized in Table. The patients with CVF were significantly older (mean of 60 versus 48 years, *P* < .001). The CVFs were distributed in the thoracic and upper lumbar spine (range T3–L1), with most located at the level of T6–T12 (18/23, 78%) and on the right side (16/23, 70%). The readers had nearly perfect agreement in identifying the presence and location of CVF ($\kappa = 0.88$; 95% CI, 0.77–0.99). The dCTM-BT was performed successfully in all patients, and all lateral decubitus studies (100%) had contrast visualized throughout the complete spine on the initial scan. The median (IQR) Trendelenburg spine angle was 10° (8° – 12°). There was a median (IQR) of 4 (4–5) CTM acquisitions obtained for each complete lateral decubitus dCTM-BT study. Early renal contrast excretion was visualized in 4/23 (17%) of the studies with CVF present and in none (0/73, 0%) of the studies without CVF present (*P* = .003). There was no significant difference between the spine angle tilt and the number of

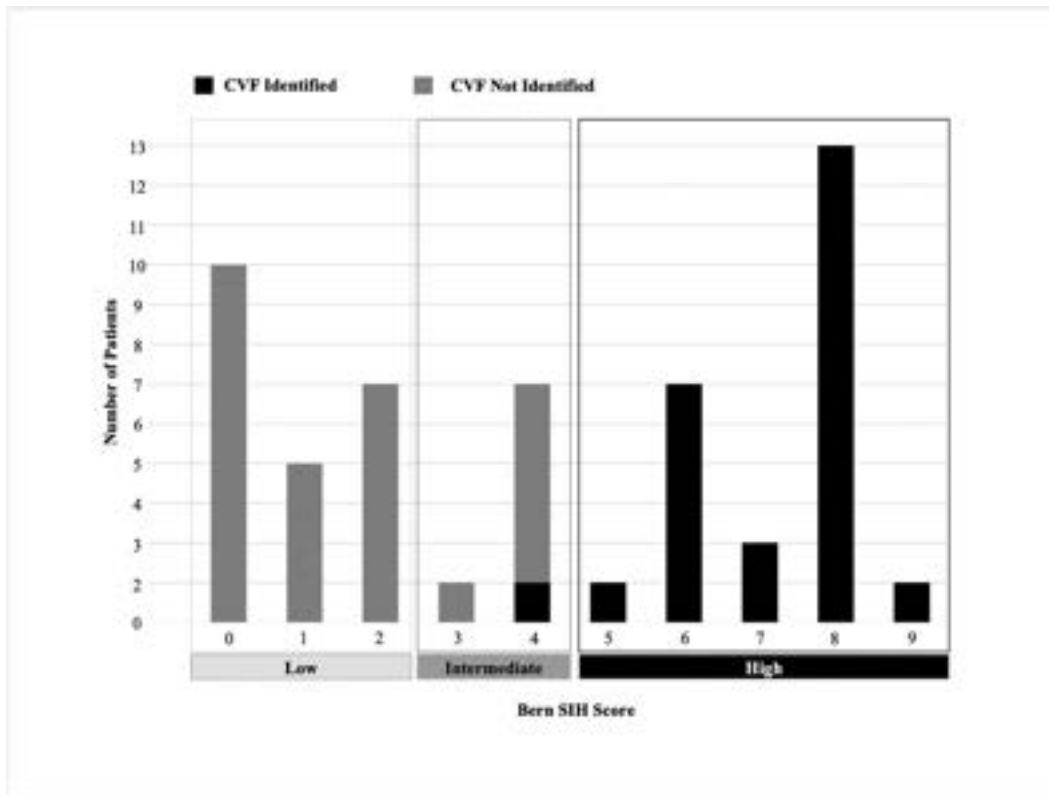


FIG 3. Bar chart illustrating the number of patients with CVF identified on dCTM-BT, across Bern SIH scores. The Bern SIH score was calculated based on the brain MRI, categorizing the probability of a spinal CSF leak as low (score of 0–2), intermediate (score of 3–4), or high (score of 5–9).

acquisitions, based on CVF presence. The median (IQR) effective dose estimate for each individual CTM acquisition was 25.3 (18.1–36.0) mSv, whereas the total dose for each complete lateral decubitus dCTM-BT was 97.6 (68.3–130.9) mSv. The total median (IQR) dose for each patient, including bilateral dCTM-BT, was 196.3 (150.7–267.7) mSv.

MRI Brain SIH Findings

The median (IQR) Bern SIH score for all patients was 4 (1–8), and there was substantial interrater agreement ($\kappa = 0.76$; 95% CI, 0.42–1.00). The median Bern SIH score (IQR) was 8 (6–8) among patients with CVF, which was significantly greater than the score of 1 (0–3) in those without CVF ($P < .001$). As shown in the Table, all Bern SIH components were more common among patients with CVF ($P < .001$), except for the presence of subdural fluid collection. However, this was possibly due to our limited number of patients with subdural collections. For all patients, the Bern SIH score tier was high in 22 (46%) patients, intermediate in 7 (15%), and low in 19 (40%).

Diagnostic Yield of dCTM-BT, Stratified by Brain MRI Findings

Using the dCTM-BT technique, stratified by the Bern SIH score, CVF was detected in 100% (22/22) of the patients who had a high Bern SIH score, 14% (1/7) of those who had an intermediate score, and 0% (0/19) of those who had a low score (Figure 3). On the ROC analysis shown in Figure 3, the area under the curve for the association between the Bern SIH score and the identification of CVF on the dCTM-BT was 0.99 (95% CI, 0.98–1.00). The

maximum value of the Youden index was at a score of ≥ 5 . A Bern SIH score of ≥ 5 had a 96% sensitivity and a 100% specificity for the presence of CVF.

DISCUSSION

We report the feasibility of performing lateral decubitus dCTM-BT and its high diagnostic yield for CVF detection, reaching 100% in the highest Bern SIH stratum and 48% in our overall cohort. The technique was successfully performed with contrast visualized throughout the spine on all CTM acquisitions. This allows proceduralists and patients to be confident in obtaining a high yield diagnostic study, despite variations in patient tilt due to the varying body habitus and morphology that are invariably encountered in patients with CVFs.¹³ This technique also overcomes some of the limitations of traditional CTM, as the bolus-tracking allows for the consistent, reliable, and standardized timing of dense contrast opacification along the length of the spine, and the multiple/dynamic acquisitions add the needed temporal resolution required for optimal CVF detection. However, the high diagnostic yield of dCTM-BT should be carefully weighed against its relatively high radiation dose, especially with multiple acquisitions, and efforts should be made to limit its use to patients with high suspicion for SIH associated with CVF.

In our early experience with dynamic CTM and most recently described using DSM by Mark et al⁸ it was noted that CVFs may often have a delayed appearance, relative to the timing of the contrast arrival, at the level of the CVF, ranging between 0 and 30 seconds, and it may appear only transiently, ranging from 24 to

68 seconds. Accordingly, if only a single CTM acquisition is performed either too early or late,⁷ a subtle CVF may be missed, ultimately negatively impacting patient outcome. In theory, the dCTM-BT technique facilitates the “catching” of transiently appearing CVFs, as has been emphasized by Mamlouk et al,⁷ and it is a natural evolution of the lateral decubitus CTM technique that was initially described by Kranz et al.⁶ dCTM-BT may also be advantageous, compared to DSM, as the technique does not require general anesthesia, is more resistant to motion/cardiac pulsation artifacts, and has improved cross-sectional spatial resolution for the detection of subtle CVFs that are draining either intraosseously or into the internal vertebral venous plexus or are possibly being obscured by overlapping bony structures or a large diverticulum.

To our knowledge, this is the first study to report the diagnostic yield of CTM for CVF identification, stratified by the Bern SIH score. Previous studies have reported the overall diagnostic yields of DSM and CTM for CVF detection in SLEC-negative patients with SIH and have varied between 50% to 75%,^{4,7,10,14} which is consistent with our overall yield of 48%. A recent study demonstrated the association of the Bern SIH score with the presence of CVF on lateral decubitus CT myelography; however, it did not evaluate the specific yield by Bern SIH score stratum.¹⁵ While there are minor differences in the procedural techniques between studies, it is important to consider that the differences in the yields may be attributable to the pretest probability of CVF diagnosis of the patient cohort selected for DSM/CTM. Therefore, it is necessary to compare the diagnostic yield of CVF identification, stratified by Bern SIH score categories, instead of the overall yield, in order to determine the diagnostic performance of a modality. Only Kim et al¹⁴ have reported the diagnostic yield of DSM for CSF leak, stratified by the Bern SIH score, in 62 SLEC-negative patients with SIH. In this study, 85% of the CSF leaks were from CVF, with an overall diagnostic yield of 53%.¹⁴ Stratified by Bern SIH categories of high, intermediate, and low probability, DSM identified the site of the CSF leak in 67%, 46%, and 0% of cases, respectively. Our 100% diagnostic yield in the high-probability Bern SIH score category was considerably higher than the 67% CSF leak detection that was reported by Kim et al. Moreover, the higher area under the ROC curve for a Bern SIH score of 0.99 in our study, compared with 0.70 in the study by Kim et al, supports the greater diagnostic performance of dCTM-BT, compared with DSM. We suspect that the reason for the greater diagnostic performance is due to the improved cross-sectional spatial resolution combined with the added temporal resolution of the dCTM-BT technique, compared with DSM.

Interestingly, in both our study and the study by Kim et al¹⁴ a Bern SIH score of ≥ 5 was the optimal threshold for the identification of a leak, with 96% sensitivity and 100% specificity for dCTM-BT versus 85% sensitivity and 52% specificity for DSM. This also corresponds precisely to the high-probability threshold established in the initial derivation and validation cohort that was established by Dobrocky et al.² Accordingly, this likely represents the ideal high-probability threshold in patients with SIH to support evaluation with either lateral decubitus DSM, CTM, or, ideally, dCTM-BT. The diagnostic yield in patients with intermediate scores varies widely, from 14% in our study to the

previously reported values of 46–73%.^{2,14} The reason for the low yield in the group in our study remains uncertain; however, we suspect that this may be due to possible variations in interobserver agreement in the scoring of the various items of the Bern SIH score, which may be expected in practice. Understanding the reliability of each Bern SIH score component requires further dedicated study. For patients with a low Bern Score of ≤ 2 , our study, the study by Kim et al¹⁴ and the internal validation cohort by Dobrocky et al² found a yield of 0%. Mamlouk et al⁷ also reported a yield of 0% in 5 patients with normal brain MRI. Deciding whether to pursue lateral decubitus myelography in this cohort must be a highly individualized decision between the patient and the provider after a discussion of the risks and benefits, including the expected diagnostic yield. However, it is important to note that it has been reported in several studies that patients with normal MRI of the brain may still harbor a CSF leak,^{10,16,17} and, even in the derivation cohort of the Bern SIH score, there was a 6.6% positive leak rate in the low-probability category.² The inability to identify a large portion of leaks in the intermediate and low Bern score groups remains uncertain and may be due to subtle, small, slow-flow and/or intermittently leaking CVFs that are below the resolution of conventional imaging.

The Bern SIH score was initially developed based on the ability of identifying a CSF leak source on conventional CT myelography and dynamic myelography among patients with suspected SIH.² One of the main limitations of the initial study was the generalizability of the score to predict the presence of a CVF, as the score was derived from CSF leaks between 2013 to 2017 at a single center, prior to the widespread use of lateral decubitus myelography for CVF detection.^{4,10} Accordingly, especially given that epidural contrast leakage was primarily used to identify the presence of a CSF leak in the initial study, it is likely that patients with CVFs were largely excluded from both the initial score derivation and validation. Although this easy-to-use scoring has been applied as a diagnostic and/or post-treatment marker for SIH associated with CVF using both lateral decubitus DSM^{14,17} and CTM,¹⁸ its predictive performance has not yet been validated for CVF detection on dCTM-BT. With the outstanding discriminative ability of the Bern SIH score in our study of 0.99 AUC as well as the excellent sensitivity and specificity of a high score for CVF detection correlating with the high AUC in the derivation and validation cohorts of 0.98 and 0.93, respectively, our results validate this scoring system as a highly effective tool with which to triage patients with SIH associated with CVF for further evaluation with dCTM-BT.

Our study has several limitations. Our sample size was small, which limits statistical power and potentially introduces patient selection bias that could influence our results; however, our results and sample size are similar/larger, compared with prior publications.^{6,7,10,14} All dCTM-BT was performed by a single proceduralist, which may affect the generalizability and dissemination of the results; however, this technique helps provide confidence to proceduralists by ensuring adequate contrast coverage and timing for the initial scans, and, ultimately, diagnostic performance, which should help support adoption. We only included the initial evaluation for patients without prior surgery or embolization. It is known that embolic material may cause

significant artifact, which may limit the visualization of a leak at the prior embolization site.³ We also did not study same-day bilateral procedures;¹⁹ however, we have since performed the dCTM-BT technique without difficulty in same-day bilateral procedures, and we expect a similarly high diagnostic yield. Further detailed study is needed to evaluate the yield by phase as well as the optimal timing and number of phases to be acquired. Our preliminary data suggest that the first 1 to 3 phases provided the highest yield, and we recommend performing at least 2 acquisitions and additional scans as needed to ensure the filling of large diverticula. The number of acquisitions and the greater radiation dose for CTM overall, compared with DSM,²⁰ should be balanced against its high diagnostic performance, the age of the patient, and local expertise. The improved efficacy of this technique, compared with non-bolus-tracked and single-phase CTM, also remains uncertain and requires further study. We included the complete cervical spine in our scan range; however, to reduce the radiation dose, the upper and mid cervical spine could theoretically be omitted, as CVFs are extremely rare in this location. It should also be noted that this technique does not evaluate CVFs in the lumbosacral region, which is known to harbor a small minority of leaks.²¹ The further incorporation of photon-counting CT with this technique may also provide greater diagnostic performance with a lower radiation dose and is a promising avenue for further research.²² We did not perform dedicated resisted inspiration in our study. The additional use of resisted inspiration may provide additional diagnostic yield; however, this also requires further study.^{23,24} Spinal needles were used for the lumbar puncture in the study due to operator experience; however, it is universally recommended to use atraumatic needles for lumbar puncture, especially during the work-up of patients with SIH, to prevent post-dural puncture headaches and iatrogenic CSF leaks.²⁵

CONCLUSIONS

dCTM-BT is feasible and has excellent diagnostic performance for identifying and localizing CVFs associated with SIH. The yield approaches 100% in patients with the highest probability of harboring CVF, as categorized by the Bern SIH score. The Bern SIH score is strongly associated with the identification of a CVF in SLEC-negative patients with SIH and may be potentially used as a triage tool with which to identify patients who will benefit from dCTM-BT.

Disclosure forms provided by the authors are available with the full text and PDF of this article at www.ajnr.org.

REFERENCES

- Schievink WI, Moser FG, Maya MM. CSF-venous fistula in spontaneous intracranial hypotension. *Neurology* 2014;83:472–73 CrossRef Medline
- Dobrocky T, Grunder L, Breiding PS, et al. Assessing spinal cerebrospinal fluid leaks in spontaneous intracranial hypotension with a scoring system based on brain magnetic resonance imaging findings. *JAMA Neurol* 2019;76:580–87 CrossRef Medline
- Kranz PG, Amrhein TJ. The promise and challenges of CSF-venous fistula treatment. *J Neurointerv Surg* 2022;14:951–52 CrossRef Medline
- Schievink WI, Maya MM, Moser FG, et al. Lateral decubitus digital subtraction myelography to identify spinal CSF-venous fistulas in spontaneous intracranial hypotension. *J Neurosurg Spine* 2019;31:902–05
- Kim DK, Brinjikji W, Morris PP, et al. Lateral decubitus digital subtraction myelography: tips, tricks, and pitfalls. *AJNR Am J Neuroradiol* 2020;41:21–28 CrossRef Medline
- Kranz PG, Gray L, Amrhein T. Decubitus CT myelography for detecting subtle CSF leaks in spontaneous intracranial hypotension. *AJNR Am J Neuroradiol* 2019;40:754–56 CrossRef Medline
- Mamlouk MD, Ochi RP, Jun P, et al. Decubitus CT myelography for CSF-venous fistulas: a procedural approach. *AJNR Am J Neuroradiol* 2021;42:32–36 CrossRef Medline
- Mark I, Madhavan A, Oien M, et al. Temporal characteristics of CSF-venous fistulas on digital subtraction myelography. *AJNR Am J Neuroradiol* 2023;44:492–95 CrossRef Medline
- Headache Classification Committee of the International Headache Society. The International Classification of Headache Disorders, 3rd edition (beta version). *Cephalalgia: An International Journal of Headache* 2013;33:629–808
- Farb RI, Nicholson PJ, Peng PW, et al. Spontaneous intracranial hypotension: a systematic imaging approach for CSF leak localization and management based on MRI and digital subtraction myelography. *AJNR Am J Neuroradiol* 2019;40:745–53 CrossRef
- Amrhein TJ, Gray L, Malinzak MD, et al. Respiratory phase affects the conspicuity of CSF-venous fistulas in spontaneous intracranial hypotension. *AJNR Am J Neuroradiol* 2020;41:1754–56 CrossRef
- Landis JR, Koch GG. The measurement of observer agreement for categorical data. *Biometrics* 1977:159–74 Medline
- Mamlouk MD, Shen PY, Jun P, et al. Spontaneous spinal CSF leaks stratified by age, body mass index, and spinal level. *AJNR Am J Neuroradiol* 2022;43:1068–72 CrossRef Medline
- Kim DK, Carr CM, Benson JC, et al. Diagnostic yield of lateral decubitus digital subtraction myelogram stratified by brain MRI findings. *Neurology* 2021;96:e1312–18 CrossRef Medline
- Callen AL, Pattee J, Thaker AA, et al. Relationship of Bern score, spinal elastance, and opening pressure in patients with spontaneous intracranial hypotension. *Neurology* 2023;100:e2237–46 CrossRef Medline
- Kranz PG, Gray L, Amrhein TJ. Spontaneous intracranial hypotension: 10 myths and misperceptions. *Headache* 2018;58:948–59 CrossRef Medline
- Brinjikji W, Garza I, Whealy M, et al. Clinical and imaging outcomes of cerebrospinal fluid-venous fistula embolization. *J Neurointerv Surg* 2022;14:953–56 CrossRef Medline
- Parizadeh D, Fermo O, Vibhute P, et al. Transvenous embolization of cerebrospinal fluid-venous fistulas: Independent validation and feasibility of upper-extremity approach and using dual-microcatheter and balloon pressure cooker technique. *J Neurointerv Surg* 2023;15:1234–41 CrossRef
- Carlton Jones L, Goadsby PJ. Same-day bilateral decubitus CT myelography for detecting CSF-venous fistulas in spontaneous intracranial hypotension. *AJNR Am J Neuroradiol* 2022;43:645–48 CrossRef Medline
- Nicholson PJ, Guest WC, van Prooijen M, et al. Digital subtraction myelography is associated with less radiation dose than CT-based techniques. *Clin Neuroradiol* 2021;31:627–31 CrossRef Medline

21. Mark IT, Morris PP, Brinjikji W, et al. **Sacral CSF-venous fistulas and potential imaging techniques.** *AJNR Am J Neuroradiol* 2022;43:1824–26 CrossRef Medline
22. Schwartz FR, Malinzak MD, Amrhein TJ. **Photon-counting computed tomography scan of a cerebrospinal fluid venous fistula.** *JAMA Neurol* 2022;79:628–29 CrossRef Medline
23. Mark IT, Amans MR, Shah VN, et al. **Resisted inspiration: A new technique to aid in the detection of CSF-venous fistulas.** *AJNR Am J Neuroradiol* 2022;43:1544–47 CrossRef Medline
24. Kranz PG, Malinzak MD, Gray L, et al. **Resisted inspiration improves visualization of CSF-venous fistulas in spontaneous intracranial hypotension.** *AJNR Am J Neuroradiol* 2023;44:994–98 CrossRef Medline
25. Uppal V, Russell R, Sondekoppam R, et al. **Consensus practice guidelines on postdural puncture headache from a multisociety, international working group: A summary report.** *JAMA Netw Open* 2023;6:e2325387 CrossRef Medline

Prevalence of Incidental Extraplural Findings on MR Imaging of the Lumbar Spine in Adults: A Systematic Review and Meta-analysis

Philip J. Broadhurst, Eileen Gibbons, Amy E. Knowles, and Joe E. Copson



ABSTRACT

BACKGROUND: Low back pain is common worldwide. MR imaging may identify extrapural findings that are not related to the proposed clinical question. The prevalence of extrapural incidental findings and their clinical significance has not been well-established.

PURPOSE: This review aimed to evaluate the prevalence of extrapural findings on MR imaging of the lumbar spine in adults and the prevalence of clinically significant incidental findings.

DATA SOURCES: A systematic search of MEDLINE and EMBASE was performed, including studies published before June 14, 2023.

STUDY SELECTION: Studies presenting a prevalence of extrapural findings in patients 16 years of age or older were included.

DATA ANALYSIS: A random effects meta-analysis was used to generate composite prevalence measures of extrapural findings, patients with extrapural findings, and clinically significant findings.

DATA SYNTHESIS: Sixteen studies were included in this meta-analysis, with a total of 19,593 patients and 6,006 extrapural incidental findings. The overall prevalence of extrapural findings was 19.9% (95% CI, 11.1%–30.7%). Overall, 26.7% of patients had an extrapural finding identified (95% CI, 14.8%–40.6%). The most common subgroup of extrapural findings was genitourinary findings in males (27.1%; 95% CI, 25.6%–28.8%). Data from 8 studies demonstrated the prevalence of clinically significant findings at 5.4% (95% CI, 3.2%–8.1%).

LIMITATIONS: Retrospective populations with small numbers of participants in clinically relevant subgroups may result in heterogeneity and imprecision within composite outcome measures.

CONCLUSIONS: Extrapural findings are common, detected in more than one-quarter of patients. Five percent of findings are clinically significant and may require further action.

ABBREVIATIONS: C-RADS = CT Colonography Reporting and Data System; ESIF = extrapural incidental finding; LBP = low back pain

Low back pain (LBP) is a commonly reported symptom globally and, owing to an ever-growing and aging population, prevalence is rapidly increasing. The lifetime prevalence of LBP internationally is approximately 80%–85% and accounts for 7.4% of global years lived with disability, the highest of any disease.^{1,2} MR imaging of the lumbosacral spine is the recommended technique for investigation of LBP.

Although most causes of LBP will represent neuromusculoskeletal pathologies, other findings may be identified on imaging. Extrapural incidental findings (ESIFs) on MR imaging of the lumbar spine are those detected on a study which does not relate to the clinical question of LBP. ESIFs detected on lumbar spine imaging will commonly be found within the abdomen or pelvis, relating to the gastrointestinal, genitourinary, and gynecologic systems. The detection of these findings will vary depending on the imaging protocols, namely, FOV sampled, the use of saturation banding, and imaging sequences acquired. With the development of modern imaging software and improvement of imaging techniques and quality, diagnostic opportunity has increased.³ Subsequently, it follows that with more MR imaging examinations being performed, more ESIFs will be identified. ESIFs pose a challenge for clinicians. Some of these findings may allow earlier diagnosis and treatment of a significant pathology. However, some findings may not be of clinical significance or remain indeterminate. Insignificant incidental findings may lead

Received June 26, 2023; accepted after revision October 18.

From the Department of Radiology (P.J.B.), Wythenshawe Hospital, Manchester, UK; Department of Medicine (E.G.), Salford Royal Hospital, Manchester, UK; Barts Health London National Health Service Trust (A.E.K.), London, UK; and University of East Anglia (J.E.C.), Norwich, UK.

Please address correspondence to Philip J. Broadhurst, MBChB (Hons), Department of Radiology, Wythenshawe Hospital, Southmoor Rd, Manchester, United Kingdom, M23 9LT; e-mail: pbroadhurst@doctors.org.uk

Indicates article with online supplemental data.

<http://dx.doi.org/10.3174/ajnr.A8065>

to unnecessary follow-up diagnostic tests. Patients may be exposed to unnecessary procedures that may have inherent risks, in addition to the psychological impact of diagnostic uncertainty in the interim period. Insignificant incidental findings may culminate in an unnecessarily increased burden on global health systems.

This systematic review aimed to determine the prevalence of ESIFs in adults who underwent MR imaging of the lumbar spine. The prespecified secondary outcomes of this review were to determine the prevalence of clinically significant ESIFs and the prevalence of ESIFs stratified by age, sex, and body region.

MATERIALS AND METHODS

The protocol for this systematic review and meta-analysis was published on the PROSPERO database (CRD42023430740). The review has been reported in accordance with published Preferred Reporting Items for Systematic Reviews and Meta-Analyses (PRISMA) guidelines.⁴

Search Strategy

Published articles and abstracts were identified following comprehensive searches of the MEDLINE and EMBASE databases using the Ovid platform. The search strategy (Online Supplemental Data) used the following search terms (and related synonyms): “spine,” “MR imaging,” “incidental,” and “extraspinal.” No date restrictions were applied. Search results were updated to include studies published before June 14, 2023.

Studies were considered eligible for inclusion in the systematic review if they satisfied the following criteria: 1) patients 16 years of age or older, 2) patients referred for lumbar spine MR imaging with LBP, and 3) studies reporting a prevalence of ESIFs. Studies were considered ineligible if prevalence data could not be extracted, the patients were derived from disease cohorts, or the article was published in a language other than English. Two reviewers (P.J.B. and J.E.C.) independently screened abstracts and identified full-text articles for review. All reference and citation lists of included full-text articles were interrogated using Google Scholar to identify further potential records. In the event of any discrepancies, these were resolved through consensus agreement between reviewers.

Data Extraction

Three reviewers (P.J.B., E.G., and A.E.K.) independently extracted data from each included study. Study characteristics extracted included the following: 1) study design, 2) study population, 3) setting, 4) geographic location, 5) recruitment period, 6) sample size, 7) imaging protocol, 8) exclusion criteria, 9) interpretation definition, 10) extraspinal finding definition, 11) clinically significant finding definition, 12) number of patients with extraspinal findings, 13) number of extraspinal findings, 14) number of clinically significant findings, and 15) number of patients who underwent imaging follow-up. The number of extraspinal findings was stratified by body systems, when outlined by the original study. Participant characteristics extracted included sex, age, and ethnicity.

Quality Assessment

Two reviewers (P.J.B. and J.E.C.) independently performed a risk of bias assessment of all included studies using a modified risk of

bias assessment tool designed for prevalence studies (Online Supplemental Data).⁵ Studies were scored across 9 domains with a total score of 9. Studies with a low risk of bias had a score of 0–3; moderate risk, 4–6; and high risk, 7–9. Discrepancies between reviewers were resolved through consensus discussion.

Statistical Analysis

The primary outcome was a composite of the prevalence of extraspinal findings identified on MR imaging of the lumbar spine. Secondary outcomes included the percentage of patients with extraspinal findings, extraspinal findings within each body system, and the number of clinically significant findings identified. Statistical analyses were performed using STATA, Version 17.0 (StataCorp). The STATA program `metaprop` was used to perform a random effects meta-analysis of proportions extracted from each study.⁶ The random effects model was used on the basis of the assumption of heterogeneity among studies. The Freeman-Tukey double arcsine transformation was used to stabilize the variances of the reported proportions, with confidence intervals calculated using the Wald method. Univariate and multivariable (sex- or age-adjusted) meta-regression was performed to explore the effects of participant characteristic on the prevalence of extraspinal findings. Heterogeneity across studies was estimated using the I^2 statistic. I^2 values of >75% suggested substantial heterogeneity. Publication bias and small study effects were evaluated through visual inspection of the Doi plot and Egger test.⁷

RESULTS

Following the database search, 782 articles were identified and screened for eligibility. Of these, 26 full-text articles were assessed for inclusion, and 6 studies were selected.^{8–13} Twenty studies were excluded, on the basis of data presented being insufficient to meet the aims of the review ($n = 16$), patients included derived from a known disease cohort ($n = 2$), and the study population not including imaging of the lumbar spine ($n = 1$). One study was excluded because it was not published in English. Following a search of reference and citation lists, 16 full-text articles were screened for eligibility and 10 of these were selected for inclusion.^{14–23} In total, 16 studies were included in this review (Online Supplemental Data).^{8–23}

Study Characteristics

The characteristics of the 16 studies are summarized in the Online Supplemental Data. Eight studies were from Europe,^{10,13,15–18,20,22} 5 were from Asia,^{9,11,14,19,21} 2 were from the United States,^{12,23} and 1 was from Africa.⁷ All were retrospective cross-sectional studies. All 16 studies reported the number of ESIFs.^{8–23} Ten studies reported the number of patients with ESIFs.^{8–13,15,19,22,23} Eight studies reported the number of clinically significant ESIFs.^{10–13,15,18,22,23} Studies that provided data for body system subgroup analysis can be found in the Online Supplemental Data. Four studies used a minimum imaging protocol consisting of axial T2WI, sagittal T1WI, and T2WI sequences.^{10,13,14,21} Ten studies included additional sequences as part of their imaging protocol.^{8,9,11,12,15,17,19,20,22,23} Two studies did not report the imaging protocol used.^{16,18} Six studies operationalized the nomenclature for extracolonic findings from the modified CT Colonography Reporting and Data System (C-RADS) classification to report clinically significant findings.^{10,12,13,15,18,22}

Table 1: Estimated prevalence for extraspinal findings, patients, and clinically significant findings

Groups	Studies	Total	Events	Proportion (95% CI)	I ² (%) ^a
All extraspinal findings					
Overall	16 ⁸⁻²³	19593	6006	19.93 (11.05–30.65)	99.7
Men	3 ^{10,12,15}	4344	1463	33.28 (24.50–42.69)	97.7
Women	3 ^{10,12,15}	5692	2722	55.05 (12.72–93.22)	99.9
Men and women (<40 years)	1 ¹⁹	269	5	1.86 (0.61–4.28)	–
Men and women (≥40 years)	4 ^{11,19,21,23}	1261	150	13.81 (0.80–37.82)	98.9
All patients with extraspinal findings					
Overall	10 ^{8-13,15,19,22,23}	14992	5215	26.65 (14.76–40.57)	99.7
Men	3 ^{8,10,12}	2934	902	24.34 (11.03–40.81)	98.7
Women	3 ^{8,10,12}	3490	1919	51.04 (2.91–97.76)	99.9
Men and women (<40 years)	2 ^{12,19}	540	55	8.29 (6.09–10.79)	–
Men and women (≥40 years)	4 ^{11,12,19,23}	3961	785	16.23 (4.78–32.67)	99.0
All clinically significant findings					
Overall	8 ^{10-13,15,18,22,23}	12778	901	5.35 (3.15–8.08)	97.1
Men	3 ^{10,12,15}	4344	260	5.92 (4.61–7.39)	74.2
Women	3 ^{10,12,15}	5692	533	9.77 (4.67–16.48)	98.3
Men and women (≥40 years)	2 ^{11,23}	672	67	9.96 (7.80–12.36)	–

Note:— Subgroups not stated if no studies reported data for such.

^a I² not estimable for some individual subgroups and marked as en dash.

The C-RADS reporting method numbers both colonic (C) and extra-colonic (E) findings. Findings labeled E3 and E4 are defined as “likely unimportant finding, incompletely characterized— subject to local practice and patient preference, work-up may be indicated” and “potentially important finding,” respectively.²⁴ One study defined clinically significant findings as “findings with MR appearance characteristics of significant diseases, indeterminate lesions requiring further assessment by clinical lab/correlation, or findings requiring further imaging studies or histopathological or surgical confirmation after a discussion with the relevant physician.”¹¹ One study defined clinically significant findings as the detection of an abdominal aortic aneurysm of ≥3 cm.²³

Participant Characteristics

A summary of the participant characteristics is presented in the Online Supplemental Data. The age of participants was between 16 and 95 years. Eleven studies reported the distribution of sex in their total cohorts, with 44% of participants being males. Participant ethnicity was not recorded in any of the studies. Common reasons for participant exclusion in studies included a history of recent trauma, known malignancy, previous spinal surgery, or nondiagnostic images acquired.

Prevalence of All Extraspinal Findings

The total prevalence of all ESIFs identified from MR imaging of the lumbar spine, comprised 19,593 participants from 16 studies, was 19.9% (95% CI, 11.1%–30.7%) (Table 1). The prevalence of ESIFs in females from 3 studies was 55.1% (95% CI, 12.7%–93.2%). The highest proportion of ESIFs was identified in the genitourinary system in males (Table 2). Incidental genitourinary findings were more common in males compared with females 27.1% (95% CI, 25.6%–28.8%) versus 17.5% (95% CI, 16.3%–18.7%). The prevalence of gastrointestinal and urinary tract findings was 2.0% (95% CI, 0.3%–5.2%) and 8.7% (95% CI, 4.7%–13.8%), respectively. Studies that included additional sequences as part of their imaging protocol did not demonstrate a higher reported prevalence of findings (22.0%; 95% CI, 13.2%–32.4%)

compared with studies that performed the minimal imaging sequences (24.5%; 95% CI, 2.9%–57.9%).

Prevalence of All Patients with Extraspinal Findings

The total prevalence of all patients with ESIFs identified on MR imaging of the lumbar spine, comprised of 14,992 participants across 10 studies, was 26.7% (95% CI, 14.8%–40.6%) (Table 1). The prevalence in females from 3 studies was 51.0% (95% CI, 2.9%–97.8%). The prevalence in patients older than 40 years of age from 4 studies was 16.2% (95% CI, 4.8%–32.7%). There was no difference in the prevalence of patients with ESIFs when stratified by sex or age.

Prevalence of Clinically Significant Findings and Imaging Follow-Up

The total prevalence of clinically significant ESIFs, comprised of 12,778 participants from 8 studies, was 5.4% (95% CI, 3.2%–8.1%) (Table 1). There was no difference in the prevalence of clinically significant findings in patients stratified by sex. No studies reported the prevalence of clinically significant findings in patients younger than 40 years of age. Two studies reported the prevalence of clinically significant findings in patients 40 years of age or older (10.0%; 95% CI, 7.8%–12.4%). Only 1 study reported the number of patients who underwent imaging follow-up; 32.6% of patients with extraspinal findings required further imaging.⁸

Meta-Regression Analysis

Following univariate meta-regression, no predefined characteristics (sex, age, or continent) demonstrated a significantly higher proportion of extraspinal findings (Online Supplemental Data). In univariate analysis, the risk difference for males was –18.4% (95% CI, –61.8%–25.0%). The risk difference for patients 40 years of age and older was 15.5% (95% CI, –32.6%–63.4%). These findings persisted in the multivariable analysis performed, with no predefined characteristic demonstrating a statistically significant difference in the percentage risk difference.

Table 2: Estimated prevalence of extra-spinal findings by body region

Body Regions	Studies	Total	Events	Proportion (95% CI)	I ² (%) ^a
Gastrointestinal					
Overall	12 ^{8,10-18,20,21}	16592	929	2.04 (0.29–5.22)	99.2
Men	2 ^{10,15}	2993	254	6.90 (6.02–7.84)	–
Women	2 ^{10,15}	4019	460	8.15 (7.33–9.02)	–
Men and women (≥40 years)	2 ^{11,21}	330	8	2.31 (0.82–4.38)	–
Genitourinary					
Overall	14 ^{8,10-22}	17689	2631	8.74 (4.73–13.81)	99.1
Men	2 ^{10,15}	2993	814	27.14 (25.56–28.75)	–
Women	2 ^{10,15}	4019	725	17.49 (16.33–18.68)	–
Men and women (<40 years)	1 ¹⁹	269	0	0.19 (0.00–0.56)	–
Men and women (≥40 years)	3 ^{11,19,21}	866	82	8.93 (0.00–35.57)	98.7
Gynecologic					
Women	3 ^{8,10,15}	4289	1004	24.03 (9.44–42.70)	99.3
Vascular					
Overall	13 ^{8,10-18,20,22,23}	16941	296	1.41 (0.73–2.30)	94.0
Men	2 ^{10,15}	2993	55	1.79 (1.34–2.30)	–
Women	2 ^{10,15}	4019	60	1.42 (1.08–1.82)	–
Men and women (≥40 years)	2 ^{11,23}	672	53	7.76 (5.84–9.92)	–
Musculoskeletal					
Overall	8 ^{8,12,14-17,20,21}	11537	54	0.52 (0.13–1.14)	91.1
Men	1 ¹⁵	1540	5	0.32 (0.11–0.76)	–
Women	1 ¹⁵	2472	6	0.24 (0.09–0.53)	–
Metastases					
Overall	7 ^{8,14-17,20,21}	8513	20	0.28 (0.01–0.77)	86.9
Men	1 ¹⁵	1540	0	0.03 (0.00–0.53)	–
Women	1 ¹⁵	2472	1	0.04 (0.00–0.23)	–
Miscellaneous					
Overall	7 ^{12,14-17,20,21}	11137	6	0.05 (0.00–0.13)	21.6
Men	1 ¹⁵	1540	0	0.03 (0.00–0.53)	–
Women	1 ¹⁵	2472	0	0.02 (0.00–0.52)	–

Note:— Subgroups not stated if no studies reported data for such.

^a I² not estimable for some individual subgroups and marked as en dash.

Study Quality and Small Study Effects

Following an assessment of risk bias using an adapted tool for prevalence studies, total scores ranged from 1 to 7 (Online Supplemental Data). All studies scored in domain 2 due to single-center study design. All studies scored zero in domain 9, given that sufficient data to extract prevalence proportions formed part of the inclusion criteria for this systematic review. Eight studies were assessed as a low risk of bias.^{9-11,13,15,17,18,20} Seven studies were evaluated as having a moderate risk of bias,^{8,12,14,16,19,21,23} with only 1 study evaluated as having a high risk of bias.²² Post hoc analysis showed that the prevalence of ESIFs in the study evaluated as having a high risk of bias was 36.3% (95% CI, 30.8%–42.1%) versus 27.6% (95% CI, 12.9%–45.2%) in studies evaluated as having a low risk of bias. Therefore, no studies were excluded from analysis on the basis of risk of bias assessment. Visual inspection of the Doi plot demonstrated lateralizing asymmetry with a LFK index value of -1.71 , suggesting small study effects (Egger test, $P = .059$) (Online Supplemental Data).

DISCUSSION

In summary, this systematic review consisted of 16 studies including 19,593 participants with 6,006 extraspinal findings identified on MR imaging of the lumbar spine. In 10 studies, including 14,992 patients, 5,215 patients had extraspinal findings. The overall prevalence of an extraspinal finding was 19.9%, and the prevalence of a patient having an extraspinal finding was 26.7%. Clinically significant findings were identified in 5.4% of participants. The prevalence of ESIFs was most pronounced in patients 40 years of age or older.

To the best of our knowledge, this is the first systematic review and meta-analysis to assess the prevalence of ESIFs on MR imaging of the lumbar spine in adults. Incidental findings on MR imaging of the lumbar spine in asymptomatic pediatric patients have previously been reported and subsequently included in an umbrella review of incidental findings across multiple imaging modalities.^{25,26} Our reported composite prevalence is similar to the prevalence reported in the pediatric population and the prevalence across other imaging in the umbrella review. Studies that were excluded from our review because they included some patients younger than 16 years of age also reported similar prevalence figures.^{27,28} When one considers multitechnique evidence, the prevalence of extraspinal findings on outpatient lumbar spine CT in a cohort of 400 adults was 40.5%, with 14.8% of patients having indeterminate/clinically significant findings, which required further clinical assessment or follow-up imaging.²⁹ The higher percentage of ESIFs on CT may be explained by technical factors relating to image acquisition (for example, contiguous section interval and section thickness) and the differential sensitivity of detecting findings with fat or air densities through this technique.

The findings of this review have both clinical and research implications. Our results demonstrate that extraspinal findings are common, with more than one-quarter of examinations having identified ESIFs. Our analysis showed that there was a pronounced difference in the percentage of genitourinary findings in males compared with females. The proportion of genitourinary incidental findings in males was calculated from 2 studies.^{10,15}

These studies included renal cysts, some of which were classified as clinically important. Our analysis is similar to previously reported studies evaluating the prevalence of renal cysts, which demonstrated more prevalent cystic disease in males.^{30,31} The clinical implications pertain to the responsibility of the radiologists to identify these ESIFs and, if appropriate, notify referring clinicians of clinically significant findings. Radiologists should consider revising routine search patterns to place a greater emphasis on the genitourinary tract in males. This change could be made by including such review areas in standard reporting templates. Five percent of findings were deemed clinically significant. This translates to a sizeable proportion of examinations that may include actionable findings that require further work-up. Both radiologists and referring clinicians should be equipped to appropriately manage detected extraspinal findings and manage the uncertainty of suspected significant findings. This recommendation is important to minimize overlooking significant diagnoses but also to avoid unnecessary further imaging or procedures, which may bring their own physical risk and elevated patient anxieties.

This review has also highlighted the relative paucity of evidence when stratifying for participant characteristics. Only 1 study included in this review reported the number of patients who underwent follow-up on the basis of the extraspinal findings detected. There is a need for further observational studies designed to capture the prevalence and impact of extraspinal findings in clinically relevant subgroups. Another future research question is the potential impact of technical imaging factors on the prevalence of ESIFs. Technical differences, namely, FOV, section thickness, and the use of saturation bands are likely to influence the detection of ESIFs. Inclusion of saturation banding will limit assessment of the prevertebral structures. This phenomenon is explained by the reduced detection of lymphovascular disease on MR imaging of the lumbar spine compared with CT.^{29,32} Anecdotally, localizer images could identify ESIFs, and their utility could be quantified. The included studies did have variance in their predetermined imaging protocols. Studies that included additional imaging sequences did not report a higher proportion of ESIFs; however, this observation seems counterintuitive.

Strengths and Limitations

This review has multiple strengths. First, the review protocol was preregistered and the review used a robust and comprehensive search strategy to exhaustively ensure that all relevant studies from the published literature were included. Second, we intentionally included studies without a prespecified definition of extraspinal findings. We thought that during data extraction, extraspinal findings could be pragmatically identified among all documented findings. This idea has allowed us to generate stratified analyses for clinically relevant patient characteristics, body regions, and clinically significant findings. Third, we excluded studies reporting data from pre-existing disease cohorts because this would introduce bias.

One limitation of this systematic review is that only 2 databases were included. However, this has been mitigated by using a third database when reviewing the reference and citation searches. Other limitations of this review arise from the included studies. First, most studies are from single centers

and demonstrate marked heterogeneity with small study effects, limiting the generalizability at a population level. However, there was global geographic coverage from the studies, and this will likely mitigate the former. Second, the estimated proportions, particularly in subgroup analysis and univariate analysis, are limited because few studies reported extraspinal findings stratified by clinically relevant subgroups. This may result in some imprecision in the composite prevalence calculations. Third, there was heterogeneity in the interpretation and definition of imaging findings across studies, with multiple subspecialty radiologists reporting studies. This will introduce subjective bias in the reporting rate across studies. Last, there were differences in the reporting of an extraspinal finding and a clinically significant finding, with some authors having lower or higher thresholds. For example, in 1 study, pelvic free fluid was documented as a positive finding; this influenced the prevalence of findings in females.¹⁰ Another study only reported the presence of an abdominal aortic aneurysm of ≥ 3 cm as clinically significant, which will introduce bias into the vascular subgroup.²³ However, there was a relative consensus among the remaining studies on how to document a finding as clinically significant, improving the external validity, with most studies adopting the modified C-RADS classification.

CONCLUSIONS

ESIFs detected on MR imaging of the lumbar spine are common and were reported in approximately one-quarter of studies. Clinically significant findings were reported in 5%. Incidental genitourinary findings were more prevalent in males compared with females. Both referring clinicians and reporting radiologists should be aware of the implications of incidental findings and how to manage them in their routine clinical practice. There is a relative paucity of evidence in some patient subgroups, and future population-based studies should address this.

ACKNOWLEDGMENTS

We thank Dr Leo Alexandre, for his thorough teaching in systematic review methods, without whom this review would not be possible.

Disclosure forms provided by the authors are available with the full text and PDF of this article at www.ajnr.org.

REFERENCES

1. World Health Organization. **Low Back Pain**. <https://www.who.int/news-room/fact-sheets/detail/low-back-pain>. Accessed June 4, 2023
2. Wu A, March L, Zheng X, et al. **Global low back pain prevalence and years lived with disability from 1990 to 2017: estimates from the Global Burden of Disease Study 2017**. *Ann Transl Med* 2020;8:299 CrossRef Medline
3. Wagner SC, Morrison WB, Carrino JA, et al. **Picture archiving and communication system: effect on reporting of incidental findings**. *Radiology* 2002;225:500–05 CrossRef Medline
4. Page MJ, McKenzie JE, Bossuyt PM, et al. **The PRISMA 2020 statement: an updated guideline for reporting systematic reviews**. *BMJ* 2021;372:n71 CrossRef Medline

5. Hoy D, Brooks P, Woolf A, et al. **Assessing risk of bias in prevalence studies: modification of an existing tool and demonstration of inter-rater agreement.** *J Clin Epidemiol* 2012;65:934–39 CrossRef Medline
6. Nyaga VN, Arbyn M, Aerts M. **Metaprop: a Stata command to perform meta-analysis of binomial data.** *Arch Public Health* 2014;72:39–203 CrossRef Medline
7. Furuya-Kanamori L, Barendregt JJ, Doi SA. **A new improved graphical and quantitative method for detecting bias in meta-analysis.** *Int J Evid Based Healthc* 2018;16:195–203 CrossRef Medline
8. Ibrahim H, Elsadawy ME. **Incidental findings in lumbar spine MRI: their prevalence and potential impact on patient management.** *Egypt J Radiol Nucl Med* 2019;50:59 CrossRef
9. Khasawneh RA, Mohaidat Z, Khasawneh FA, et al. **Extraspinal findings prevalence and clinical significance in 4250 lumbar spine MRI exams.** *Sci Rep* 2021;11:1190 CrossRef Medline
10. Quattrocchi CC, Giona A, Di Martino AC, et al. **Extra-spinal incidental findings at lumbar spine MRI in the general population: a large cohort study.** *Insights Imaging* 2013;4:301–08 CrossRef Medline
11. Rashid SA. **Prevalence and clinical potential of extraspinal incidental findings in lumbosacral spine MRI of patients with suspected disc diseases.** *Medical Journal Indonesia* 2021;30:256–63 CrossRef
12. Semaan HB, Bieszczyk JE, Obri T, et al. **Incidental extraspinal findings at lumbar spine magnetic resonance imaging: a retrospective study.** *Spine (Phila Pa 1976)* 2015;40:1436–43 CrossRef Medline
13. Tuncel SA, Çağlı B, Tektaş A, et al. **Extraspinal incidental findings on routine MRI of lumbar spine: prevalence and reporting rates in 1278 patients.** *Korean J Radiol* 2015;16:866–73 CrossRef Medline
14. Abdullah AR, Odish HY, Mohamedamin HA. **Incidental findings on magnetic resonance imaging of lumbosacral spine in patients with back pain and/or radiculopathy.** *Zanco Journal of Medical Sciences* 2018;22:300–06 CrossRef
15. Dağistan E, Coşgun Z. **Extraspinal findings on routine lumbar spinal MR imaging: prevalence and etiologies in 4012 patients.** *Experimental Biomedical Research* 2020;3:110–16 CrossRef
16. Eroglu A, Yilmaz I. **Coincidental lesions that have been seen in patients with lumbar discopathy at spinal MR examination.** *Medical Science and Discovery* 2018;5:137–40 CrossRef
17. Kahraman AN, Vural A. **Added value of coronal-T1W sequence to the lumbar MR imaging protocol for low back pain** [Article in English, Spanish]. *Biomedica* 2022;42:33–40 CrossRef Medline
18. Kaya S, Hatirli H, Sahin M, et al. **Incidental findings detected on magnetic resonance imaging scans of the cervical, thoracic and lumbar spine of patients prediagnosed with discopathy.** *Marmara Medical Journal* 2023;36:210–14 CrossRef
19. Qasim H, Al-Bayati H, Mahmood NA. **Incidental finding during MRI evaluation of lumbosacral disc prolapse in adults in Al-Hilla Teaching Hospital.** *Medical Journal of Babylon* 2017;14:537–49
20. Romeo V, Cavaliere C, Sorrentino C, et al. **Clinical impact of coronal-STIR sequence in a routine lumbar spine MR imaging protocol to investigate low back pain.** *Medicine (Baltimore)* 2018;97:e10789 CrossRef Medline
21. Sobhan M, Samiee M, Asgari Y, et al. **Incidental findings of the lumbar spine at MRI in patients diagnosed with discopathy.** *International Journal of Medical Imaging* 2016;4:44–47 CrossRef
22. Zeh OF, Goujou EG, Awana AP, et al. **Extraspinal incidental findings at lumbar spine magnetic resonance imaging in two hospitals: prevalence and clinical importance.** *Open J Radiol* 2017;07:241–48 CrossRef
23. Zucker EJ, Prabhakar AM. **Lumbar spine MRI: missed opportunities for abdominal aortic aneurysm detection.** *Curr Probl Diagn Radiol* 2020;49:254–59 CrossRef Medline
24. Zalis ME, Barish MA, Choi JR, et al; Working Group on Virtual Colonoscopy. **CT colonography reporting and data system: a consensus proposal.** *Radiology* 2005;236:3–9 CrossRef Medline
25. Ramadorai U, Hire J, DeVine JG, et al. **Incidental findings on magnetic resonance imaging of the spine in the asymptomatic pediatric population: a systematic review.** *Evid Based Spine Care J* 2014;5:95–100 CrossRef Medline
26. O'Sullivan JW, Muntinga T, Grigg S, et al. **Prevalence and outcomes of incidental imaging findings: umbrella review.** *BMJ* 2018;361:k2387 CrossRef Medline
27. Zidan MM, Hassan IA, Elnour AM, et al. **Incidental extraspinal findings in the lumbar spine during magnetic resonance imaging of intervertebral discs.** *Heliyon* 2018;4:e00803 CrossRef Medline
28. Dilli A, Ayaz UY, Turanli S, et al. **Incidental extraspinal findings on magnetic resonance imaging of intervertebral discs.** *Arch Med Sci* 2014;10:757–63 CrossRef Medline
29. Lee SY, Landis MS, Ross IG, et al. **Extraspinal findings at lumbar spine CT examinations: prevalence and clinical importance.** *Radiology* 2012;263:502–09 CrossRef Medline
30. Chang CC, Kuo JY, Chan WL, et al. **Prevalence and clinical characteristics of simple renal cyst.** *J Chin Med Assoc* 2007;70:486–91 CrossRef Medline
31. Mensel B, Kühn JP, Kracht F, et al. **Prevalence of renal cysts and association with risk factors in a general population: an MRI-based study.** *Abdom Radiol (NY)* 2018;43:3068–74 CrossRef Medline
32. Gouliamos AD, Tsiganis T, Dimakakos P, et al. **Screening for abdominal aortic aneurysms during routine lumbar CT scan: modification of the standard technique.** *Clin Imaging* 2004;28:353–55 CrossRef Medline

Frequency of Coexistent Spinal Segment Variants: Retrospective Analysis in Asymptomatic Young Adults

Edward S. Yoon, Farhad Pishgar, Avneesh Chhabra, Filippo Del Grande, and John A. Carrino



ABSTRACT

BACKGROUND AND PURPOSE: Spinal segment variants are highly prevalent and can potentially lead to incorrect spinal enumeration and, consequently, interventions or surgeries at the wrong vertebral levels. Our aim was to assess the prevalence of spinal segment variants and to study the potential association among these variants in a population without histories of spine symptoms.

MATERIALS AND METHODS: Consecutive computed tomography exams of 450 young adults originally evaluated for non-spinal conditions and without a history of spinal diseases from a single institution. In addition to using descriptive statistics for reporting frequencies of spinal segment variants, the association between these variants was studied by calculating odds ratios and their 95% confidence interval. Consecutive CT exams were evaluated to determine the total number of presacral segments, presence of cervical rib, thoracolumbar transitional vertebra, iliolumbar ligament, and lumbosacral transitional vertebra.

RESULTS: The spinal segment distribution variants (an atypical number of presacral segments or an atypical distribution of thoracolumbar vertebrae), cervical rib, thoracolumbar transitional vertebra, and lumbosacral transitional vertebra were reported in 23.8%, 4.2%, 15.3%, and 26.4% of cases in our study population. The presence of a cervical rib or a thoracolumbar transitional vertebra was associated with concurrent lumbosacral transitional vertebra (OR = 3.28; 95% CI, 1.29–8.47 and 1.87; 95% CI, 1.08–3.20, respectively). The inability to visualize the iliolumbar ligament was also associated with the presence of cervical ribs (OR = 3.06; 95% CI, 1.18–7.80).

CONCLUSIONS: In a population of asymptomatic young adults, spinal segment variants are both highly prevalent with a high rate of coexistence. When a spinal segment variant (eg, transitional vertebra) is diagnosed, additional imaging might be considered for accurate spine enumeration before interventions or operations.

ABBREVIATIONS: ILL = iliolumbar ligament; LSTV = lumbosacral transitional vertebra; TLTV = thoracolumbar transitional vertebra

Spinal segment variants can potentially lead to incorrect identification of vertebral levels and, subsequently, cause wrong-level interventions or operations.^{1,2} For instance, selective nerve root blocks require administering epidural spinal injections at specific vertebral levels, which can be confounded by spinal segment distribution variants or the presence of a transitional vertebra.

The most prevalent number of presacral segments in the vertebrae is the 24 presacral segments with 7 (non-rib-bearing) cervical,

12 (rib-bearing) thoracic, and 5 (non-rib-bearing) lumbar vertebrae. However, other spinal segment distribution variants with an atypical number of presacral segments (23 or 25 segments) or with atypical distribution of the thoracolumbar vertebrae (11 or 13 thoracic and 4 or 6 lumbar vertebrae) are also common. Other frequently encountered spinal segment variants with relevant clinical implications include cervical ribs and transitional vertebrae, among others.³

The cervical rib is diagnosed when an additional rib originates from the last cervical segment (ie, the seventh cervical segment or C7).³ The cervical rib may vary in length and may have a fibrous connection to the first rib; however, it can potentially tighten the space between the first rib and the anterior scalene muscle and impinge the nerves and arteries that pass through this space to the upper extremity.⁴ Therefore, its presence may cause pain, paresthesia, and muscle weakness in the upper extremity on the affected side.

Received August 22, 2023; accepted after revision October 19.

From the Hospital for Special Surgery (E.S.Y., J.A.C.), New York, New York; University of Washington (F.P.), Seattle, Washington; University of Texas Southwestern (A.C.), Dallas, Texas; and Institute of Imaging of Southern of Switzerland (F.D.G.), Bellinzona, Switzerland.

Please address correspondence to Edward S. Yoon, MD, Hospital for Special Surgery, Radiology, 535 East 70th St, New York, NY 10021; e-mail: yoone@hss.edu
<http://dx.doi.org/10.3174/ajnr.A8071>

Table 1: The Castellvi classification for LSTV

Classification	Laterality	Description
I	Unilateral (a) Bilateral (b)	Dysplastic transverse process with a ≥ 19 -mm width on the craniocaudal dimension
II		Lumbarization or sacralization with an enlarged transverse process that has a diarthrodial joint with the sacrum
III		Lumbarization or sacralization with complete osseous fusion of the transverse process to the sacrum
IV	–	Unilateral IIa transition with a IIIa transition on the contralateral side

Note:—The en dash indicates duplicate entries.

Transitional vertebrae are diagnosed when the segment at the junction of the thoracic, lumbar, or sacral vertebrae has partial characteristics from both upper and lower vertebrae.³ The thoracolumbar transitional vertebra (TLTV), for instance, is diagnosed when the last thoracic (rib-bearing) segment shows features of a non-rib-bearing segment and has hypoplastic ribs.⁵ Moreover, the lumbosacral transitional vertebra (LSTV) is diagnosed when either the last lumbar segment shows a transition toward the sacral vertebrae (ie, sacralization) or the first sacral segment shows features of the lumbar vertebrae (ie, lumbarization).⁶ The symptoms associated with TLTV or LSTV are not well-documented; however, the presence of these transitional vertebrae is associated with other spinal segment variants.⁷ Thus, it is suggested that when a transitional vertebra is diagnosed, additional imaging should be considered to confirm spine enumeration before interventions or operations.⁸

The prevalence of the spinal segment variants in patients with upper-extremity involvement (for a cervical rib)⁹ or back pain (for spinal segment distribution variants and transitional vertebra)¹⁰ has been reported before. This study aimed to assess the prevalence of these spinal segment variants and investigate the potential association among these variants in a population without histories of neck, dorsum, or low-back pain.

MATERIALS AND METHODS

This retrospective observational study was reviewed and approved by the institutional review board of The Johns Hopkins University to be compliant with the Health Insurance Portability and Accountability Act (this study was exempted from the informed-consent requirements).

Study Population

The integrated PACS of The Johns Hopkins Hospital was searched for records of young adults or older patients (17 years of age or older) who had undergone cross-sectional CT examinations of the whole spine in an inpatient or outpatient setting for indications such as trauma or oncologic surveys, during 4 years.

Cases with incomplete scans, with significant artifacts, and with inadequate visualization of the spine were excluded, and a total of 450 consecutive patients (sex: 62.0% [$n = 279$] women and 28.0% [$n = 171$] men; mean age, 31.2 [SD, 8.4] years; range, 17–45 years) evaluated for nonspinal conditions without a history of spinal diseases were included in this study.

Image Acquisition

CT examinations were obtained using the 16-section multidetector row CT scanner (Somatom Sensation 16; Siemens). Examinations were performed following the institutional protocol (voltage of 120 kV[peak] and the effective current setting based on the body mass index and indication). Examinations were reconstructed at 3.0 mm.

Image Interpretation

Several characteristics and features of vertebrae were extracted from each CT examination. The total number of presacral segments was documented by counting the vertebrae downward from C2. The cervical vertebrae included the reliable number of 7 segments,^{8,11} and the following rib-bearing segments downward were counted as thoracic vertebrae. The non-rib-bearing segments following the thoracic vertebrae were counted as the lumbar vertebrae.

The cervical ribs on CT examinations were identified using the following criteria: 1) must be attached to the C7 vertebral process, 2) must have no connections to the manubrium of the sternum, though it may form synostosis with the first rib (which differentiates it from a rudimentary first rib), and 3) must be separate from, though it may articulate with, the transverse process of C7 (if fused with the segment, it was classified as an elongated cervical process).^{3,12} The elongated C7 transverse processes were classified as any C7 transverse process longer than the T1 (first thoracic vertebra) transverse process.

The TLTV was identified as the segment with hypoplastic ribs (unilateral or bilateral, ribs with lengths of < 3.8 cm) or accessory ossification centers⁸ on the lowest rib-bearing segment. The iliolumbar ligament (ILL) was identified and visualized as the structure extending from the transverse process of a vertebra to the posteromedial iliac crest on the axial view of CT examinations. The LSTV was identified and classified using the Castellvi classification.⁶ Table 1 shows the criteria used for LSTV classification.

The image interpretation was performed by 2 readers (G.K.T., radiology research fellow, and J.A.C., senior musculoskeletal radiologist) in consensus.

Statistical Analysis

Descriptive statistics were used for assessing frequencies and distributions of spinal segment variants. The frequencies of these variants in women and men were compared using the χ^2 test (reporting P value).

The potential correlation between spinal segment variants was assessed using correlation studies reporting the Spearman

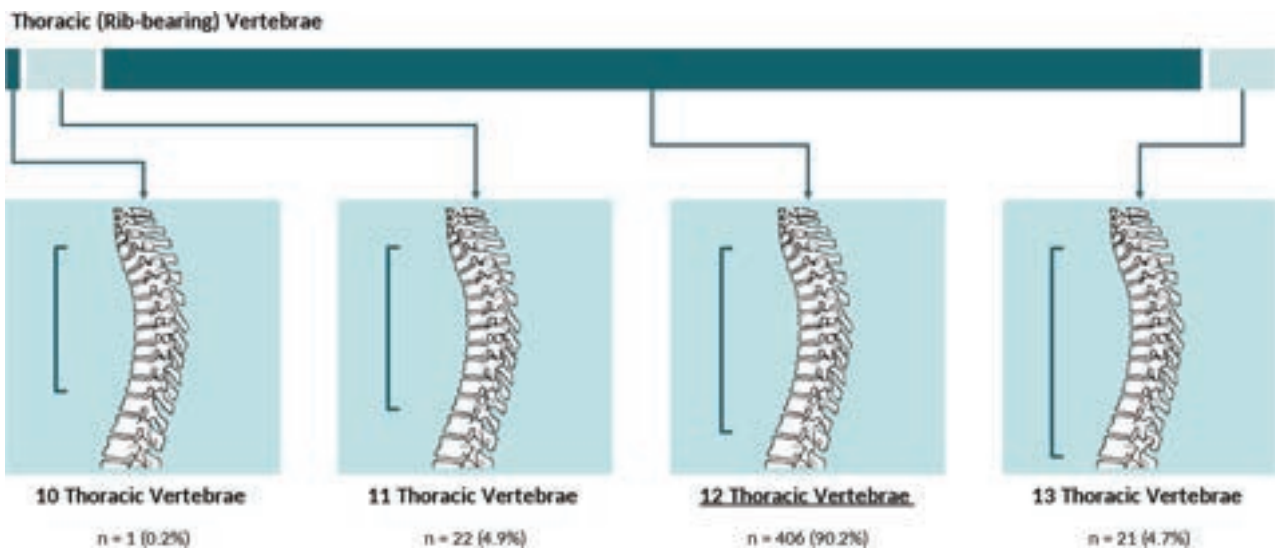


FIG 1. Allocation of spinal segment distribution variants in thoracic (rib-bearing) vertebrae.

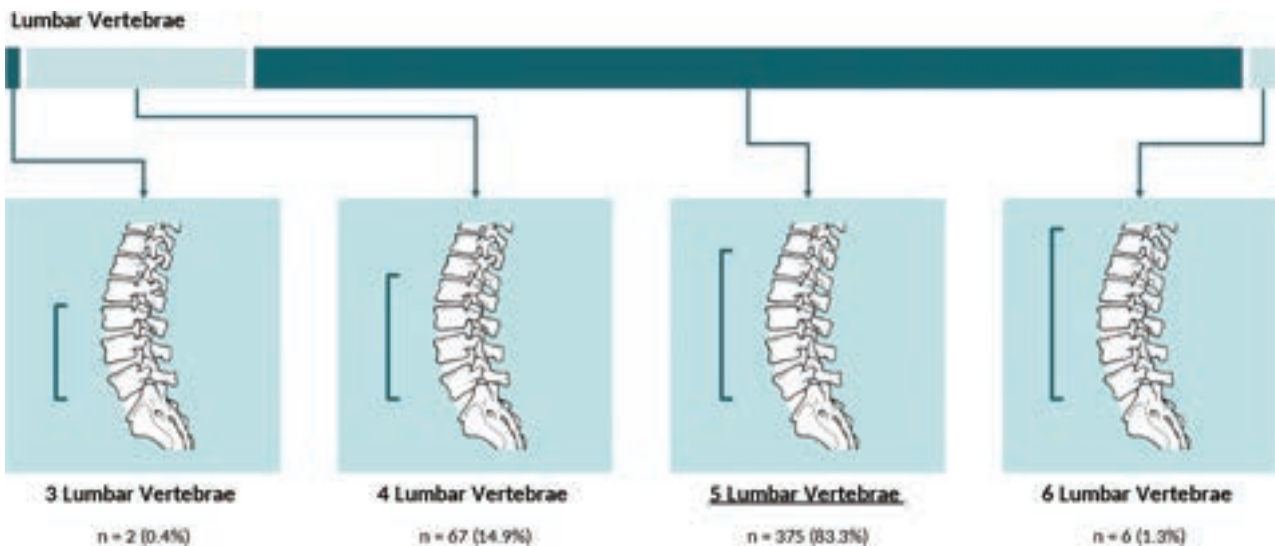


FIG 2. Allocation of spinal segment distribution variants in lumbar vertebrae.

ρ with 95% CIs (calculated by using the bootstrapping method with 1000 replicates) and P values. Results of the correlation studies are presented using a correlation matrix. Moreover, the potential association between these variants was studied using logistic regression models reporting ORs with 95% CIs and P values.

In this study, $P < .05$ was statistically significant. All statistical analyses were performed in the R platform (<http://www.r-project.org/>).

RESULTS

Among the 450 cases included in our study, frequencies of spinal segment distribution variants were as follows: 0.2% ($n=1$) of cases had twenty-two, 1.8% ($n=8$) had twenty-three, 93.3% ($n=420$) had 24, and 4.7% ($n=21$) had 25 presacral segments. Figures 1 and 2 show the spinal segment

distribution variants in the thoracic (Fig 1) and lumbar vertebrae (Fig 2) in our study.

Overall, 23.8% ($n=107$) of cases in our study had a spinal segment distribution variant (an atypical number of presacral segments or an atypical distribution of thoracolumbar vertebrae). The frequency of spinal segment distribution variants in women (25.4% [$n=71$]) was similar to that in men (21.1% [$n=36$], P value = .343, Table 2).

Cervical Rib

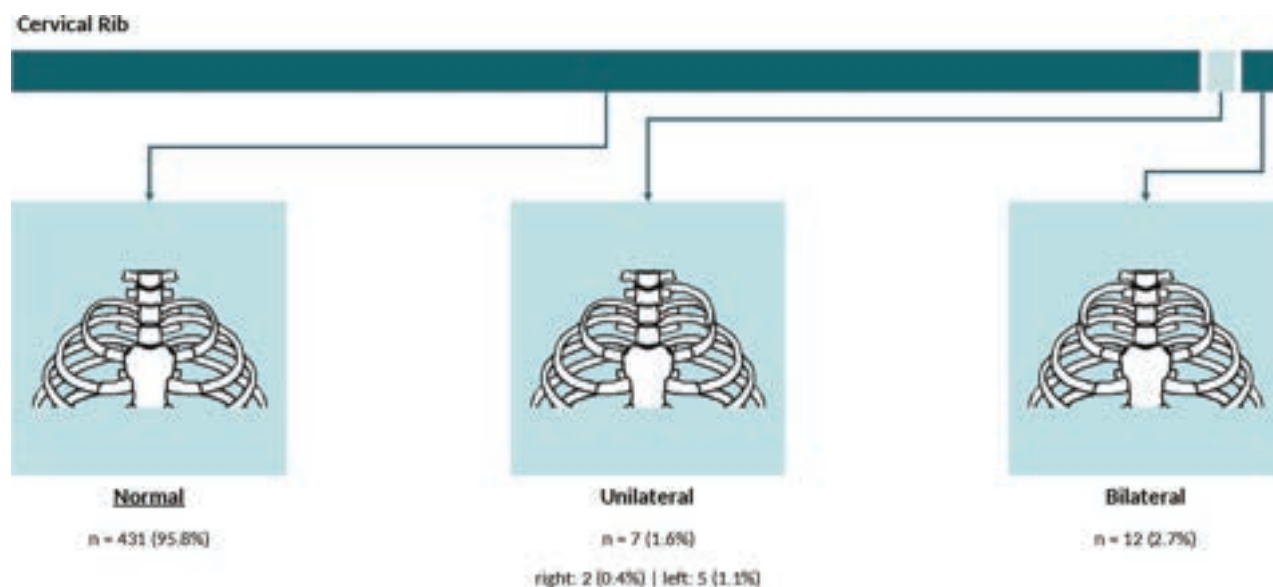
Of the 450 included cases, 4.2% ($n=19$) had unilateral (1.6% [$n=7$]) or bilateral (2.7% [$n=12$]) cervical ribs (Fig 3). The frequency of cervical ribs in women (4.7% [$n=13$]) was slightly higher compared with men (3.5% [$n=6$]) in our study, though the difference was not statistically significant (P value = .728, Table 2).

Table 2: Comparative distribution of spinal segment variants

Spinal Segment Variant	Overall (n = 450)	Women (n = 279)	Men (n = 171)	P Value ^a
Spinal segment distribution variant ^b	107 (23.8%)	71 (25.4%)	36 (21.1%)	.343
Cervical rib	19 (4.2%)	13 (4.7%)	6 (3.5%)	.728
TLTV	69 (15.3%)	36 (12.9%)	33 (19.3%)	.091
LSTV	119 (26.4%)	60 (21.5%)	59 (34.5%)	.003

^aResult of the χ^2 test for the difference between frequencies of spinal segment variants by sex.

^bAn atypical number of presacral segments or an atypical distribution of thoracolumbar vertebrae.

**FIG 3.** Frequency and distribution of the cervical rib.**TLTV**

A TLTV was present in 15.3% ($n = 69$) of cases in our study (unilateral: 7.3% [$n = 33$], bilateral: 8.0% [$n = 36$], Fig 4). Frequencies of the TLTV in women (12.9% [$n = 36$]) and men (19.3% [$n = 33$]) were similar (P value = .091, Table 2).

LSTV

ILL was identified in 95.8% ($n = 431$) of cases (partially visualized: 12.4% [$n = 56$], definitely visualized: 83.3% [$n = 375$]). Of the 450 included cases, 26.4% ($n = 119$) had LSTV, of which 6.0% ($n = 27$) of cases had LSTV type I, 13.3% ($n = 60$) of cases had LSTV type II, 4.9% ($n = 22$) of cases had LSTV type III, and 2.2% ($n = 10$) of cases had LSTV type IV. Figure 5 shows the frequency and distribution of LSTVs in our study. LSTV was less frequent in women (21.5% [$n = 60$]) compared with men (34.5% [$n = 59$], P value = .003, Table 2).

Correlation and Association between Spinal Segment Variants

In our study, spinal segment distribution variants (an atypical number of presacral segments or an atypical distribution of thoracolumbar vertebrae) were correlated and associated with the presence of a concurrent TLTV (OR = 66.13; 95% CI, 30.34–166.85; P value = .001), an inability to visualize the ILL (OR = 3.06; 95% CI, 1.18–7.80; P value = .018), and a concurrent LSTV (OR = 5.47; 95% CI, 3.43–8.80; P value < .001, Fig 6 and Table 3).

The presence of a cervical rib was correlated and associated with the inability to visualize the ILL (OR = 4.86; 95% CI, 1.06–

716.54; P value = .020) and a concurrent LSTV (OR = 3.28; 95% CI, 1.29–8.47; P value = .012). Moreover, the presence of a TLTV was correlated and associated with a concurrent LSTV (OR = 1.87; 95% CI, 1.08–3.20; P value = .023, Fig 6 and Table 3).

An inability to visualize the ILL was not associated with the presence of TLTV or LSTV (Fig 6 and Table 3).

An example of both a thoracolumbar and lumbosacral transitional anatomy is given in Fig 7.

DISCUSSION

Our study confirms that the prevalence of spinal segment variants, even in asymptomatic young adults, is relatively high. The spinal segment distribution variants (an atypical number of presacral segments or an atypical distribution of thoracolumbar vertebrae), the cervical rib, TLTV, and LSTV, affected 23.8%, 4.2%, 15.3%, and 26.4% of our study population. We also showed that the presence of a TLTV and LSTV is associated with higher odds of concurrent spinal segment distribution variants. Although not associated with the presence of TLTV and LSTV, the inability to visualize the ILL was also associated with the spinal segment distribution variants (atypical number of presacral segments or atypical distribution of thoracolumbar vertebrae) and the presence of a cervical rib.

The most prevalent number of presacral segments is 24 with 12 (rib-bearing) thoracic and 5 lumbar vertebrae. However, other spinal segment distribution variants are also common. The prevalence of atypical numbers of presacral segments was

Thoracolumbar Transitional Vertebra (TLTV)

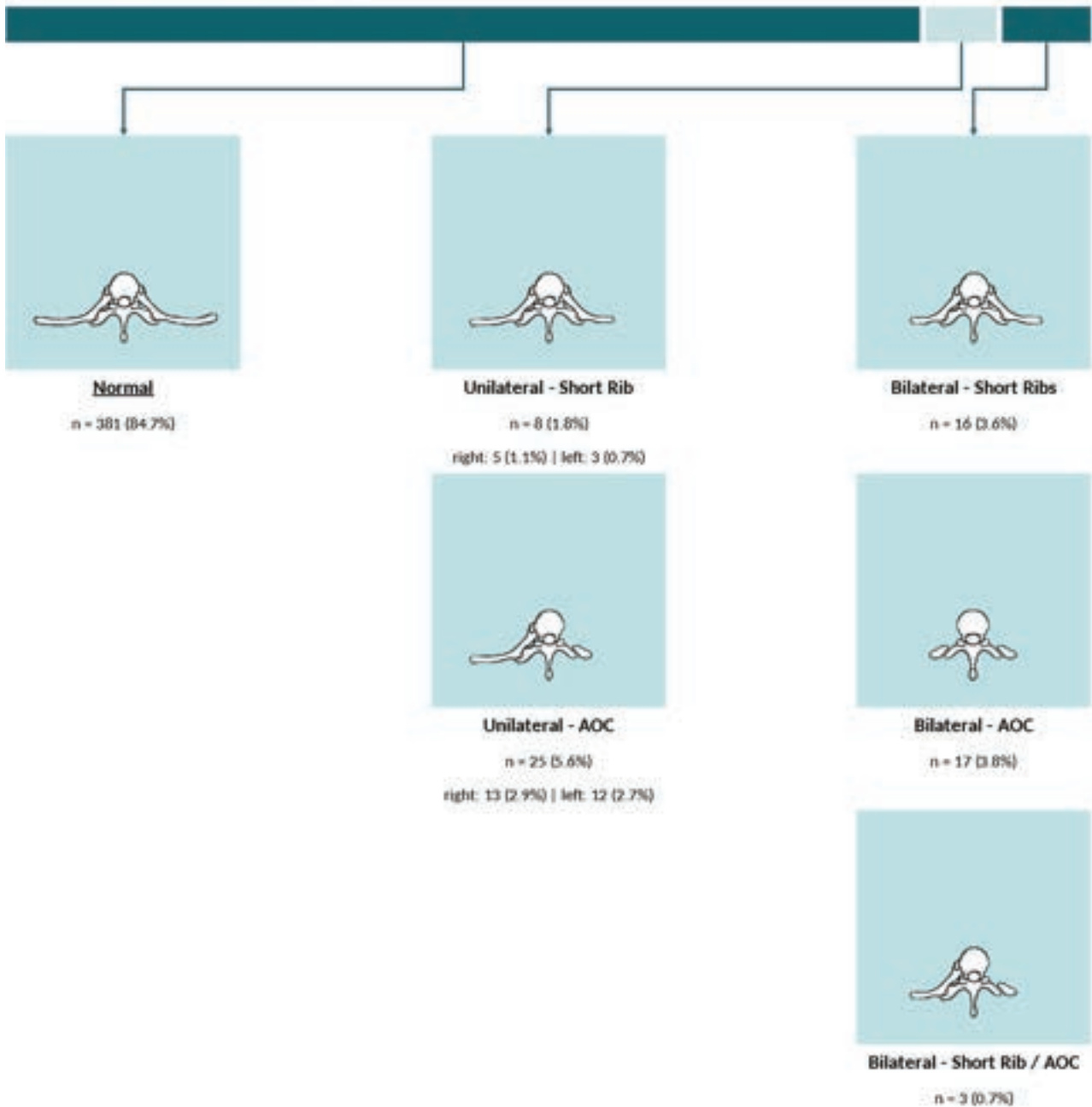


FIG 4. Frequency and distribution of the TLTV. AOC indicates accessory ossification center.

estimated to be as high as 8.2% (adults in an American population),⁸ 7.9% (asymptomatic adults in a Chinese population),¹³ or 10.0% (adolescents with idiopathic scoliosis in an American population).¹⁴ In our study, atypical numbers of presacral segments were seen in 6.7% of cases, while 23.8% of cases were diagnosed with spinal segment distribution variants. Moreover, the pooled prevalence of a cervical rib is estimated to range from 1.1% (in adults without thoracic outlet syndrome) to 29.5% (in adults with thoracic outlet syndrome),⁹ depending on race/ethnicity, sex, or symptoms of the population, while in our study, this number was estimated as 4.2%. Among the other frequently encountered spinal

segment variants, transitional vertebrae are estimated to be present in 11.2% (for TLTV)¹⁵ to 29.0% (for LSTV).¹⁶ Similar to other spinal segment variants, the prevalence of transitional vertebrae varies across subgroups of race/ethnicity and sex, and in our study on asymptomatic adults, the prevalence of transitional vertebra was on the order of 15.3% (for TLTV) and 26.4% (for LSTV).

It is estimated that the rate of wrong-level spine surgery is about 0.1%–2.1%,¹⁷ and considering the relatively high prevalence of spinal segment variants (eg, spinal segment distribution variant or transitional vertebrae) as contributors to the wrong-level

Lumbosacral Transitional Vertebra (LSTV)

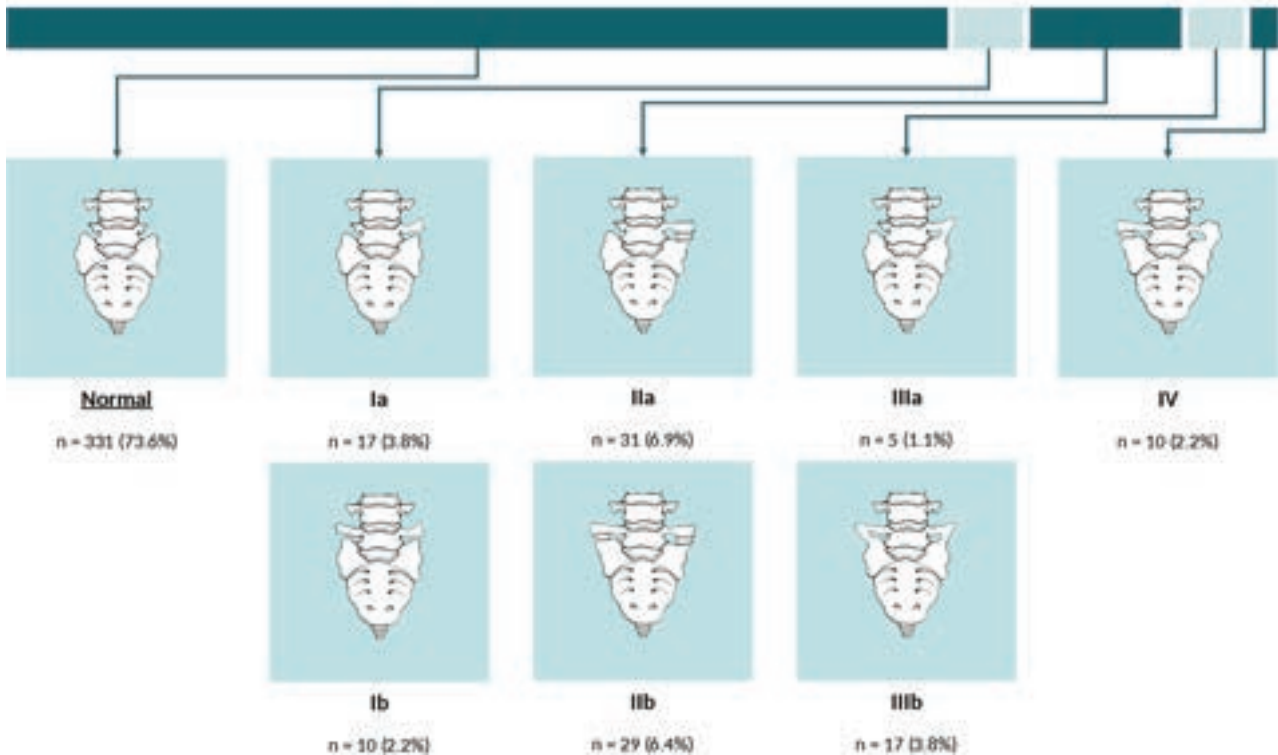


FIG 5. Frequency and distribution of the LSTV.

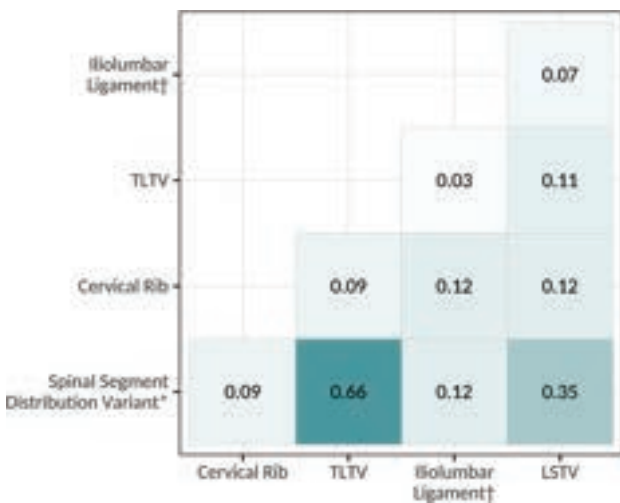


FIG 6. Correlation between spinal segment variants. The asterisk indicates an atypical number of presacral segments or an atypical distribution of thoracolumbar vertebrae; dagger, the inability to visualize the ILL.

spine interventions or operations.^{1,2} Although few anatomic landmarks have been suggested for the identification of vertebral levels, the unreliability of these landmarks limits their clinical use.¹⁸⁻²⁰ For instance, conus medullaris, dural sac termination (among the intradural landmarks), and abdominal vasculature (eg, the origin of major blood vessels like renal or common iliac arteries) location may change with aging,²¹ and

the accuracy of using the ILL for identifying L5 (fifth lumbar vertebra) is shown to be insufficient.⁸

In our study, we showed an association between transitional vertebrae or an inability to visualize the ILL with a spinal segment distribution variant. In other words, when a transitional vertebra is seen on imaging or the reader is unable to visualize the ILL, additional imaging should be considered to avoid wrong-level spine interventions or operations.

The findings of our study may have been tempered by a few, albeit important, limitations. First, the single-center design of our work and the lack of race/ethnicity diversity may limit the generalizability of our findings. Second, the use of CT examinations for assessing spinal segment variants (cervical rib, TLTV, or LSTV) has acceptable accuracy. However, compared with MR imaging, the CT examinations might not be the most accurate imaging technique for studying the ILL. Therefore, the frequency reported for the inability to visualize the ILL in our study may be an overestimate of the correct frequency in the clinical setting.

CONCLUSIONS

Our study shows that spinal segment variants are highly prevalent, ranging from 4.2% (cervical rib) to 26.4% (LSTV), even in a population of asymptomatic young adults. We showed that these variants are associated with each other, and for instance, the presence of TLTV or LSTV increases the odds of concurrent spinal segment distribution variants. These findings emphasize the previous suggestion by Carrino et al⁸ that when a spinal segment variant (eg, transitional vertebra) is diagnosed, additional

Table 3: Association among spinal segment variants

	Cervical Rib	TLTV	ILL ^a	LSTV
	OR (95% CI), P Value	OR (95% CI), P Value	OR (95% CI), P Value	OR (95% CI), P Value
ILL ^a	—	—	—	2.10 (0.79–5.31), .121
TLTV	—	—	1.50 (0.42–4.29), .482	1.87 (1.08–3.20), .023
Cervical rib	—	2.70 (0.92–7.09), .053	4.86 (1.06–16.54), .020	3.28 (1.29–8.47), .012
Spinal segment distribution variant ^b	2.44 (0.92–6.19), .062	66.13 (30.34–166.85), <.001	3.06 (1.18–7.80), .018	5.47 (3.43–8.80), <.001

Note:—The en dash indicates duplicate entries.

^aInability to visualize iliolumbar ligament.

^bAn atypical number of presacral segments or an atypical distribution of thoracolumbar vertebrae.

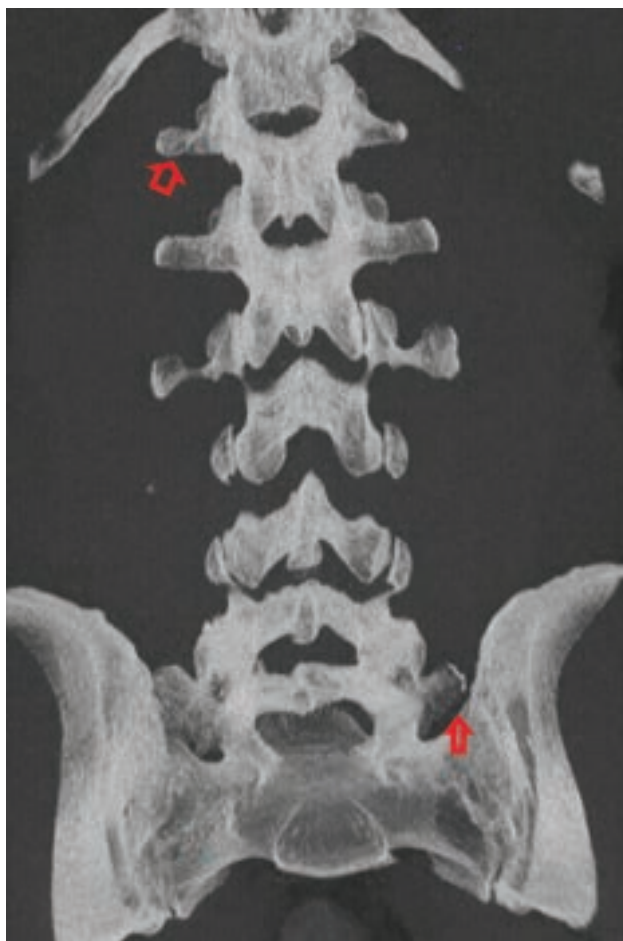


FIG 7. Example of thoracolumbar and lumbosacral transitional anatomy. Coronal MIP CT image of the lumbar spine demonstrates thoracolumbar and lumbosacral anatomy with an accessory ossification center on the right at T12 (open arrow) as well as a partially sacralized L5 vertebral body with an unfused left transverse process (closed arrow).

imaging should be considered for spine enumeration before interventions or operations.⁸

Disclosure forms provided by the authors are available with the full text and PDF of this article at www.ajnr.org.

REFERENCES

- Malanga GA, Cooke PM. Segmental anomaly leading to wrong level disc surgery in cauda equina syndrome. *Pain Physician* 2004;7:107–10 Medline

- Shah M, Halalmeh DR, Sandio A, et al. Anatomical variations that can lead to spine surgery at the wrong level, Part III: lumbosacral spine. *Cureus* 2020;12:e9433 CrossRef Medline
- Thawait GK, Chhabra A, Carrino JA. Spine segmentation and enumeration and normal variants. *Radiol Clin North Am* 2012;50:587–98 CrossRef Medline
- Redenbach DM, Nelems B. A comparative study of structures comprising the thoracic outlet in 250 human cadavers and 72 surgical cases of thoracic outlet syndrome. *Eur J Cardiothorac Surg* 1998;13:353–60 CrossRef Medline
- Wigh RE. The thoracolumbar and lumbosacral transitional junctions. *Spine (Phila Pa 1976)* 1980;5:215–22 CrossRef Medline
- Castellvi AE, Goldstein LA, Chan DP. Lumbosacral transitional vertebrae and their relationship with lumbar extradural defects. *Spine (Phila Pa 1976)* 1984;9:493–95 CrossRef Medline
- Furman MB, Wahlberg B, Cruz EJ. Lumbosacral transitional segments: an interventional spine specialist's practical approach. *Phys Med Rehabil Clin N Am* 2018;29:35–48 CrossRef Medline
- Carrino JA, Campbell PD Jr, Lin DC, et al. Effect of spinal segment variants on numbering vertebral levels at lumbar MR imaging. *Radiology* 2011;259:196–202 CrossRef Medline
- Henry BM, Vikse J, Sanna B, et al. Cervical rib prevalence and its association with thoracic outlet syndrome: a meta-analysis of 141 studies with surgical considerations. *World Neurosurg* 2018;110:e965–78 CrossRef Medline
- Shaikh A, Khan SA, Hussain M, et al. Prevalence of lumbosacral transitional vertebra in individuals with low back pain: evaluation using plain radiography and magnetic resonance imaging. *Asian Spine J* 2017;11:892–97 CrossRef Medline
- Galis F. Why do almost all mammals have seven cervical vertebrae? Developmental constraints, Hox genes, and cancer. *J Exp Zool* 1999;285:19–26 Medline
- Brewin J, Hill M, Ellis H. The prevalence of cervical ribs in a London population. *Clin Anat* 2009;22:331–36 CrossRef Medline
- Yan YZ, Li QP, Wu CC, et al. Rate of presence of 11 thoracic vertebrae and 6 lumbar vertebrae in asymptomatic Chinese adult volunteers. *J Orthop Surg Res* 2018;13:124 CrossRef Medline
- Ibrahim DA, Myung KS, Skaggs DL. Ten percent of patients with adolescent idiopathic scoliosis have variations in the number of thoracic or lumbar vertebrae. *J Bone Joint Surg Am* 2013;95:828–33 CrossRef Medline
- Doo AR, Lee J, Yeo GE, et al. The prevalence and clinical significance of transitional vertebrae: a radiologic investigation using whole spine spiral three-dimensional computed tomographic images. *Anesth Pain Med (Seoul)* 2020;15:103–10 CrossRef Medline
- Hanhivaara J, Määttä JH, Niinimäki J, et al. Lumbosacral transitional vertebrae are associated with lumbar degeneration: retrospective evaluation of 3855 consecutive abdominal CT scans. *Eur Radiol* 2020;30:3409–16 CrossRef Medline
- Grimm BD, Laxer EB, Blessinger BJ, et al. Wrong-level spine surgery. *JBJS Reviews* 2014;2:e2 CrossRef Medline
- Tureli D, Ekin G, Baltacioglu F. Is any landmark reliable in vertebral enumeration? A study of 3.0-Tesla lumbar MRI comparing skeletal, neural, and vascular markers. *Clin Imaging* 2014;38:792–96 CrossRef Medline

19. Farshad-Amacker NA, Lurie B, Herzog RJ, et al. **Is the iliolumbar ligament a reliable identifier of the L5 vertebra in lumbosacral transitional anomalies?** *Eur Radiol* 2014;24:2623–30 CrossRef Medline
20. Tokgoz N, Ucar M, Erdogan AB, et al. **Are spinal or paraspinal anatomic markers helpful for vertebral numbering and diagnosing lumbosacral transitional vertebrae?** *Korean J Radiol* 2014;15:258–66 CrossRef Medline
21. Kornreich L, Hadar H, Sulkes J, et al. **Effect of normal ageing on the sites of aortic bifurcation and inferior vena cava confluence: a CT study.** *Surg Radiol Anat* 1998;20:63–68 CrossRef Medline

Response to Letter Regarding the Article “Automated Segmentation of Intracranial Thrombus on NCCT and CTA in Patients with Acute Ischemic Stroke Using a Coarse-to-Fine Deep Learning Model”

We thank M. Tortora and F. Pacchiano for their interest in our recent study on using a coarse-to-fine deep learning model for automated segmentation of intracranial thrombus on NCCT and CTA in patients with acute ischemic stroke (AIS). We agree that accurate segmentation and quantification of intracranial thrombus in patients with AIS is complex and likely influenced by many pathophysiologic factors, such as calcifications, acute hemorrhagic, aneurysm, postischemic defects, and hyperattenuated media signs, which usually have image characteristics similar to those of intracranial thrombus and could be concurrent in the clinical scenario of suspected AIS.^{1,2}

However, our study aimed to develop an automated segmentation tool to replace manual delineation to segment thrombi from images of patients with AIS with confirmed large-vessel occlusion in the MCA region. This tool is the first step in assessing thrombus characteristics such as radiomics, location, length, volume, and permeability, because these image features could be used to predict recanalization with IV alteplase and first-attempt recanalization with thromboaspiration.^{3,4} In this regard, we included only patients with anterior circulation occlusions, excluding patients with posterior and basilar occlusions and those with complex pathophysiologic factors. In addition, we deliberated using thin-section noncontrast CT and CTA as input to eliminate image interference, such as artifacts in downstream radiomics analyses.

An interesting finding in our article is that our trained model can detect and segment thrombi in patients with small- and medium-sized vessel occlusions even if those images were not used for training. Although this experiment shows the great generalizability of our model, it was only tested on a limited data set. More training images with different pathologies and image quality are required to

refine our model, and more comprehensive evaluations are also desired to incorporate the model into current clinical routine.

Disclosure forms provided by the authors are available with the full text and PDF of this article at www.ajnr.org.

REFERENCES

- Schmitt N, Mokli Y, Weyland CS, et al. **Automated detection and segmentation of intracranial hemorrhage suspect hyperdensities in non-contrast-enhanced CT scans of acute stroke patients.** *Eur Radiol* 2022;32:2246–54 CrossRef Medline
- Seyam M, Weikert T, Sauter A, et al. **Utilization of artificial intelligence-based intracranial hemorrhage detection on emergent non-contrast CT images in clinical workflow.** *Radiol Artif Intell* 2022;4:e210168 CrossRef Medline
- Qiu W, Kuang H, Nair J, et al. **Radiomics-based intracranial thrombus features on CT and CTA predict recanalization with intravenous alteplase in patients with acute ischemic stroke.** *AJNR Am J Neuroradiol* 2019;40:39–44 CrossRef Medline
- Hofmeister J, Bernava G, Rosi A, et al. **Clot-based radiomics predict a mechanical thrombectomy strategy for successful recanalization in acute ischemic stroke.** *Stroke* 2020;51:2488–94 CrossRef Medline

● **Kairan Zhu**

Department of Clinical Neurosciences & Hotchkiss Brain Institute
Cumming School of Medicine, University of Calgary
Calgary, Alberta, Canada

College of Electronic Engineering
Xi'an Shiyou University
Xi'an, Shaanxi, China

● **B.K. Menon**

Department of Clinical Neurosciences & Hotchkiss Brain Institute
Cumming School of Medicine, University of Calgary
Calgary, Alberta, Canada

● **W. Qiu**

School of Life Science and Technology
Huazhong University of Science and Technology
Wuhan, Hubei, China

This work was supported by Natural Science Basic Research Plan in Shaanxi Province of China (Program No. 2021JM-413), Distinguished Young Scholars of the National Natural Science Foundation of China (Overseas), and National key research and development program (No. 2022YFE0209900).
<http://dx.doi.org/10.3174/ajnr.A8075>